UNIVERSITY OF SOUTHAMPTON

Faculty of Engineering and Physics
School of Physics and Astronomy

Auroral X-ray emissions from the gas giant planets: remote sensing and in situ magnetospheric diagnostics

DOI: 10.1002/0470841559.ch1

by

Dale Michael Weigt

MSci

ORCiD: 0000-0001-5427-6537

A thesis for the degree of
Doctor of Philosophy

June 2022

University of Southampton

Abstract

Faculty of Engineering and Physics
School of Physics and Astronomy

Doctor of Philosophy

Auroral X-ray emissions from the gas giant planets: remote sensing and in situ magnetospheric diagnostics

by Dale Michael Weigt

The thesis begins by introducing the reader to the fundamental concepts used throughout the field of space physics today (Chapter 1) and then applies them to the the jovian magnetosphere, the largest coherent object (or fully unified structure if visible to the naked eye) within our Solar System (Chapter 2). This chapter focuses on the structure and internal dynamics of the jovian magnetosphere observed throughout the literature, with particular emphasis of the complex X-ray auroral emissions at the poles. This chapter concludes by analysing previous literature and the ongoing effort to search for the complicated magnetospheric driver, or drivers, responsible for these complex emissions at the gas giant planets - the largest open question in our field, which this thesis aims to answer.

The studies that are contained within this thesis focus on constraining the magnetospheric driver, or drivers, responsible for the X-ray auroral emissions at the gas giants, in particular at *Jupiter*. The research throughout focuses on observations performed by the *Chandra X-ray telescope (CXO)*, using the onboard high resolution camera *(HRC)*, combined with by other remote sensing data, such as ultraviolet observations form the *Hubble Space Telescope (HST)*, and *in situ* spacecraft data from *Juno* , when available to provide vital magnetospheric context (Chapter 3). The first work chapter (Chapter 4) is a case studying analysing a *Chandra* observation during a compression event while *Juno* was near its apojove position, the furthest point from Jupiter in its orbit. The mapping analysis of the X-ray auroral emissions was carried on using a newly developed and freely available Python pipeline (Weigt, 2021), utilising the high spatial resolution of *Chandra*. This mapping algorithm is used throughout this thesis. Chapter 5 then applies these analytical methods, techniques and definitions to the full $\sim$ 20-year *Chandra* dataset of the northern auroral emissions to determine the more extreme and typical behaviour of the northern X-ray emissions. This case study eludes to the possibility of numerous magnetospheric drivers likely located in the noon and dusk flank of the jovian magnetosphere, based on the Grodent Anomaly Magnetic field model (Grodent et al., 2008), with a statistically significant

region at noon. Comparisons of the timing and mapping analysis with previous literature highlight that the X-ray emissions may be associated with ultra-low frequency wave activity in the form of Shear Alfvén waves.

Chapter 6 expands on the the idea of multiple drivers through the creation of physics-informed *auroral families* during the *Juno*-era, allowing us to associate morphological features with magnetospheric drivers located throughout the jovian system. The X-ray auroral morphologies identified in this case study may also be a useful monitor of magnetospheric conditions at Jupiter.

The penultimate chapter (Chapter 7) changes focus to the exploration of kronian X-rays, analysing *Chandra* observations aimed to monitor Saturn's magnetospheric response during a rare planetary alignment with Jupiter. Due to the orbits of the planets, this event occurs once in every $\sim$ 19-20 years, analysing this unique parameter space for the first time. This case study predicts the flux and power of the emissions and compares with solar flux data from *Geostationary Operational Environmental Satellites (GOES)* to find any correlations between solar activity and the counts detected from Saturn's disk emissions.

The thesis concludes with an exploration into future work, further utilising the *Chandra* data as much as possible and comparing with other datasets to provide more coherent catalogues of the temporal and spatial behaviour of the auroral emissions that can be used for future studies.

Contents

Declaration of Publications

The research I present here was undertaken during the course of this doctoral program and has led to the submissions and publication of the following three first author scientific papers in important journals:

D. M. Weigt, C. M. Jackman, W. R. Dunn, G. R. Gladstone, M. F. Vogt, A. D. Wibisono,G. Branduardi-Raymont, D. Altamirano, F. Allegrini, R. W. Ebert, P. W. Valek, M. F.Thomsen, G. Clark, and R. P. Kraft, 2020, *Chandra Observations of Jupiter's X-rayAuroral Emission During Juno Apojove 2017*, Journal of Geophysical Research: Planets, 125(4): e2019JE006262, DOI: 10.1029/2019JE006262

D. M. Weigt, C. M. Jackman, M. F. Vogt, H. Manners, W. R. Dunn, G. R. Gladstone,R. Kraft, G. Branduardi-Raymont, C. K. Louis, and S. C. McEntee, 2021a, *Characteristics of Jupiter's X-Ray Auroral Hot Spot Emissions Using Chandra*, Journal of Geophysical Research: Space Physics, 126(9), DOI: 10.1029/2021JA029243

D. M. Weigt, W. R. Dunn, C. M. Jackman, R. Kraft, G. Branduardi-Raymont, J. D. Nichols, A. D. Wibisono, M. F. Vogt, and G. R. Gladstone, 2021b, *Searching for Saturn's X-rays during a rare Jupiter Magnetotail crossing using Chandra*, Monthly Notices of the Royal Astronomical Society, 506(1):298–305, DOI: 10.1093/mnras/stab1680

Index of Figures

Index of Tables

Declaration of Authorship

I declare that this thesis and the work presented in it is my own and has been generated by me as the result of my own original research.

I confirm that:

1. This work was done wholly or mainly while in candidature for a research degree at this University;
2. Where any part of this thesis has previously been submitted for a degree or any other qualification at this University or any other institution, this has been clearly stated;
3. Where I have consulted the published work of others, this is always clearly attributed;
4. Where I have quoted from the work of others, the source is always given. With the exception of such quotations, this thesis is entirely my own work;
5. I have acknowledged all main sources of help;
6. Where the thesis is based on work done by myself jointly with others, I have made clear exactly what was done by others and what I have contributed myself;
7. None of this work has been published before submission

Signed:..... Date:.....

Acknowledgements

There is no question that the past few years in my PhD has been quite the challenge both mentally and emotionally, but I can honestly say I have never wanted to throw in the towel even when crippled with anxiety. I have been very close to giving up but the solid support network composed of my friends, family and colleagues has always given be the strength to persevere, and for that I will be forever grateful. Thank you to my physics teacher Gerry Burns for making physics really interesting at school and eventually helping me to pursue an astrophysics degree.

I apologise in advance that this may be the longest Acknowledgements section you may have to read and if I unintentionally miss anyone out, there are just so many people I want to thank...

First of all I want to give a quick thank you to my fantastic and enthusiastic undergraduate supervisor Lyndsay Fletcher, without whom, I would not have embarked on this journey. I will always remember the day you scheduled time in your busy schedule to make time to have a chat and a cup of tea with me, someone in their final year undergoing an existential crisis about 'what next?'. You sat me down, got me to pull myself together and gave me a list of names of people to contact about projects related to what I was doing at the time. That cup of tea will always be the most memorable and, not to sound too cliché, life changing.

One of those names on Lyndsay's list was my amazing supervisor Caitríona Jackman. Caitríona has always been so supportive from the very beginning, even before she hired me with a pre-interview Skype call just to make sure that we had compatible personalities to work together (and that I would support Ireland in the Six Nations). From then, Caitríona has supported me and been the voice of reason when I have been frustrated and struggling in academia (during a global pandemic - had to be mentioned); my (many) rants about science in our field and when I was dealing with more personal, family matters - the trait of a great supervisor in my opinion. I will forever be thankful for Caitríona's sixth sense of spotting my grammar mistakes a mile off, even before they have entered my mind, which has genuinely revolutionised the way I write. Finally, I just want to say that how Caitríona developed a brand new, and flourishing, research group at DIAS during a pandemic and got us all working (and living in my case) together is genuinely inspirational. I hope I have absorbed some of her wisdom and perseverance during this time.

I would like to thank my secondary supervisor Diego Altamirano who supported me through difficult times at the beginning of my PhD and has taught me how to be very rigorous with my timing analysis. When I witnessed Caitríona and Diego high-fiving each other while passing each in the corridor during a normal working day, that's

when I knew I was lucky with my supervisor team at Southampton and I was in safe hands.

The Space Environment Physics Group in Southampton has always been a place of great joy, great advice and questionable puns (special mention to John Coxon) and it has been a delight being part of it. I would like to thank those, past and current members, in my research group: David Price (or 'Senior PhD student), Laura Fryer, James Waters (Captain Cool), John Coxon, Rob Fear, Dan Whiter, Imogen Gingell, Betty Lanchester, Tadhg Garton, James Plank, Rowan Dayton-Oxland and Patrik Krcelic for all their insights and keeping me sane during the pandemic (last time I will mention it) with our weekly coffee breaks and check-ups. David in particular helped me a lot during the beginning and was a source of wisdom and advice which I have tried to pass on to the new PhD students (apologies to Laura who I imparted my advice on). Finally, I want to give a special mention to Rob Fear and Dan Whiter who have allowed me to bounce off ideas and introduced me to the world of public engagement and outreach, which I love and hope to continue. I would say though that just because "Earth is the only planet with pubs in the Solar system", does not make it the best.

The entire Astronomy Group has been one of the friendliest group of people I have known and it has been a privilege to be part of. Special mentions to: Bella Boulderstone, Claire Greenwell, Triana Almeyda, David 'Kiwi Dave' Williamson, Peter Boorman, Edward Parkinson, Miika Pursianen (and his epic badminton skills), Ella Guise, Michael Johnson, Phil Wiseman and many more. Bella and Claire in particular have been very supportive and always allowed me to have many a rant. Thank you to everyone in the Astro group for being so welcoming.

Outside of the Southampton group, I have many more people to thank. First I want to give a HUGE thanks to Will Dunn who has pretty much been my third supervisor throughout my PhD. It has been a genuine privilege to collaborate with someone who is so unbelievably hard-working, enthusiastic, determined to make a positive change in our field and also has time to be someone to talk to or a shoulder to cry on outside of work. His ongoing work with the ORBYTS project is nothing short of inspirational and is changing many children's lives. Will is never short on ideas and his passion is infectious and definitely encouraged me to be a better researcher. Thank you again Will, it has been absolute delight to have met you and I hope we continue to work together.

Another special thank you goes to the *Jovian X-ray Team*: Affelia Wibisono, Graziella Branduardi-Raymont, Seán McEntee, Ralph Kraft, Randy Gladstone as well as Will and Caitríona. I have nothing but the upmost respect for all these people and it is has been amazing to work with each of you. Their ideas, guidance and contributions and made all of this research possible and I will be forever grateful. It has been a joy to

watch this small and unique research field grow over the past 3-4 years and to add my contribution. I would also like to give a huge thank you to honourable X-ray team members Marissa Vogt and Arthur Manners whose support, guidance and ideas I will cherish, especially during the more difficult times of my PhD. Outside of the jovian X-ray family, I would like to give a special shout-out to Sarah Badman, Gabby Provan and Licia Ray who have always been a friendly face at many conferences and have always offered some great advice.

Finally, I would like thank the new Magnetospheres group at DIAS: Corentin Louis (best flatmate), Alexandra Fogg, Kevin Smith, Elizabeth O'Dwyer, as well as Seán, Caitríona, Tadhg and James W for being such lovely people all brought together under unique and difficult circumstances. It is safe to say this new group is flourishing and has a very bright and successful future which I look forward to continue being part of. A special thank you to the Astronomy and Astrophysics section DIAS for making me feel welcome as a visiting PhD student, in particular Sophie Murray and Peter Gallagher for also making the difficult transition to the quirky and fascinating Dunsink Observatory relatively stress-free. I will however not miss the cows...

Unfortunately for the reader, I still have much gratitude to express to those outside of academia. First of all I want to give the biggest thank you to my largest supporters who I dedicate my thesis to: my Mum and Dad (Terri and Mark) and the rest of the *'Spangles'* family. I cannot thank my Mum and Dad enough for being my rock throughout this whole process and effectively providing me with free therapy sessions. They have supported me from the very beginning and only ever wanted me to be happy. They never once questioned any of my career choices and have just brought me up to be as independent as possible and just follow my dreams. I love you guys so much and will always be appreciative of Mum letting me phone her at **all** hours before and after any exam (which there were a lot of...), just to calm me down. Her words still echo in my head: *"And what do I keep saying to you, nobody has died. Just do your best and we will love you no matter what"*. This unwavering support is echoed throughout my family who have been the strongest support and have never doubted my abilities, even when I was stuck in a rut. A special thank you to Auntie Gina and Auntie Kathleen who I adore and provide me the strength to carry on. They will definitely make sure they will be first in the guest list if I one day move somewhere exotic. I am also dedicating this thesis to those family members who are no longer. Over the course of my university career, our family has lost too many amazing people: Uncle Kenny, Aunt Trisha and Uncle Malcolm - all would light up anyone room and each of them had their own quirky characters. Years before we also lost our beloved Auntie Georgie, Granny Jeanie, Nana, Aunt Lisa and Horst, again I had nothing but love and admiration for them all and myself, and the family, were devastated when we lost all of them. My Aunt Lisa in particular seemed to think I had the ability to

attend and study hard at university before anyone else did! I hope I have made each and every one of them proud.

Finally I would like to say a huge thank you to all my great friends who have been supporting me and keeping me grounded throughout this journey. Special mention to Ellie Bird, Matt Graham, Rowan Knight and Cameron MacNab who have kept me sane and grounded during this process; been my rock as well during the difficult times; allowed me to practice my talks with them and forever correcting me on my bad grammar - I did good guys! A huge thank you and big hug to my great friend, and basically sister, Bethan Ceiriog Simpson - I love you loads and you never fail to make me laugh and smile, no matter how I am feeling. I cannot wait to see you blossom as a nurse, this is your true calling. My undergrad physics buddies: Kris, Sara, Lisa, Matt, Lindsey and George who I still keep in touch with despite us going out separate ways, thank you for making a difficult and gruelling undergrad bearable and, again, keeping me grounded. A special shout-out to Kris and Sara who embarked on this journey at the same time, you guys are brilliant and doing amazing - drinks on me when we all pass. To my friends in Southampton: Jesse Rolfe, Cory Flanagan, Mikey Jennings, Stella Harrison, Ed Guy, Sophie Hart, Daisy Woodley, Hannah Baird, Katie Walker and many, many more you made my final year in Southampton so much fun. It was a difficult decision to move to Ireland and I miss you all loads. And finally my dear friend Laura Turpeinen, I will always hold our friendship and all the Finnish wisdom you impart close to my heart - I will definitely be visiting you soon.

There are so many more people I would like to thank but this section is getting excessively long. Thank you again to all who supported me and continue to do so today - without you, none of this would be possible.

All my work has been supported by the Science and Technology Facilities Council (STFC) studentship ST/S505703/1 and long term attachment grant to work at the Dublin Institute for Advanced Studies (DIAS) as a visiting PhD student.

To my Mum and Dad, the Spangles family and for loved ones sadly no longer with us,

Thank you for all your support and I love you loads.

Chapter 1

Introduction

"I now see the necessity of a beginning"
- Albert Einstein

The research presented in this thesis focuses on observations and analysis of auroral X-ray emissions from the gas giants, massive planets mainly composed of hydrogen and helium which cannot escape the planet's atmosphere, primarily using data from the Chandra X-ray Telescope (CXO). These *Chandra* X-ray observations are supported and compared with other remote sensing (measurements taken at a distance from the source) and *in situ* (measurements taken from the surrounding environment of the detector) datasets, across multiple wavelengths, to provide diagnostics of the magnetospheres during each observation window. The definition and structure of a planetary magnetosphere is presented in Section 2. The instrumentation and datasets used in this thesis are discussed in Chapter 3. The use of *in situ* data to determine the state of the jovian magnetosphere and the implications that has on the pulsating X-ray auroral driver(s) is explored further in Chapter 4. In Chapters 5 and 6, the typical and extreme temporal and morphological behaviour of the most intense auroral emissions are first examined in a thorough and extensive statistical study, followed by further characterising auroral structures by comparing with other datasets (such as *Juno* and the Hubble Space Telescope). Chapter 7 concludes the research discussions by exploring the first detection of auroral X-rays at Saturn during a rare planetary alignment with Jupiter that occurs once every ~ 20 years.

The first three chapters of this thesis will provide the background knowledge that supports and forms the foundations of the aforementioned studies. In this introductory chapter, the fundamental physical concepts, theorems and definitions of space plasma physics will be reviewed and examined. The fundamentals discussed here will be contextualised in a magnetospheric setting in Chapter 2.

1.1 Definition of a plasma

One useful definition of a plasma states that *a plasma is a quasineutral gas of charged and neutral particles which exhibits collective behaviour* (e.g., Chen, 2016). The "quasineutral" nature results from the density of the ion (n_i) and electron species (n_e) in the plasma being approximately equal such that $n_\mathrm{i} \simeq n_\mathrm{e} \simeq n$, where n is the plasma density. The "collective" interactions of a plasma are derived from the plasma motions that depend on both local conditions and the state of the plasma at long ranges from forces produced by the surrounding magnetic and applied electric field. The remainder of this section will look at the criteria required to formally define a plasma.

1.1.1 Debye shielding

Considering an isolated ion of charge q, the electrostatic potential, ϕ, of the ion is defined to be

$$\phi = \frac{q}{4\pi\epsilon_0 r} \tag{1.1}$$

where r is the distance at which the ion is observed and $\epsilon_0 = 8.854 \times 10^{-12}$ F m^{-1} is the permittivity of free space. If it is then assumed that the ion is enveloped in a gas containing other ions and electrons (e.g. a plasma), the positive ion will attract the oppositely charge electrons and repel other positive ions. The electron distribution will change the potential, reducing ϕ at large distance scales (e.g., Kivelson, 1995). As the surrounding ions are more massive than the electrons, as they are composed of protons and neutrons with a single proton being ~ 1836 time more massive than electrons, their motion as a response to any change of the potential is negligible in comparison. The now "shielded" ion will have a shielded potential, ϕ_s, of the form

$$\phi_\mathrm{s} = \frac{q \exp\left(-\frac{r}{\lambda_\mathrm{D}}\right)}{4\pi\epsilon_0 r} \tag{1.2}$$

where λ_D is the *Debye length* (Debye and Hückel, 1923). Compared to the electric potential of an ion in a vacuum (Equation 1.1), the shielded ion now has an additional exponential decay term which dominates when $r \geq \lambda_\mathrm{D}$. For an electron-proton plasma, this parameter is given by

$$\lambda_\mathrm{D} = \left(\frac{\epsilon_0 kT}{ne^2}\right)^{\frac{1}{2}} \tag{1.3}$$

where $k = 1.381 \times 10^{-23}$ m^2 kg s^{-2} K^{-1} is the Boltzmann constant, T is the plasma temperature, n is the plasma density and $e = 1.602 \times 10^{-19}$ C is the charge of an electron. The Debye length therefore is the greatest distance over which any departures form charge neutrality may occur in a plasma in thermal equilibrium. Therefore, if the system dimensions L are far greater than λ_D, the plasma is shielded from any large electric potentials or fields that may be introduced into the system, otherwise known as *Debye shielding* (e.g., Chen, 2016).

If a foreign charge enters the surrounding region of a plasma and disturbs its quasi-neutral state, the response time for the plasma, t_D, to adjust and return to quasi-neutrality can be calculated from the ratio of λ_D and thermal velocity of the plasma, $v_{th} = \sqrt{(kT/m)}$ (where m is the mass of the plasma), as follows

$$t_D \approx \frac{\lambda_D}{v_{th}} = \left(\frac{\epsilon_0 kT}{ne^2} \cdot \frac{m}{kT} \right)^{\frac{1}{2}} = \omega_p^{-1} \tag{1.4}$$

where ω_p is the plasma angular frequency (with units of radians s^{-1}) and all symbols have the same definitions as before (e.g., Gibbon, 2016). By dividing ω_p by one revolution (or 2π radians), we obtain the *plasma frequency*, f_p

$$f_p = \frac{\omega_p}{2\pi} \ [\text{Hz}] = 9\sqrt{n_e} \ [\text{kHz}] \tag{1.5}$$

where n_e has units cm^{-3} when expressing the plasma frequency for electrons, for example, in terms of the density of the plasma. The multiplicative term is calculated from the constants in Equation 1.4. This parameter is important as it provides a useful way to measure plasma density of a given region using the frequency observed from, for example, a spacecraft.

1.1.2 The plasma parameter

In order for the Debye shielding condition to hold, there must be enough particles in the plasma. The number of particles, N_D, is known as the *plasma parameter* and can be calculated for a sphere with radius λ_D (a *Debye sphere*) using Equation 1.3

$$N_D = \frac{4}{3}\pi n \lambda_D^3 \tag{1.6}$$

Therefore, for "collective" behaviour to occur for a plasma, $N_D \ggg 1$ otherwise the system is described as a neutral or ionised gas containing independent charged particles.

1.1.3 Plasma collision frequency

The rate at which a single particle within the plasma experiences collisions with other surrounding particles (e.g. feels an electrostatic force from all other particles within a Debye sphere) is known as the *plasma collision frequency*. As a result, each particle inside the plasma will feel a continually fluctuating electric field and undergo a random walk with some velocity. Therefore for a gas to behave like a plasma, the product of the plasma collision frequency, ν_B, and mean time between collisions involving any charged particles, τ, must be > 1 (e.g., Chen, 2016). Therefore this conditions reiterates that we need a vast number of particles within the Debye sphere for the plasma conditions to hold.

The remainder of this chapter will look at the how plasma physics defines the behaviour of a plasma in many different magnetic and electric field configurations, using a variety of descriptions.

1.2 Maxwell's equations

The behaviour of space plasmas observed throughout the observable universe are governed by electromagnetic fields. These electromagnetic fields must follow four fundamental laws known as Maxwell's equations (e.g., Griffiths, 1999). Therefore the behaviour of space plasmas can be also be derived from Maxwell's equations (in SI units) which are as follows

$$\nabla \cdot \mathbf{E} = \frac{\rho}{\epsilon_0} \tag{1.7}$$

$$\nabla \cdot \mathbf{B} = 0 \tag{1.8}$$

$$\nabla \times \mathbf{E} = -\frac{\partial \mathbf{B}}{\partial t} \tag{1.9}$$

$$\nabla \times \mathbf{B} = \mu_0 \mathbf{J} + \mu_0 \epsilon_0 \frac{\partial \mathbf{E}}{\partial t} \tag{1.10}$$

where $\mathbf{E}$ and $\mathbf{B}$ are the electric and magnetic field vector respectively, ρ is charge density, $\mathbf{J}$ is the current density vector and $\mu_0 = 1.257 \times 10^{-6}$ m kg s^{-2} A^{-2} is the permeability of free space with ϵ_0 having the same definition as before.

The first two equations, Equations 1.7 and 1.8 or Gauss' laws for electricity and magnetism respectively, state how these electromagnetic fields are created. Gauss' law for electricity (Equation 1.7) relates the electric field, $\mathbf{E}$, on a given surface to the total charge of the enclosed source with density, ρ. This holds for both static and moving charges and fundamentally states that an electric field is produced when a charge

exists. Gauss' law for magnetism (Equation 1.8) states that no magnetic monopoles can exist. This means that the divergence of the magnetic field, **B**, is always zero implying that all magnetic fields must always exist in a continuous loop and never as a single "magnetic charge" or monopole (e.g., Griffiths, 1999).

The latter two Maxwell's equations, Equations 1.9 and 1.10 or Faraday's law and Ampère-Maxwell's law respectively, state how the spatial and temporal behaviour of the electric and magnetic field are coupled together. Faraday's law (Equation 1.9) states how a time-dependent magnetic field, **B**, evolving over time induces an electric field. As a result, the line integral of the electric field around a closed loop surrounding will always generate an electromotive force (EMF) or potential difference which is equivalent to the rate of change of magnetic flux through the enclosed loop. The final of Maxwell's equations, the Ampère-Maxwell's law (Equation 1.10), states that an induced magnetic field is created when a current is produced. The displacement current contributions are shown in the second term of the right hand side of Equation 1.10 (e.g., Griffiths, 1999).

The Maxwell's equations can be simplified in many different regimes. For example, in free space no charge or currents can exist (e.g. $\rho = 0$, $\mathbf{J} = 0$) and therefore Equations 1.7 and 1.10 will read as $\nabla \cdot \mathbf{E} = 0$ and $\nabla \times \mathbf{B} = \mu_0 \epsilon_0 \frac{\partial \mathbf{E}}{\partial t}$ respectively. In the theory of magnetohydrodynamics to explain the behaviour of plasmas (discussed further in Section 1.4), the displacement current contributions are neglected and assumes that there is charge neutrality throughout the plasma (e.g. Kivelson, 1995) . Maxwell's equation will therefore read:

$$\nabla \cdot \mathbf{E} = 0 \tag{1.11}$$

$$\nabla \cdot \mathbf{B} = 0 \tag{1.12}$$

$$\nabla \times \mathbf{E} = -\frac{\partial \mathbf{B}}{\partial t} \tag{1.13}$$

$$\nabla \times \mathbf{B} = \mu_0 \mathbf{J} \tag{1.14}$$

The remainder of this chapter will apply Maxwell's equations in many plasma descriptions to explore a variety of different plasma behaviours and diagnostics.

1.3 Particle orbit theory

Plasmas observed in a laboratory or space setting have be found to exhibit behaviours associated with both a fluid and a collection of individual particles. In order to understand the unusual, mixed behaviour of plasmas, the motions of the individual particles in external electric and magnetic fields first need to be understood (e.g.,

Chen, 2016). This is called *particle orbit theory* and is applicable to a low-density plasma regime (i.e. small N_D) where only single-particle trajectories need to be considered. In this section, the external electric and magnetic fields are assumed to dominate over any electromagnetic interactions between the charged particles and thus not affected by the plasma.

The equation of motion for a non-relativistic charged particle is this regime is given by

$$m\frac{d\mathbf{v}}{dt} = q\left(\mathbf{E} + \mathbf{v} \times \mathbf{B}\right) \tag{1.15}$$

where m is the mass of the particle, $\mathbf{v}$ is the velocity vector and all other symbols have the same meaning as defined previously. Equation 1.15 shows how the force created from the acceleration of the particle (left hand side) is equal to the Lorentz force produced from the electric and magnetic field enveloping the charged particle. We now examine how this equation of motion is affected by different electric and magnetic field configurations.

1.3.1 Particle motion in a constant B-field

In this description, the magnetic field is assumed to be constant in one direction ($\mathbf{B} = B\hat{\mathbf{e}}_z$, where $\hat{\mathbf{e}}_z$ is the unit vector in the z-direction) and there is no electric field ($\mathbf{E} = 0$). From Equation 1.15, without the presence of an electric field, no work is done on the charged particle by $\mathbf{B}$ as the particle's kinetic energy remains constant (e.g., Chen, 2016). Therefore the motion of the particle can be split into the perpendicular and parallel components. From computing the cross product in Equation 1.15, there is no parallel component to $\mathbf{B}$. The time derivative of perpendicular components of motion show that the charged particle gyrates at angular frequency, ω_c, given by

$$\omega_c = \frac{|q|B}{m} \tag{1.16}$$

where B is the magnetic field component associated with ω_c. Equation 1.16 defines the *gyrofrequency* or *cyclotron angular frequency* of the particle and is dependent on the mass of the particle. Since the mass of an electron ($m_e = 9.109 \times 10^{-31}$ kg) is far less than the mass of a proton ($m_p = 1.673 \times 10^{-27}$ kg), the electron gyrofrequency is greater than the proton gyrofrequency (i.e. $\omega_{ce} \gg \omega_{cp}$). The solutions to the particle's equation of motion describe the *gyromotion* around the z-axis at ω_c. The radius of the orbit is known as the *Larmor radius* given by

$$r_L = \frac{v_\perp}{\omega_c} = \frac{mv_\perp}{qB} \tag{1.17}$$

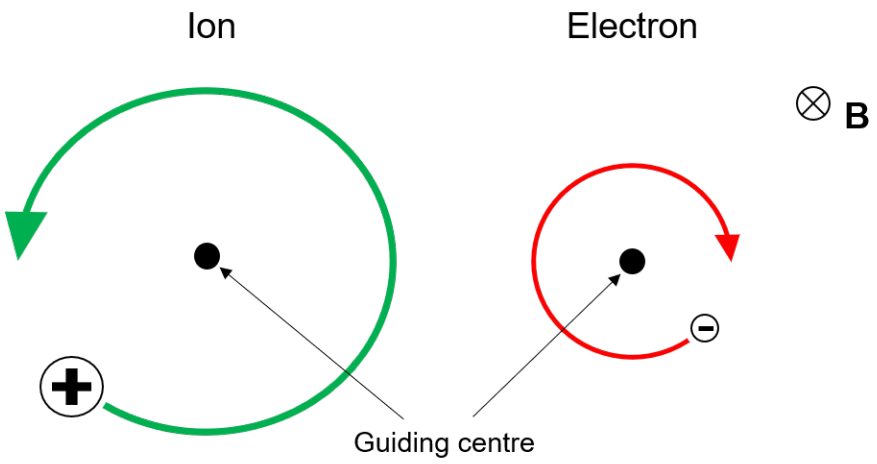

FIGURE 1.1: Larmor orbits around the guiding centre of an ion (left) and an electron in a constant magnetic field. **B** is directed into the page. Figure adapted from Figure 2.1 in Chen (2016).

where $v_\perp$ is the constant perpendicular velocity component of the charged particle. As the Larmor radius is also dependent on the mass of the particle, the orbit for an ion is larger than the electron equivalent (i.e. $r_{\mathrm{Li}} \gg r_{\mathrm{Le}}$). The centre of the orbit is called the *guiding centre* which moves uniformly along **B**. Therefore the trajectory of the particle in this description is a circular orbit around a guiding centre (or a helix) which can drift in a direction perpendicular to **B** (e.g., Chen, 2016; Kivelson, 1995). When **B** and everything else in the system remains constant, there is no drift of the guiding centre perpendicular to **B**. The direction of gyration is determined by the magnetic field generated by the charged particles in the plasma which opposes the prescribed magnetic field (i.e. electrons and ions gyrate in opposite directions due to the opposite signs of the charges). This is shown in Figure 1.1 for an ion and an electron, with the magnetic field going into the page.

1.3.2 Particle motion in non-uniform E- and B- fields

For this description, the electric field is non-zero, $\mathbf{E} = (E_x, 0, E_z)$, $\mathbf{B} = B\hat{\mathbf{e}}_z$ like before and both kinetic and potential energy are conserved. The electric field is found to do work on a charged particle in this setting, producing an acceleration in the component of the electric field parallel to **B**, E_z. The component of **E** perpendicular to the magnetic field, $E_\perp$, causes the guiding centre to drift across the field lines. In this field configuration, an ion in a circular orbit when moving parallel to **E** will result in an increase in $v_\perp$ and r_{L} as the ion gains energy. In the second half of the cycle, the ion is anti-parallel to **E** and will lose energy (e.g. r_{L}). The difference in the Larmor radius on either side of the orbit results in an $\mathbf{E} \times \mathbf{B}$ *drift*, v_{E}, at a constant velocity with the gyro-orbit being not a closed circles. This is generalised by:

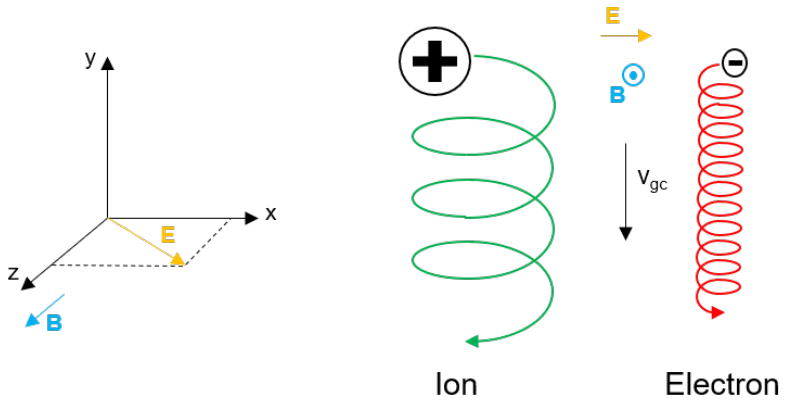

FIGURE 1.2: Same nomenclature as Figure 1.1. Schematic of particle drifts, with drifting velocity v_{gc}, in perpendicular electric and magnetic fields. **B** is directed pointing out of the page. Figure adapted from Figure 2.2 in Chen (2016).

$$\mathbf{v}_{\mathrm{E}} = \frac{\mathbf{E} \times \mathbf{B}}{B^2} \tag{1.18}$$

In this description, solving Equation 1.18 finds that the guiding centre drifts in the negative y-direction (-$\hat{\mathbf{e}}_{\mathrm{y}}$) with velocity $v_{\mathrm{gc}} = v_{\mathrm{E}} = \frac{E_x}{B}$ i.e. the drift only occurs when $E_x > 0$ (e.g., Chen, 2016). An electron would gyrate in the opposite direction with a smaller orbit as shown in Figure 1.2.

In a unidirectional, non-uniform magnetic field (i.e. there is a change of gradient) without an applied electric field, a charged particle will experience a drift perpendicular to the direction of **B** and the gradient of the field, ∇B. In this description, the magnetic field strength is found to increase in the positive y-direction, the direction of increasing gradient (e.g. $B_z = B_z(y)$). The configuration is shown in Figures 1.3a) and (b). The resulting drift is called a ∇B *('grad B') drift*, $\mathbf{v}_{\nabla \mathrm{B}}$, and is given by the following equation

$$\mathbf{v}_{\nabla \mathrm{B}} = \pm \frac{v_{\perp}^2}{2\omega_{\mathrm{c}}} \frac{\mathbf{B} \times \nabla B}{|B|^2} \tag{1.19}$$

where the '$\pm$' indicates the sign of the charged particle and the factor of $1/2$ arises from averaging the external force over a gyro-period. As shown in both Equation 1.19 and Figure 1.3c), oppositely charged particles will drift in opposite directions unlike the $\mathbf{E} \times \mathbf{B}$ drift. For the case of ions and electrons, a current will be produced across **B** (e.g., Chen, 2016).

The curvature of the magnetic field will also produce a centrifugal force felt by gyrating charged particles. This contributions made from the curvature accompany

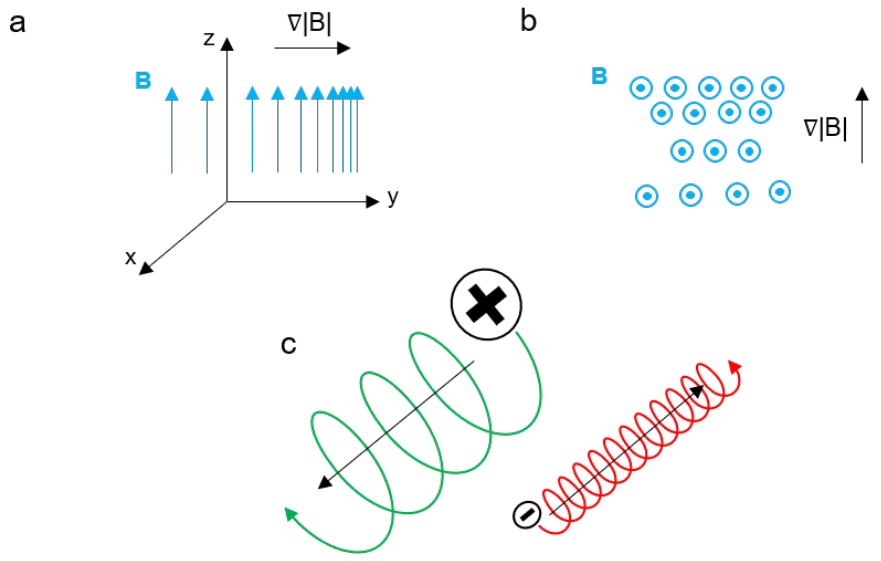

FIGURE 1.3: Similar format to Figure 1.2 with a change of axis direction for illustration purposes. Configuration shows a unidirectional, non-uniform **B** field with no applied electric field with (a) the **B** pointing upwards in the z-direction with increasing gradient, ∇B, in the y direction (e.g. $B_z = B_z(y)$). The same schematic is depicted with **B** pointing out the page in panel (b). (c) shows the drifts for an ion and electron in this regime in the direction of the x-axis, perpendicular to both **B** and ∇B. The direction of the drift is represented by the black arrow inside the gyro-orbits. Figure adapted from Figure 2.5 in Chen (2016).

the ∇B drift when the field strength decreases with radius. Equation 1.19 can therefore be adapted to find an expression for the total drift in an inhomogeneous magnetic field

$$\mathbf{v}_B = \mathbf{v}_{\nabla B} + \mathbf{v}_R = \frac{m}{q}\left(v_\parallel^2 + \frac{v_\perp^2}{2}\right)\frac{\mathbf{R}_C \times \mathbf{B}}{|B|^2 R_C^2} \tag{1.20}$$

where $\mathbf{v}_R$ is the drift contribution due to the curvature of the magnetic field and R_C is the constant radius of curvature which is larger than the Larmor radius of the charged particle. From Equation 1.20, the drift is perpendicular to $\mathbf{R}_C$ and **B** and is dependent on both the parallel and perpendicular components of the particle's velocity. This drift contribution is often present in particle transport effects and is useful when understanding particle acceleration at shock waves and current sheets (where $\mathbf{J} \neq 0$) (e.g., Chen, 2016; Kivelson, 1995). This has been observed in a magnetosphere setting where the charge-dependent drift produced from an inhomogeneous magnetic field (e.g. Earth's dipole field) induces a *ring current* surrounding the planet. For the case of Earth, the ring current is created by azimuthally drifting particles trapped by the geomagnetic field. For the case of Jupiter (and Saturn), due to the plasma source being internal (see Section 2), the particle pressure is comparable to that of the magnetic pressure produced by the planet's magnetic field (e.g., Bagenal, 1992). Coupled with a rapid planetary rotation, the centrifugal forces causes the field lines in the planet's

equatorial plane to stretch. This strong perturbation of the planetary field generates a very strong ring current surrounding the gas giant planet in a region known as the magnetodisc or current sheet. The structure of the magnetosphere as well as the dynamics and behaviour of magnetospheric plasma will be discussed further in Chapter 2.

1.3.3 Magnetic mirroring and trapping

In an inhomogeneous **B** field, a charged particle will move from a region of weaker field strength, B_{min}, to a stronger region, B_{max}, where the field gradient is parallel to the magnetic field (Figure 1.4). As the particle gyrates along the field line, a *magnetic moment* (strength and orientation of the field), μ, is produced with area, A, and induced current I with the following expression

$$\mu = IA = \left(\frac{|q|\omega_c}{2\pi}\right)\left(\pi r_L^2\right) = \frac{mv_\perp^2}{2B} \tag{1.21}$$

where the definition of the Larmor radius is used (Equation 1.17) in the final step. As the particle moves along this field configuration, a force is produced as a result of the gradient of the magnetic field being parallel **B**. This is known as the *mirror force*. From solving the equation of motion, the magnetic moment is found to be invariant on timescales less than the particle's gyrofrequency and is therefore conserved at all points along the magnetic field (known as the *first adiabatic invariant)*. Therefore, for μ to be conserved in Equation 1.21, the $v_\perp$ must increase and $v_\parallel$ decreases and eventually becomes zero. At the point where $v_\parallel = 0$, the *mirror point*, the charged particle is reflected back towards the region of weaker field due to the mirror force (as shown in Figure 1.4b)). The process repeats in the opposite direction thus *magnetically trapping* the charged particle. A particle that bounces between two mirrors, with guiding centre drifting across field-lines, will produce (quasi-)periodic motion at the *bounce frequency* (also known as the *second adiabatic invariant)* (e.g., Kivelson, 1995).

In principle, magnetic trapping is not perfect. When the perpendicular component of the velocity is very small and approaching zero, the particle will no longer experience a mirror force. Using the first adiabatic invariant and conservation of the magnitude of velocity along the field line, the *pitch angle* (α) of the particle can be defined as

$$\frac{\sin^2\alpha}{B} = \text{const.} \tag{1.22}$$

The pitch angle is therefore defined to be the angle between the particle's velocity vector and the magnetic field line it travels along. The angle will determine if a

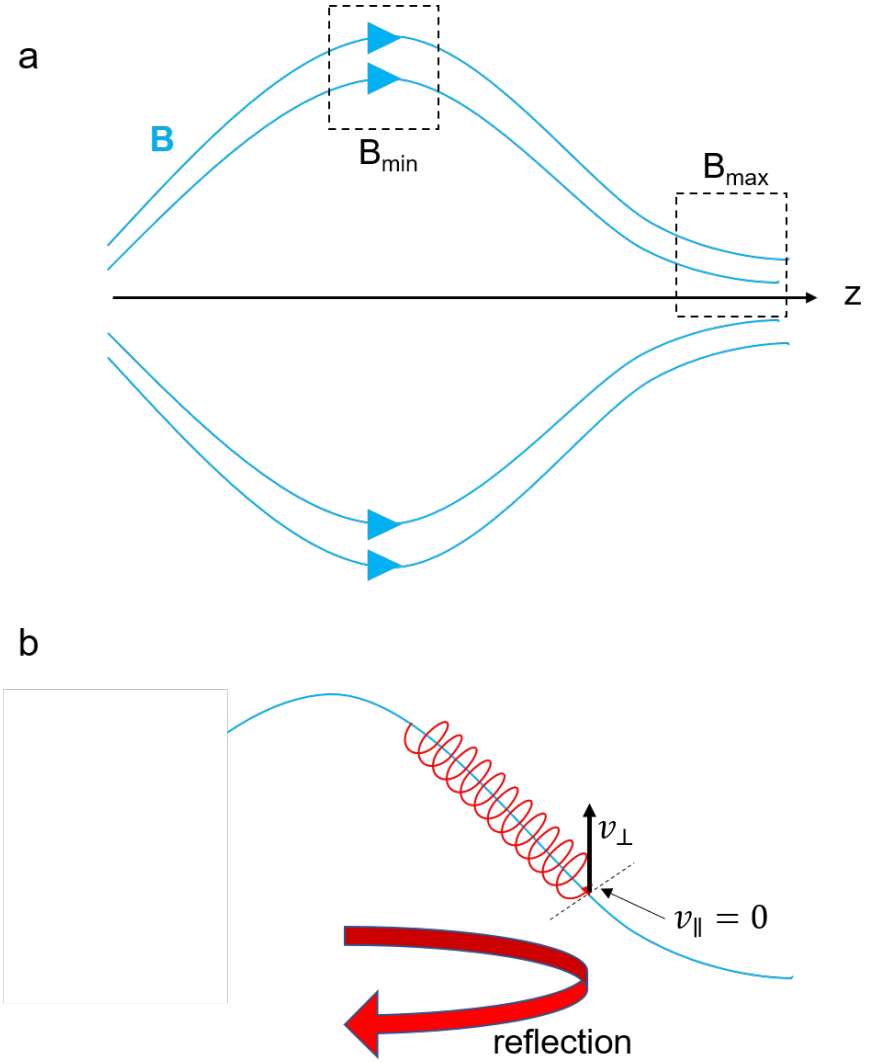

FIGURE 1.4: Schematics of (a) a configuration of an inhomogenous magnetic field, varying along the z-axis (where $\nabla B \parallel \mathbf{B}$) and a (b) charged particle trapped between magnetic mirrors (i.e. point at which $v_{\parallel} = 0$) with the direction of reflection. The points where the field string is weakest and strongest are denoted by B_{min} and B_{max} respectively.

particle will still be magnetically trapped or not. The pitch angle can be found for each point in a particle's trajectory by combining Equations 1.21 and 1.22, assuming the first adiabatic invariant is not violated.

The set of angles at which the particle may escape the magnetic trap are called *loss-cone angles*. If the initial pitch angle, α_0, is smaller than the loss-cone angle, the particle will escape from the magnetic trapping and will be lost to the atmosphere. A simple schematic of this process is shown in Figure 1.5, showing the trajectory of particles inside and outside of the loss cone in a simple dipole field in a planetary magnetosphere (not to scale). The altitude of the mirror point depends on the pitch angle of the charged particle and the magnetic field strength at the planet's equator.

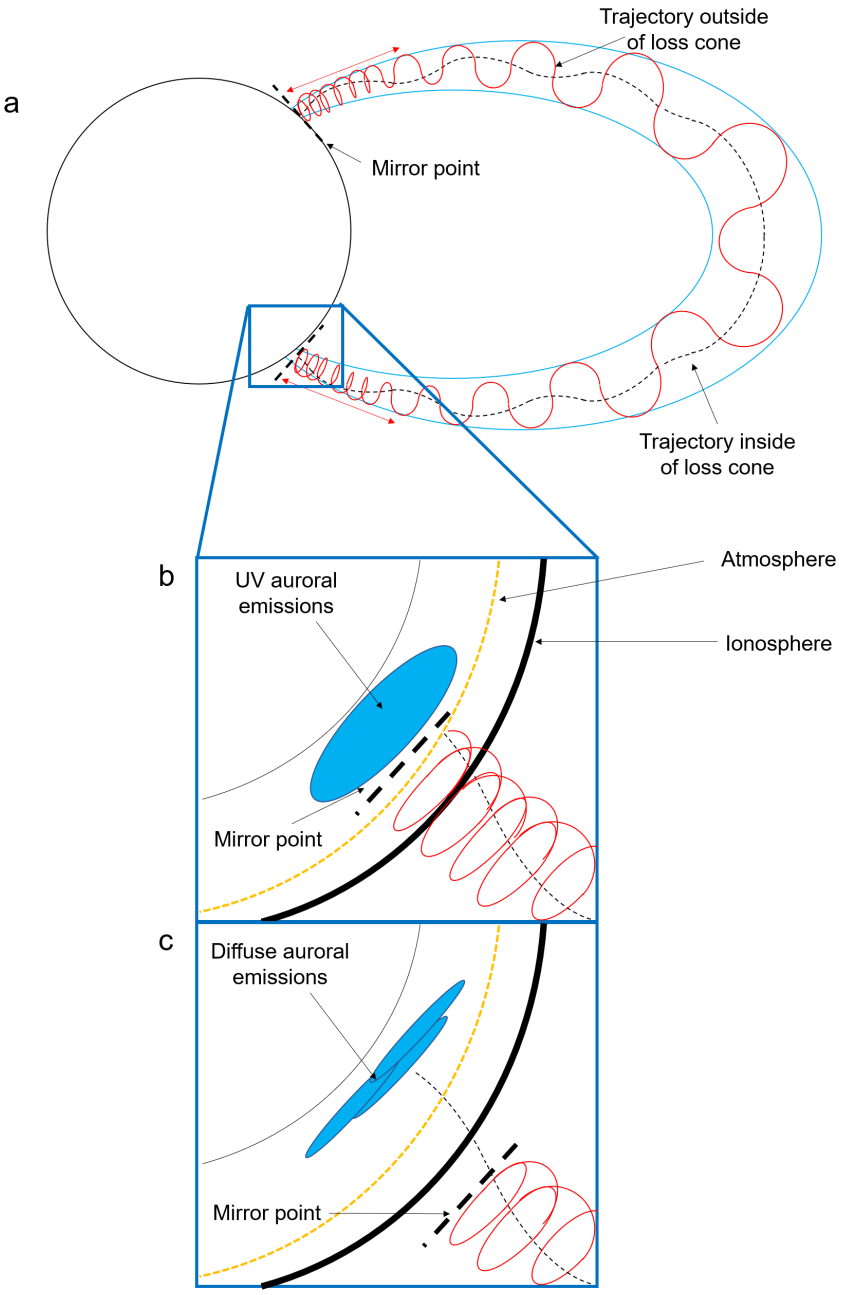

FIGURE 1.5: Schematic of magnetic mirroring shown in Figure 1.4 in the context of (a) a simple terrestrial-like magnetosphere and the cases where the mirror point is (b) below and (c) above the atmosphere (not to scale). Similar to Figure 1.4, the magnetic field and particle trajectory outside of the loss cone are shown in light blue and red respectively. The particle trajectory inside the loss cone is shown by the dashed-black line. Bold dashed lines are labelled as the mirror points in both panels. The radius of the gyro-orbit increases as the magnetic dipole field strength decreases with distance to the planet. Panel (b) shows the production of UV auroral when mirrored electrons are lost by collisions with the atmospheric molecules. Panel (c) shows that when the mirror point is outside of the ionosphere, the mirrored electrons produce weaker, diffuse auroral emissions, as there are less electrons, from the loss cone population only.

Figure 1.5b) shows the case where the mirror point is inside the atmosphere and mirrored (or magnetically trapped) electrons (outside of loss cone; red trajectory) are lost by collisions with the atmospheric molecules. As a result, UV auroral emissions will be created. Panel (c) shows that when the mirror point is outside of the ionosphere, for a simple terrestrial magnetosphere, the mirrored electrons produce no auroral emissions. The only contribution to the auroral emissions are from the loss cone population (black-dashed trajectory), producing weaker or diffuse emissions across the poles (for the terrestrial case) with zero magnetic trapping. Whether "diffuse" emissions are generated at the gas giant planets is still up for debate in the field today. Both mirrored and loss cone particles are important when analysing magnetospheric plasma populations and how they precipitate from the magnetosphere to the ionosphere. This is known as *magnetosphere-ionosphere coupling (M-I coupling)* . In the case of Jupiter, ions as well as electrons can also precipitate via a similar process. The auroral processes associated with M-I coupling and the behaviour of different magnetospheric plasma populations will be discussed further in Chapters 2, 4 and 5.

1.4 Magnetohydrodynamics

When studying the behaviour of space plasmas, in many cases it is more useful to treat the plasma as a single conducting fluid (i.e. all particle species move together) which carry currents and electromagnetic fields. This is known as *magnetohydrodynamics* (MHD) and combines Maxwell's equations (Equations 1.11 - 1.14) with fluid dynamics and thermodynamics to describe the behaviour of plasma as a single conducting fluid. As stated in Section 1.2, this description assumes that there are no displacement currents and therefore the plasma will not produce any electromagnetic waves. The plasma is assumed to have a net charge of zero (i.e. quasineutral). For simplicity, any plasma discussed in the remainder of this chapter will be composed of ions and electrons with the same magnitude of charge, q. The properties of a plasma described using MHD are defined by the following expressions (e.g., Chen, 2016)

$$\rho_{\mathrm{m}}(\mathbf{r},t) = \sum_{\mathrm{s}} m_{\mathrm{s}} n_{\mathrm{s}}(\mathbf{r},t) \approx n(m_{\mathrm{i}} + m_{\mathrm{e}}) \tag{1.23}$$

$$\mathbf{u} = \frac{\sum_{\mathrm{s}} m_{\mathrm{s}} n_{\mathrm{s}} \mathbf{v}_{\mathrm{s}}}{\sum_{\mathrm{s}} m_{\mathrm{s}} n_{\mathrm{s}}} \approx \frac{m_{\mathrm{i}}\mathbf{v}_{\mathrm{i}} + m_{\mathrm{e}}\mathbf{v}_{\mathrm{e}}}{m_{\mathrm{i}} + m_{\mathrm{e}}} \tag{1.24}$$

$$\mathbf{J} = q(n_{\mathrm{i}}\mathbf{v}_{\mathrm{i}} - n_{\mathrm{e}}\mathbf{v}_{\mathrm{e}}) \approx qn(\mathbf{v}_{\mathrm{i}} - \mathbf{v}_{\mathrm{e}}) \tag{1.25}$$

where $\rho_{\mathrm{m}}(\mathbf{r},t)$ is the mass density of the plasma, m_{s} and $n_{\mathrm{s}}(\mathbf{r},t)$ are the mass and number density of one species, s, respectively, $\mathbf{u}$ is the bulk velocity of the plasma, $\mathbf{v}_{\mathrm{s}}$

is the velocity of one species and **J** is the current density of the plasma like before. The right hand side of all three equations show the contributions from both electrons and ions in the plasma. Both properties shown in Equations 1.23 and 1.24 are summed over all species in the plasma. In the description discussed here, the species will be ions and electrons (subscript 'i' and 'e' respectively, or two-fluid MHD) with $\mathbf{u} \ll c$, where $c = 2.998 \times 10^8$ m s^{-1} is the speed of light in a vacuum. The gyroradii of the species within the plasma are far less than the system scales. As the plasma is quasineutral and only contains electrons and singly charged ions, the assumption that $n_\mathrm{e} \approx n_\mathrm{i} = n$ has also been made. With these assumptions and plasma parameters, the behaviour of plasmas in this description can be described using the *MHD equations* (e.g., Chen, 2016; Kivelson, 1995).

In the MHD description of plasma, matter (or mass) can neither be created or destroyed. This is given by the *continuity equation*, the first MHD equation

$$\frac{\partial \rho_\mathrm{m}}{\partial \mathrm{t}} + \nabla \cdot (\rho_\mathrm{m} \mathbf{u}) = 0 \tag{1.26}$$

where Equations 1.23 and 1.24 are used to define ρ_m and **u**. Equation 1.26 takes into account all of the mass continuity equations for each separate species within the plasma (i.e. treats the plasma as one single fluid), flowing through a closed surface. The equations of motion for an ion and electron in the plasma, incorporating contributions from the fluid flow of the plasma, electromagnetic fields, gravitational acceleration and collisions, are given by

$$m_\mathrm{i} n \frac{\partial \mathbf{v}_\mathrm{i}}{\partial \mathrm{t}} = en(\mathbf{E} + \mathbf{v}_\mathrm{i} \times \mathbf{B}) - \nabla p_\mathrm{i} + m_\mathrm{i} n \mathbf{g} + \boldsymbol{P}_\mathrm{ie} \tag{1.27}$$

$$m_\mathrm{e} n \frac{\partial \mathbf{v}_\mathrm{e}}{\partial \mathrm{t}} = -en(\mathbf{E} + \mathbf{v}_\mathrm{e} \times \mathbf{B}) - \nabla p_\mathrm{e} + m_\mathrm{e} n \mathbf{g} + \boldsymbol{P}_\mathrm{ei} \tag{1.28}$$

where $p_\mathrm{i,e}$ is the pressure term of the ions and electrons respectively, resulting from the fluid flow of the plasma, **g** is the gravitational acceleration vector and $\boldsymbol{P}_\mathrm{ei} = -\boldsymbol{P}_\mathrm{ie}$ are the drag force terms (or momentum contribution from collisions) between the ions and electrons and other terms have been defined previously. The charge of the ions and electrons are given by $q = \pm e = \pm 1.602 \times 10^{-19}$ C. By summing all equations of motion for all species in the plasma and using the definitions of the plasma parameters (Equations 1.23 - 1.25) we obtain the second MHD equation or *momentum equation*

$$\rho_\mathrm{m} \frac{\partial \mathbf{u}}{\partial \mathrm{t}} = -\nabla p + \mathbf{J} \times \mathbf{B} + \rho_\mathrm{m} \mathbf{g} \tag{1.29}$$

where $p = p_i + p_e$ is the total pressure term and the drag force terms cancel out as the ions and electrons move in opposite directions (as stated by $\boldsymbol{P}_{ei} = -\boldsymbol{P}_{ie}$), assuming equal contributions from electron-ion and ion-electron collisions. The electric field contribution also cancels out and does not explicitly appear in Equation 1.29 as the plasma is treated as a neutral fluid. The right hand shows the three body forces due to the magnetic field, pressure gradient and gravity as expected.

The third MHD equation can be derived by subtracting the equations of motion for the electrons and ions and describes how **J** evolves with time. This is known as the *generalised Ohm's Law* and given by

$$(\mathbf{E} + \mathbf{u} \times \mathbf{B}) = \eta \mathbf{J} + \frac{1}{en} (\mathbf{J} \times \mathbf{B} - \nabla p_e) \tag{1.30}$$

where the momentum contribution from collisions between the ions and species has been defined as $\boldsymbol{P}_{ei} = \eta e^2 n^2 (\mathbf{v}_i - \mathbf{v}_e)$ with η being the specific resistivity of the plasma (e.g., Chen, 2016). Equation 1.30 neglects any contributions from inertial effects due slow motions of the plasma and is in the limit $\frac{m_e}{m_i} \to 0$. The first term on the right hand side, $\eta \mathbf{J}$, defines the contribution from resistive forces and the term that follows, $\mathbf{J} \times \mathbf{B}$ is called the *Hall current* term. The final contribution is due to the pressure from the electrons alone as they are less massive and therefore more mobile than the ions. If the plasma is fully ionised, collisionless, and the macroscopic behaviour of the plasma extends beyond the electron collision timescales, the resistive forces due to the electrical conductivity dominate. Therefore the last two terms on the right hand side can be neglected and therefore Ohm's law can be simplified to

$$\mathbf{J} = \sigma(\mathbf{E} + \mathbf{u} \times \mathbf{B}) \tag{1.31}$$

where $\sigma = \frac{1}{\eta}$ is the plasma conductivity. The final MHD equation, the *energy equation*, assumes the plasma is in thermodynamic equilibrium and can undergo adiabatic compressions and expansions. The energy equation therefore defines the equation of state for a plasma.

$$\frac{\mathrm{d}}{\mathrm{dt}} \left(p \rho_m^{-\gamma} \right) = 0 \tag{1.32}$$

where $\gamma = \frac{c_p}{c_v}$ is the adiabatic index or the ratio of the specific heat capacity at constant pressure (c_p) and constant volume (c_v) (e.g., Kivelson, 1995).

The MHD equations allow the bulk motion and behaviour of the plasma to be described in detail. The next few sections will discuss and examine some of the key plasma diagnostics that can be derived from the MHD equations.

1.4.1 Hydromagnetic Equilibrium

In order to understand how plasma is contained in various magnetic field configurations (e.g. loop structures in the solar atmosphere, magnetospheric plasma along field lines), the steady state or equilibrium of the plasma can help provide a solution. In this steady state MHD description, the plasma does not evolve with time (i.e. $\frac{\partial}{\partial t} = 0$) and is assumed to be not gravitationally bound to the plasma source (e.g. $\mathbf{g} = 0$). Therefore, the momentum equation of the plasma (Equation 1.29) reads

$$\nabla p = \mathbf{J} \times \mathbf{B} \tag{1.33}$$

where, in an equilibrium state, the pressure gradient and Lorentz forces are balanced. Using the definition of current density from Ampère-Maxwell's law in MHD (Equation 1.14) and some algebraic manipulation, Equation 1.33 can be rewritten as

$$\nabla \left(p + \frac{B^2}{2\mu_0} \right) = \frac{1}{\mu_0} (\mathbf{B} \cdot \nabla) \mathbf{B} \tag{1.34}$$

where the gradient of the sum of the particle pressure (p) and magnetic field pressure ($B^2/2\mu_0$) is equal to the magnetic tension, as shown on the right hand side. In many cases, when the curvature of the field lines is so small they can be assumed to be straight, the magnetic tension is negligible and therefore the total particle and magnetic pressure must be constant (e.g., Chen, 2016). For example, if the plasma density is high, the magnetic field must be low in order to maintain equilibrium (e.g. Equation 1.33) and vice versa. The magnitude of the magnetic pressure contribution can be determined from the ratio of the particle and field pressure

$$\beta = \frac{\text{particle pressure}}{\text{magnetic pressure}} = \frac{\sum nkT}{B^2/2\mu_0} \tag{1.35}$$

where the ideal gas law is used to define particle pressure in which all (if any) collisions between plasma particles are perfectly elastic, k is the Boltzmann constant and other symbols have been defined previously. This ratio is known as the *plasma-β*. A low-β plasma (or "cold" plasma) will be dominated by the forces produced from the particles in a weak magnetic field. The field can therefore be treated as uniform (e.g. $\mathbf{B} = B\hat{\mathbf{e}}_z$ like before) when dealing with plasma waves. In a high-β plasma (or "hot" plasma), the local magnetic field can be greatly influenced by plasma currents (e.g., Chen, 2016; Kivelson, 1995). As discussed further in Chapter 2, planetary magnetospheres contain both "hot" and "cold" plasma populations which are affected by different processes.

1.4.2 Magnetohydrodynamic Wave Modes

Using the hyrdomagnetic equilibrium assumption, the perturbations of the magnetic field inside and surrounding the plasma can be examined via a first-order linearised form of the MHD equations. These perturbations are a result of an external force being applied to the system and can be analysed from the waves produced which propagate through the plasma. The configuration of the system will determine what types of MHD waves, or *wave modes*, the plasma produces. This section will discuss these modes, their direction of propagation and set up the foundations for these waves to be explored in greater detail in the later relevant Chapters.

If the perturbation of the field is perpendicular to the background magnetic field and propagates along it at a frequency less that the cyclotron frequency (ω_c), the dispersion relation for a slow or *shear Alfvén wave* (SAW) can be calculated for an incompressible plasma (e.g., Goertz and Strangeway, 1995). The SAW mode is found to only propagate along the field lines of which they are produced. The perturbation produced is analogous to the ”wave in a box” or a ”wave on a string” in quantum mechanics with the field line acting as the string for the SAW. As the SAW is a transverse wave, the perturbation does not affect the plasma density or pressure as they are purely a product from the threaded magnetic field. Therefore the restoring force, to return the field back to equilibrium, is the magnetic tension of the field line. SAWs are ubiquitous in planetary magnetospheres (e.g., Wilson and Dougherty, 2000a; Rae et al., 2005; Manners and Masters, 2020) and play a vital role in transporting energy and information from the magnetosphere to the ionosphere.

If the velocity of the perturbation is *not* perpendicular to the direction of its propagation, the dispersion relation produces two modes for a *magnetosonic wave* or compressional waves. When the pressure gradient forces from the particles and magnetic field are combined, the speed of the wave propagation is greater than the *Alvén speed*, c_A, and a *fast* mode magnetosonic wave is produced. When the forces oppose each other, a *slow* mode magnetosonic wave is produced instead, at a slower velocity than their fast mode counterpart. As the magnetosonic waves move through the plasma, the fluid is moved in the direction of the compressional mode propagation. This results in the plasma having a non-uniform density profile (e.g., Goertz and Strangeway, 1995). Fast modes are found to propagate in any direction from the perturbation source and can propagate faster than c_A as the fluctuations due to the plasma and magnetic pressure are nearly in phase with each other. Slow mode waves can only move along the field lines of the background field as these fluctuations are out of phase with each other. The nature of the waves and their propagation velocity is highly dependent on the plasma-β, for example, in a hot plasma ($\beta >> 1$) slow mode waves behave like SAWs. Examining and understanding the difference between SAWs and compressional waves are important when dealing with a changing

state of a planetary magnetosphere, for example, as it undergoes a rapid compression. In a planetary magnetosphere, compressional waves can be found across a cavity whereas the SAWs propagate along perturbed field lines. Both SAWs and compressional mode waves will be discussed in more detail in Chapters 2, 4 and 5.

1.4.3 Alfvén's frozen-in theorem

In many cases, the magnetic field that encompasses the plasma will be in the presence of a prescribed velocity field generated from the plasma. The evolution of **B** in this case can be derived from combining Ohm's law (Equation 1.31) with the MHD Maxwell's equations that describe how **E** and **B** evolve with time (Equations 1.12, 1.13 and 1.14)

$$\frac{\partial \mathbf{B}}{\partial t} = \nabla \times (\mathbf{u} \times \mathbf{B}) + \widetilde{\eta} \nabla^2 \mathbf{B} \tag{1.36}$$

where $\widetilde{\eta} = \eta / \mu_0$ is the magnetic diffusivity of the plasma and all other symbols have been previously defined. Equation 1.36 is known as the *induction equation* and states that, in the presence of the plasma velocity field, the time evolution of **B** depends on the resistive diffusion, $\widetilde{\eta} \nabla^2 \mathbf{B}$, and the advection of the plasma, $\nabla \times (\mathbf{u} \times \mathbf{B})$.

If $\widetilde{\eta}$ is very small (i.e. when $\eta \to 0$ in the ideal MHD regime), the resitivity term in the induction equation is negligible in comparison to the advection contribution. For a closed contour, C, enclosing a surface, S with area $\mathrm{d}^2\mathbf{S}$, the total magnetic flux through the contour, Φ_B is $\int_S \mathbf{B} \cdot \mathrm{d}^2\mathbf{S}$. The rate of change of magnetic flux through C is therefore

$$\frac{\mathrm{d}\Phi_B}{\mathrm{d}t} = \frac{\partial}{\partial t} \int_S \mathbf{B} \cdot \mathrm{d}^2\mathbf{S} = \iint_S \frac{\partial \mathbf{B}}{\partial t} \cdot \mathrm{d}\mathbf{S} + \frac{\partial}{\partial t} \left(\oint_S \mathbf{B} \cdot (\mathbf{u}\mathrm{d}t \times \mathrm{d}\mathbf{l}) \right) \tag{1.37}$$

where the double integral over the surface in the first right hand side term is equivalent to a single integral over the area element and the path integral (second term) describes the change in area of the contour due to the motion of the plasma. This is described by considering an interval of time, dt, where the area changes due to the movement of a line element, d**l**. Using Stoke's Theorem and the properties of the scalar triple product, Equation 1.37 can be rewritten as

$$\frac{\mathrm{d}\Phi_B}{\mathrm{d}t} = \iint_S \left(\frac{\partial \mathbf{B}}{\partial t} - \nabla \times (\mathbf{u} \times \mathbf{B}) \right) \cdot \mathrm{d}\mathbf{S} \tag{1.38}$$

Substituting the induction equation (Equation 1.36) for very small $\widetilde{\eta}$, $\frac{\mathrm{d}\Phi_B}{\mathrm{d}t} = 0$. This is known as *flux freezing* or *Alfvén's frozen-in theorem* for a fluid with infinite electric conductivity (or zero diffusivity). The magnetic field is frozen into the plasma and is

therefore forced to move with the motion of the conducting fluid and vice versa (Alfvén, 1942). For the case of space plasmas, they can not cross magnetic field lines unless under certain regimes which break ideal MHD, such as magnetic reconnection. Magnetic reconnection is a process that occurs between sets of oppositely directed magnetic field lines in a plasma with high conductivity. These field lines break and join together, converting the stored magnetic energy into plasma thermal and kinetic energy (e.g., Chen, 2016). Chapter 2 will discuss magnetic reconnection in context with the dynamics of the jovian magnetosphere. The remainder of this chapter will look at how we can apply the plasma diagnostics derived from MHD to the structure and behaviour of the magnetic fields and plasma produced by the Sun and how they permeate the Solar System.

1.5 Solar Magnetic Field

In order to understand the space plasma populations in the Solar System, the properties of the Sun's atmosphere and magnetic field need to be discussed. The Sun is the largest plasma source in the Solar System and its atmosphere and magnetic field propagate throughout via open (*heliospheric*) and closed (*coronal*) field lines. Both sets of field lines play a vital role on understanding space weather throughout our Solar System and how they are coupled to planetary magnetospheres (discussed more in Chapter 2). The effect the solar magnetic field has on Earth's geospace has been studied since the the mid 1800's when the largest solar storm recorded impacted Earth, the *Carrington Event* (Carrington, 1859; Hodgson, 1859). It was found that the currents induced by the solar storm caused telegraph poles to catch fire and powerful auroral displays found to occur at lower latitudes than where is typically expected. It is therefore important to understand how powerful the Sun can be from both a magnetospheric and infrastructure perspectives. The remainder of this chapter will build up the foundations to discuss the former in Chapter 2.

1.5.1 Heliospheric and Coronal fields

The Solar System is enveloped by a "magnetic bubble" produced by solar open or *heliospheric* field lines. This is known as the *heliosphere* and the field lines are found to originate from *coronal holes* - co-rotating dark, cooler regions of plasma in the solar outer atmosphere or *corona* which generate fast solar winds (e.g., Priest, 1995). As stated by Gauss' law of magnetism (Equation 1.8), no magnetic monopoles can exist and therefore the structure of a magnetic field must be a loop and cannot be "open". The term "open" used in context with the heliospheric field lines suggest that locally, the field is unipolar and stretch themselves to long distances in interplanetary space.

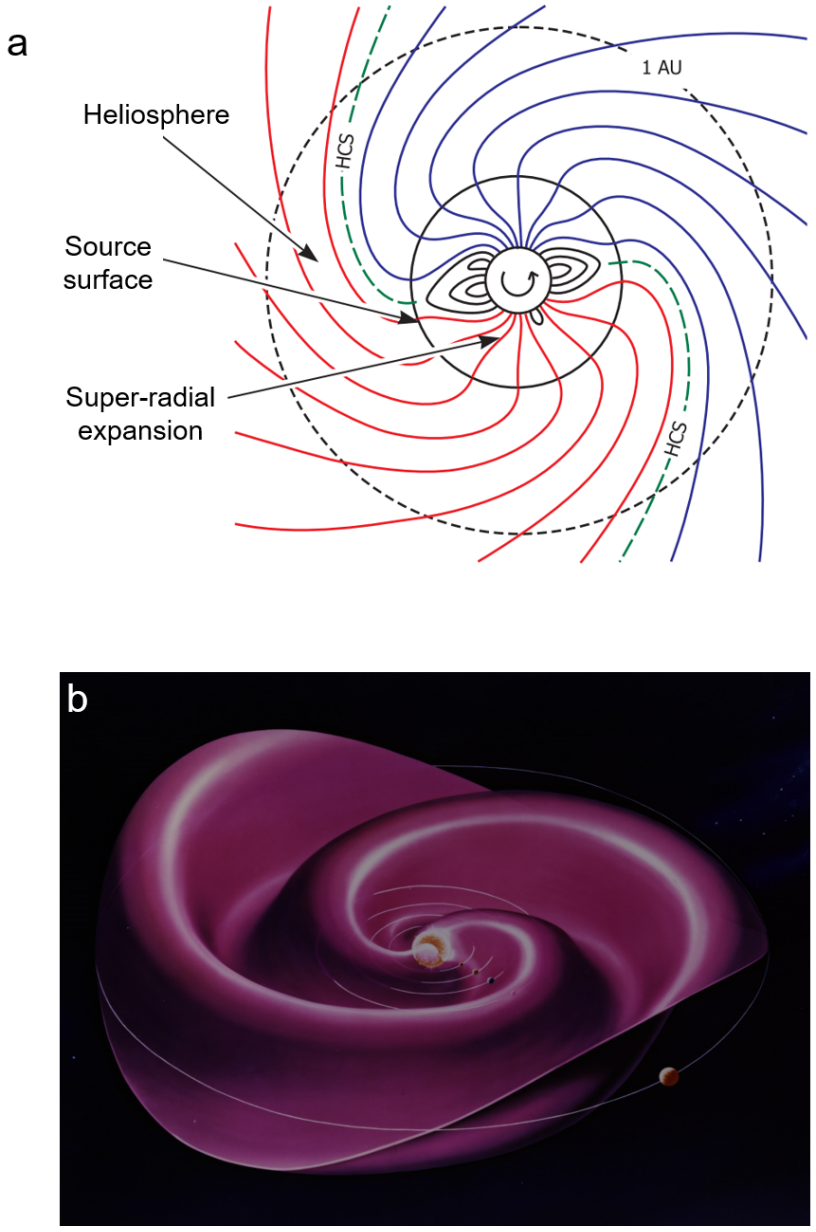

FIGURE 1.6: (a) Schematic of the steady-state solar heliospheric magnetic field as shown in the ecliptic plane, showing the orientation and polarity of the "open" field lines (North; red, South; blue) at labelled regions. "Closed" field lines are shown as black solid lines in the equatorial plane of the Sun. Close to the solar surface, the high-β coronal plasma produces a a super-radial expansion of the field. The source surface defines the region of pressure-driven expansion and the field and flow is radial. The rotation of the Sun beyond this point adds an azimuthal component to the field, leading to the spiral structures predicted. Field lines of opposite polarity are separated by the heliospheric current sheet (HCS; green-dashed line) with an artists impression of the "ballerina skirt" shown in (b). Panel (a) is adapted from Figure 1 in Owens and Forsyth (2013) and (b) is taken from `https://www.esa.int/ESA_Multimedia/Images/2019/03/Parker_spiral`. *Copyright (b): NASA – Werner Heil.*

The heliospheric field lines are believed to reconnect in the expanses of the heliosphere, beyond Pluto's orbit (e.g., Echer et al., 2005). Therefore the time evolution of these fields coupled with the Sun's rotation are the main driving mechanism for space weather throughout the Solar System. As discussed in detail in Chapter 2, it is known that planetary magnetospheres respond to changes to the solar wind and the magnetic field it carries with it, the *interplanetary magnetic field* (IMF) forming the interplanetary medium.

As the Sun rotates, the geometry of the heliospheric field lines twist into an Archimedes spiral. At boundaries of opposite field polarity, the *heliospheric current sheet* (HCS) is produced. The HCS is believed to "wave" as a result of the tilt angle between the Sun's magnetic dipole and rotation axis (e.g., Owens and Forsyth, 2013), creating a "ballerina skirt". This configuration was first predicted by Parker (1958) and is shown schematically in Figure 1.6. The strength of the field falls with the inverse square of the distance from the Sun, due to conservation of magnetic flux, and is shown to change the field geometry (Figure 1.6a)). Near the solar surface in the inner solar corona, the high-β coronal plasma (i.e. magnetic field dominates the plasma flow) produces a a super-radial (or non-radial) expansion of the field. As the field extends, it reaches the "source surface" - the boundary where pressure dominates the field, leading to both the field and plasma flow to be radial. Beyond this boundary, the rotation of the Sun adds an azimuthal component to the magnetic field, leading to the spiral structures predicted by Parker (1958). Magnetic field of opposite polarities (as anchored to different hemispheres) are separated by the HCS. The "ballerina skirt" shape of the HCS is shown in as an artists impression in Figure 1.6b).

The closed *coronal* field lines are observed on the visible "surface", or *photosphere*, of the Sun and are usually confined to regions of largest magnetic field concentration, *sunspots*. The emissions flowing along the closed field lines tend to be brighter against the solar "surface" when observed, with the sunspot being the footpoints of the magnetic field or *coronal loops* in the solar photosphere. Each rooted anchor of the coronal loop is of a different polarity and therefore producing a bipolar field within the coronal loop (e.g., Echer et al., 2005). These loops are subject to intense twisting which stores magnetic energy (therefore increasing magnetic pressure) and changes the topology of the loop. The building pressure causes the loop to bend and twist further, straining the curvature and eventually causing the closed field lines to "break" and reconnect with the surrounding field due to change in the hydromagnetic equilibrium. This leads to a large release of plasma and magnetic field from the corona known as a *coronal mass ejection* (CME). As a result of the eruption, the anchored coronal loop points in the photosphere then become the the footpoints of intense particle acceleration, producing a *solar flare*. As depicted in Figure 1.7, the emissions from a solar flare are observed across the electromagnetic spectrum depending on the energies of the electrons/ions (Fletcher et al., 2011), including hard X-rays ($>$ 20 keV

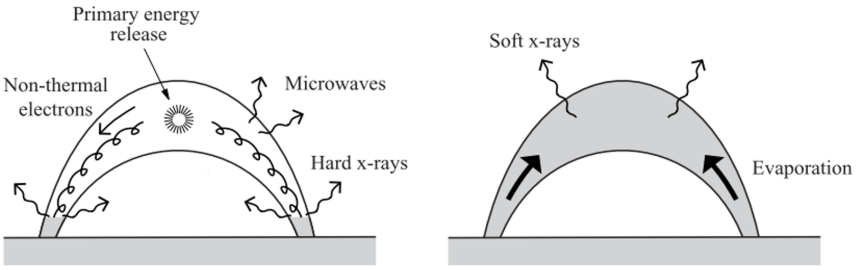

FIGURE 1.7: Schematic of a solar flare, showing the production of emissions across the electromagnetic spectrum. Left panel shows the initial downward spiralling of electrons along the closed loop field lines after particle acceleration, generating microwaves. As the electrons reach the footpoints anchored to the solar surface, hard X-rays are produced. The right hand panel highlights the interval after hard X-ray production which drive an evaporation process that fills the loop with hot plasma which produces softer solar X-rays. Taken and adapted from Priest and Forbes (2002), Figure 3.

in solar physics) at the footpoints and plasma emitting soft X-rays within the coronal loop (0.1-10 keV in solar physics) driven by an evaporation process (e.g., Priest and Forbes, 2002).

When the Sun is more active and produces more sunspots due to increased disturbances of a stronger solar magnetic field (via a 11-year solar cycle), solar flares are likely to be more frequent and tend to be more powerful. The solar X-rays then propagate throughout the Solar System. In the case of the gas giants Jupiter and Saturn, the reflection of the solar X-ray photons off the upper atmosphere can generate planetary disk X-ray emissions which have been detected from X-ray telescopes (e.g., Bhardwaj et al., 2005a; Branduardi-Raymont et al., 2004). We examine the X-ray mechanism in more detail in Chapter 2 and the instrumentation used to detect X-rays in Chapter 3. At Earth in particular, a solar flare eruption can also disrupt radio communications as the radio waves travel along the ionosphere. Therefore flaring activity will have a different effect on the space weather at the planets than the heliospheric "open" fields as the solar X-ray photons are not affected by the magnetic field of the heliosphere. Chapter 7 will examine how we can try to correlate solar flare activity with planetary disk emissions. The remainder of this chapter will focus on how the heliospheric field propagates through our Solar System and how its motion can be described: the solar wind.

1.5.2 The Solar Wind

As well as being the driver for propagating the solar heliospheric field, the solar wind is a flow of ionised plasma released form the solar corona as the Sun evaporates. This flow results from the vast difference in gas pressure between the corona itself and the

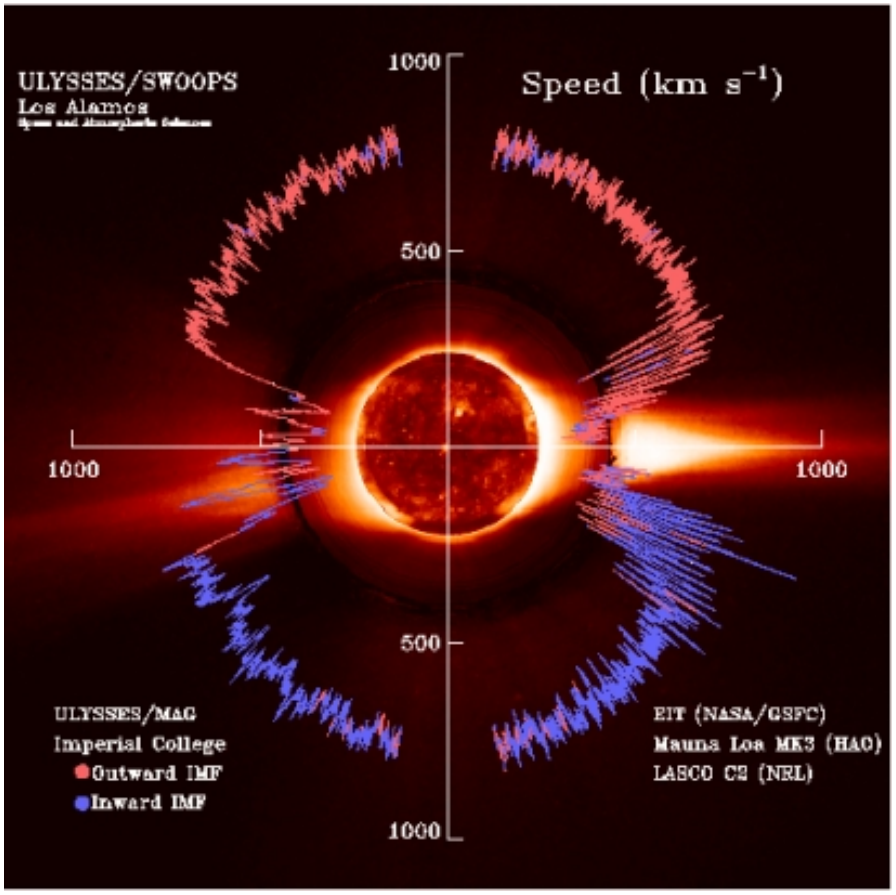

FIGURE 1.8: Polar plot of solar wind data from the Solar Wind Observations Over the Poles of the Sun (SWOOPS) experiment on-board Ulysses. the solar wind data is overplotted on images from two detectors on board NASA's Solar and Heliospheric Observatory (SOHO), the Large Angle and Spectrometric Coronagraph Experiment (LASCO) and Extreme UV Imaging Telescope (EIT), and the Mauna Lao Solar Observatory of the solar corona. This highlights the slow solar wind at the solar equator from the streamer belt and fast solar wind towards the poles (i.e. coronal holes) with the different field polarities shown in red and blue. This is plot shows the behaviour of the Sun during the declining phase to solar minimum. Image taken from https://sci.esa.int/s/8YrYl4A.
Copyright: ESA.

surrounding interstellar space and dominates the gravitational influence of the Sun (e.g., Hundhausen, 1995). There are three types of typical solar wind that flow from the Sun: *slow* ($\sim$ 300 - 500 km s^{-1}), *fast* ($\sim$ 700 - 900 km s^{-1}) and *transient* ($<$ 200 - $\gtrsim$ 2000 km s^{-1}). The fast winds, as stated previously, are produced from co-rotating coronal holes or result from magnetic field disturbances from solar flare activity. The slow solar wind originate in the equatorial belt region of the Sun known as the *streamer belts* (e.g., Xystouris et al., 2014). The transient solar wind results from CMEs travelling through the interplanetary medium, the velocity of which depends on the ambient wind speed. When a co-rotating coronal hole passes the line-of-sight of a planet (or any other Solar System object), the fast solar wind streams catch up with the slower winds produced from the streamer belt. When they interact, a compressed

interfaced in the surrounding interplanetary medium is created called a *co-rotating interacting region* (CIR) (e.g., Morley et al., 2009). These characteristics of the solar wind are shown from Ulysses solar wind data from the Solar Wind Observations Over the Poles of the Sun (SWOOPS) experiment and images from various solar observatories in Figure 1.8 of the solar corona. The image underneath the polar plot of solar wind speed combines data from two detectors on board NASA's Solar and Heliospheric Observatory (SOHO) (the Large Angle and Spectrometric Coronagraph Experiment (LASCO) and Extreme UV Imaging Telescope (EIT)) and the Mauna Lao Solar Observatory. All data shown in Figure 1.8 was taken when the solar activity was in a declining phase to solar minimum.

As each of these solar wind mediums propagate throughout the Solar System, the interactions created with other magnetised bodies (e.g. a planetary magnetosphere) is governed by their associated dynamic pressure, P_{dyn}, and the orientation of the anchored IMF. As P_{dyn} is proportional to the density and squared velocity of the plasma flow, the faster solar wind will exert a higher dynamic pressure onto the magnetised body. In the context of Earth's magnetosphere, P_{dyn} dominates the magnetic pressure produced from the less dense magnetosphere causing it to become compressed. In the case of the gas giants, there is an additional internal pressure contribution due to the rapid rotation which inflates the magnetosphere and needs to be considered when looking at the pressure balance between the internal pressures and P_{dyn} of these systems. A shock-front produced by a CIR, as a fast solar wind stream reaches the slow solar wind, will generate a rapid compression of a magnetosphere as it passes through the system. The magnetosphere will expand when exposed to a slow solar wind flow (e.g., Blanc et al., 2005). These effects are more apparent at the gas giant magnetospheres where the plasma is more rarefied due to the magnetospheres being larger in volume and more compressible than their terrestrial counterparts (e.g., Bagenal, 1992). The ramifications and magnetospheric processes produced from different types of solar wind interactions will be discussed in more detail in Chapter 2.

Chapter 2

Planetary Magnetospheres

> *"That is a question with too complicated an answer."*
> - Philip Pullman, *His Dark Materials*

Reflects the sheer complexity of the jovian magnetosphere, although I hope this chapter will make some things clearer[1]

The space physics concepts introduced in Chapter 1 will now be applied and thoroughly examined in a magnetospheric context. The chapter begins by defining what we mean by a *planetary magnetosphere* and how we define the structure of Jupiter's magnetosphere in particular (Section 2.1). The jovian magnetosphere, auroral observations across many wavelengths and their associated mechanisms are then examined in detail (Section 2.2). The chapter concludes by discussing the X-ray mechanisms observed in a planetary science context (Section 2.3) with particular focus on the jovian X-ray auroral emissions (Section 2.4).

2.1 The Jovian Magnetosphere

As discussed in Section 1.5, the interplanetary magnetic field (IMF) is carried by the solar wind and permeates the solar system. When the IMF (and therefore solar wind) interacts with an obstacle with a magnetic field, atmosphere or high internal conductivity, a cavity is produced surrounding the obstacle. For the case of a magnetised planet (e.g. Earth, Jupiter and Saturn), the magnetic pressure (and other internal pressure for the case of the gas giants) is responsible for creating a cavity in the solar wind due to the frozen-in nature of both plasma populations. Within this

[1] Recommend listening to The Planets, Op. 32: 4 Jupiter, the Bringer of Jollity by Gustav Holst for inspiration: https://www.youtube.com/watch?v=BUM_zT3YKHs&list=PLQOOFhV_OKWicAu2Yw2AziV9OsHlU6qci&index=4

cavity, the plasma motions are dominated by the planetary magnetic field. This region is what is defined to be a *planet's magnetosphere*. The remainder of this section will examine the sub-structures within Jupiter's magnetosphere, many of which are ubiquitous to all magnetised planets.

2.1.1 Observational history

Nine spacecraft have visited Jupiter between 1973 - 2022 (7 shown in Figure 2.1), each unveiling new discoveries and mysteries at our largest planet. The first historic flybys of Jupiter were performed by *Pioneer 10* and *Pioneer 11* in 1973 and 1974 respectively. *Pioneer 10* allowed us to sample the jovian inner magnetosphere ($< 20\ R_J$: where 1 jovian equatorial radius, R_J = 71492 km) for the very first time, taking magnetometer measurements of the system from $\sim$ 3 - 6 R_J away from the planet. The magnetic field measurements revealed that the structure is mainly dipolar in the inner magnetosphere and is slightly offset from the centre of the planet. The field was found to be tilted by $\sim 10\ ^\circ$ with respect to Jupiter's spin axis with a magnetic moment of $\sim$4.0 G R_J^3 (or $\sim 1.5 \times 10^{20}$ T m^3, where 1 Gauss (G) = 1×10^{-4} T) as determined by Smith et al. (1974). This data from *Pioneer 10* also aided in the discovery of the jovian current sheet (Figure 2.2). The magnetometer data taken from the Pioneer missions (and the *Voyager* flybys $\sim$ 5 years later) helped develop the first empirical internal field model for Jupiter: Voyager Io Pioneer 4 (VIP4) developed by Connerney et al. (1998). The VIP4 model uses the coefficients from spherical harmonics of Jupiter's magnetic field (dipole, quadrupole, octupole and higher-order spherical harmonics) taken from *in situ* magnetic field data and remote observations of the foot of the *Io flux tube* (IFT) anchored into Jupiter's ionosphere. The IFT is a bundle of magnetic field lines with trapped plasma, originating from a toroidal cloud of plasma surrounding Io's orbit (at 5.9 R_J) known as the *Io plasma torus* (IPT). This provides a "link" between the jovian ionosphere and the IPT. The source of the plasma torus is Jupiter's volcanic moon Io which releases $\sim$ 1000 kg s^{-1} of sulphur, oxygen and sulphur dioxide out into space which creates a neutral torus. This neutral torus then becomes ionised via electron bombardment and irradiation from ultraviolet (UV) solar photons (e.g., Krupp et al., 2004) and creates the IPT that was discovered years earlier via ground spectroscopy observations (e.g., Kupo et al., 1976) and later flown through by *Voyager 1* in 1979, revealing its composition in extreme-UV (EUV) observations (e.g., Broadfoot et al., 1979; Bagenal, 1985). The footprint connected to Jupiter's ionosphere from the IPT is a mapping constraint for the magnetic field model, providing valuable "ground truth" for regions close to the planet that were not sampled at the time Connerney et al. (1998).

As well as providing vital data for magnetic field models, the *Voyager 1* EUV observations of the IPT allowed direct observations of the plasma energy and density

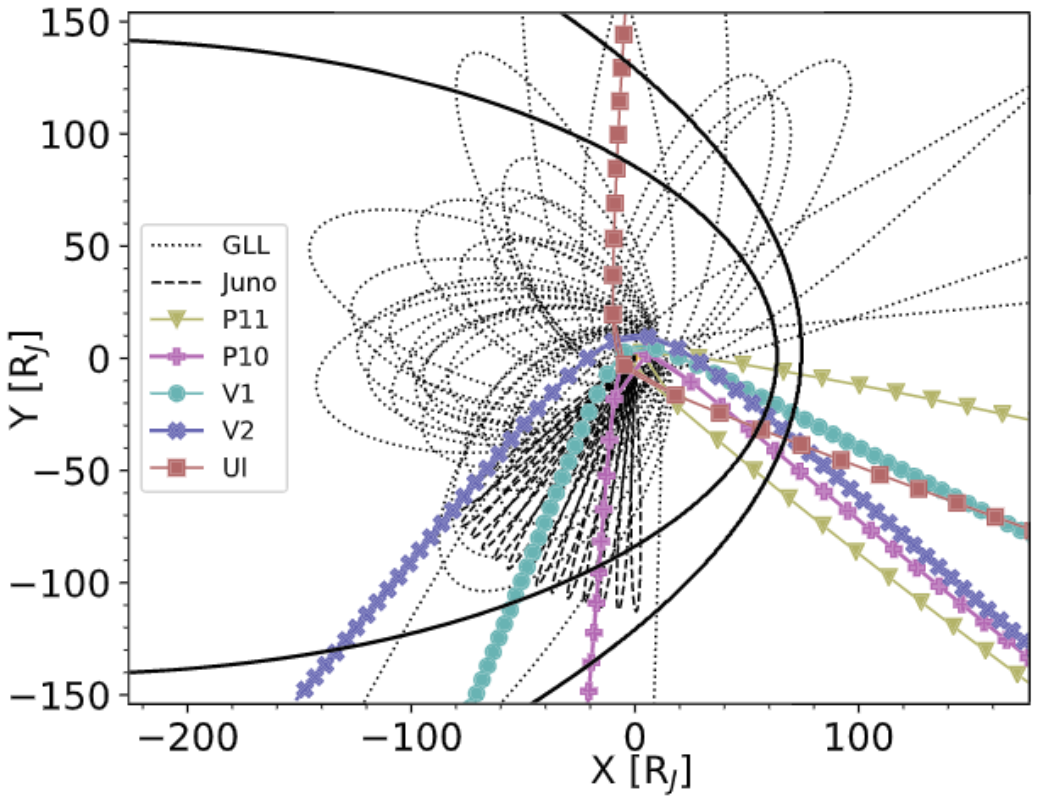

FIGURE 2.1: Schematic of most spacecraft trajectories which have visited Jupiter from 1973 - 2018 with the Sun to the right of the image. Not included are *Cassini*'s flyby of the dusk flank and *New Horizon*'s flyby of the jovian magnetotail as in entered the system from noon. At the time of writing, *Juno* is still in orbit around Jupiter in its extended mission. Figure taken from Figure 1 of Lorch et al. (2020).

and the radial extent of the torus. When *Pioneer 10*, *Voyager 1* and *2* journeyed out from the inner magnetosphere into the middle magnetosphere (20 - ∼60 R_J), magnetic field observations found that the field was stretched into a spiral-like topology (e.g., Smith et al., 1974; Khurana and Kivelson, 1993). *Voyager 2*'s journey into the outer magnetosphere ($\gtrsim$ 60 R_J) found that the plasma sheet, first sampled by the Pioneer missions, starts to bend beyond 40 R_J, where the plasma sheet is found to be parallel with the solar wind (e.g., Behannon et al., 1981). On its journey to Saturn, *Voyager 2* found the jovian magnetotail to extend beyond the orbit of Saturn at $\sim$ 9000 R_J (Lepping et al., 1983).

The early *Pioneer* and Voyager flybys paved the way for new discoveries at the jovian system but were restricted in their position, or local time, within the magnetosphere. As shown in Figure 2.1, with the Sun to the right of the image, the Pioneer and Voyager spacecraft entered Jupiter's magnetosphere in the pre-noon local time (LT) sector and exited pre-dawn to dawn. The trajectory of *Pioneer 11* had a higher inclination and therefore left the jovian system near noon. More complete local time coverage of Jupiter's magnetosphere was made available when the *Galileo* spacecraft

performed its orbit insertion at the planet in December 1995. *Galileo*'s near-equatorial orbit allowed the first observations of clear dawn-dusk local time asymmetries in many magnetospheric properties including the magnetic field configuration and plasma sheet thickness (e.g., Krupp et al., 2001). *Galileo*'s coverage allowed the development of three-dimensional models of the probable locations of the jovian bow shock (shock front produced as the solar wind encounters a magnetised obstacle - see Section 2.1.2) and magnetopause through a combination of data and MHD simulations Joy et al. (2002). The models determined that Jupiter's magnetopause has two probable standoff distances dependent on the dynamic pressure (P_{dyn}) of the solar wind. For high P_{dyn}, the standoff distance is $\sim 60\ R_{\mathrm{J}}$ as a limit for a highly compressed magnetosphere and $\sim 90\ R_{\mathrm{J}}$ for low values of P_{dyn} corresponding to the fully expanded jovian magnetosphere. The Joy et al. (2002) model is discussed in more detail in Chapters 4 and 5. *Galileo*'s trajectory also allowed for flybys of Jupiter's four largest moons, the Galilean moons: Io, Europa, Ganymede and Callisto.

During the *Galileo* mission, *Cassini* performed a flyby along the dusk flank of the jovian magnetosphere during December 2000 - January 2001 (Figure 2.1), obtaining data of this sector for the very first time. The charge-energy-mass spectrometer on-board detected energetic charge states of iogenic ions (ions originating from the moon Io: O^+, O^{2+}, S^+, S^{2+} and S^{3+}) at $\sim 200\ R_{\mathrm{J}}$ in the jovian outer magnetosphere (Allen et al., 2019). Comparing the charge state abundances of these heavy ions in the outer magnetosphere with previously observed populations closer to Io allows the evolution of plasma transport away from Jupiter to be studied in detail. During the flyby along the jovian magnetotail, exceeding distances of $\sim 2500\ R_{\mathrm{J}}$, a diverse range of slow-moving plasma populations were observed in the from of *plasmoids* - magnetic islands containing trapped plasma resulting from reconnection processes on the nightside of the planet McComas et al. (2007). The various plasmoid structures were found to contain iogenic, thermal and jovian ionospheric ions with different energies and densities.

Almost 10 years after the New Horizons flyby, the second orbiter to enter the jovian magnetosphere, *Juno* (Bolton et al., 2017), performed its orbit insertion in the dawn flank. Unlike *Galileo*, *Juno*'s orbit focuses on the polar regions of the planet (Figure 2.1), with the of the main focuses to analyse the jovian auroral emissions with its suite of instruments across multiple wavelengths. One of the key milestones was to update the VIP4 field model using updated magnetometer observations of the jovian internal field Connerney et al. (2017). The latest field model from *Juno* , JRM33 (field model from Juno's main mission), uses updated spherical harmonic coefficients of higher order than VIP4 (Connerney et al., 2022). Due to the orbit of *Juno* bringing it closer to the planet, JRM33 provides greater resolution than previous models as the lower altitude provides more detailed measurements of the jovian field from the *Juno* magnetometer. This is an update from the previous *Juno* field model, JRM09

(Connerney et al., 2018), which we use throughout this research. The *Juno* mission and its instrument suite are examined in more detail in Chapter 3. The remainder of this chapter will examine the jovian magnetosphere and the complex dynamics within in detail, applying context to these earlier observations and how this affects the jovian auroral emissions.

2.1.2 Structure of the jovian magnetosphere

Jupiter's magnetosphere is the largest coherent structure in the solar system due to the planet being the largest, producing the strongest internal magnetic field (surface magnetic field $\sim$ 4.2 Gauss = 4.2 $\times$ 10^{-4} T with magnetic moment, μ, $\sim$ 1.5 $\times$ 10^{20} T m^3) coupled with the fastest planetary rotation period ($\sim$ 10 hours). As briefly mentioned in Section 2.1.1, *Voyager 2* spacecraft found the jovian magnetotail extending beyond Saturn's orbit. The effect this has on the kronian magnetosphere, the second largest in the solar system, will be discussed in more detail in Chapter 7. This large and complex magnetic environment at Jupiter producing the most intense and energetic auroral emissions in our solar system. As a planet of extremes, Jupiter is a unique, mysterious and exciting choice for magnetospheric studies as well as providing a useful comparison for objects beyond our solar system (e.g."hot Jupiter" exoplanets).

2.1.2.1 The outer magnetosphere

The outermost structure of the jovian magnetosphere, in the direction facing the Sun, is known as the *bow shock*. This shock, as shown in Figure 2.2, signifies an abrupt transition of the solar wind as it encounters a magnetised obstacle, slowing it down and causing the trapped plasma to be heated and deflected around the sides of the cavity. This is a consequence of the solar wind velocity being greater than that of the compressional waves of the magnetospheric plasma (e.g., Russell, 1995; Fedder and Lyon, 1995). The solar wind interacts with the planetary field (via reconnection for the terrestrial case, or magnetosheath friction for the gas giants) causing the magnetic field lines to stretch away from the Sun and behind the planet to create the *magnetotail* (Figure 2.2). The magnetotail acts as a reservoir of magnetospheric plasma and energy which can be released towards the planet, or inner magnetosphere, or further downtail. At the centre of the magnetotail lies a current sheet which separates two regions known as the *tail lobes*. The current sheet (or *plasma sheet* or *magnetodisk* - used interchangeably in this thesis to explain and define the same structure) is embedded within a region of hot plasma of which the geometry and orientation depends on the size of the magnetosphere and rotational velocity of the planet (e.g., Bagenal, 1992; Hughes, 1995) and has a finite thickness. The abrupt boundary between solar wind

and magnetospheric plasma and is known as the *magnetopause* (Figures 2.2 and 2.2) and is downstream of the bow shock, surrounding the current sheet and tail lobes (e.g., Hughes, 1995). The distance between the 'nose' of the magnetopause and the centre of the planet is known as the *subsolar stand-off distance* (R_{MP}) and is a useful measure of the state of compression (or expansion) of the magnetosphere. The importance of the magnetotail and plasma sheet to auroral processes and plasma transport at the gas giants will be examined in further detail in Section 2.2.

As examined in Chapter 1.5.2, the varying solar wind dynamic pressure (P_{dyn}) will affect the size of the magnetosphere with the greatest effect being at the subsolar point. By balancing P_{dyn} with the planetary magnetic field pressure (Equation 1.34), neglecting the pressure contributions from the IMF and planetary plasma, the standoff-distance can be calculated. By assuming that solar plasma particles are reflected at the magnetopause (e.g. $P_{dyn} = 2\rho_{SW}v_{SW}^2$ where ρ_{SW} and v_{SW}^2 are the density and velocity the solar wind respectively) and that the planetary field is a simple dipole, the pressure balance equation becomes

$$P_{dyn} = 2\rho_{SW}v_{SW}^2 = \frac{B_{mp}^2}{2\mu_0} = P_{mag} \tag{2.1}$$

where B_{mp} is the magnetic field strength at the subsolar point at the magnetopause given by

$$B_{mp} = 2B_{eq}\left(\frac{R_P}{R_{mp}}\right)^3 \tag{2.2}$$

where B_{eq} is the equatorial field strength, R_P is the radius of the planet and all other symbols in Equations 2.1 and 2.2 have their usual meanings. By combining both equations, we get an expression for the stand-off distance: the Chapman-Ferraro distance equation (e.g., Blanc et al., 2005)

$$R_{mp} = R_P\left(\frac{B_{mp}^2}{\rho_{SW}v_{SW}^2\mu_0}\right)^{1/6} \tag{2.3}$$

To account for a non-dipolar magnetic field, it is common place to double the value of B_{mp}.

Between the magnetopause and jovian bow shock lies the *magnetosheath*, a region filled with heated, shocked plasma from the solar wind due to the rapid deceleration undergone at the bow shock (Figure 2.2). As a result, the plasma in this region is far slower and hotter than the incoming solar wind plasma (e.g., Hughes, 1995). The magnetic field structure in this region is complex with a mixture of open (i.e. magnetic

TABLE 2.1: Properties of the Solar Wind and Planetary Magnetosphere Scales for Earth, Jupiter and Saturn. Table adapted from Kivelson and Bagenal (2007).

	Earth	**Jupiter**	**Saturn**
Average Planet-Sun distance (au)[a]	1	5.2	9.5
Solar wind density, ρ_{SW} (amu cm^{-3})[b]	8	0.3	0.1
Equatorial radius (R_{eq}, km)	6373	71492	60268
Surface/equatorial magnetic field, B_{eq} (Gauss = 10^{-4} T)	0.31	4.28	0.22
Standoff-distance, R_{mp} (R_{planet})[†]	10 R_E	63 - 92 R_J^* (42 R_J)[†]	20 - 27 R_S^{**} (19 R_S)[†]

[a] 1 astronomical unit (au) = 1.5×10^8 km
[b] 1 atomic mass unit (amu = 1.66×10^{-27} kg
[†] calculated using Equation 2.3 for typical solar wind conditions of ρ_{SW} and $v_{SW} \sim 400$ km s^{-1}.
* Joy et al. (2002)
** Achilleos et al. (2008)

field lines connected to the solar wind) and closed (i.e. field lines connected the to the planet) with the possibility of many turbulent field structures (as modelled for the terrestrial case by Gingell et al. (2019)). The role of the magnetosheath in jovian magnetospheric diagnostics and auroral mechanisms will be examined further in later sections.

As found by *Galileo* and the Joy et al. (2002) magnetospheric model, the jovian magnetopause standoff distance on the dayside is bi-modal with a most probable distance of 63 and 92 R_J for high and low solar wind dynamic pressure respectively. When these values are compared with the Chapman-Ferraro distance of ~ 42 R_J (Table 2.1), assuming a pressure balance between the magnetic pressure produced from a dipolar field and the solar wind dynamic pressure, we see that the Chapman-Ferraro model does not hold for Jupiter (and Saturn), suggesting the assumptions made may not apply to the case of gas giant magnetospheres. The complex jovian magnetic field and its effect on auroral mechanisms will be examined further in Section 2.2. The discrepancy in these values arises from the dipolar assumption being too strong to describe the jovian field and the plasma pressure generated from Io, neglected from the Chapman-Ferarro picture. As the plasma pressure cannot be neglected due to the dominant internal plasma source, it must be included with the magnetic pressure contribution. The added plasma pressure term therefore makes jovian magnetosphere more compressible and sensitive to solar wind dynamic pressure than the terrestrial magnetosphere.

The local time asymmetries found by *Galileo* in the plasma flow and magnetic field are most prominent in the outer magnetosphere as the solar wind has more influence on this region. The jovian magnetotail, as illustrated in Figure 2.2, contains two lobes

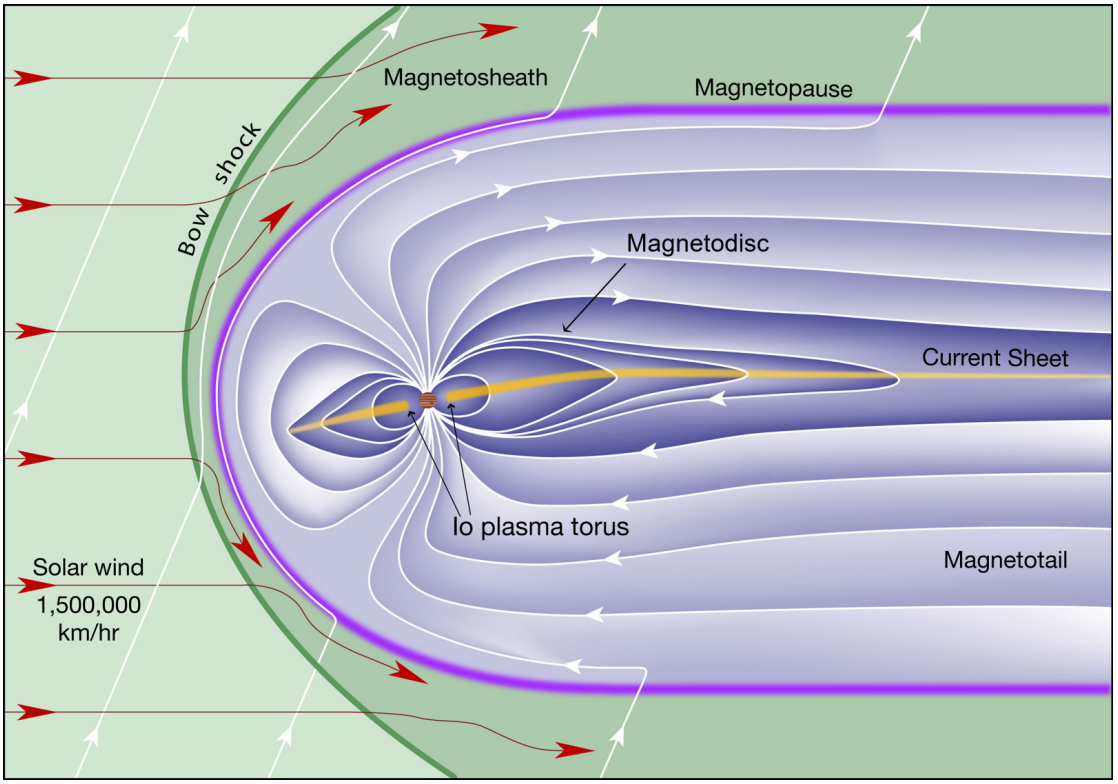

FIGURE 2.2: Labelled schematic of the jovian magnetosphere. The Sun is to the left of the image with the solar wind flow indicated by red arrows. Image taken and adapted from: https://lasp.colorado.edu/home/mop/resources/graphics/
Credit: Fran Bagenal and Steve Bartlett

separated by thin current sheet with stretched, radial field configuration containing low density plasma. Flow velocity vectors from particle data collected by *Galileo* shown in Figure 2.3 found that the plasma flow here is subcorotational (i.e. slower than the corotation velocity) with an azimuth and outward radial component and is fastest near the dawn local time (Krupp et al., 1998), where the field has the strongest bend-back due to interactions with the opposing solar wind flow (Khurana et al., 2004). On the pre-noon to pre-dusk magnetosphere outside of the magnetodisk lies a disturbed plasma region called the *cushion region*, believed to be formed from strongly fluctuating magnetic field preferentially dawnside due to the transport of empty flux moving dayside, emptied by night-side magnetic reconnection (e.g., Kivelson and Southwood, 2005; Delamere and Bagenal, 2010; Went et al., 2011). Gershman et al. (2017) found evidence of *Juno* flying through the cushion region during its orbital insertion. The magnetospheric dynamics found throughout the jovian magnetosphere and their effect on auroral emissions will now be examined in greater detail.

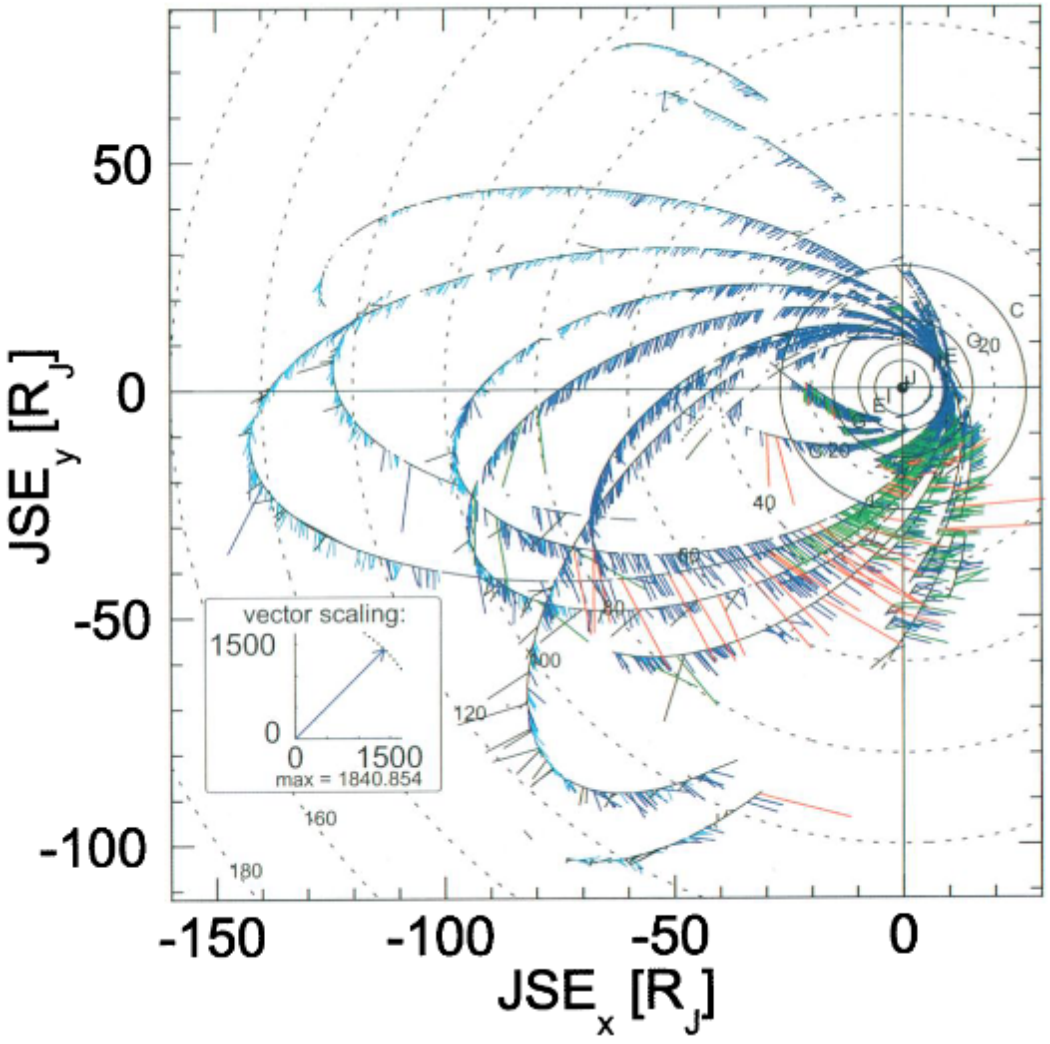

FIGURE 2.3: Cartesian plot in the jovian equatorial plane of time-averaged flow velocity vectors of sulphur ions found by *Galileo*. The colours of each vectors here represent whether the plasma is in corotation (green), lagging corotation (blue and cyan) or leading the corotation velocity (red) Black vectors indicate instances where the radial components are greater than those found in the direction of corotation. Figure taken from Plate 5 in Krupp et al. (1998).

2.1.2.2 The middle magnetosphere

As shown in Figure 2.2, most of the plasma in the jovian magnetosphere is confined to the jovian current- or plasma- sheet, hinged at $\sim 47\ R_J$ as observed from *Pioneers 10 and 11, Voyagers 1 and 2, Ulysses, and Galileo* magnetometer data (Behannon et al., 1981; Khurana and Schwarzl, 2005) and is shaped by the magnetodisk. Planetward of the hinge feature, the current sheet is found to be aligned with the jovian magnetic equator (9.6° tilt with respect to the joviographic equator) 10 - 30 R_J from the planet. Throughout the remainder of the middle magnetosphere away from the planet, the current sheet resides between the centrifugal and magnetic equator and the inertia of

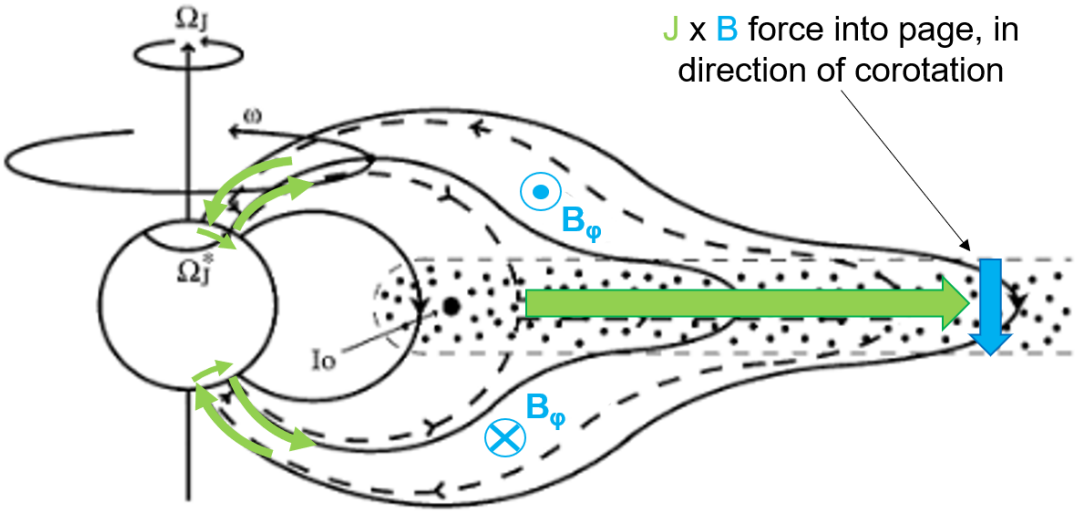

FIGURE 2.4: Cartoon showing the current system with the directions of current flow responsible for generating a $\mathbf{J} \times \mathbf{B}$ force (directed into the page as is the direction of corotation) to drive plasma in the azimuthal direction back to corotation velocities. Angular velocities of the planet, magnetic field field lines anchored to the planet and the jovian ionosphere are denoted by Ω_J, ω and Ω_J^* respectively on the figure. The azimuthal field direction is shown in light blue and the current flow shown in green. Figure taken and adapted from Figure 1 in Cowley and Bunce (2001).

the plasma exceeds that due to corotation, causing the sheet to lag the planetary field (beginning between $\sim$ 20 - 30 R_J). This results from the plasma angular velocity decreasing to obey the conservation of angular momentum as the iogenic plasma flows radially outward from the IPT. Due to the Alfvén's theorem (described in Section 1.4.3) and provided the plasma behaviour can be described using ideal MHD, the plasma is threaded into the field and the decreasing plasma angular velocity near the equatorial plane will deform and sweep back the field into a spiral configuration (e.g., Khurana et al., 2004). The resulting Io flux tube (IFT) also lags corotation as a result. In this region, the radial currents (or Hall currents as defined by the MHD momentum and Ohm's law: Equations 1.29 and 1.30) provide a $\mathbf{J} \times \mathbf{B}$ force to counteract the lag by accelerating the plasma back towards corotational velocities, transferring angular momentum from the jovian ionosphere to the plasma in the process. The described *corotation enforcement currents* are part of the closed current system responsible for driving the jovian UV main auroral emissions as shown in Figure 2.4, with the current and azimuthal field direction shown in green and light blue respectively. How this current system is responsible for the main auroral emissions is examined further in Section 2.2.

2.1.2.3 The inner magnetosphere

As found by *Pioneer 10*, the magnetic field in the jovian inner magnetosphere is mainly dipolar in nature, trapping very energetic particles (tens of MeV) producing very high

intensities (e.g., Bolton et al., 2015). This results in the *jovian radiation belts* (within 5 R_J of the planet) being the most inhospitable in the solar system, making it difficult for visiting spacecraft to pass through without significant damage to on-board electronics (e.g., Woodfield et al., 2014). The belts are formed from plasma diffusing radially due to dynamo fields (produced from planetary rotation and the convection and electrical conductance of the plasma) exhibited by ionospheric flows. As the plasma conserves the first and second adiabatic invariants (Section 1.3.3), it gains more energy as it moves inwards. Further out from the radiation belts is the most dominant feature in this region: the Io plasma torus (IPT). The IPT is formed from the sputtering of sulphur, oxygen and sulphur dioxide from Io's volcanic surface and atmosphere, ionised from solar UV photons and electron bombardment from cosmic ray albedo neutron decay (CRAND), due to cosmic rays scattering of the planetary neutral atmosphere producing decaying neutrons (e.g., Thomas et al., 2004). The effect the IPT has on auroral activity will be examined further in the remainder of this chapter.

2.2 Magnetospheric dynamics and associated auroral processes

The rapid planetary rotation of the gas giants coupled with their internal plasma sources not only change the structure of the magnetosphere but also the dynamics that occur within it. Examination of auroral emissions is an excellent way to assess, analyse and understand the magnetospheric dynamics is to look at the auroral emissions produced by the planet across the electromagnetic spectrum. The auroral emissions are often described as the "tv screen" for the magnetosphere, with the consequences of a broad range of solar wind and magnetospheric processes being focused into a relatively small area near the northern and southern poles. Information is communicated along the magnetic field lines throughout the magnetosphere which have their footprints in these regions, affecting the auroral emissions. These processes vary depending on whether the magnetosphere is driven mainly by the solar wind (e.g. Earth) or by the rotation of the planet (e.g. Jupiter). This section will examine the auroral dynamics of the jovian magnetosphere.

2.2.1 Dynamics associated with a rotationally-driven magnetosphere

As Jupiter's magnetosphere is rapidly rotationally-driven magnetosphere with a dominant internal plasma source, Io, the mass and energy required to drive the magnetosphere will also be produced by these sources and eventually released from the system via processes like magnetotail reconnection. Therefore the centrifugal forces produced within the system relative to the solar wind play a more important

role at Jupiter than the terrestrial magnetosphere. Due to Jupiter's rapid rotation and large magnetospheric scale size, the potential energy from corotation is ~ 50 times greater than the induced solar wind cross potential across the poles, ~ 10 times more dominant than at Earth (e.g., Khurana et al., 2004). This emphasises that the forces due to rotation play a critical role in driving jovian magnetospheric dynamics.

Vasyliūnas (1983) put forward a picture of the cycle of plasma flow which can take place in an internally mass-loaded, rapidly rotating magnetosphere like Jupiter. This new model stated that magnetic reconnection takes place on filled, or mass-loaded, flux tubes that are stretched by the exerted centrifugal forces. These flux tubes pinch and form a plasmoid, as observed by the New Horizons flyby (McComas et al., 2007). This process is more commonly referred to as the *Vasyliūnas cycle* and is shown in Figure 2.5. The mass-loaded flux tubes rotate anticlockwise (when viewed in the equatorial plane) towards nightside (1). These flux tubes are then stretched due to the centrifugal forces of the plasma within them (2) and eventually pinch off, releasing an isolated filled magnetic island, or plasmoid, down the magnetotail (3, 4). Figure 2.5 also highlights the site of magnetic reconnection where oppositely directed magnetic field lines are predicted to reconnect, the *magnetic X-line*, and potential regions of whirlpool-shaped vortices where the rotation of the planet cause magnetic field lines twist together, *magnetic O-line*. *Galileo* observations found that the local time asymmetries in the jovian plasma sheet were qualitatively similar where the rotation towards the dusk sector causes it to thicken (Kivelson and Southwood, 2005) and found evidence for plasmoid release in the jovian magnetotail (e.g., Vogt et al., 2014).

The Vasyliūnas (1983) model considers internally driven dynamics and circulation of jovian and iogenic plasma, accounting for nightside reconnection which can lead to implications in auroral structure (e.g. dipolarisation of the magnetic field leading to injection events found by Yao et al. (2020): see Section 2.2.2). As argued by Cowley et al. (2003), a second large-scale plasma flow cycle can operate at Jupiter in tandem with the Vasyliūnas cycle: the *'single-cell' Dungey cycle* (adapted from the terrestrial case modelled by Dungey (1961)). The Dungey cycle describes the interaction between the solar wind and a planetary magnetosphere via cyclic behaviour of magnetic reconnection. This cyclic process is one mechanism in a planetary magnetosphere responsible for plasma mixing anf transport inside the system. In the terrestrial magnetosphere, the reconnection sites are located on the dayside magnetopause boundary and in the magnetotail (e.g., Dungey, 1961). When more reconnection occurs on the dayside than in the magnetotail (i.e., increased dayside reconnection rate), the polar cap is observed to expand to compensate for the increase in opened flux and vise versa (Milan, 2013). For the case of Jupiter, a 'single-cell' flow would be produced from the Dungey cycle starting with reconnection driven by the solar wind on the dayside magnetopause at lower latitudes for a northward interplanetary magnetic field (IMF), which opposes Jupiter's southward directed equatorial field.

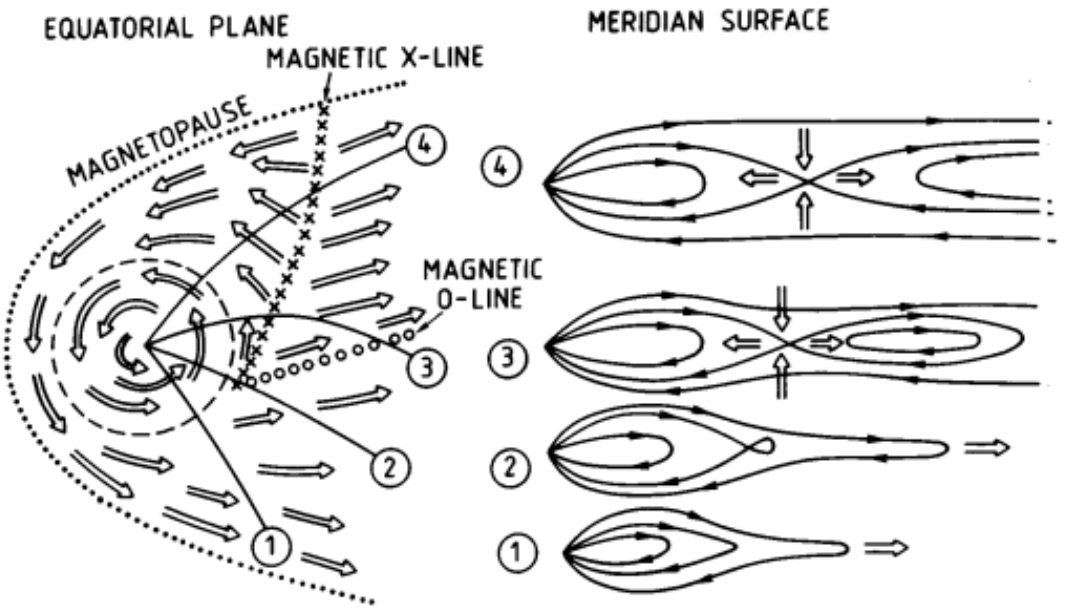

FIGURE 2.5: Schematic from Vasyliūnas (1983) explaining the mass loading and release process of the Vasyliūnas cycle. The filled flux tubes (1) rotate anticlockwise, in the equatorial plane, towards night side, (2) stretch as a consequence of the centrifugal forces produced from accelerating particles, (3, 4) and separate, due to magnetic reconnection, as a plasmoid. The magnetic X- and O- lines are also indicated in the figure.

The reconnection would open flux from dusk to dawn, as shown in Figure 2.6a), and close at the X-line in the tail near the dawn magnetopause where a boundary layer is formed as a result of empty flux tubes produced from the process.

The set of flows from the Cowley et al. (2003) mode; are shown in Figure 2.6, with the same labels panel (a), and produces flows (both in and out the page) for both the northern auroral emissions and the polar ionosphere. The Pedersen current structure, similar to the case for Earth, produced by such flows generate a downward current system located just within the upward current system at the dawn edge. The implications of these current systems and how they affect the main auroral emissions will be examined in greater detail in Section 2.2.3. The single-cell nature of the flow is argued by Cowley et al. (2003) who suggested that the Dungey-like X-line would be restricted to the dawn jovian magnetosphere only (see Figure 2.6, opposite to that of the Vasyliūnas cycle, as a result of strong outflows from corotation and the Vasyliūnas cycle itself. These flows oppose the direction of the sunward flow in the dusk-midnight sectors.

In contrast, McComas and Bagenal (2007) argue that the opened magnetic flux due to dayside reconnection with the solar wind does not necessarily need to close in the jovian magnetotail. They propose that the newly opened flux closes on the magnetopause situated near the polar cusps - direct entry points into the

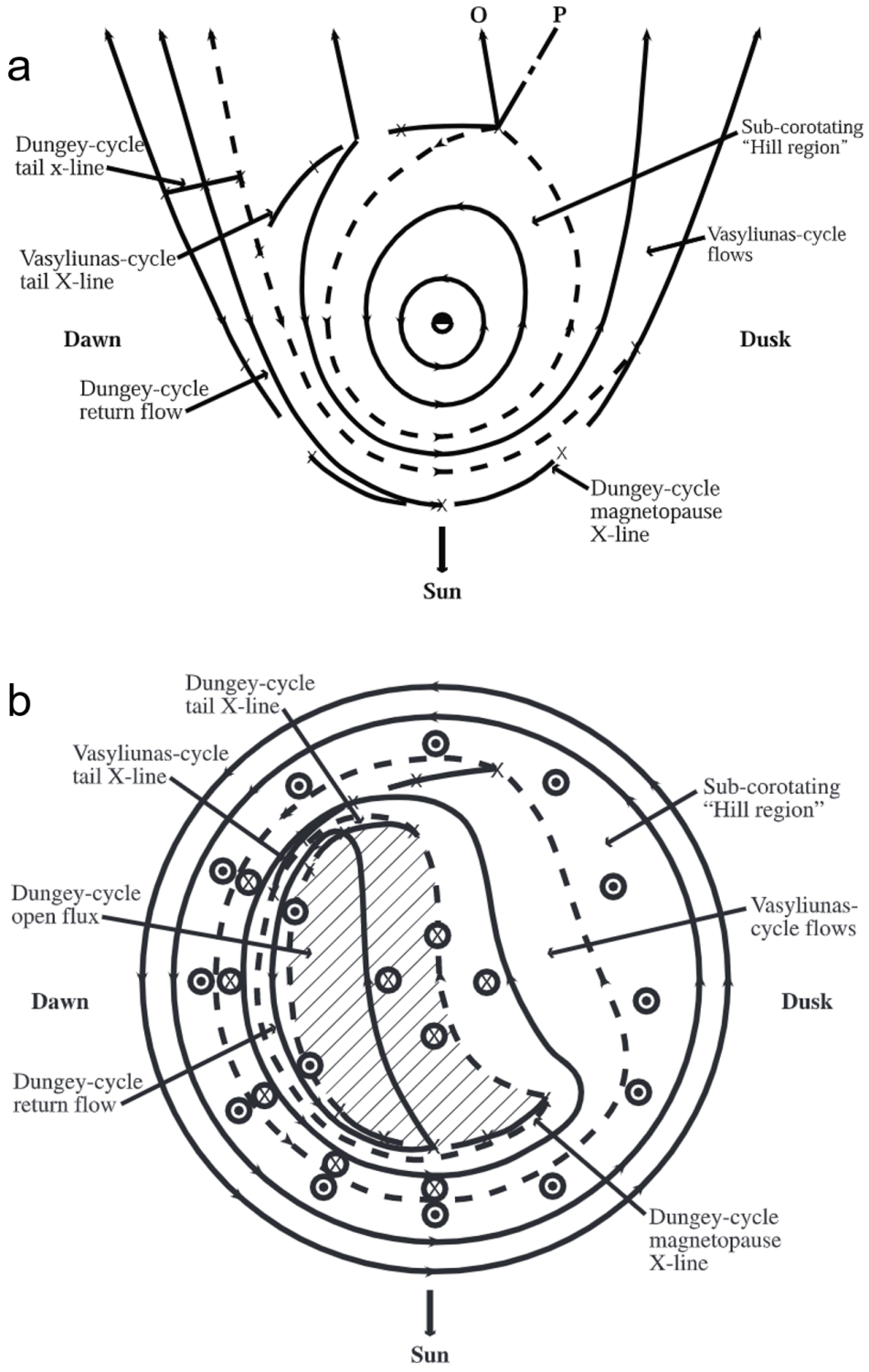

FIGURE 2.6: Schematic of (a) the jovian magnetosphere in the equatorial plane illustrating possible 'single-cell' Dungey cycle as argued by Cowley et al. (2003) with the corresponding flows throughout the magnetosphere. The middle magnetosphere is dominated by the subcorotating 'Hill region'. Radially outward from here represent the region where current sheet dynamics take and Vasyliūnas (1983)-like tail reconnection takes place on the labelled dashes and X's tail X-line (process shown in Figure 2.5). The O-type line of the plasmoid (denoted by 'O') and the outer edge of the plasmoid (dot-dahed line: marked 'P') are also shown to show how a Dungey-like process can be linked to a rapidly-rotating magnetosphere. Panel (b) shows the corresponding ionospheric flows in the northern polar region. Taken and adapted from Figures 1 and 2 from Cowley et al. (2003).

magnetosphere due to the field configuration - and therefore stating that tail reconnection is unnecessary in the process. Their other counter-argument raises concerns regarding the inefficiency of tail reconnection returning flux to the dayside due to the timescale of the returning plasma flow from a distant neutral point via a Dungey-like process ($\sim$ 750 - 1000 hours corresponding to $\sim$ 75 -100 jovian rotations). As a result, an alternative mechanism must exist to close the returning flux opened on the dayside opposed to the return flow from a distant X-line suggested by Cowley et al. (2003). However, Cowley et al. (2008) state that substorm-like reconnection may take place more planetward that the suggested distant neutral line, and the timescale of the returning flux calculated by McComas and Bagenal (2007) was an overestimate.

Other studies propose that the jovian magnetospheric dynamics may be driven by a more viscous-like solar wind interaction opposed to reconnection due to the fact that electric fields produced from reconnection processes are weaker the further the planet is from the Sun (e.g., Masters, 2018). Alternative mechanisms along the magnetopause boundary such as Kelvin-Helmholtz instabilities (KHI) may be the more dominant driver for jovian magnetospheric dynamics as the boundary hosts more unstable regions, allowing the instability to grow. The possible role of KHIs associated with the aurora will be explored further this chapter and later in this research (Chapters 4 and 5).

2.2.2 Overview of imaging the jovian auroral emissions

The auroral emissions at Jupiter have been observed across the electromagnetic spectrum in radio, infrared, visible, UV and X-ray wavelengths for many decades. In this research, our discussions will only briefly cover the UV and largely focus on the X-ray emissions. Having a good understanding of the UV emissions provides a a good proxy for magnetospheric processes and dynamics, and vital context to the X-ray emissions we observe. A more thorough and complete discussion about the history and processes behind the jovian aurora can be found in review chapters such as Bhardwaj and Gladstone (2000) and Badman et al. (2015).

The first satellite observation of Jupiter's auroral emissions were orchestrated by *Voyager 1* during its flyby of the planet, using the Ultraviolet Spectrometer (UVS) on board (Broadfoot et al., 1979). Following this landmark discovery, temporal variations in the UV auroral emissions were studied extensively by the *International Ultraviolet Explorer (IUE)*, a remote sensing telescope in Earth's orbit, for more than 15 years (1979 - 1996) (Clarke et al., 1980). With the launch of the *Hubble Space Telescope (HST)* in 1990, revolutionary high resolution auroral imaging was finally made possible with the Faint Object Camera (FOC), observing Jupiter for the first time in 1992 (Caldwell et al., 1992). The vast majority of UV images taken nowadays, and briefly discussed in

later chapters, are from the Space Telescope Imaging Spectrograph (STIS) onboard *HST* with the instrumentation discussed further in Chapter 3.

From an X-ray point of view, the first observation of the jovian auroral emissions were made by the *Einstein Observatory* in 1979, with the exponent of the power law of found from the slope of the X-ray spectrum and shape of the X-ray response suggesting extremely soft X-rays from line emissions from iogenic ions (i.e. O and S) (Metzger et al., 1983). With the launch of the *Chandra* X-ray Observatory, with its high spatial resolution, as part of NASA's Great Observatories campaign in 1999, the first spatially resolved jovian auroral X-ray image was taken on December 18 1999 with a so-called "hot spot" of concentrated auroral emissions (Gladstone et al., 2002). With the high spectral resolution of *XMM-Newton*, detailed spectra of the auroral emissions and their X-ray constituents were observed underpinning X-ray production from both precipitating electrons, found close to the UV main oval, and ions, found more poleward. The associated jovian auroral X-ray processes and more details about the *Chandra* instrument, the main source of the data used in this research, are discussed further in this chapter and Chapter 3 respectively.

2.2.3 Main auroral emissions

The jovian UV auroral emissions can be separated into three main categories: (1) the satellite footprints, due to moon-planet interactions, (2) the main oval or main emissions, and (3) the polar emissions (Clarke et al., 1998). Each UV component is shown in Figure 2.7a) as a polar projection of these emissions at the North pole. Although we can image the aurora structures with high resolution, not all are well understood when linking them to their drivers in the magnetosphere, generating a whole host of dynamics. For example, the driver linking the satellite footprints to the auroral emissions is relatively well-understood when compared to the more enigmatic polar emissions which are very difficult to reliably map to their magnetospheric source. In the remainder of this section, we briefly discuss the current understanding these features of the UV aurora as a proxy for magnetospheric dynamics to allow us to compare these emissions to their X-ray equivalent.

2.2.3.1 Satellite footprints

The satellite footprints allow us to constrain the global mapping models we use in the field today, for example, when mapping the internal magnetic field (e.g., Connerney et al., 1998, 2018) or mapping sources out into the magnetosphere from their ionospheric position (e.g. Vogt et al., 2011, 2015). This is because the orbital locations of the moons and the magnetic field line they are connected to are known, providing

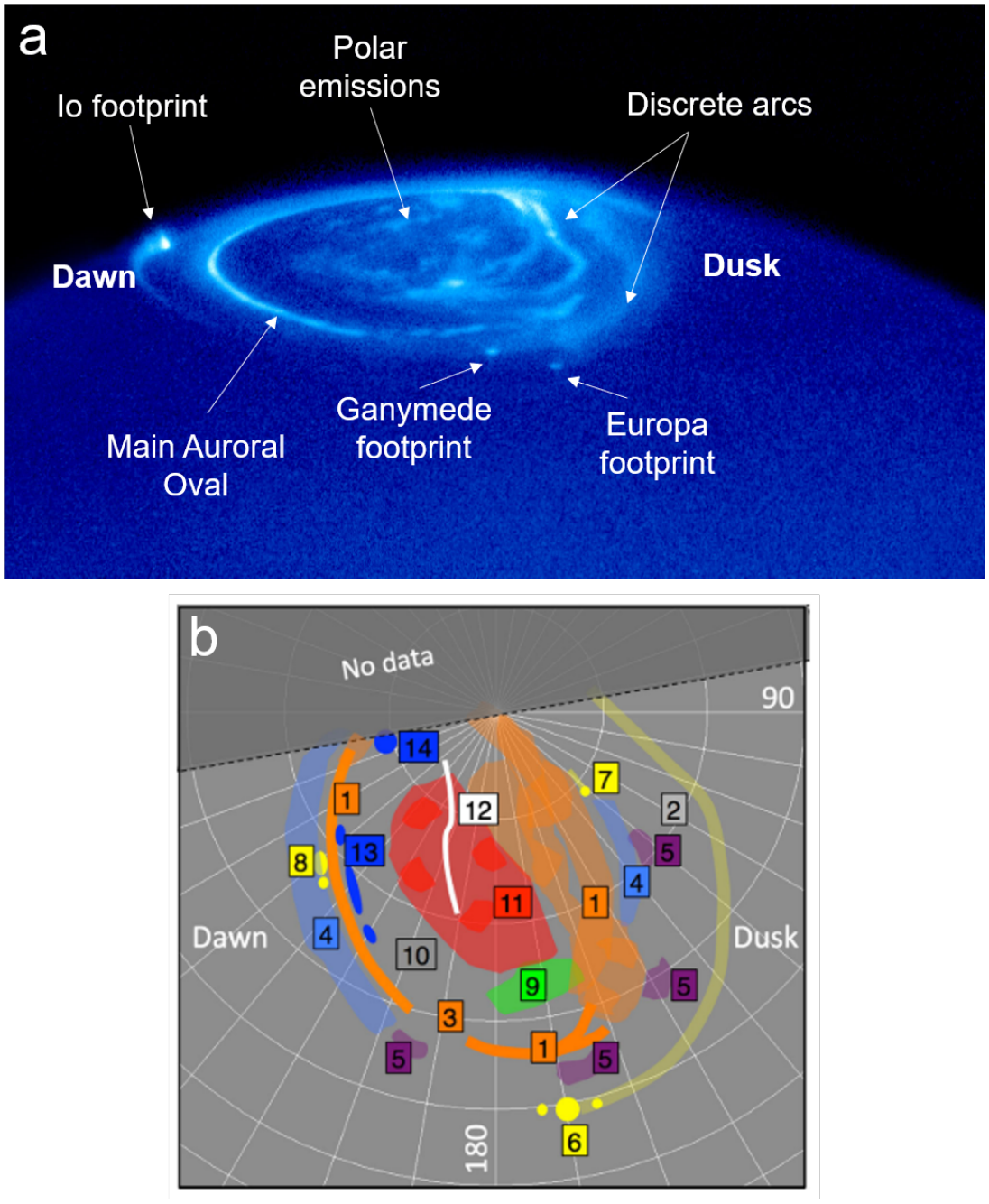

FIGURE 2.7: (a) The UV auroral emissions as observed by *HST* with major auroral structures and features labelled. These auroral structures can be further separated into finer, physics-informed sub-structures as shown in (b). The main oval (1), with the kink region (2) and discontinuity (3), and satellite footprints for Io (6), Europa (7) and Ganymede (8) are highlighted in both panels with their extended tail emissions. The polar emissions can be further split into the active (9) and swirl regions where emissions are observed in UV (11) with a mysterious dark polar region (10) where very little to no UV emissions are observed. Further substructures inside the polar region can be identified from an observation-to-observation basis associated with dynamics in the magnetosphere at dawn (13) and midnight (14). Outside of the polar emissions, particle injections (5) can also cause auroral emissions. Analysing these features in great detail is beyond the scope of this research however comparisons with the X-ray emissions are beneficial.
Panel (a) is adapted from https://www.nasa.gov/mission_pages/juno/multimedia/pia03155.html with *credit given to NASA/ESA, Hubble Heritage Team (STScI/AURA) and John Clarke (University of Michigan)*. (b) is taken from Figure 2 in Grodent (2015)

us with the ability to link the footprint's ionospheric location to its radial position in the jovian magnetosphere with a high degree of accuracy, as well as their associated longitude with a small uncertainty due to the signal propagation time (e.g., Clarke et al., 2002). With this invaluable information, the accuracy of many global field models can be checked in detail using the orbital radial distances of Io (5.9 R_J), Europa (9.4 R_J) and Ganymede (15 R_J).

As shown in Figure 2.7 with the labelled satellite footprints (yellow spots marked (6) - (8)), the morphology consists either of a single spot (Europa) or multiple, distinct spots (Io and Ganymede) (e.g., Bonfond et al., 2009), followed by a trailing tail of emissions for Io and Europa (e.g., Clarke et al., 2002). Recent studies using the infrared imager on board *Juno* have found the "tail" of the footprints to consist of sub-dots which corotate with Jupiter (e.g., Moirano et al., 2021). Each of the distance between the luminous sub-dots are the same in both hemispheres and could suggest possible wave-particle interactions associated with a perturbed magnetic field such as Alfvén and ion cyclotron waves (e.g., Gershman et al., 2019; Sulaiman et al., 2020). In this research, we use the Io and Ganymede orbit as an indicator of driver location for the X-ray emissions and how the morphology evolves as well as to constrain any global mapping models used (see Chapters 4 - 6 for more details).

2.2.3.2 Main oval emissions

As shown in Figure 2.7, the main oval emissions are poleward of the satellite footprints and are found to be be located in a narrow band, fixed in System-III (S3) longitude - a coordinate system that rotates with the planet (Grodent et al., 2003a). The S3 coordinate system is left handed and rotates with the sidereal S3 spin period of the planet (9.925 hours or angular velocity, Ω, of 1.76×10^{-4} rad s^{-1}). The z-axis defined by the spin axis of Jupiter and the x-axis is defined by 0° latitude (θ_{III}) on the prime meridian (System III longitude, λ_{III} , of 0°). The y-axis is defined as the cross-product of the x- and z- axis and completes the orthogonal set[2]. As labelled in Figure 2.7b), the main oval emissions in the North are actually shaped as a kidney bean due to a "kink" (label (2)) caused by a magnetic anomaly in the jovian field (Grodent et al., 2008). This anomaly is only observed in the northern hemisphere, the more dipole magnetic field in the South has a more typical oval topology.

As briefly discussed in Sections 2.2 and 2.2, the jovian main auroral emissions are not associated with a Dungey-like open/closed field line boundary as observed at Earth but due to corotation breakdown of iogenic plasma in the middle magnetosphere (e.g., Hill, 1979, 2001; Cowley and Bunce, 2001). The iogenic plasma begins to diffuse radially as a result of flux tube interchange (mainly convective (e.g. Southwood and

[2] https://lasp.colorado.edu/home/mop/files/2015/02/CoOrd_systems7.pdf

Kivelson, 1989)), causing its angular velocity to decrease in order to maintain the conservation of angular momentum between the jovian ionosphere and plasma. The decrease in angular velocity causes the frozen-in field lines to lag and be swept back azimuthally (provided the plasma follows the ideal MHD picture), closing a current system produced from field-aligned current going to and from the ionosphere, at field lines $\sim 20\ R_J$ from the planet, by generating an outward radial corotation enforcement current field-aligned current in the equator (e.g., Cowley and Bunce, 2001). The corotation current in the equatorial plane produces $\mathbf{J} \times \mathbf{B}$ in the direction of corotation to drive the angular plasma velocity back to corotation velocities. The UV main emissions are produced from electrons accelerating downwards to carry the upward field-aligned current (e.g. out of the jovian ionosphere). The intricacies of this current system is beyond the scope of this research (see Cowley and Bunce (2001) for more details) but the location and driver of the electrons are essential to understand the X-ray auroral emissions (Section 2.4).

A recent study by Bonfond et al. (2020) found evidence to suggest that the assumptions made for the theory of corotation enforcement current begins to break when trying to account for local time variations and temporal variability in the auroral emissions. They note that the evidence found is related to the generation of the auroral emissions which are not strictly linked to the magnetosphere-ionosphere coupling of the jovian system. Their findings suggest that due to many observed features of the main auroral emissions, such as local axisymmetry, response to the solar wind changes and the dawn/dusk asymmetry in auroral brightness, challenge the widely accepted theory of corotation enforcement currents as the auroral driver. Another argument Bonfond et al. (2020) put forward is the lack of net field-aligned currents (FACs) observed from recent Juno observations (Kotsiaros et al., 2019). They found that the FAC was more fragmented and confined in longitude as opposed to the expected thin and regular current shells, as expected from corotation breakdown. Such fragmented FACs questions the current-aurora relation in the jovian magnetosphere. Alternatively, more emphasis should be placed on calculating the Poynting flux and Alfvén wave power contribution when comparing the outputs of auroral images.

When observing the main oval emissions, there are recognisable spatial features that can be related to changes in the auroral driver. One key feature is a "discontinuity" (labelled (3) in Figure 2.7, a region of where the intensity of the emissions are very dim compared to the typical main oval brightness. The region is found to map to the pre-noon magnetosphere and is associated with a reverse in flow and direction of the field-aligned current (e.g. reversed to flow downward into the jovian ionosphere) (Radioti et al., 2008). Other features of the main UV emissions include major enhancements of the dawn auroral arc accompanied with a dramatic broadening in latitude called an *auroral dawn storm* (e.g., Bonfond et al., 2021). Such jovian auroral phenomena have been found to be possibly connected with injections of hot plasma in

the middle magnetosphere (labelled as (5) in Figure 2.7: purple patches) (Kimura et al., 2017). A recent study by Yao et al. (2020) suggested that both features are causally connected. Dawn storms were found to be linked to dawnside magnetic reconnection resulting and dipolarisations of the jovian magnetic field (e.g. the field line changing from a stretched topology to a relaxed, dipole shape, causing it to move towards the planet in the middle magnetosphere) mapping to auroral injection sites. Magnetic reconnection and dipolarisations have been observed to be connected and therefore explains why auroral dawn storms and injections are sometimes observed simultaneously. *Juno* also found an extended region of highly energetic particles near the magnetopause following the dawn storm while in the dawn outer magnetosphere, possibly associated with a reconfiguration of the magnetosphere (Swithenbank-Harris et al., 2021), again agreeing with previous literature. The importance of dawn storms and how they relate to the X-ray auroral emissions will be discussed later in this chapter and in more detail in this research (Chapter 6).

2.2.3.3 Polar aurora

The third more elusive main feature of the jovian auroral emissions is the polar region. As previously mentioned, these emissions are very difficult to map due to the associated field lines occurring at very high latitudes as well as the morphology of these features varying with time during a jovian rotation (e.g., Grodent et al., 2003b).

The most dynamic emissions from within the polar aurora are found in the active region, characterised by flaring of the UV emission accompanied with bright spots and arc-like sub-structures (labelled as (9) in Figure 2.7: green patch). The brightness of such flares in this region are found to be comparable to that of the main oval (a few hundred kilo-Rayleigh (Grodent et al., 2003b), a unit of photon flux where 1 Rayleigh = $4\pi \times 10^{-10}$ photons m^{-2} s^{-1} steradian^{-1}, compared to the intensity of the main oval of 50 - 500 kR (Grodent et al., 2003a)) and have characteristic timescale of the order of $\sim$ minutes. The unit of 'Rayleighs' is used to define the brightness, or apparent emissions rate, of planetary aurora along a column of emissions throughout the field. The active region is found to map to approximately noon and is located poleward of the main oval and therefore likely to be associated with interactions with the solar wind or the cusp reconnection (e.g., Bunce et al., 2004). Grodent et al. (2003b) interpreted the flaring of the UV emissions as a signature of "explosive" reconnection occurring on the dayside jovian magnetosphere due to their minutes-long time scale and the arc-like sub-structures as a possible dayside X-line associated with Dungey-like processes, as argued by Cowley et al. (2003).

As shown by region (10) in Figure 2.7, the dark region is a crescent-shaped and appears mainly dark in the UV emissions, only peaking $\sim$ 0 - 10 kR above background

(Grodent et al., 2003b), significantly dimmer than the main oval emissions. This dark region is fixed in local time but has been observed to contract and expand as Jupiter rotates, mapping to the outer magnetosphere (Pallier and Prangé, 2001) ($\sim 70\ R_J$; based on the VIP4 model (Connerney et al., 1998)). Southwood and Kivelson (2001) argued that the dark polar region will most likely map to the cushion region if the main emissions are driven in the plasma disc, as the dark polar region is found to be slightly poleward of the main auroral emissions (e.g., Grodent et al., 2003b; Grodent, 2015) e.g. a region where empty flux tubes rotate to the dayside after being emptied by Vasyliūnas-type reconnection on the night side (as depicted in Figure 2.5).

The swirl region, located poleward of the dark and active regions (red region (11): Figure 2.7), is composed of patchy and turbulent auroral emissions and forms the centre of the polar aurora. Previous literature associates this patchy region with open field lines (e.g., Pallier and Prangé, 2001; Cowley et al., 2003), as it is found to almost coincide with a feature in the infrared emissions, the fixed Dark Polar region (f-DPR), where the flows produced from the ionosphere are found to be nearly stagnant (in a frame of reference fixed to the jovian magnetic poles, rotating with the planet) (Grodent et al., 2003b; Stallard et al., 2003). These stagnant flows in the f-DPR, mapping to the swirl region, are found to map to possible open field lines linked with a Dungey-like return flow (Cowley et al., 2003), flowing across the ionosphere slowly due to the vast length of the jovian magnetotail. A recent study by Greathouse et al. (2021) analysing *Juno* UV data, form the Ultra-Violet Spectrograph (UVS) (Gladstone et al., 2017), observed a local time dependence in the swirl region (and the entire polar aurora region). Greathouse et al. (2021) analysed several UVS data during numerous *Juno* perijove passes, the point in its orbit closest to the planet, as the spacecraft was above the poles. They observed a strong ionospheric local time dependence in the swirl region with the emissions being more intense at $\sim$ 5 - 7 ionospheric local time and found to disappear $\sim$ 20 - 22-hr. The higher colour ratio, ratio of emissions driven by the spectrum of methane absorption in the UV emissions, observed in the swirl region than the dark and active regions imply that the emissions are driven by different mechanisms. A higher colour ratio implies more energetic electrons impacting that region of the ionosphere and therefore different ratio values may correspond to different electron populations or magnetospheric drivers located in the jovian magnetosphere.

Additional features in the auroral emissions such as the polar auroral filament (white line (12): Figure 2.7) and dawn and midnight spots, (13) and (14) respectively, are beyond the scope of this research. This is because the brightest auroral X-ray emissions at Jupiter, the main focus of this research, are located equatorward from these regions, coinciding with the swirl and active regions. However, the dawn and midnight spots are still a useful proxy to decipher the dynamics of the jovian magnetosphere. Understanding the dynamical process and where the polar aurora

map to is imperative in order to fully develop the full picture of the jovian magnetosphere. When comparing UV images and X-ray maps, the majority of the X-ray emissions are co-located with the UV polar emissions with some overlap with the main auroral emissions suggesting a possible link between the auroral drivers. This idea is explored in more detail through the rest of this research.

2.3 General X-ray Mechanisms

Astronomical X-ray emissions span across wavelengths of $\sim$ 10 - 0.01 nm (or energies, E, $0.1 \leq E \leq 100$ keV) on the electromagnetic spectrum and are absorbed by the molecular gases of Earth's atmosphere, through photoelectric scattering. Therefore, astronomical X-ray observations are carried out $>$ 400 km above the Earth's atmosphere to ensure all X-ray photons can be detected from celestial objects without any contaminant from the Earth. Key current operational space-based X-ray telescopes include Chandra (CXO, see Chapter 3), XMM-Newton and NuSTAR. As discussed in more detail in Chapter 3, the geometric design of the X-ray telescope dictates the resolution of your observations. For the higher end of the X-ray energies telescopes resemble collimators, a device to narrow the X-ray beam onto the detector at the end of the telescope. For lower X-ray energies ($0.1 < E < 1$ keV), grazing incidence optics can be used to image the X-rays onto the focal plane of the telescope which is difficult to do for X-rays beyond this range as the telescopes need to be significantly longer to account for the smaller grazing incidence angles of the higher energy photons (e.g., Longair, 2011). This research focuses on data taken from the latter type of telescope. The remainder of this section will discuss the X-ray mechanisms and contextualise the processes for the jovian X-ray observations.

2.3.1 X-ray regimes

In the field of X-ray astronomy, it is common to separate the emissions into two categories based on their energy: *soft* ($0.1 < E < 5 - 10$ keV) and *hard* ($E > 5 - 10$ keV) X-rays. For Jupiter, this regime is slightly altered to define soft X-rays having $E < 2$ keV and the harder X-ray emissions having energies $E > 2$ keV due to the different mechanisms involved in X-ray production (Branduardi-Raymont et al., 2008). These X-ray emissions will therefore be produced from different processes depending on the energy of the charged particles involved in the interaction. The more energetic hard X-rays will have a greater penetration depth than their softer counterpart. For example, hard X-rays are used for medical imaging and crystallography as they are energetic enough to penetrate through the materials and allows the interior structure and composition of the objects to be imaged. In the field of X-ray astronomy, the more

energetic X-ray photons are associated with relativistic processes such as Inverse Compton scattering and synchrotron radiation (e.g., Longair, 2011), where the charged particles responsible for X-ray production have velocity, v, close to the speed of light, c (e.g. $v \gtrapprox 0.8c$). The softer X-rays are more likely to be generated from a non-relativistic process, such as Thomson scattering and thermal bremsstrahlung, where the velocity of the charged particle is $v \ll c$. The remainder of the section will briefly describe astrophysical X-ray processes relevant to Jupiter.

2.3.2 Bremsstrahlung

Bremsstrahlung (translated as 'braking radiation') or *free-free radiation* is the emitted radiation associated with the acceleration or deceleration of a charged particle in the vicinity of an electrostatic field produced from another charged particle. X-ray emissions are produced when the charged particle loses kinetic energy due to deceleration which is then converted into emitted radiation (e.g. X-ray photons: see Figure 2.8). For the case of an incoming, free-ranging charged particle affected by the electrostatic field, the photons emitted can have variety of energies associated with the velocity and amount of deceleration/acceleration the charged particle has undergone[3]. The distribution of these photon energies produces a continuous spectrum or *continuum emissions* where the peak frequency is dictated by the extent of the particle deceleration/acceleration (e.g. Rybicki and Lightman, 1986; Longair, 2011).

As the research examined in this thesis focuses mainly on the spatial and temporal behaviour of jovian auroral X-rays as opposed to X-ray spectra, we do not fully derive the expression for bremsstrahlung radiation here (full derivation can be found in Rybicki and Lightman (1986) and Longair (2011)). Here, we state and explain the meaning behind the expressions describing emitted bremsstrahlung radiation in different regimes. The expression for non-relativistic bremsstrahlung emission of an electron with charge $-e$ moving past an ion of charge Ze (in CGS units), ε_ν^{ff}, is

$$\varepsilon_\nu^{ff} = \frac{\mathrm{dW}}{\mathrm{dV\ dt\ d}\nu} = \frac{32\pi^2 e^6}{3\sqrt{3}c^3 m^2 v} n_\mathrm{e} n_\mathrm{i} Z^2 g_{ff}(v,\omega)\ \ [\mathrm{erg\ s^{-1}\ cm^{-3}\ Hz^{-1}}] \tag{2.4}$$

where $\frac{\mathrm{dW}}{\mathrm{dV\ dt\ d}\nu}$ is the emission spectrum of bremsstrahlung emissions (energy per unit volume, frequency range and time), n_e and n_i are the density of electrons and ions in the medium (or plasma), m is the mass of the electron, c is the speed of light, v is the velocity of the electron and $g_{ff}(\nu,\omega)$ is the *Gaunt factor* (a correction term used when deriving the emission using a quantum mechanical treatment) given by (Rybicki and Lightman, 1986)

[3] https://www.chandra.si.edu/edu/formal/snr/bg5.html

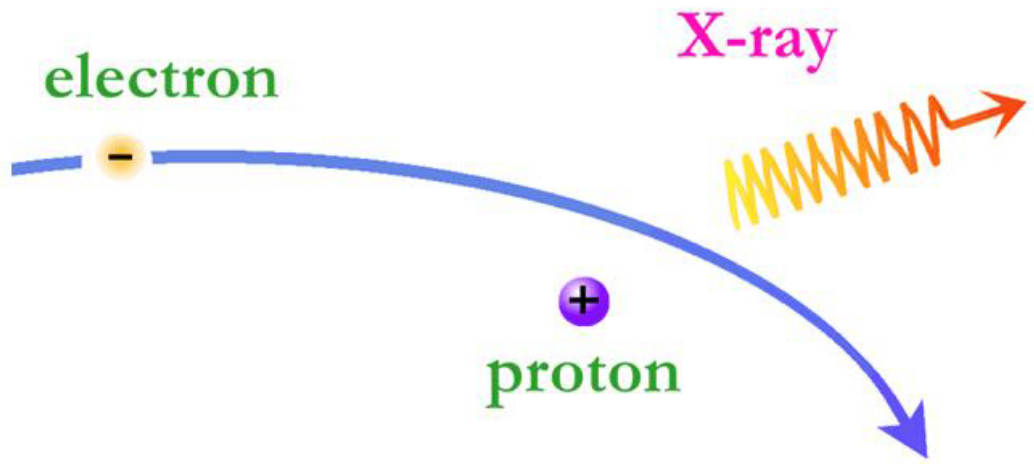

FIGURE 2.8: Cartoon showing production of X-ray photons via bremsstrahlung or free-free radiation. Image taken from https://www.chandra.si.edu/edu/formal/snr/bg5.html.
Credit: CXC team/NASA

$$g_{ff}(v,\omega) = \frac{\sqrt{3}}{\pi} \ln\left(\frac{b_{max}}{b_{min}}\right) \tag{2.5}$$

where b_{max} and b_{min} are the extrema of dimensionless collision parameters related to the electron interacting with the ion in close proximity over a time interval, τ. The Gaunt factor is a specific function calculated from the energy of the electron and the frequency (and therefore angular frequency) of the bremsstrahlung emission. Again, the full quantum mechanical derivation is beyond the scope of this research but it is important to note the different types of bremsstrahlung emissions found relating to the distribution of the particles. *Thermal bremsstrahlung* is observed when we average Equation 2.4, a single-speed expression, over a Maxwell-Boltzmann distribution (thermal distribution). The probability, dP, of the particle speed lying within a Maxwell-Boltzmann velocity distribution in the speed range dv is given by

$$dP \propto v^2 \exp\left(-\frac{mv^2}{2kT}\right) dv \tag{2.6}$$

where k is the Boltzmann constant, T is the temperature found from the thermal distribution of speeds and we have assumed an isotropic distribution of thermal velocities.

Similarly for *non-thermal bremsstrahlung*, where the single speed expression (Equation 2.4) is averaged over the actual distributions of velocities (e.g. not assumed to be a thermal distribution), expressions can be found using the appropriate Gaunt (correction) factors (e.g., Rybicki and Lightman, 1986). Further corrections need to be applied for the relativistic case. The different types of bremsstrahlung can be isolated from an X-ray spectra as non-thermal emissions occur at higher energies as a power law, following from the bremsstrahlung curve. This will be examined further for the case of Jupiter's hard X-ray aurora in Section 2.4.

2.3.3 Charge Stripping and Charge Exchange

The jovian soft X-ray auroral emissions are produced from an excitation reaction following from the ions being first charge stripped to a highly ionised state and the products undergoing charge exchange (e.g., Cravens et al., 1995; Bhardwaj and Gladstone, 2000). Charge stripping occurs when an ion interacts with a neutral or collision partner causing a free electron to be stripped from the ion, leading to the product ion having a more positive charge than the initial ion. For the case of jovian aurora, the ion collides with neutrals in the jovian atmosphere (e.g., Cravens et al., 1995). This process can be represented by

$$Y^{(q-1)+} + X \rightarrow Y^{q+} + X + e_s \tag{2.7}$$

where Y represents the ion (for Jupiter, iogenic ions oxygen (O) and sulphur (S)), X is the neutral in the atmosphere (in this case hydrogen (H) or molecular hydrogen (dihydrogen: H_2)), q is an integer number stating the charge state of the ion or the number of electrons short of the ion being neutral and e_s is the secondary electron produced from this process.

The products of the charge stripping process (Equation 2.7) can then undergo a charge exchange (or charge transfer) reaction. Charge exchange occurs when a colliding ion captures one or more electrons from a neutral atom in the atmosphere, summarised by the following reaction

$$Y^{q+} + X \rightarrow Y^{(q-1)+^*} + X^+ \tag{2.8}$$

where Y^{q+^*} denotes ions in an electronically excited state and other symbols have their previously defined meanings. The once neutral atom becomes ionised as a result of the process. After charge exchange, the ion in an excited electronically state can relax and release a photon ($h\nu$, where $h = 6.626 \times 10^{-34}$ m^2 kg s^{-1} is Planck's constant and ν is the frequency of the emissions) with energy corresponding to change of energy level

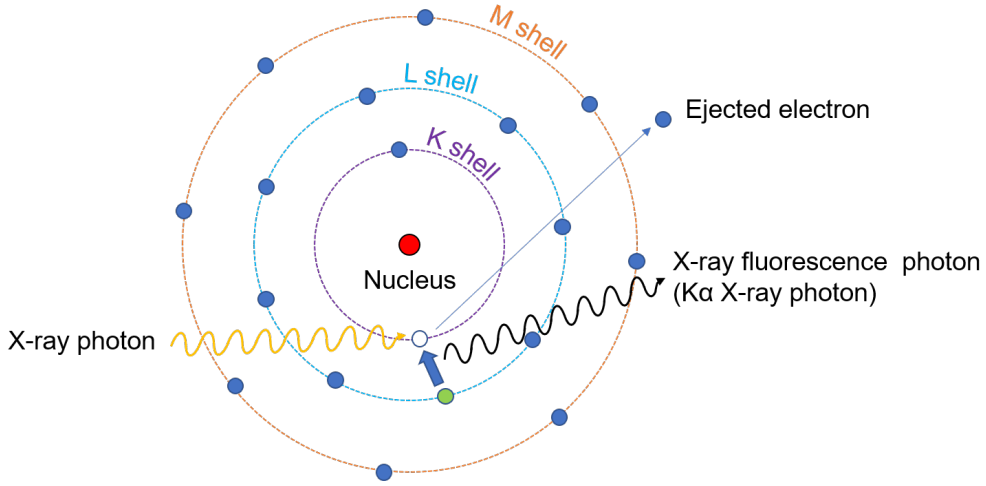

FIGURE 2.9: Schematic of the fluorescence process for the case of ionisation and ejection of an electron, relaxing an L-shell electron to the vacant K-shell orbital. All orbitals are labelled with nuceleus at the centre

$$Y^{(q-1)+*} \rightarrow Y^{(q-1)+} + h\nu \tag{2.9}$$

Therefore different values of q will produce a spectrum of photon energies from the cascade of photons produced in this process. The sequence of reactions above are responsible for the jovian soft X-ray aurora and will be examined further in later sections.

2.3.4 Fluorescence

When observing X-ray emissions from the planetary disk, fluorescence of solar X-rays in the atmosphere play an important role. This has been observed at Jupiter in the form of certain line emissions in the X-ray spectra. The fluorescence process takes place when an X-ray photon (e.g. from solar X-rays) is absorbed by the ion, resulting in either: (1) the excitation of an electron to a higher orbital where it then relaxes and emits an X-ray photon or 2) the ionisation and ejection of an electron located in the inner orbital (i.e. K-shell) creating a vacancy for an electron in an outer orbital (e.g. L-shell) to relax and occupying the inner orbital, ejecting a photon in the process. The latter case is shown in Figure 2.9 where the energy of the emitted photon is the energy difference between the higher orbital and the inner orbital that the electron occupies after relaxing (e.g. from L-shell ($n = 2$) to K-shell ($n = 1$), a Kα X-ray photon is released where n is the principal quantum number). This case results in characteristic X-ray line emissions observed in the spectra. For the case of Jupiter, emission from carbon fluorescence in methane is observed in the planetary disk (Maurellis et al., 2000).

2.3.5 Elastic scattering

The K-shell fluorescence emissions from oxygen and carbon dominate the X-ray emissions in the atmospheres of the terrestrial planets such as Venus, due to their dioxide atmospheres containing more of these species than the gas giant atmospheres (e.g., Cravens and Maurellis, 2001). For the atmospheres of the gas giant planets, elastic scattering with the neutrals and hydrogen dominate the observed disk emissions (e.g., Maurellis et al., 2000; Cravens et al., 2006). For non-relativistic charged particles (i.e. low energy regime), elastic scattering of electromagnetic radiation is the dominant scattering process, known as *Thomson scattering*. This only occurs when the incident photon energy is less than the energy of the charged particle (e.g. $h\nu \ll mc^2$). As the photon collides with the charged particle, the particle accelerates in the direction of the oscillating electric field from the photon re-emitting electromagnetic radiation of the same wavelength as the incoming photon in the process. The direction of the re-emitted photon is perpendicular to the particle motion.

For the high energy regime, *Compton scattering* dominates: inelastic scattering between incoming photons and charged particles where the X-ray photon loses energy at the expense of the charged particle gaining kinetic energy. When the charged particle loses energy at the expense of the incoming photon, *Inverse Compton scattering* applies. This scattering regime may be more applicable to the jovian radiation belts where the charged particles are highly relativistic (as discussed in Section 2.1).

The X-ray mechanisms discussed in this section are summarised in Table 2.2. The name of the mechanism (in the order discussed in the text), the associated charged particles and a summary of the process are all shown in the table.

The remainder of this section and research will mainly focus on X-ray production from bremsstrahlung and the series of reactions/excitations from charge exchange and charge stripping, the mechanisms relevant to jovian aurora. The kronian disk emissions (from fluorescence and scattering processes) and how this applies to this research will be briefly discussed in Chapter 7.

TABLE 2.2: Table summarising X-ray mechanisms likely to occur at the gas giants.

Mechanism	Associated charged particle(s)	Summary
Thermal Bremsstrahlung	electrons and/or ions	Emitted radiation due to the acceleration/deceleration of a charged particle in the vicinity of an electrostatic field produced from another charged particle. The single-speed expression (Equation 2.4) of the incoming particle is averaged over a Maxwell-Boltzmann distribution, assuming an isotropic distribution of thermal velocities.
Non-thermal Bremsstrahlung	electrons and/or ions	Similar mechanism as above except the single-speed expression is averaged over the actual distribution of velocities, using the appropriate correction factors.
Charge stripping	ions and neutrals	Ion interacting with neutral (or collision partner) causing a free electron to be stripped from the ion. The resulting ion has a more positive charge than the parent.
Charge exchange	ions and neutrals	Colliding ion captures one or more electrons from a neutral atom. The resulting ion becomes electronically excited. Relaxation of this ion leads to a release of a photon with energy $h\nu$.
Fluorescence	ions	Incoming X-ray photon is absorbed by ion. This results in either: 1) excitation of an electron to a higher orbital where it relaxes and releases a photon or 2) the ionisation and ejection of an electron in an inner orbital, creating a vacancy for an electron in an outer orbital to relax into, ejecting a photon in the process.
Thomson scattering	electrons and ions	Elastic scattering of EM radiation. Photon collides with charged particle causing it accelerate in the direction of the oscillating electric field, re-emitting EM radiation of the same wavelength perpendicular to particle motion. This occurs when photon energy is less than the energy of the charged particle (e.g., $h\nu \ll mc^2$).
Compton scattering	electrons and ions	Inelastic scattering at higher particle energies. X-ray photon collides with charged particle and loses energy, causing the kinetic energy of the charged particle to increase.
Inverse Compton scattering	electrons and ions	Same process as above except the charged particle loses energy at the expense of the incoming photon.

2.4 Jovian Auroral X-ray emissions

As briefly discussed in Section 2.2, the first observation of jovian X-ray aurora, and indeed X-ray emissions detected from another planet other than Earth, were found by the imaging proportional counter and high resolution camera on board the *Einstein X-ray observatory* in 1979. Metzger et al. (1983) analyse three observations taken during 1979 (April 13, November 24 and December 2) and show the first X-ray image of Jupiter's X-ray aurora during the 6 January 1981 observation. They report finding X-rays in the 0.2 - 3.0 keV energy band, emitting from both poles of Jupiter as mapped in Figure 2.10b) with the locations of Jupiter and the Galilean moons shown in panel (a) for the January 1981 observation which lasted $\sim$ 6 hours. Showing the location of Jupiter in this way allows the brighter emissions observed on the superimposed disk (panel (b)) to be distinguished from any other bright sources on the detector. With the spatial resolution of the camera, it was confirmed that the bright "lobes" of emissions corresponded to the jovian poles.

The three observations taken during the 1979 campaign utilised the imaging proportional counter on board the telescope. Figure 2.11 shows the resulting background-subtracted count rate spectra for each observation and found that the corresponding energy spectrum was extremely soft (i.e. detected in the 0.2 - 3.0 keV band) and can be characterised by a power law with an exponent of $\sim$ 2.3 (e.g. a possible indicator of non-thermal bremsstrahlung). The luminosity of the X-rays were found to be $\sim 4 \times 10^9$ W (or 4 GW) for the northern and southern emissions combined, in the 0.2 - 3.0 keV energy band. Metzger et al. (1983) postulated that the shape of the response and observed X-ray power suggested that the auroral emissions were less likely associated with electron bremsstrahlung but from line emissions from iogenic ions (O and S) between 0.03 and 4.0 MeV/nucleon located on the outer limits of the Io plasma torus (magnetic fields $\sim 8\ R_J$ from the planet). Metzger et al. (1983) found evidence of O Kα and S Kα (e.g. potential line emissions from fluorescence) at 0.52 keV and 2.3 keV respectively from fitting the spectra with the identified power law. They state the soft line spectrum could not be distinguished from the continuum due to the insufficient energy resolution of the instrument, therefore softer X-rays may still be emitted from the aurora.

Metzger et al. (1983) rule out solar wind and solar X-ray flux (i.e. sources providing external energy to the jovian system) as both sources are insufficient to provide the energy needed to produce the X-rays. Previous studies found that the solar wind provides a very minor contribution to jovian aurora (e.g., Eviatar and Siscoe, 1980) and the recorded quiet time solar flux during the *Einstein* observations was out by a factor of 10^4 when comparing to the X-ray flux values. Metzger et al. (1983) therefore argued that ion precipitation (internal sources) was the likely source of X-ray production, stating that the electron precipitation would supply insufficient energy to

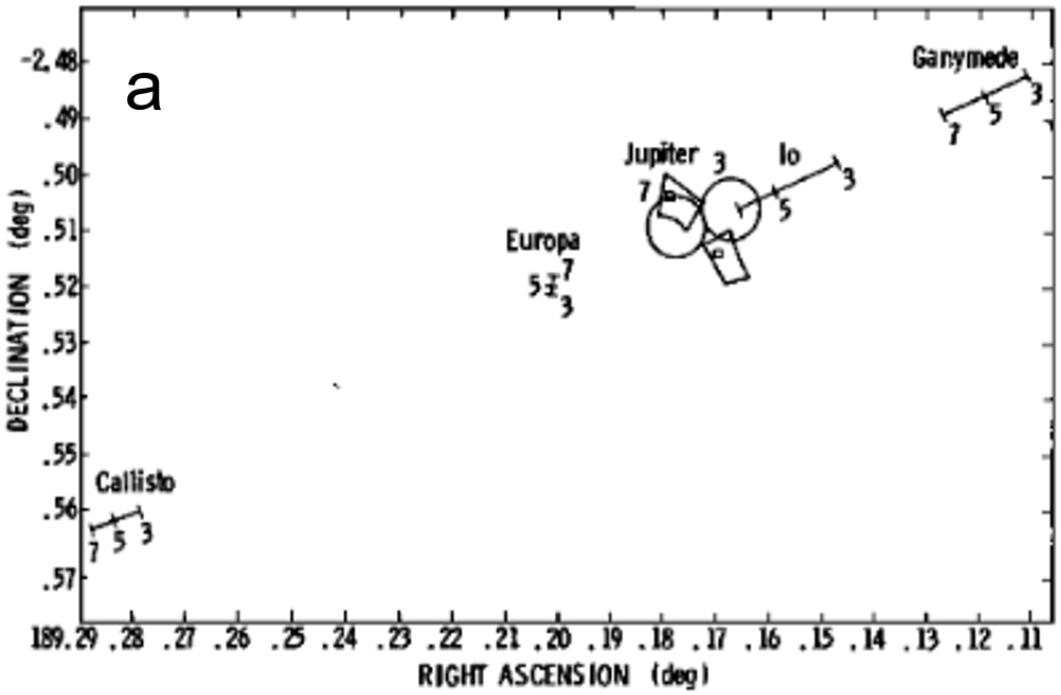

FIGURE 2.10: One of the first observations of jovian X-ray auroral emissions found by the high resolution imager on board the *Einstein Observatory* (Metzger et al., 1983), taken January 6 1981. The location of Jupiter and the Galilean moons are shown during this interval (given in right ascension and declination) in panel (a). The numbers correspond to the location of each object during the time interval which spanned from 2.1h - 7.8h UT. The quadrilaterals mark the outline of the two sources associated with Jupiter as shown in (b), with the maxima shown by small squares. Panel (b) shows the emission regions in terms of X-ray intensity, superimposed on the location of Jupiter's disk (orange circle) and the location of the jovian equator (straight line). The motion of Jupiter is from right to left. Image taken from Plate 2 Metzger et al. (1983).

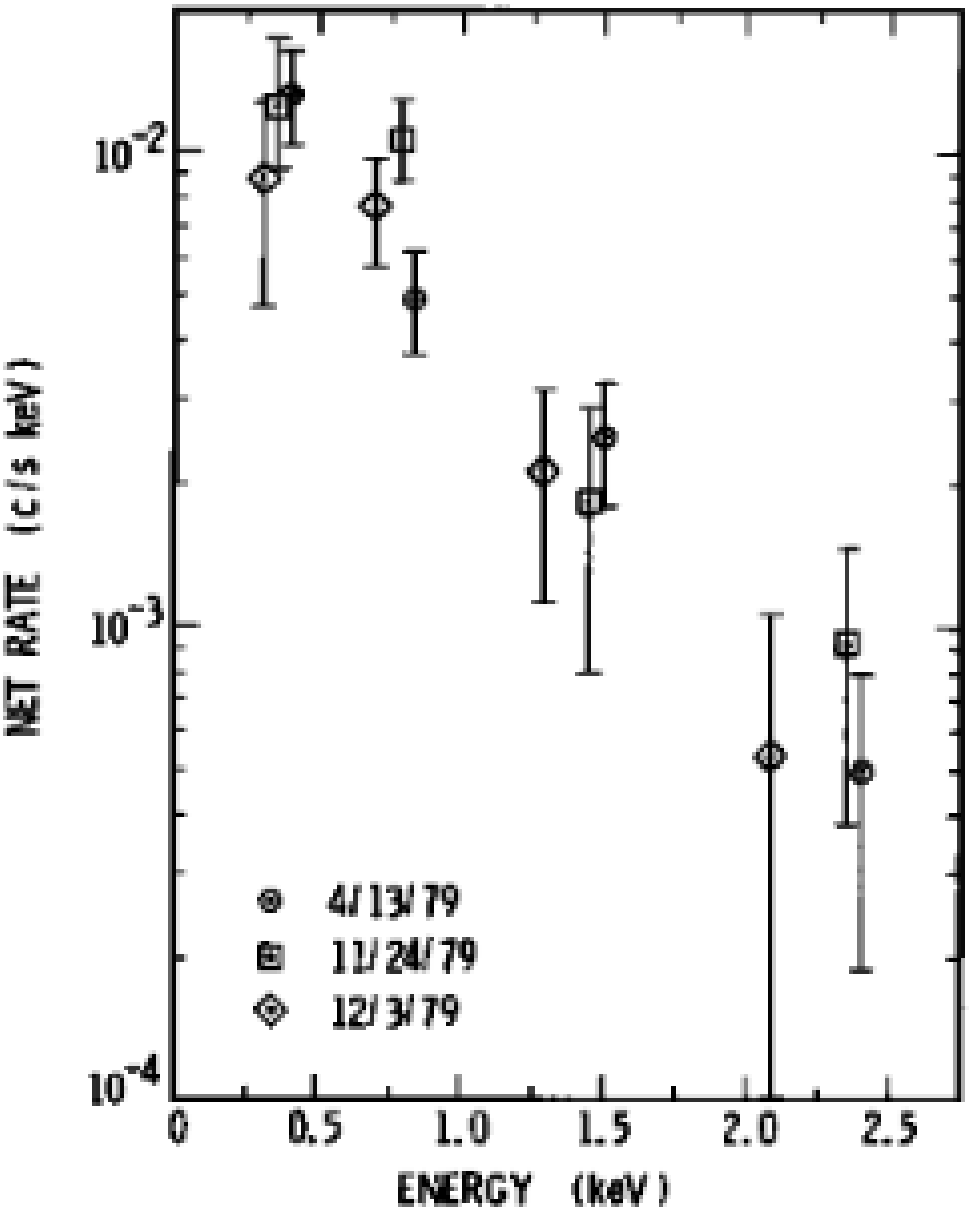

FIGURE 2.11: The spectra taken from the three 1979 observations (denoted with different markers) using the imaging proportional counter. The spectra represent the background-subtracted X-ray ray count rate (energy (keV) vs. net count rate (counts s^{-1} keV^{-1})) for each observation. Note the log-scale on the y-axis. Figure taken from Figure 2 in Metzger et al. (1983).

generate the aurora. This sparked many studies to search for a plausible mechanism for X-rays involving ion precipitation.

As discussed in Section 2.3, ionisation and excitation processes producing the auroral energy needed may be one possibility for the observed X-ray aurora involving ions. Horanyi et al. (1988) presented a theoretical model explaining the interaction of oxygen precipitating into the upper atmosphere with neutrals in the jovian atmosphere (some processes summarised in Equations 2.7 and 2.8, where Y is replaced with O) based on auroral particle precipitation found from Voyagers 1 and 2 (e.g., Sandel et al., 1979; Broadfoot et al., 1981). Their models suggests that sulphur and oxygen lines occur at 1256 Å and 1304 Å respectively (where 1 Å $= 10^{-10}$ m) if S- and O- precipitation was the source of the main auroral emissions (e.g. UV emissions). Therefore they suggest energetic ion and electron precipitation will have similar effects for the jovian atmosphere (with H and H_2) and ionosphere. A followup study by Waite et al. (1988) analysing high signal-to-noise spectra at UV wavelengths from the *International Ultraviolet Explorer (IUE)* Observatory found no detection of the 1304 Å oxygen line and an non-significant detection of the sulphur line. They concluded that the UV auroral emissions were likely to be from electron precipitation, as there was little to no contribution from the ions, and the precipitation of more energetic ions (> 300 keV/nucleon) are responsible for the X-ray auroral emissions. This was therefore consistent with the hypothesis stated by Metzger et al. (1983) that ion precipitation was the source of the X-ray auroral emissions and not the UV.

The original Metzger et al. (1983) hypothesis was further supported from later observations from the Röntgen satellite (*ROSAT*) with a higher energy resolution than the *Einstein Observatory*. Waite et al. (1994) analysed observations from *ROSAT's* high-resolution imager (HRI) and position sensitive proportional counter (PSPC) taken in April 1991 and May 1992 of the jovian emissions. With the improved spatial resolution, the HRI found that the X-ray auroral emissions originated from the northern hemisphere at all jovian longitudes and were time-variable and also sensitive to the rotation of Jupiter. This is shown in Figure 2.12 for the May 22 1992 observation at different observer longitudes (stated in each panel), or *central meridian longitudes*, to show the behaviour changes with rotation. The PSPC data revealed a very soft X-ray spectrum that was difficult to extract from previous observations. When fitting the spectra (as shown in Figure 2.13) with models for electron bremsstrahlung and line emissions for iogenic ions, Waite et al. (1994) found a better statistical fit with the line emissions from S and O ions (e.g. the χ^2 value was closer to 0, as labelled on Figure 2.13). This again showed the line emissions dominated the jovian auroral spectrum and agreed with the results and arguments first suggested by Metzger et al. (1983).

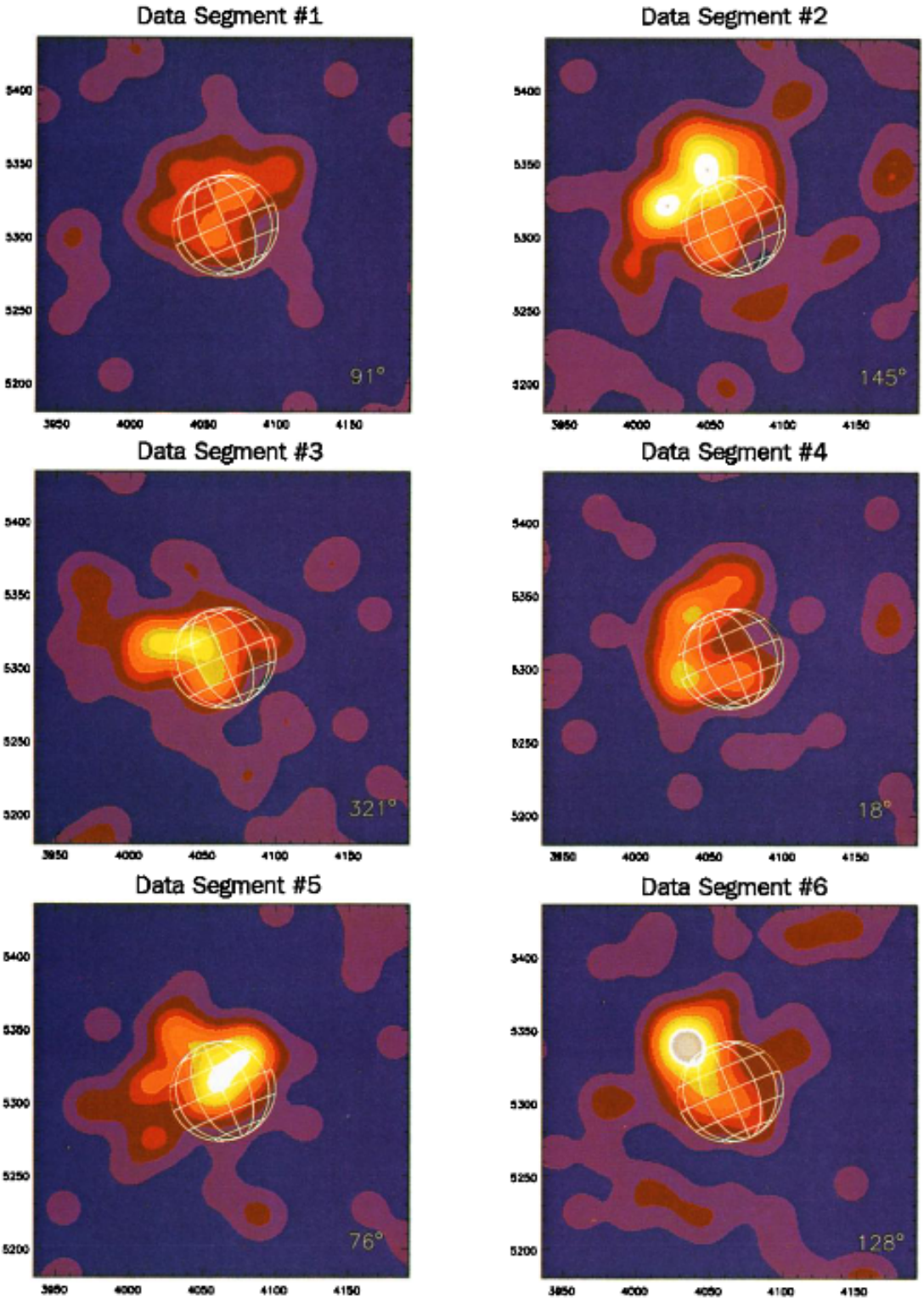

FIGURE 2.12: Individual X-ray images of 6 ROSAT HRI data intervals at various central meridian longitudes (CML), noted in the bottom right of each panel. The images show how the northern hemisphere X-ray emissions change in time and over a jovian rotation. The disk, equator, latitude and longitude are shown in each panel. The position of the planet is shown in right ascension coordinates. Image taken from Plate 2 in Waite et al. (1994).

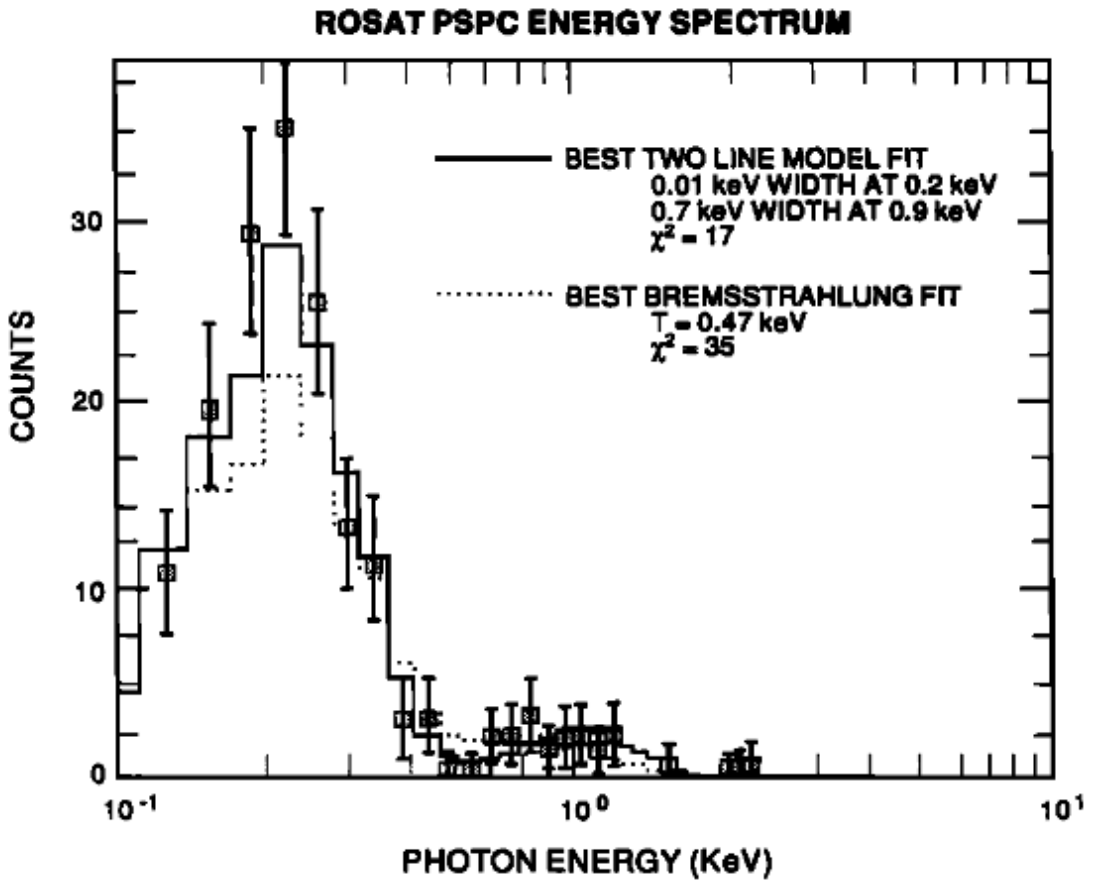

FIGURE 2.13: The photon energy spectrum from the combined ROSAT PSPC observations with 1-σ errors. The curves of the best fit for O and S emission lines (solid line) and bremsstrahlung model (dotted) convolved with the detector response are also shown with their associated statitsics also shown. Spectrum taken from Figure 5 in Waite et al. (1994).

The results from Waite et al. (1994) provided valuable information to extend the model for auroral production associated with ions first proposed by Horanyi et al. (1988). Cravens et al. (1995) extended the original model for oxygen by including all charge states from neutral oxygen up to fully stripped oxygen. The Horanyi et al. (1988) model only considered the four lowest charge states (O, O^+, O^{2+}, O^{3+}). This extension of the model provided the needed requirements to study jovian auroral X-ray emissions associated with highly energetic charged ions in more detail. Cravens et al. (1995) calculated that the total auroral X-ray power from highly charged oxygen ions was $\sim 10^8$ W ($\sim$ 0.1 GW), in agreement with the ROSAT observations analysed by Waite et al. (1994) and therefore provided further evidence that ion precipitation may be responsible for jovian auroral X-ray emissions. All the observations and models up to this point provided a likely series of mechanisms for the observed jovian auroral X-ray power regarding the precipitation of O ions interacting with neutrals. This can be summarised as the following

$$O^{(q-1)+} + H_2 \rightarrow O^{q+} + H_2 + e_s \tag{2.10}$$
$$O^{q+} + H_2 \rightarrow O^{(q-1)+^*} + {H_2}^+$$
$$O^{(q-1)+^*} \rightarrow O^{(q-1)+} + h\nu$$

where all the steps and symbols of the above reaction are previously defined in Equations 2.7 - 2.9 for the general case and $0 \leq q \leq 8$ (e.g., $q = 8$ corresponds to O^{8+} or O IXas shown by Horanyi et al. (1988); Cravens et al. (1995) and references therein). The above set of reactions also apply to precipitating S ions for different values of q (e.g. Bhardwaj and Gladstone, 2000). During the *Cassini* flyby of Jupiter of the outer dusk magnetosphere (December 2000 - Januaray 2001), heavy iogenic ions with ion charge states ($q \leq 3$) were observed confirming the existence of charge stripped ions in the jovian environment (Allen et al., 2019). However, how the ions get fully stripped to account for the X-ray auroral emissions and the driver behind energising the ions to the required high energies is still up for debate in the field today.

2.4.1 First detection of the pulsating "hot spot"

Following the *ROSAT* telescope, NASA launched the Chandra X-ray Observatory in July 1999 (see Section 3.1) with unrivalled spatial resolution from its high resolution camera (HRC) and imaging spectrometer (ACIS). On December 18 2000, Chandra performed its first observation of Jupiter for $\sim$ 10 hours (10 - 20 UT) (Gladstone et al., 2002). Figure 2.14 shows the resulting intensity map (in Rayleighs), in planetocentric coordinates, with each X-ray photon convolved with the point spread function of the instrument. The jovian disk and S3 longitude-latitude grid with the Io (orange lines) and 30 R_J (green lines) magnetic footprints from the VIP4 model are also plotted. Due to the higher spatial resolution of HRC, the auroral emissions were found to be mapped to a higher latitude than expected from previous observations suggesting a possible connection to the outer magnetosphere.

As discussed in greater detail in Chapter 3, Gladstone et al. (2002) were the first to map Chandra photons to the jovian poles and disk in a polar projection to allow the full auroral morphology to be examined in detail. Figure 2.15a) shows the polar projection of the individual Chandra photons (crosses, where the size gives an idea of uncertainty in position) overlaid on multiple auroral images of UV *HST* averaged intensity (as shown by the colour bar). The mapping assumes that the peak auroral emissions (both UV and X-ray) occur at 240 km above the 1-bar pressure level in the jovian atmosphere. The VIP4 model is shown by the dark blue contours with the same magnetic footprints in Figure 2.14 also plotted. With high spatial resolution images of *HST*, the X-ray aurora appeared to be more poleward than the UV main auroral

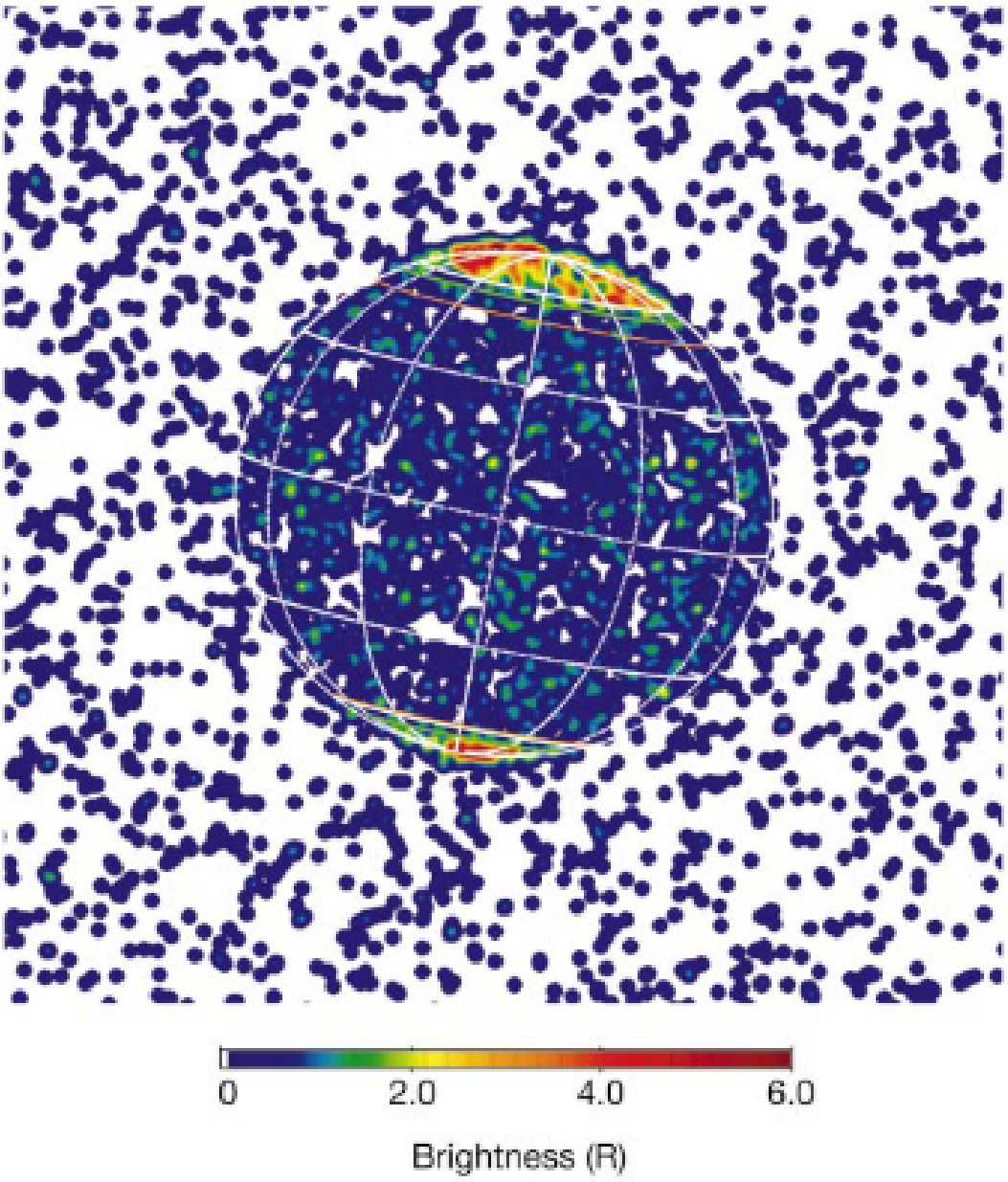

FIGURE 2.14: Chandra image in planetocentric coordinates of the 10 hour X-ray observation on 18 December 2000. Each individual photon has been convolved with the point spread function of the high resolution camera (more details in Chapter 3). The colour bar shows the intensity of the X-ray emissions in units of Rayleighs. The Io and 30 R_J magnetic footprints of the VIP4 model are shown by orange and green lines respectively (for both hemispheres). Image taken from Figure 1 in Gladstone et al. (2002).

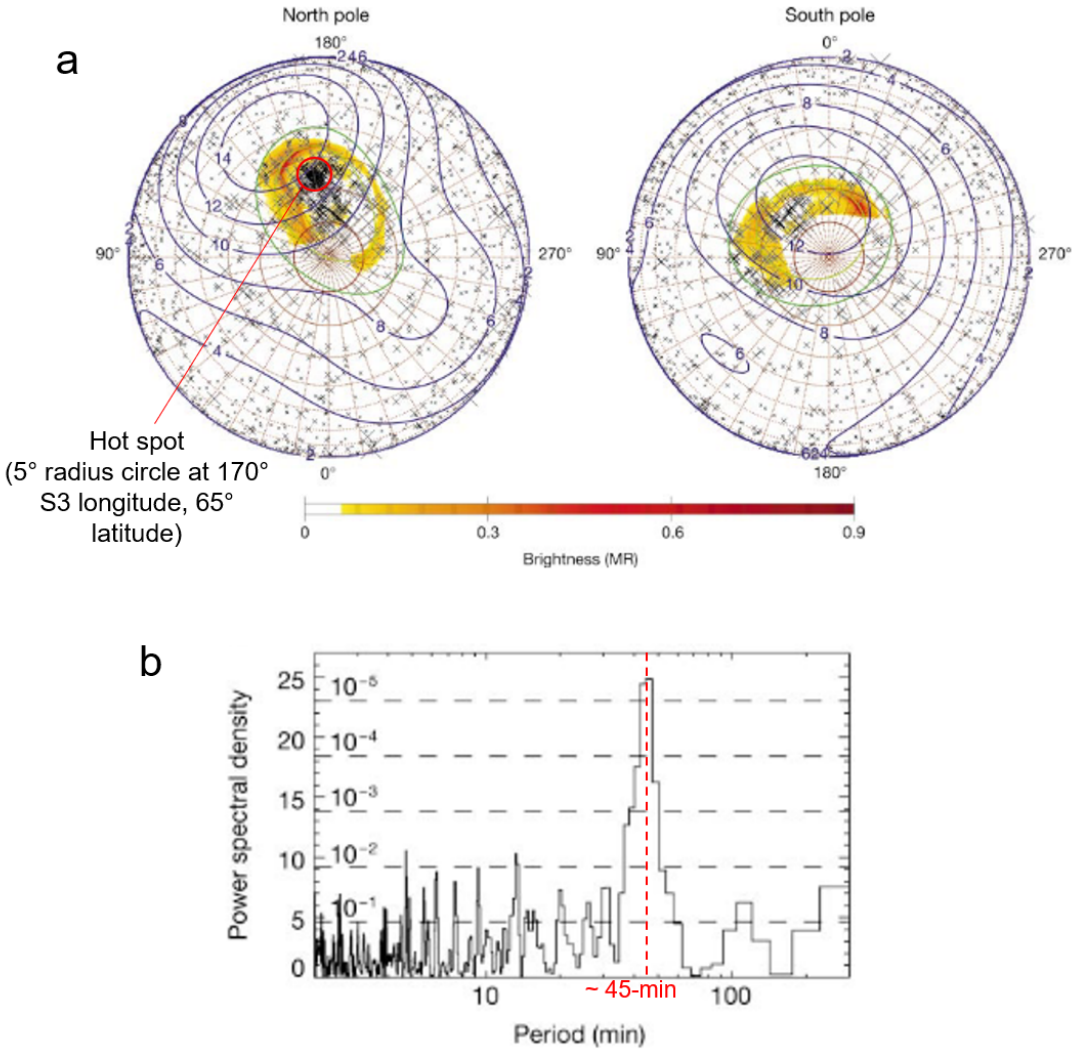

FIGURE 2.15: Figure summarising analysis of the "hot spot" from Gladstone et al. (2002). (a) Polar projections of Chandra X-ray photons (crosses with size proportional to uncertainty in position) overlaid onto averaged *HST* images (colour bar). Surface magnetic field strength from the VIP4 (dark blue contours) and the magnetic footprints shown in Figure 2.14 are also plotted. The X-ray auroral emissions are found to be poleward of the UV emissions with the hot spot identified by a red circle. The timing analysis results of the hot spot is shown in panel (b) with the peak $\sim$ 45-min period identified. The dashed lines labelling the probability of a random signal occurring at that frequency bin (i.e. the $\sim$ 45-min period had a 4×10^{-6} likelihood of occurring at random). Image adapted from Figures 2 and 3b in Gladstone et al. (2002).

emissions in both hemispheres (left: North, right: South). As shown clearly in the North, a collection of photons occur within the labelled 5° circle at $\sim$ 170° S3 longitude and 65° latitude. This region was found to be the first observation of the so-called *X-ray auroral hot spot*. The "hot spot" was found to be fixed in magnetic longitude and latitude (i.e. rotated with the planets magnetic field) and could only be viewed when the emissions rotated into view.

More puzzling than the high-latitude aurora, timing analysis of the light curve of the

photons within the identified hot spot region revealed the emissions to be pulsating. Figure 2.15b) shows the resulting power spectrum from the Gladstone et al. (2002) hot spot signal with the dashed lines labelling the probability of a random signal occurring at that frequency bin. In this observation, a peak period of $\sim$ 45-min is found from the timing analysis with the peak having a 4×10^{-6} likelihood random chance occurrence. This periodic signal was not found in contemporaneous *Galileo* and *Cassini* particle data or *Cassini* upstream solar wind data at $\sim$ 200 R_J. A $\sim$ 40-min periodicity was found from radio data during the *Ulysses* flyby (MacDowall et al., 1993) with the origins remaining unclear.

Gladstone et al. (2002) argued that these results put the original Metzger et al. (1983) hypothesis into questions as the pulsations suggest the precipitation of heavy ions is not steady. Alternatively, they propose the unknown driver of these emissions resides in the outer magnetosphere, producing highly localised and variable emissions. They suggest the pulsations may arise from global ultra-low frequency (ULF) oscillations of the magnetic field line the ions precipitate down into the jovian ionosphere, previously observed to have a 10 - 20-min period in the middle magnetosphere (e.g., Khurana and Kivelson, 1989; Wilson and Dougherty, 2000a), with the periodicities in the X-ray auroral emissions possibly associated with the bounce periods of the magnetically trapped charged particles. This revolutionary study changed how we viewed the pulsating jovian X-ray auroral emissions and opened many avenues of study in this interesting field. The key discoveries of jovian X-ray auroral emissions since this revolutionary discovery will be examined in the remainder of this chapter.

2.4.2 Discovery of jovian disk emissions and auroral hard X-rays

The launch of Chandra revolutionised how we could resolve the observable universe in X-rays in fine detail. Soon after the *Chandra* launch, in December 1999 the European Space Agency (ESA) launched their X-ray imaging spectrometer *XMM-Newton* (Jansen et al., 2001) which had unrivalled spectral resolution. *XMM-Newton* therefore had the capabilities to fully resolve the jovian auroral spectra for the first time with its greater energy resolution that the previous generation of X-ray telescopes (Einstein, ROSAT etc.). The first *XMM-Newton* observation of Jupiter occurred for 110 ks ($\sim$ 3 jovian rotations, where 1 rotation $\approx$ 36 ks) between April 28 and April 29 2003 (Branduardi-Raymont et al., 2004). The spectral analysis conducted by Branduardi-Raymont et al. (2004) found that all X-ray emissions in the auroral hot spot were confined to 0.2 - 2.0 keV and found an X-ray spectrum from a southern hot spot for the first time. Both spectra were modelled with emission lines of highly ionised oxygen (O^{6+}, O^{7+}) and a model consisting of a superposition of many weaker lines (a pseudo-continuum). They found a 2.8σ enhancement in the spectrum at $\sim$ 0.57 keV associated with the identification of O^{6+} therefore supporting the arguments of

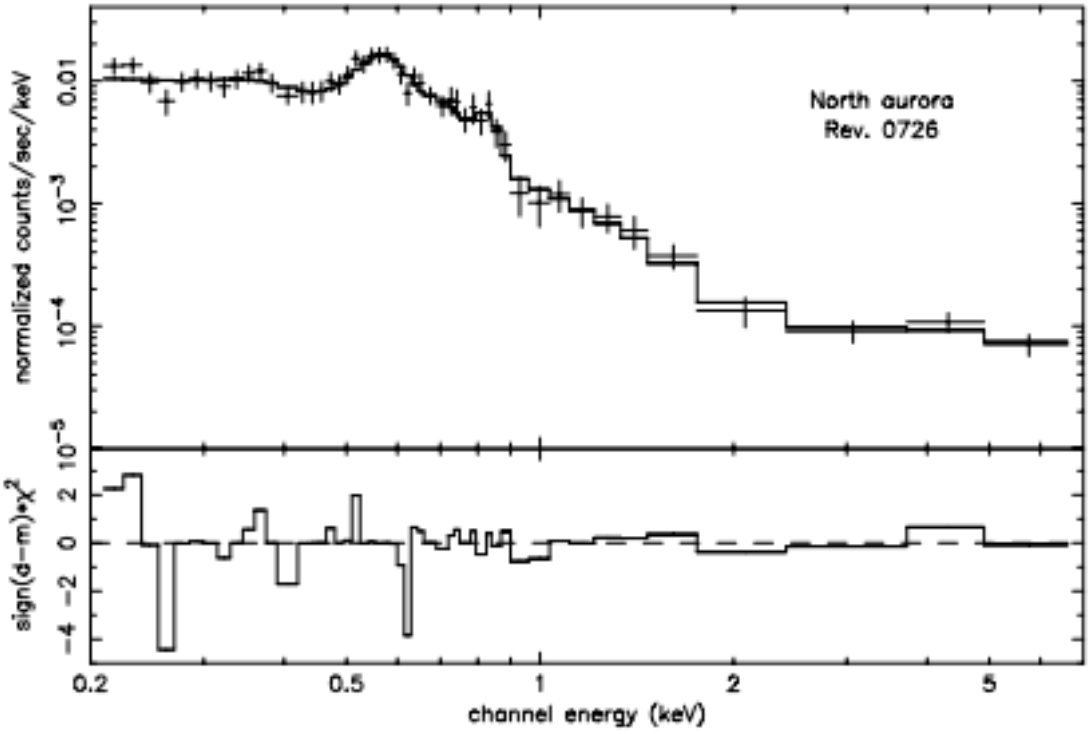

FIGURE 2.16: Example *XMM-Newton* photon spectrum of the northern X-ray aurora during November 2003. The spectrum has been fitted with a combination of a thermal bremsstrahlung model, power law continua and four emission lines. Taken from Figure 10 in Branduardi-Raymont et al. (2007b).

ions being captured and charge stripped in the jovian magnetosphere before undergoing charge exchange to produce X-rays (e.g., Horanyi et al., 1988; Cravens et al., 1995). Timing analysis of the hot spot regions found no statistically significant ∼ 45-min oscillation discovered by Gladstone et al. (2002).

With the finer spectral resolution, the X-ray spectrum of the planetary disk was retrieved and isolated from the auroral emissions. Elsner et al. (2005) found the spectrum to be consistent with a picture of scattered solar X-rays off the upper atmosphere with little evidence of the fluorescence lines as predicted by Maurellis et al. (2000). Although the main focus of this research is the jovian auroral emissions, it is important to separate these emissions, and therefore the processes responsible, to understand fully the magnetosphere-ionosphere coupling to energise the ions responsible for the X-ray aurora.

Followup *XMM-Newton* observations of the jovian emissions in November 2003 discovered the existence of an electron bremsstrahlung component in the auroral spectra Branduardi-Raymont et al. (2007b), previously predicted in the literature but never found due to the lack of sensitivity at the softer energies (e.g., Metzger et al., 1983; Waite et al., 1988, 1994). An example spectrum is shown in Figure 2.16, where the fitted model consists of a thermal bremsstrahlung component, power law continua

(e.g. non-thermal emissions) and line emissions. The bremsstrahlung component was found to vary in shape and intensity over the 3.5 days observed in November 2003 and was found to harden (i.e. the peak increased in energy, changing the power law index) with increasing flux. Branduardi-Raymont et al. (2007b) found that this new component accounted for all X-ray flux $>$ 2 keV and hypothesised that the variability may be linked to solar wind activity.

Using the high spatial resolution of Chandra and its ACIS instrument, Branduardi-Raymont et al. (2008) mapped the photons according to energy as a polar projection (similar to Gladstone et al. (2002)) to analyse the spectral morphology of the northern X-ray auroral emissions. The X-ray photons observed in February 2003 were overplotted on simultaneous far-UV *HST* data (as shown in Figure 2.17 for 4 *HST* orbits) to analyse their difference in location within the auroral regions. Branduardi-Raymont et al. (2008) argue that the same population of energetic electrons may be responsible for both the hard X-rays ($>$ 2 keV: big green dots in Figure 2.17) and far-UV emissions as both ionospheric photons are located close to each other during this observation window. The soft X-rays ($<$ 2 keV: small green dots) were located more poleward, found to cluster in the classic hot spot region and associated with the classic ion charge exchange idea. They state the difference between hard and soft X-rays in the auroral emissions due to the different spectral shapes.

Unfortunately due to the degradation of the Chandra ACIS instrument (see Chapter 3), mapping the hard X-rays in recent studies is an impossible task. Therefore recent studies looking into the hard X-ray component of the auroral emissions utilise a combination of *XMM-Newton*, *HST* and Hisaki (planetary spectrometer launched by JAXA, looking at the UV and extreme-UV (EUV) wavelengths) to analyse the variability and spectral properties of these emissions. A very recent study by Wibisono et al. (2021) found that the hard X-ray auroral emissions observed by *XMM-Newton* got more intense with the EUV auroral emissions observed by Hisaki during a dawn storm. An increase in brightness in both spectra suggest an increase in electron precipitation caused by the dawn storm (e.g., Bonfond et al., 2021). Interestingly, the dawn storm did not cause the soft X-ray aurora, associated with iogenic ions, to increase in brightness or trigger any periodic pulsations. This therefore shows how both components of the X-rays are dependant on different magnetospheric processes and require further analysis. Trying to determine a way to map the hard X-rays using Chandra is discussed further in Chapter 6.

2.4.3 First resolved image of the southern auroral "hot spot"

Following the discovery of the southern hot spot emissions by Branduardi-Raymont et al. (2004), the next step was to determine the location and morphology of these

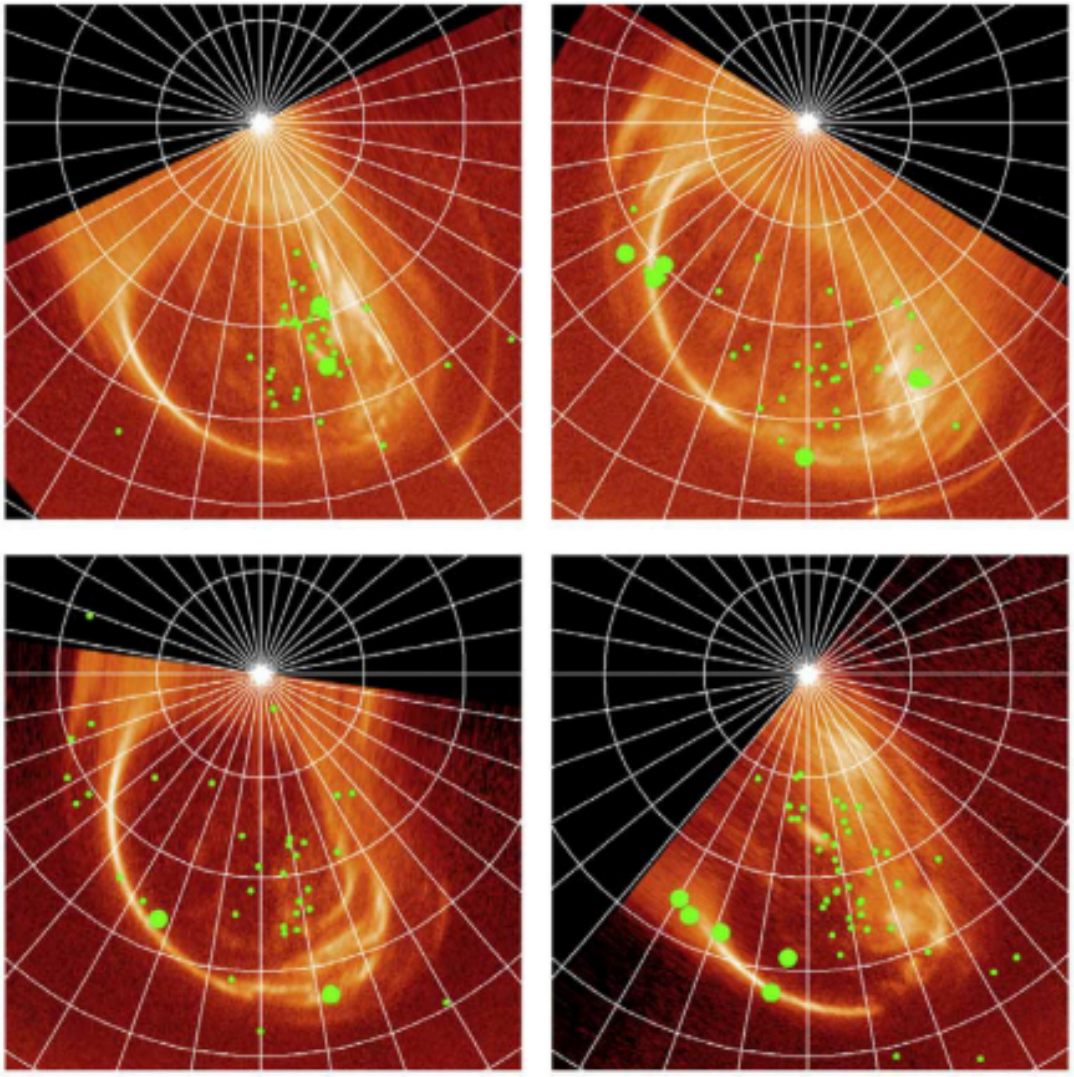

FIGURE 2.17: Polar projections showing the spectral morphology of the hard X-rays (big green circles) and soft X-rays (small green circles). The Chandra X-ray photons are overplotted on *HST* data (orange emissions) during 4 orbits. The full exposure is shown in Chapter 3. Projection grid split into 10° graticules. Image taken from Figure 5 in Branduardi-Raymont et al. (2008).

emissions. Dunn et al. (2017) analysed Chandra observations on May 24 and June 1 2016 and a simultaneous *XMM-Newton* observation on May 24 to compare timing analysis and analyse spectral properties of the emissions. The ACIS degradation meant that no Chandra spectral observations were taken during this time.

Figure 2.18a shows the combined projection of the May and June X-ray photons Chandra observations (per 2° bin) with the VIP4 surface model overplotted as gold contours. The thick gold contours represent the magnetic footprints of Io, Ganymede (15 R_J) and 50 R_J. The red dot indicates the location of the jovian magnetic pole. As shown in the polar projections, the southern emissions were found to be far more diffuse and less intense than their northern counterpart. To determine if this was a

result of different magnetospheric drivers, Dunn et al. (2017) used the Vogt et al. (2011, 2015) flux equivalence mapping model to find the location of potential X-ray drivers in the jovian magnetosphere. The flux equivalence mapping model relates a position in the ionosphere to a source region in the equator, at a given radial distance from the planet (in units of R_J) and local time. This model assumes that the flux through a given region in the joviographic equator, calculated using a 2-D fit to *Galileo* data, should match the flux through the ionosphere in the region to which it maps. The mapping depends on the sub-solar longitude (SSL) and the internal field model used (examined further in Chapter 5). In this instance, Dunn et al. (2017) use the VIP4 model and found that driver of the X-ray auroral emissions were found to lie in the noon-dawn sector for the southern hot and noon-dusk for the North (Figure 2.18b)), between the predicted compressed and expanded magnetopause limits of the Joy et al. (2002) model.

To unveil new light on the potential auroral drivers for the hot spot emissions in both hemispheres, Dunn et al. (2017) performed Fourier transforms on the light curves for both the North and South (Figure 2.19). The light curves alone showed that the peak of the emissions were out of phase (i.e. rotation dependant when observed) and had a different underlying envelope with the southern emissions being more "spread out". The resulting periodograms (or power spectra from the timing analysis) from the Chandra data (both observations; Figure 2.19b)) showed that southern emissions exhibited a significant regular period of 9-11-min ($> 10^{-6}$ likelihood of the pulsation occurring from random chance, using similar methods to Gladstone et al. (2002)). Interestingly, the northern auroral emissions were found to exhibit no significant pulsations during this time, indicating that the northern and southern hot spots behave independently during this observation. This was the first discovery of non-conjugate behaviour between the poles, raising questions whether the drivers of both emissions were different (coupled with the slightly different locations in the magnetosphere) or whether it was lagged emissions.

Dunn et al. (2017) proposed that the location of the ion populations (drivers) on the magnetopause suggest that Kelvin-Helmholtz Instability (KHI)-driven Alfvén waves may generate the observed periodicity of the emissions and provide a possible mechanism. This argument agrees with the ULF wave hypothesis originally made by Gladstone et al. (2002) although with no clear idea of what could produce such ULF wave activity. A very recent case study by Yao et al. (2021) argued that the potential driver for pulsed auroral emissions may be ion cyclotron waves modulated by planetary electromagnetic waves; they say that such a process would cause periodic heavy precipitation of ions, producing the observed pulses. Yao et al. (2021) analysed simultaneous *in situ Juno* data (particle, magnetic field and wave data) with *XMM-Newton* light curves and found the pulsations caused by ion cyclotron waves evident across all datasets.

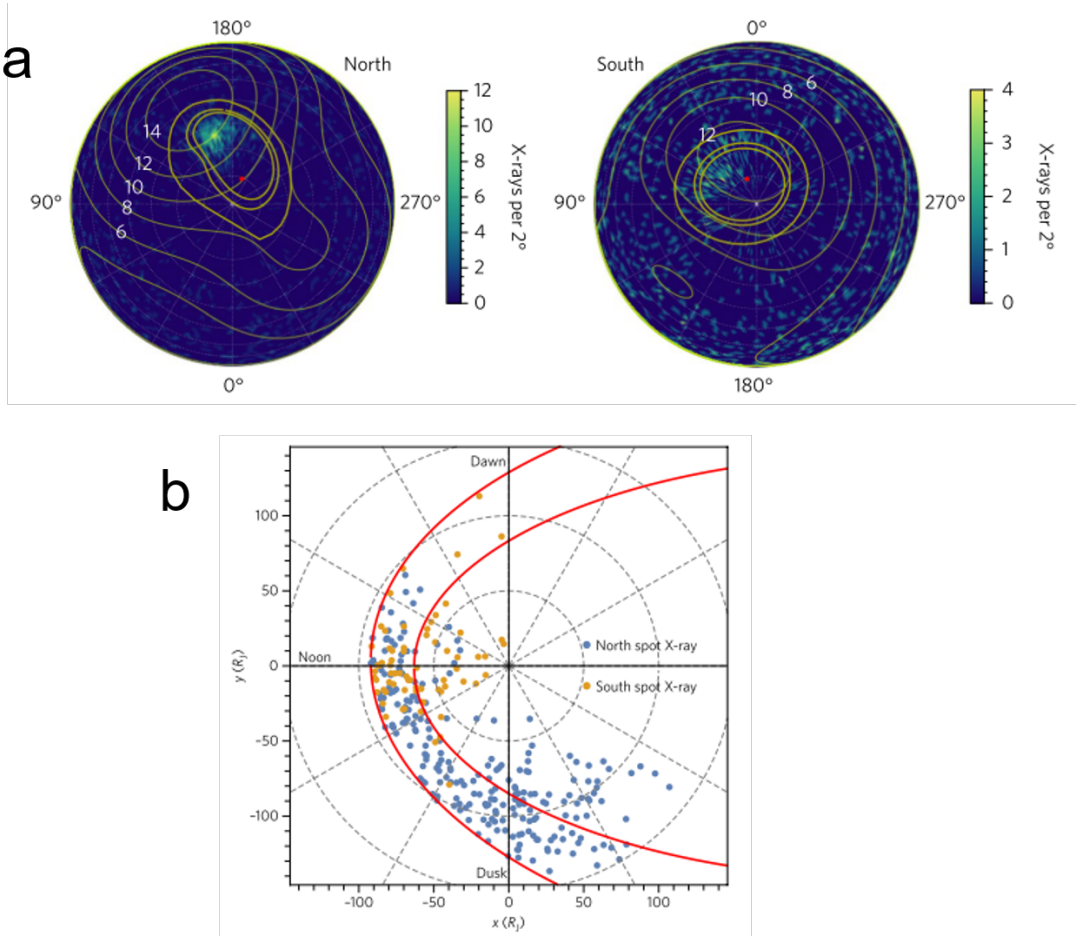

FIGURE 2.18: Results of the mapping analysis from Dunn et al. (2017). Panel (a) shows the combined projection of the May and June X-ray photons for the Chandra observations (per 2° bin) with the VIP4 surface model overplotted as gold contours. The thick gold contours represent the magnetic footprints of Io, Ganymede (15 R_J) and 50 R_J and the red dot indicates the location of the jovian magnetic pole. Panel (b) shows the results of the Vogt et al. (2011, 2015) flux equivalence model (see text for details) with the VIP4 internal field model. Northern and southern emissions are shown in blue and gold respectively. Images adapted from Figures 1 and 4 from Dunn et al. (2017).

Regarding the southern emissions, Dunn et al. (2017) state that the lack of southern emissions may be associated with the viewing geometry (i.e. planetary tilt), causing the southern emissions to be tilted out of view in previous campaigns. This can therefore lead to the southern X-ray photons having to travel through more of the jovian atmosphere which have a likelihood of being absorbed due to opacity effects (as modelled by Ozak et al. (2010)) not accounted for in the mapping and timing analysis. The effects of geometry are explored further in Chapters 5 and 6. The possible theories and evidence surrounding X-ray auroral drivers are discussed in greater detail in Chapters 4 - 7.

Another contributing factor to the less intense and more diffuse auroral X-rays in the South may be a preference for electron precipitation over ions due to stronger and more persistent electron currents, as found from recent *Juno* observations (Kotsiaros

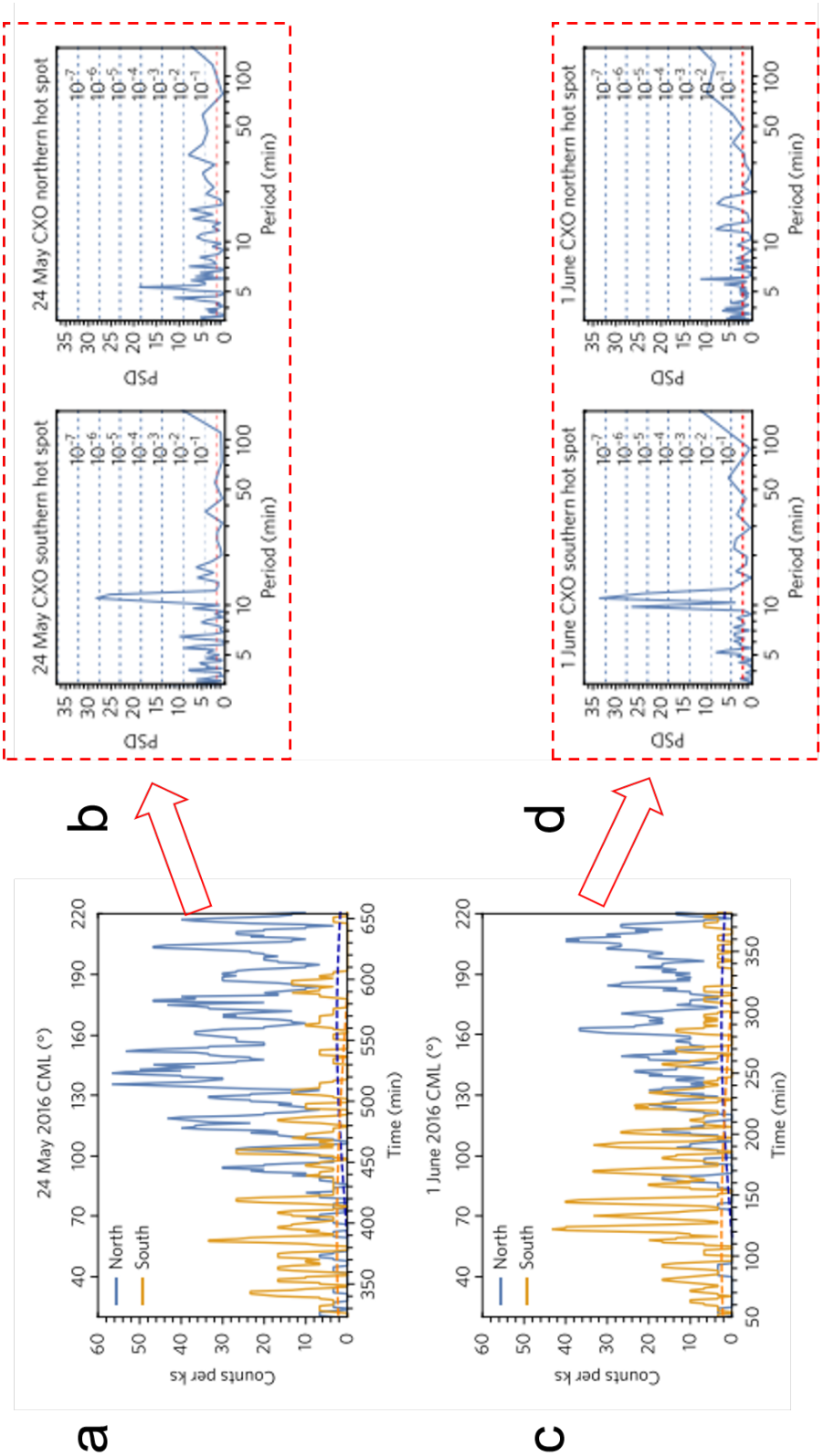

FIGURE 2.19: Panels (a) and (c) show the light curves for the northern (blue) and southern (gold) emissions for the two Chandra observations. The normalised visibility of the emissions are shown in the corresponding dashed line with the same colourings. Panels (b) and (d) show the resulting timing analysis of the light curves via Fourier transforms with the horizontal dashed lines representing the likelihood of random occurrence as used by Gladstone et al. (2002). Figure adapted from Figures 2 and 3 from Dunn et al. (2017).

et al., 2019). This observation may provide the reason why the southern auroral hard X-ray emissions in the 3-20 keV range are almost twice as intense than its northern counterpart, first discovered by the Nuclear Spectroscopic Telescope Array (*NuSTAR*) from 5 observations during 2015 - 2018 (Mori et al., 2022). NuSTAR is an imaging spectrometer, capable of resolving X-rays in the 3 - 79 keV X-ray energy band, surpassing the upper energy limits of both *Chandra* and *XMM-Newton* at 10 keV. Prior to this discovery, the strongest significant jovian auroral X-rays detected had energies of ~ 7 keV from *XMM-Newton* (Branduardi-Raymont et al., 2007b). The study conducted by Mori et al. (2022) found that HXRs in this energy range are produced from non-thermal bremsstrahlung from precipitating electrons with energies of keV to MeV. They also found that the jovian auroral X-ray spectrum is found to get softer beyond 20 keV (i.e. the slope found from the power law steepens). This provides a new insight into the non-conjugate behaviour and asymmetries observed between the poles. Mori et al. (2022) suggest that due to the more powerful and persistent electron currents in the southern auroral emissions, the southern auroral region would be likely dominated by precipitating electrons where as the northern X-ray emissions are found to have a preference for ion-related processes such as charge exchange and line emissions. This opens up many new avenues to explore the southern emissions, across all wavebands, in more detail with *Juno's* extended mission taking it into the southern portion of the magnetosphere providing wider coverage of the South pole and the southern regions of the jovian magnetosphere.

2.4.4 Jovian auroral X-rays during a solar wind compression

Throughout the ongoing X-ray campaigns to provide a wealth of data to analyse the jovian X-ray auroral emissions, there are many observations which are either planned or coincidentally occur at the same time as a solar wind compression impacting Jupiter. As discussed in Chapter 1, solar wind compressions can occur in the form of irregular transients like coronal mass ejections or corotating interacting regions which have a relatively predictable occurrence rate (solar-cycle dependent). The arrival time of thee transient phenomena however is very difficult to predict and is ongoing in the space weather field. When these solar transients arrive at the jovian magnetosphere, the impact generates a shock causes the magnetosphere to compress. Dunn et al. (2016) report the first jovian observation, taken in October 2011, planned to coincide with the predicted arrival of an interplanetary coronal mass ejection (ICME) impacting the jovian magnetosphere. At the predicted arrival time calculated from the mSWiM propagation model (Zieger and Hansen, 2008), a 1-D numerical MHD model to propagate the solar wind from 1 - 10 AU in a non-rotating frame, the X-ray aurora was found to become more intense by a factor of ~ 8. Within 1.5 hours of the change of auroral intensity, STEREO-A and -B observed bursts of non-Io decametric radio

emissions possibly associated with a compression event. During the compression event, the timing analysis results from Dunn et al. (2016) found two significant periods associated with different ion populations: $\sim$ 26-min from sulphur ions and $\sim$ 12-min from a mix of carbon/sulphur and oxygen ions (e.g. a mix of heavy ions from Io and the solar wind). Using the Vogt et al. (2011, 2015) flux equivalence model, they found that the highly charge stripped sulphur ions are likely to originate between 50 and 70 R_J. Highly stripped oxygen ions and sulphur/carbon ions were found to originate between 70 and 120 R_J (e.g. in the outer magnetosphere, close to the magnetopause boundary). Dunn et al. (2016) argued that, to account for possible solar wind precipitation, the driver in this case responsible for the X-ray enhancements was likely to be cusp reconnection on the dayside magnetopause proposed by Bunce et al. (2004). This type of magnetic reconnection may be triggered from a solar wind compression, for example from an ICME, and may provide a possible mechanism for the observed pulsations in the different ion populations.

A more recent study by Wibisono et al. (2020), analysing *XMM-Newton* data from June 2017 found that, during a solar wind compression, confirmed by magnetopause crossings observed in the *in situ Juno* data, a 23 - 27-min pulsation was observed which lasted for 12.5-hours of the $\sim$ 23 hour long observation. They also found that for a period of time, the northern and southern hot spot were synchronous, pulsating at the same time. Spectral analysis revealed that iogenic ions were responsible for X-ray aurora production. This was the first observation of conjugate behaviour from the northern and southern X-ray auroral emissions. A simultaneous Chandra observation found the same (quasi-)periodicity and is examined in greater detail in Chapter 4, discussing the possible drivers behind the auroral emissions during a compression event and how we can map the pulsations to their locations in the magnetosphere.

2.4.5 Sparsity of auroral quasi-periodicities

As discussed throughout this section, many observations have found the X-ray auroral emissions to exhibit pulsations or quasi-pulsations. In order to fully understand the auroral driver responsible for energising the ions, we need to understand how often the significant pulsations occur throughout the X-ray campaigns. Jackman et al. (2018) conducted a statistical study looking at Chandra data from November 25 1999 up to and including April 20 2014, searching for quasi-periodicities in auroral X-ray data and assessing the different timing analysis methods. From their analysis, using significance threshold from Monte Carlo simulation, they showed that significant quasi-periodic oscillations (QPOs) vary from observation to observation and are infrequently observed. This has important ramifications for understanding the driver of the X-ray auroral emissions.

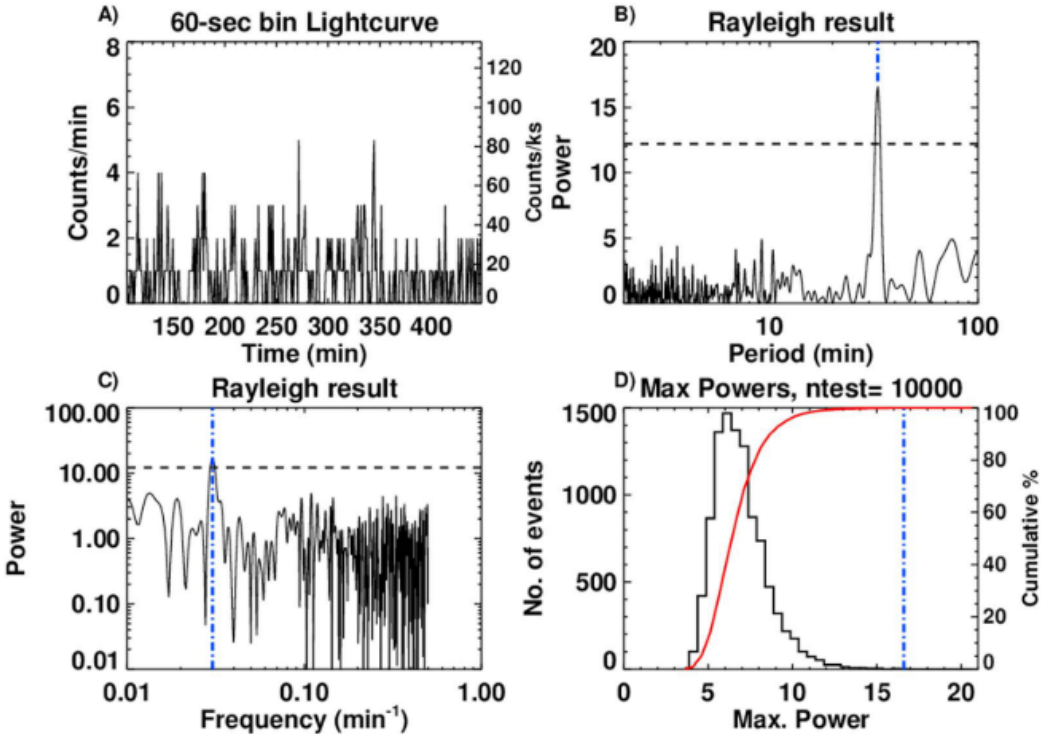

FIGURE 2.20: Example result from the Rayleigh testing method with the (A) light curve of the selected region, binned by 60-sec for viewing purposes only (the unbinned light curve is sued for analysis); (B) the resulting periodogram from the Rayleigh test using Equation 2.11, with the max period identified with the blue dot-dashed line and the 99th percentile associated with 10,000 Monte Carlo simulation shown by the horizontal black dashed line; (C) a log-log plot of frequency vs. power to determine any power law in the signal associated with coloured noise and (D) a cumulative histogram (cumulative frequency shown in red) of maximum Rayleigh powers from the 10,000 randomly shuffled light curves, highlighting where in the distribution the identified max period lies. Figure taken from Figure 2 from Jackman et al. (2018).

When assessing various timing analysis techniques for analysing the X-ray auroral emissions, Jackman et al. (2018) found that Rayleigh testing and Monte Carlo simulation seem to best-suited for the time-tagged data obtained from Chandra. The Rayleigh test is designed to work with unbinned, time-tagged sparse data and assigns each time-tagged photon with a different phase for each assumed frequency in the generated grid. This allows the full distribution of phases to be analysed to search for either a uniform signal (e.g. an absence of a quasi-pulsation) or any local anomalies associated with possible significant pulsations. This is found from the Rayleigh Power, α_{p}, expressed as

$$\alpha_{\mathrm{p}} = \frac{(\sum \cos(\omega t))^2 + (\sum \sin(\omega t))^2}{N} \tag{2.11}$$

where ω is a full set of test angular frequencies specifically chosen to correspond with

the time and cadence of the light curve, t is the arrival times of all of the time-tagged photons and N is the total number of photon counts over the observation window. The highest α_{p} corresponds to data containing a signal associated with coloured noise (when the periodogram has a significant power that can be fitted to a power law > 0 in logspace), a quasi-period or a strict periodic pulse. The advantage of using this method is that any sparse data sets are not smoothed (or binned) and therefore no temporal information is lost from the analysed light curve. An example of an output from the Rayleigh test is shown in Figure 2.20 showing: (A) the light curve used, binned only for viewing purposes here (the unsmoothed light curve is used for analysis); (B) the resulting periodogram from the Rayleigh test using Equation 2.11, with the resulting max period identified with the blue dot-dashed line. The 99th percentile associated with 10,000 Monte Carlo simulation shown by the horizontal black dashed line to show the likelihood of the signal occurring from random chance. Above this line, the signal is deemed significant in this regime. A log-log plot of frequency vs. power is shown in (C) to determine any power law in the signal associated with coloured noise. If there is slope found in this signal (e.g. red noise - see Chapter 4 for more details), it can provide us with false significances by raising the Rayleigh power. Finally, (D) shows a cumulative histogram (cumulative frequency shown in red) of maximum Rayleigh powers from the 10,000 randomly shuffled light curves (from the Monte Carlo simulation), highlighting where in the distribution the identified max period lies. If the max period lies in the tail of the distribution, as shown in his example, it is very unlikely the signal occurred by random chance using the Rayleigh test statistic.

The timing analysis examined in Chapters 4 - 6 uses the Rayleigh testing and Monte Carlo method as suggested by Jackman et al. (2018) to search for significant quasi-periods. We note that the context used in this research slightly differs from Jackman et al. (2018) by introducing specific limitations on photon concentrations and locations within the auroral regions. The remainder of this thesis will discuss how this research contributes to the field to decipher the auroral driver(s) of the X-ray auroral emissions by looking at different regions of the magnetosphere and how the quasi-pulsations produced are spatial dependant and not necessarily uniform across the auroral region. The final research chapter, Chapter 7, changes focus slightly and analyses how the jovian magnetosphere can affect the kronian X-ray emissions.

Chapter 3

Instrumentation

"Extraordinary claims require extraordinary evidence."
- Carl Sagan, 1979

Which has apparently been given the acronym *ECREE*...

The data used in this thesis were obtained primarily from the Chandra X-ray Observatory (Section 3.1) and the NASA Juno spacecraft (Section 3.2). This chapter concludes by briefly discussing one from a plethora of solar observatories used to monitor solar activity during planetary observations (Section 3.3) and how other remote sensing observations, such as ultra-violet (UV) emissions found by the Hubble Space Telescope, can be compared with *Chandra* data to provide vital magnetospheric context, absent from the X-ray data.

3.1 Chandra X-ray Observatory (CXO)

The Chandra X-ray Observatory (CXO) or *Chandra* was launched on July 23 1999 by Space Shuttle *Columbia* as part of NASA's Great Observatories campaign.
Chandra played a key role as the only X-ray telescope as part of NASA's mission, utilising its great angular resolution (full width half maximum (FWHM) $\lesssim 0.5''$) to provide detailed images of X-ray sources within our Solar System and beyond (Weisskopf et al., 2000; Wilkes et al., 2019). *Chandra* was placed in an elliptical orbit around Earth with its apogee (furthest point in orbit from Earth) at $\sim$ 133,000 km and perigee (closest point) at 16,000 km, with a period of $\sim$ 64 hours. The eccentricity of the elliptical orbit means that *Chandra* spends 85% of its orbit outside of the Van Allen belts (or Earth's radiation belts, containing highly energetic ions and electrons), resulting in $\sim$ 55 hours of uninterrupted, useful observation time[1]. This is dependent

[1] https://chandra.harvard.edu/about/tracking.html

on many factors including, but not limited to, heating effects of the on board electronics, the position of bright X-ray sources near the target and the location of the Sun. The high altitude of the orbit means that there is very limited contamination from the geocorona which affects observatories at lower/near-Earth orbits.

This unmatched spatial resolution is provided by *Chandra*'s High-Resolution Mirror Assembly (HRMA), a telescope (focal length = 10 m) composed of four pairs of concentric thin-walled, grazing-incidence, Wolter Type-I mirrors. The Type-I mirror configuration of each pair consists of a parabolic front mirror and hyperbolic back mirror (Wolter, 1952). The HRMA is shielded from sunlight as shown in Figure 3.2a). X-ray photons entering the HRMA will reach the integrated science instrument model (ISIM), comprising of *Chandra*'s two focal plane cameras: the Advanced CCD Imaging Spectrometer (ACIS) and the High Resolution Camera (HRC). ACIS was used to image Jupiter in November 1999 (4 observations), February 2003 (2 observations), February and March 2007 (6 observations) and February and April 2011 (2 observations). However in more recent years, there has been significant contamination build-up which severely inhibits the detection of X-rays below 1 keV (see Plucinsky et al. (2018)), where we expect the peak X-ray photon energy from Jupiter to lie. However, the spatial resolution ($\sim 0.4''$) of the wide-field imager on HRC (HRC-I) is $\sim$ 50% better than that of ACIS allowing us to map any detectable X-ray emissions onto the planet in greater detail (as discussed in Section 3.1.3). Therefore the X-ray observations analysed and discussed in this thesis were primarily taken by HRC-I. The timeline of all *Chandra* ACIS and HRC-I (green and black dashed lines respectively) and planned observations (orange dotted line) with respect to the solar cycle is shown in Figure 3.1. There are 14 ACIS and 33 HRC-I observations in the *Chandra data archive*[2]. The 4 planned HRC-I observations are to happen September/October 2021. Other X-ray observatories such as the X-ray Multi-Mirror Mission (*XMM-Newton*) and Nuclear Spectroscopic Telescope Array (*NuSTAR*) have observed Jupiter at this time, but the details of their instrumentation are not expanded here as those datasets are not used in the thesis chapters.

3.1.1 High Resolution Camera (HRC-I)

The *Chandra* wide-field imager on HRC (HRC-I) incorporates a single large-format microchannel plate and allows high spatial resolution of $\sim 0.4''$over a $30' \times 30'$field of view (FoV) (Weisskopf et al., 2000; Wilkes et al., 2019). The aim point is at the centre of the FoV, where the best image quality is found. The location of the aim-point is indicated in Figure 3.2b) - a schematic of HRC-I's focal plane layout. The instrument can detect photons with energies between 0.08 and 10 keV. The HRC-I detector on-board *Chandra* has limited spectral resolution. For the case of Jupiter, this cannot be

[2] https://cda.harvard.edu/chaser/

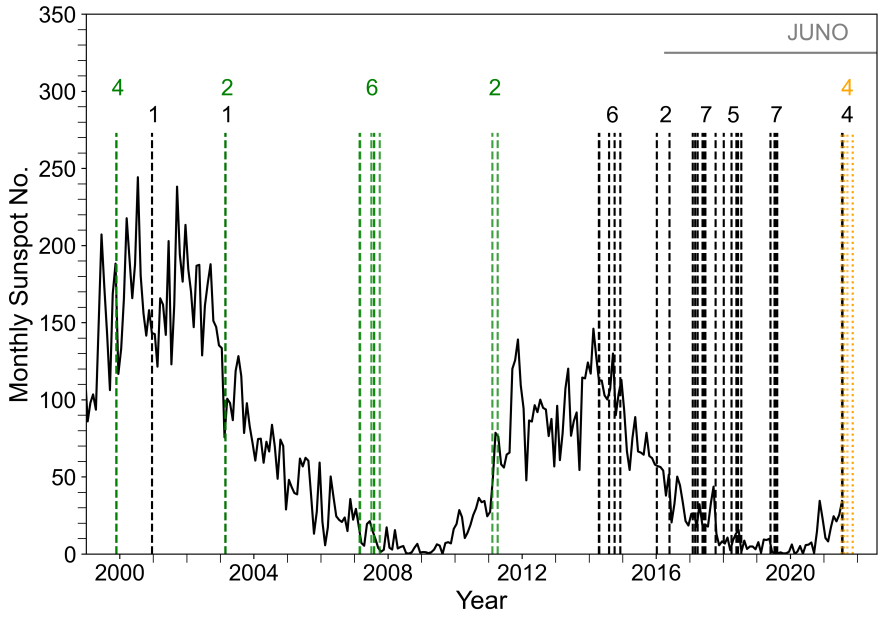

FIGURE 3.1: The sunspot number from 1999 to July 2021 plotted as a function of time is shown in black with individual *Chandra* HRC-I observations represented by dashed vertical black lines. ACIS observations are shown in dashed vertical green lines. Black and green labels on top of the *Chandra* lines show the number of HRC-I and ACIS individual observations in a given year respectively. Dotted orange lines with respective label show planned observations. The ongoing timeline of the *Juno* mission is shown in grey. *Sunspot number source: WDC-SILSO, Royal Observatory of Belgium, Brussels*

utilised as the observed photons are softer (in X-ray energy) than targets typically observed by Chandra. As a consequence, all jovian photons lie in the low pulse height amplitude (PHA) channels associated with a soft X-rays and are there not distinguishable. Therefore the X-ray photons we analyse here cannot be filtered into energy bins, making it difficult to differentiate between the different possible processes responsible for X-ray production (e.g. bremsstrahlung, solar X-ray scattering) at Jupiter which will discussed further in Chapter 2. The ongoing X-ray Multi-Mirror Mission (*XMM-Newton*) has high spectral resolution and therefore it possible, for some studies, to compare and contrast the data from both Chandra and *XMM-Newton* (Jansen et al., 2001). Future X-ray missions, such as the upcoming *Athena* mission (Barret et al., 2016) (launch date 2031), will have greatly improved X-ray sensitivity and will provide an entirely new window to explore jovian and other planetary X-rays. This is discussed further in Chapter 7.

The HRC-I instrument when pointed at Jupiter, can trace the planet's motion across the sky. As a result, the full image taken by HRC-I appears as multiple streaks of jovian X-ray emission due to the fast motion of Jupiter across the detector (see Figures 3.3a, b)). Section 3.1.2 discusses how this can be corrected for due to the data being time-tagged, enabling the photon positions to be traced back to their origin on Jupiter's disk.

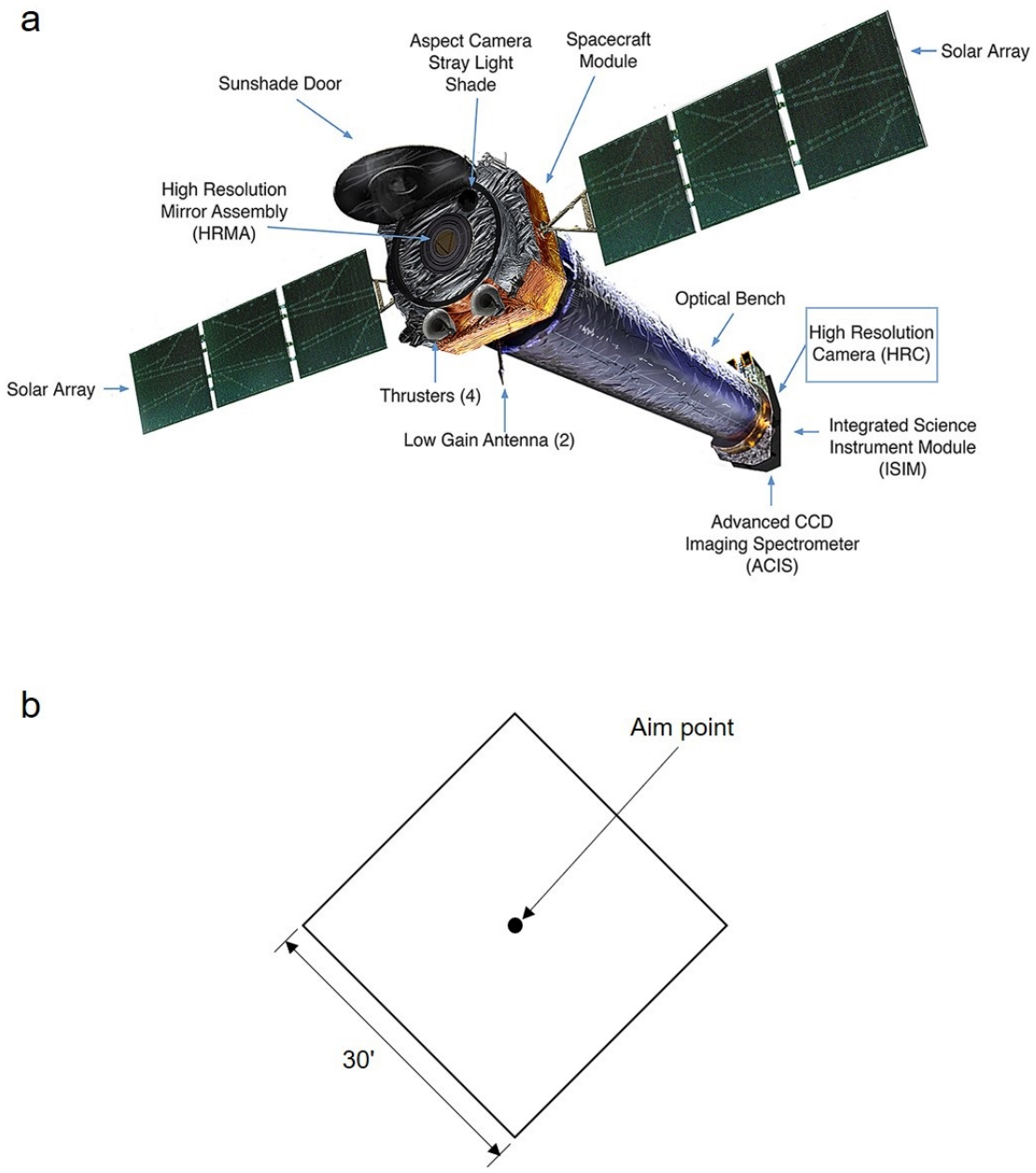

FIGURE 3.2: (a) Labelled schematic diagram of *Chandra* with (b) the focal plane layout of the imager on the High Resolution Camera (HRC-I), as highlighted in (a). Schematic diagram is taken from Wilkes et al. (2019)

3.1.2 Correcting images for Jupiter's motion

Early studies by Gladstone et al. (2002) and Elsner et al. (2005) developed methods to process the raw Chandra data into time-tagged photons fixed on Jupiter, and projected correctly onto the planet. This algorithm first correct for the motion of the planet across the HRC-I detector. Prior to image correction, as shown in Figure 3.3b) and introduced in Section 3.1.1, the X-ray emissions of Jupiter appear as multiple streaks on the detector. This streaking effect is a result of Jupiter moving across the sky during the observation window. The brightest streaks appear at the top and bottom of the planet, corresponding to the brightest emission from the poles. As the data collected by *Chandra* are time-tagged, the original positions of the photons on Jupiter's disk can be traced back and correct for the streaking effect. To perform this correction the new orbital positional coordinates of *Chandra* need to be determined. These were found from the orbit ephemeris file (found in the retrieved *Chandra* data) once a 1D-linear interpolation was performed to the Day of Year (DOY) of the time interval of the question found from JPL Horizons[3]. From this new set of coordinates, the new positional coordinates of Jupiter, using the RA and DEC found from the interpolation, can be determined and used to calculate the corrected photon positions in planetocentric coordinates (x, y). The correction algorithm then produces a new event FITS file with the new positional coordinates with Jupiter found to be placed at the centre of the chip (i.e. to minimise the error associated with viewing the source). The corrected image (as shown in Figure 3.3c) can then be used for further data analysis. Each time-tagged photon that strikes the detector will generate a charge in a PHA channel. As mentioned previously, the softer jovian photons fall in the lower PHA channels. Therefore in this research, we limit our analysis to photons lying between channels 0 - 90 (soft X-ray range), to remove most of the particle background and ensure that any photons observed on Jupiter's disk are real. The jovian disk also occults any X-rays from sources that may be situated behind Jupiter. We then select a circular region of radius $30''$at the centre of the chip that envelopes all the jovian X-rays with minimum background and accounting for possible limb effects. This method is sufficient when analysing the jovian X-ray auroral emissions as the signal-to-noise ratio (SNR) is high. However with the continued degradation of *Chandra* (implications of which are discussed in Chapter 6) due to the age of the instrument leading to increased contaminant in the background, this algorithm may need to be adapted to include these effects.

The correction algorithm is not limited for use on Jupiter but can be applied to many other sources (e.g. Saturn - see Section 7). As Jupiter is titled and the auroral emissions are fixed in magnetic latitude and longitude, the brightest auroral X-ray emissions are not present for the full *Chandra* observation and rotate into view. Therefore the

[3] https://ssd.jpl.nasa.gov/horizons.cgi

apparent brightening of the full pole in the corrected image is a result of the exposure time of the image when the X-ray emissions traverse the full disk (e.g. the full pole is illuminated as the exposure time is ≥ 1 jovian rotation).

3.1.3 Mapping jovian photons to the planet

The X-rays can then be mapped using the Gaussian point spread function (PSF) of the instrument and a coordinate transformation into jovian System III (S3) coordinates (as defined in Chapter 2.2.3) from planetocentric (x, y) coordinates. With this coordinate transformation, each time-tagged photon is associated with an ionospheric position in (λ_{III} , θ_{III}) which can be used in further analysis, such as mapping the emissions. The mapping of *Chandra* X-ray emissions is calculated using the point spread function (PSF) of the instrument which is wrapped around Jupiter's surface, showing the locations of X-ray emissions found by *Chandra* . We want to ensure Jupiter is centred on the HRC-I chip as the PSF of the detector is observed to increase with distance away from the centre. The PSF is calculated from a Gaussian function using the corrected λ_{III} and θ_{III} positions corresponding to the photon flux (counts arcsec^{-2} s^{-1}) detected by HRC-I. The photon flux, J, is then converted to brightness, I, (in Rayleighs: see Section 2.2.2) using

$$I = \frac{4\pi\theta^2 J}{10^9} \tag{3.1}$$

where $\theta = 1$ radian $\simeq 206265''$ and $\theta^2 = 1$ steradian. This conversion factor assumes that the effective area of the instrument is 40 cm^2, appropriate for X-ray photons with mean energy ~ 300 eV. The factor of 10^9 accounts for the column area of the emissions used for the analysis. The brightness is therefore proportional to the photon flux and is an easier quantity to interpret on any plots produced from the pipeline.

The maximum PSF associated with each photon is then plotted at each λ_{III} and θ_{III} on a $360^\circ \times 180^\circ$ grid, divided into 1° $\lambda_{\mathrm{III}} \times 1^\circ$ θ_{III} sized cells. This produces a 2D-histogram in Cartesian space of the X-ray emission on Jupiter's surface, providing information of the morphology of the X-ray emissions as well as the intensity. In this research, the 2D histograms are used for visual purposes to provide a general idea of the auroral morphology and intensity as applying the PSF to the photons in this way results in a slight degradation of the effective spatial resolution of HRC-I.

The auroral/polar regions can be explored in greater detail by performing a polar coordinate transformation on the Cartesian maps to create a polar 2D-histogram with radial, r, and azimuth, φ, coordinates accounting for the oblateness of Jupiter using

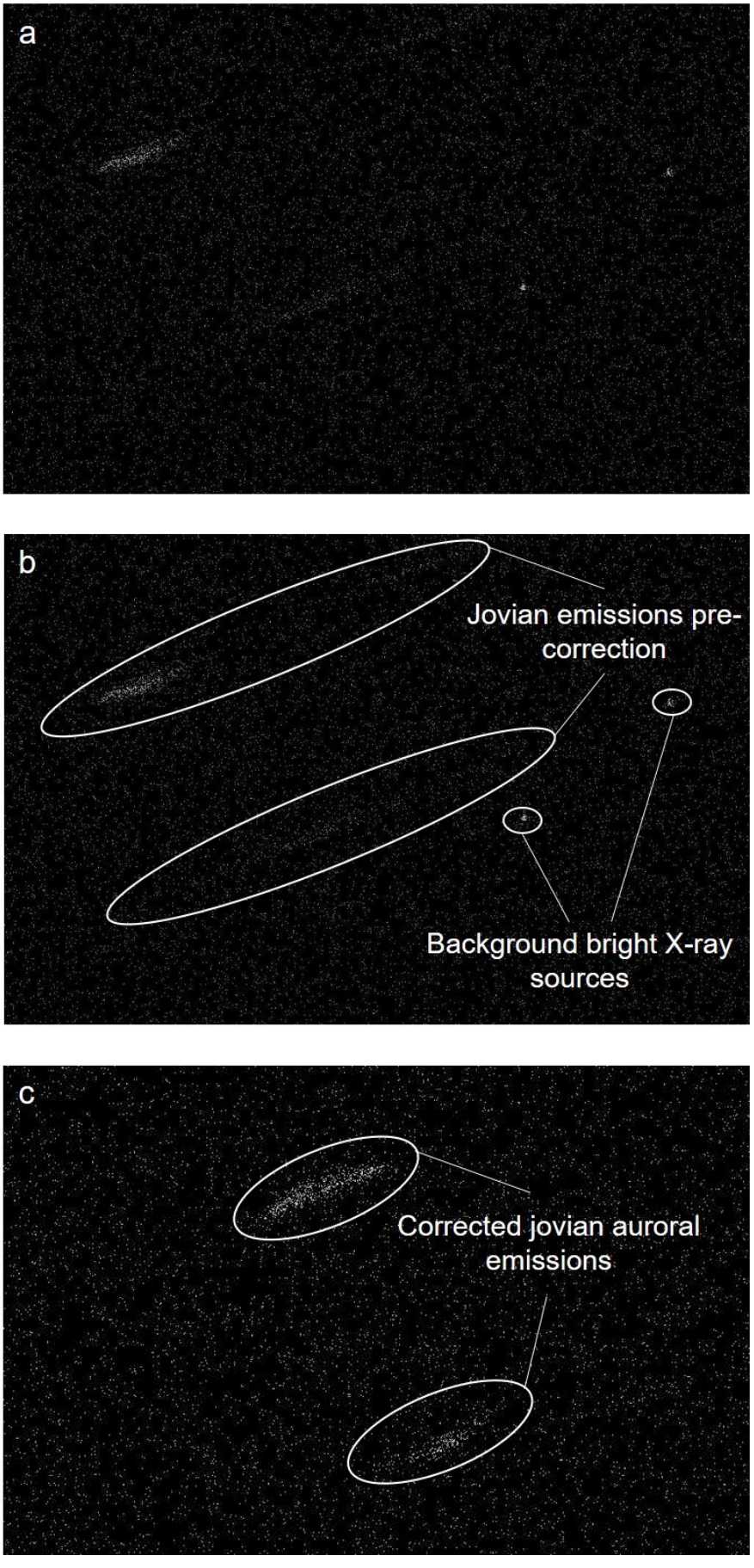

FIGURE 3.3: Example *Chandra* observation taken on May 24 2016 (ObsID 18608) with the raw image shown in (a) and emissions labelled in (b). The corrected image is shown in (c)

$$\varphi = \lambda_{\mathrm{III}} \quad \text{and} \quad r = \sqrt{1 + \left(\frac{R_{\mathrm{P}}}{R_{\mathrm{eq}}} \tan\left(\theta_{\mathrm{III}} - \frac{\pi}{2}\right)\right)^2} \tag{3.2}$$

where $R_P \simeq 66854$ km and $R_{eq} \simeq 71492$ km are the polar and equatorial radius of Jupiter respectively and λ_{III} and θ_{III} are in radians. Equation 3.2 defines the planetocentric polar projection. In many cases, the planetographic projection is more useful to compare with other datasets across multiple wavelengths and is defined as

$$\varphi_{\mathrm{PG}} = 2\pi - \varphi \quad \text{and} \quad r_{\mathrm{PG}} = \arctan\left(\tan(r)\left(\frac{R_{\mathrm{P}}}{R_{\mathrm{eq}}}\right)^{-2}\right) \tag{3.3}$$

An example of the planetographic mapping of the X-ray emissions is shown in Figure 3.4 with the planetographic polar transformed Voyager Io Pioneer 4 (VIP4) (Connerney et al., 1998) Io (dashed line) and Grodent Anomaly Model (GAM) (Grodent et al., 2008) Ganymede footprints (solid line). $\theta_{III} \geq |40^\circ|$ are labelled to help provide context to the location of the auroral emissions. Both panels in Figure 3.4 are orientated as the observer looking down onto each of the poles over the entire ObsID 18608 observation. The *Chandra* interval can also be split into equal time intervals to observe the changing morphology (as shown Chapter 4 in more detail). The assumptions used for the mapping assume that the FWHM of the HRC PSF is 0.8″with a PSF size of 25″. The altitude at which X-ray emission occurs was assumed to be 400 km above the 1-bar atmosphere (e.g., Cravens et al., 1995; Ozak et al., 2010). The scaling used for the maps was 0.13175 arcsec/pixel for *Chandra* HRC-I. The pipeline discussed was translated from the methodology used by Gladstone et al. (2002) and Elsner et al. (2005) (written in Mathematica and Interactive Data Language (IDL)) to Python. This was used for data analysis and produced the planetographic polar plots shown in the remainder of the thesis. The code by Weigt (2021) has been made public for others in the field to use[4] and can be used to correct, analyse and map data from ACIS as well as HRC-I.

3.2 Juno

NASA's Principal-Investigator (PI) led mission *Juno* was launched on August 5 2011 as part of NASA's New Frontiers Program. As part of its journey to reach the orbit of Jupiter, *Juno* performed two deep-space manoeuvres (DSM) beyond Mars's orbit on August 30 and September 14 2012 before initiating an Earth fly-by (EFB) on October 9th 2013 (Bolton et al., 2017). The spacecraft performed its Jupiter orbit insertion (JOI) on July 5 2016, entering an elliptical polar orbit to minimise the exposure time of

[4] https://github.com/waledeigt/zeno-py

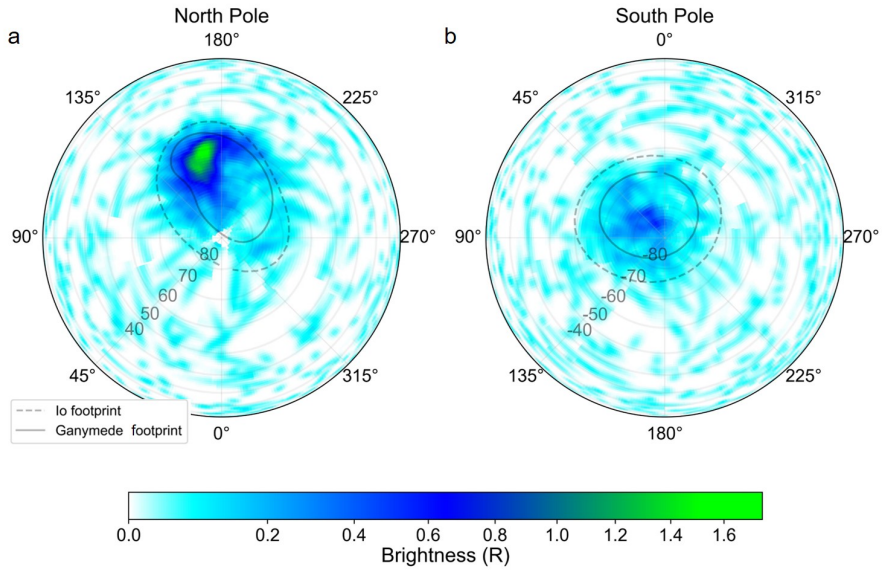

FIGURE 3.4: Polar planetographic projection of auroral emissions from the corrected data (as shown in Figure 3.3) looking down onto the (a) North and (b) South poles. $\theta_{\text{III}} \geq |40°|$ are labelled with the Voyager Io Pioneer 4 (VIP4) (Connerney et al., 1998) Io (dashed line) and Grodent Anomaly Model (GAM) (Grodent et al., 2008) Ganymede footprints (solid line).

Juno inside Jupiter's dangerous radiation belts. A schematic of *Juno*'s journey to the jovian magnetosphere as observed from the ecliptic North pole is shown in Figure 3.5. Following the JOI manoeuvre, Juno orbited Jupiter with an orbital period of $\sim$ 53.4 days. This was an unexpected change from the initial plan of $\sim$ 14 days due to a malfunction of the engine's fuel pressurisation system during *Juno*'s period reduction manoeuvre during the second perijove (PJ2)[5] (closest to Jupiter, above the poles). At the time of writing, the current orbital period of *Juno* during PJ35, during the extension of the main science mission, was reduced to 43 days after performing a fly-by of Ganymede. The trajectory of *Juno*'s elliptical polar orbit in the jovian equatorial (x-y) plane during the main science mission is shown in Figure 3.6. The compressed and expanded limits for both the bow shock and magnetopause from the Joy et al. (2002) model are also plotted. As shown in Figure 3.6, *Juno* had apojove near the dawn magnetopause from the JOI and has been moving around toward the tail in later years.

Juno orbits Jupiter with a scientific payload consisting of eight instruments (as labelled in Figure 3.7). These allow for *in situ* exploration of magnetic field, energetic particles and plasma, in concert with ultra-violet (UV) and infrared (IR) observations of the planet. *Juno* is the first spacecraft exploring the outer planets to be powered by solar arrays (three 9-metre long arrays) and spins at 2 rpm (1 full rotation every 30 s) while obtaining data on the jovian magnetosphere. The purpose of the vast array of

[5] https://www.missionjuno.swri.edu/news/next-jupiter-pass

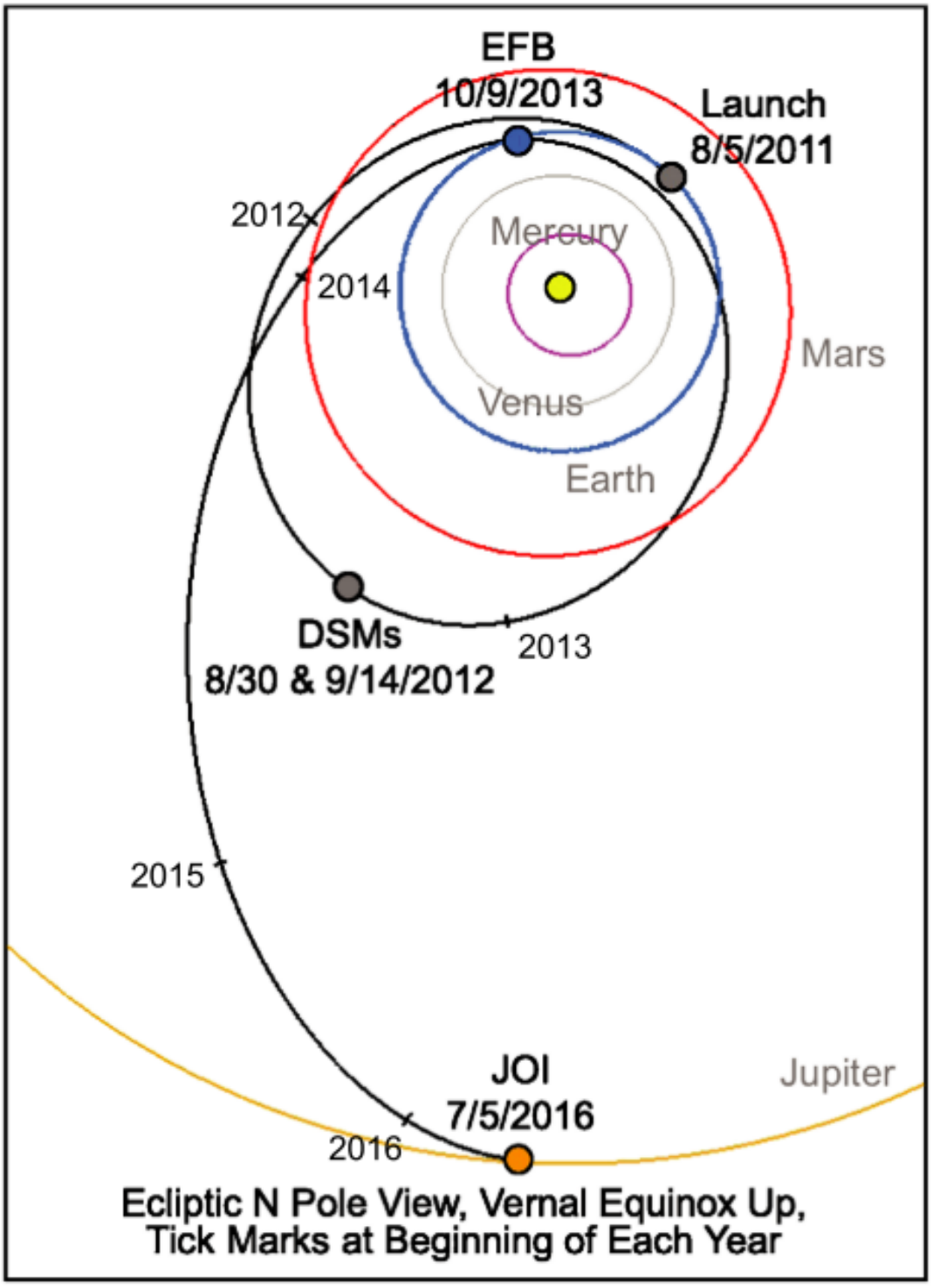

FIGURE 3.5: Ecliptic North pole view of *Juno*'s trajectory to Jupiter from launch up to and including obrit insertion (JOI). The Earth fly-by (EFB) and deep space manoeuvers (DSMs) are also shown on the plot. Taken from Bolton et al. (2017).

instruments is to help achieve the primary science objectives[6] of *Juno* (Bolton et al., 2017):

1. **Origin**: to calculate the water abundance at Jupiter and obtaining a better estimate of the mass of Jupiter's core.
2. **Interior**: to analyse the distribution and dynamics of Jupiter's internal mass as well as proprieties of interior structure.
3. **Atmosphere**: to analyse and map variation of the composition, temperature and cloud opacity across the planet
4. **Magnetosphere**: to explore and characterise the structures of the polar magnetosphere and jovian aurora in three dimensions.

The X-ray data from *Chandra* (and from other remote sensing data in other wavelengths) can be used to complement the *in situ Juno* data to address objective (4), exploring the magnetospheric drivers which produce the jovian X-ray emissions. The thesis work incorporates data from many of the instruments on-board *Juno* to help provide vital magnetospheric context to the X-ray data as well as the auroral drivers.

3.2.1 Jovian Auroral Distributions Experiment (JADE)

The *in situ* data from *Juno* Jovian Auroral Distributions Experiment (JADE) are used to measure the properties and provide diagnostics of the jovian magnetospheric election and ion populations. This provides vital magnetospheric context to the *Chandra* HRC-I observations. JADE provides measurements of the electrons and ions via 2 separate detectors: JADE-I and JADE-E. JADE-I consists of a single ion sensor and can measure ions from $\sim$ 5 eV to $\sim$ 50 keV over a 270° $\times$ 90° FoV in 2 s over all directions in each 30 s rotation of Juno and can also separate heavy and light ions in the jovian magnetosphere McComas et al. (2017). JADE-E is comprised of three electron sensors which are separated 120° apart around Juno to measure electron distributions from $\sim$ 0.1 to $\sim$ 100 keV. The arrangement of the sensors are shown in Figure 3.8. The JADE-E sesnors can view all spin phases instantaneously resulting in detailed measures of the electron pitch-angle distribution during each orbit at a high time cadence, detrended from the spin of the spacecraft. As there is only one ion sensor, JADE-I records ion data mainly perpendicular to the JADE-Es plane and can sweep out all angles during each *Juno* 30 s spin (McComas et al., 2017). These ion and electron measurements can also allow us to determine what state Jupiter's magnetosphere is in during each Chandra observation. JADE data are used in Chapter 4 of this these to elucidate the

[6] https://www.jpl.nasa.gov/news/press_kits/juno/science/

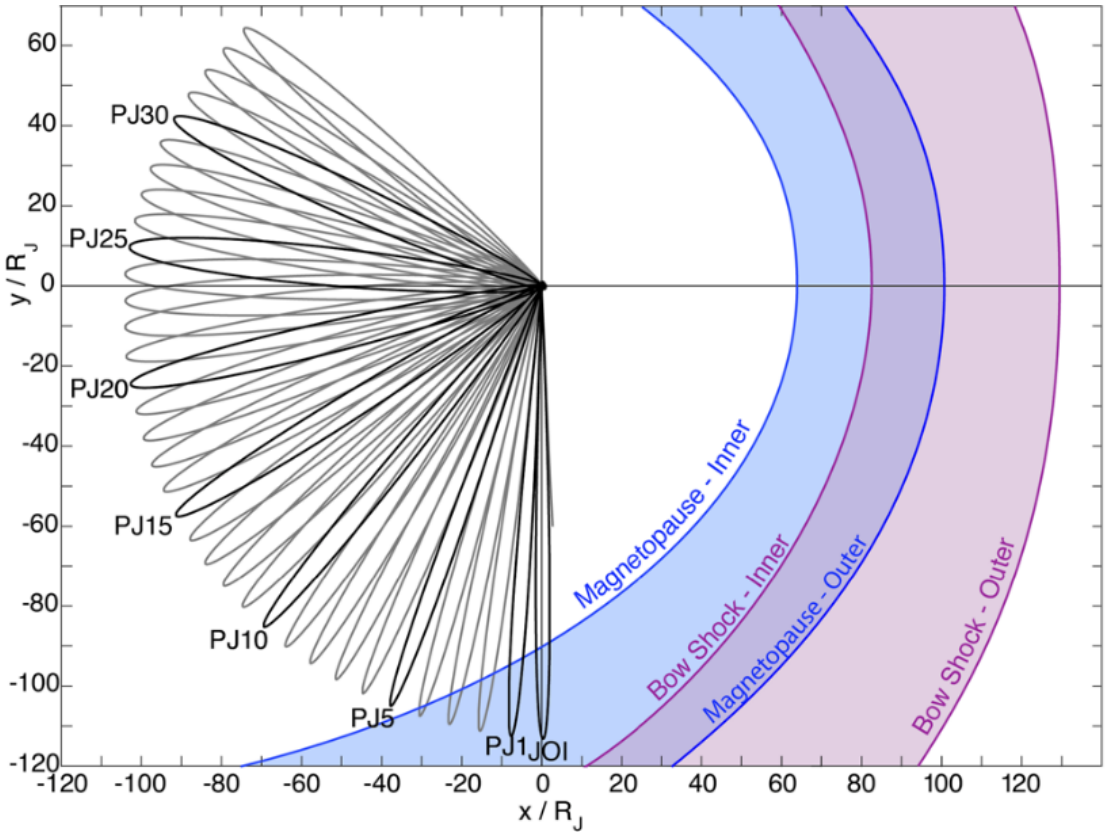

FIGURE 3.6: Obtial trajectory information of *Juno*'s science mission up to and including PJ34 (i.e. not including extended mission). Each orbit indicated on plot is 53 days long and viewed from the jovian equatorial system. The x-axis points towards the Sun, z-axis is Jupiter's spin axis and the y-axis completes the orthogonal system. *Juno*'s trajectory is plotted in the (x-y) plane. Bow shock and magnetopause limits are taken from the Joy et al. (2002) model. Image is taken from Bolton et al. (2017).

local conditions at the spacecraft during an apojove interval (point of *Juno*'s orbit furthest from the planet) in 2017 which coincided with a *Chandra* observation.

3.2.2 Jupiter Energetic-particle Detector Instrument (JEDI)

The Jupiter Energetic-particle Detector Instrument (JEDI) measures the energetic electrons and ions that: a) are a key component to the production of the aurora on Jupiter; b) are found to heat and ionize the upper atmosphere of Jupiter and c) provide signatures of the structure of Jupiter's magnetosphere, focussing mainly on particles belonging to the inner magnetosphere (Mauk et al., 2017). JEDI makes measurements of the energy, pitch angle and ion composition distributions of ions from 20 keV (H) and 50 keV (heavier O) to energies > 1 MeV from its three sensors (Figure 3.9). Each sensor runs independently from each other and are spaced as such to provide the best viewing geometry throughout *Juno*'s orbit. The energies of electrons, E, detected by JEDI are between $E < 40$ to $E > 500$ keV. The time of flight and pulse height of

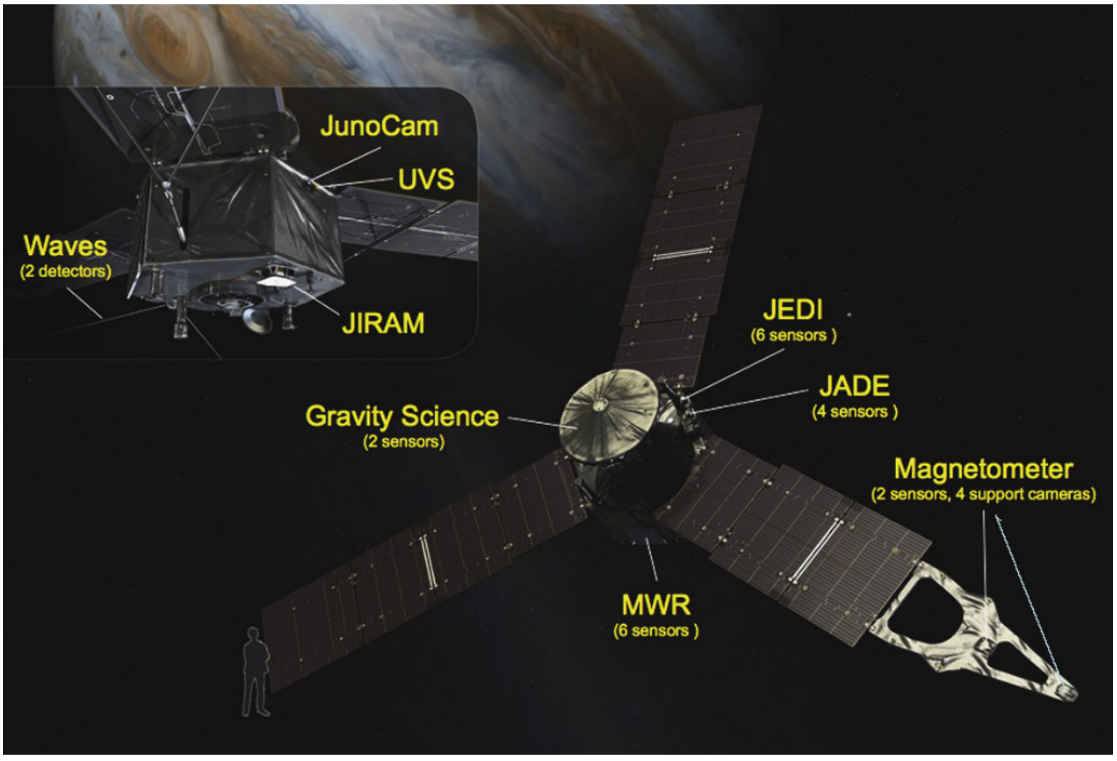

FIGURE 3.7: Image of NASA's *Juno* spacecraft and its science payload. Taken from Bolton et al. (2017).

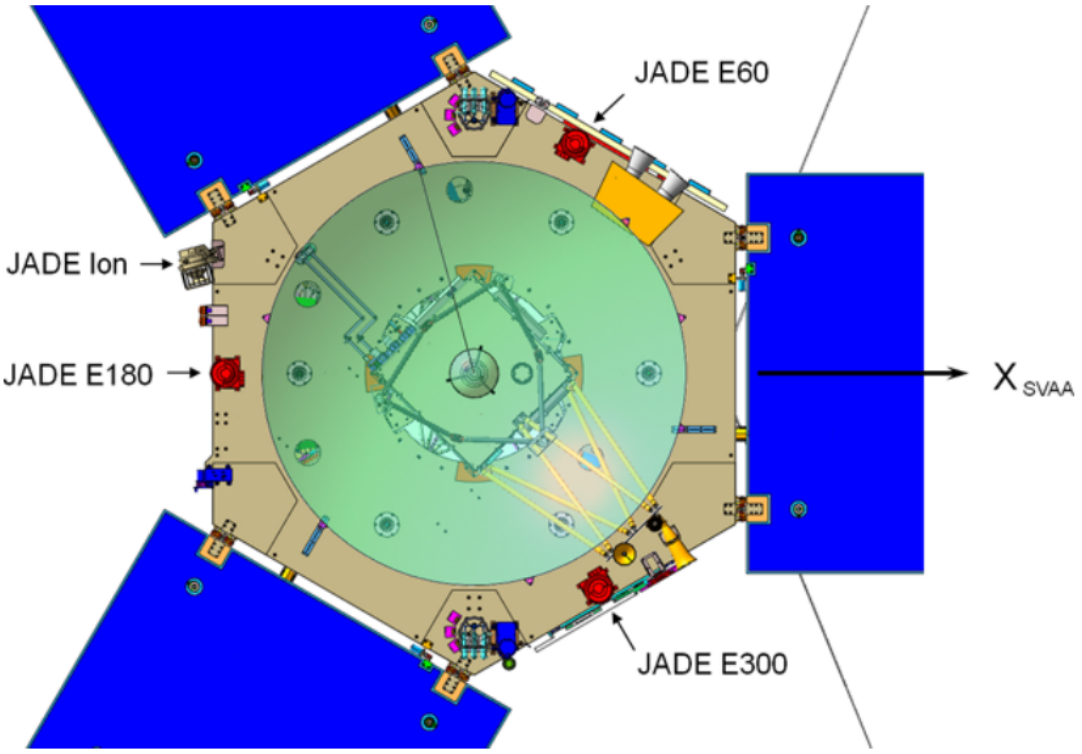

FIGURE 3.8: Locations and field of view (FoV) of JADE-I and all three JADE-E sensors on the *Juno* spacecraft. Middle structure is the high gain antenna and points towards the Sun and Earth during operations. Image taken from Mauk et al. (2017).

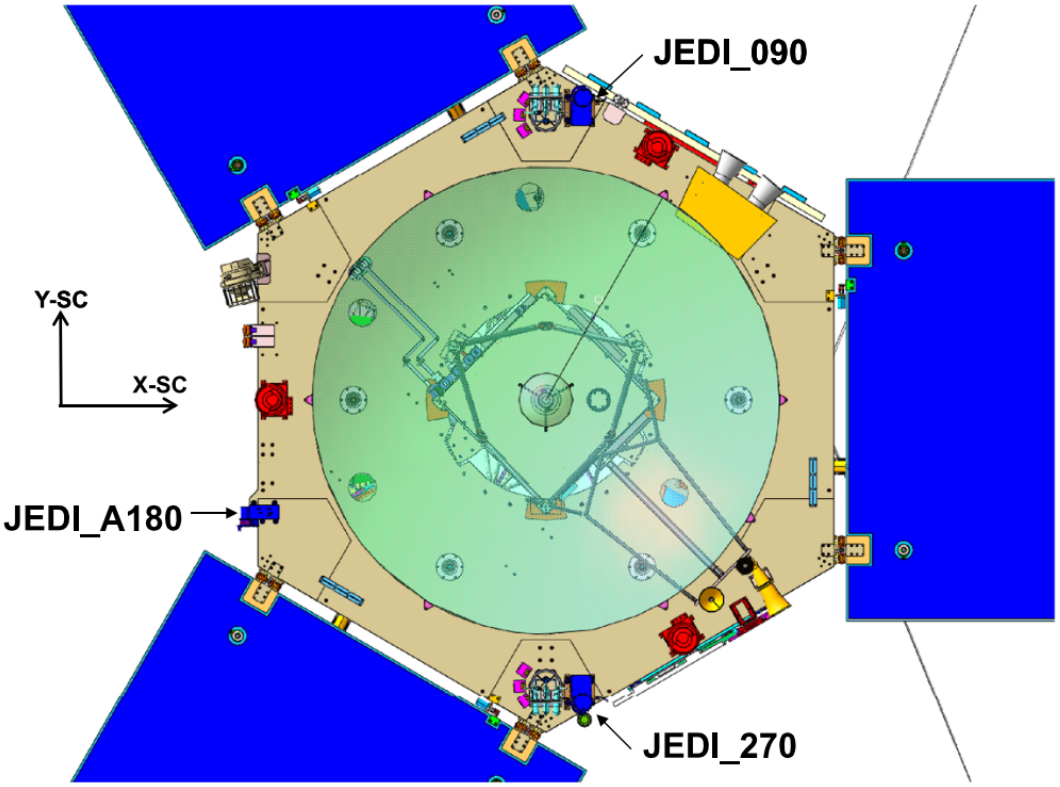

FIGURE 3.9: Similar schematic as shown in Figure 3.8 for the three JEDI sensors, with numbered labels identifying which side of the spacecraft each sensor is on.

incoming ions are measured using microchannel plates and thin foils. The total energies of both ions and electrons are measured using solid state detectors.

Like JADE, the data on the ion populations of the jovian magnetosphere are vital to understand the possible driver(s) of the X-ray auroral emissions and how the ions are accelerated to the high energies require for charge exchange to take place in the ionosphere above the poles. When *Juno* is at perijove, JEDI can be used to analyse the large potential drops also required for very energetic processes, such as charge exchange, to occur at the poles (e.g., Clark et al., 2020). Therefore combining the JEDI and *Chandra* mapping, potential correlations in ionospheric locations can be found with additional magnetospheric context from the *Juno in situ* data.

3.2.3 Juno Waves

The *Juno* Waves instrument is composed of an 2.4 m (geometric length) electric dipole antenna parallel to the spacecraft y axis and perpendicular to Juno's spin axis (as shown in Figure 3.7) and a search coil magnetometer, mounted the body of the craft (Kurth et al., 2017). The magnetometer is aligned such that the sensitive axis is parallel to the spin axis. The Waves instrument collects electric spectra (between 50 Hz and 40 MHz) and magnetic spectra (between 50Hz and 20 kHz). The cadence of the data

collected by Waves is dependent on the frequency range used and position of *Juno* during its orbit. The Waves instrument during allocated times can record waveforms that allow for enhanced temporal and spectral resolutions of the obtained spectra, when the instrument is switched periodically on and off. For the highest frequencies Waves can observe, waveforms from an ~ 1 MHz band tuned to include the electron gyrofrequency (ω_{ce}; Equation 1.16), and therefore information on the magnetic field, are collected (Kurth et al., 2017).

The spectra collected from Waves can be compared to the X-ray data to find any links between the emissions. During perijove passes, radio sources can be mapped onto the jovian poles and compared with mapped emissions at different wavelengths (e.g., Louis et al., 2019). This allows any connections between the location of the switched on radio source and any auroral features to be explored in detail. When Juno is further away from the planet, the behaviour of the radio emissions can still be observed (assuming there is no contamination from the surrounding magnetosphere) and compared to other remote sensing data. Chapter 6 will examine this in more detail when using Juno data to constrain X-ray drivers from different types of magnetospheric dynamics found by Juno.

3.2.4 The Juno Magnetic Field Investigation (MAG)

The Juno Magnetic Field Investigation (MAG) is designed to accurately measure the magnetic field vector components in Jupiter's environment, using the high temporal and spatial resolution of the magnetometer to map the planetary magnetic field (Connerney et al., 2017). The accurate field mapping is achieved from two identical sensors, one Inboard (IB) and one Outboard (OB). The sensors are aligned along a radius vector at about 10 and 12 m respectively from the centre of the spacecraft, placed at the end of one of *Juno*'s solar arrays (see Figure 3.7). Both sensors consist of a fluxgate magnetometer (FGM) to measure the three components of the vector magnetic field surrounding the spacecraft and a two non-magnetic star cameras (ASC) to provide accurate attitude support at the FGM sensor. The FGM and support camera are aligned by the MAG optical bench which all the three sensors are attached, providing enough separation between the FGM sensor and the camera heads to exclude any contaminant magnetic fields generated within the camera heads and any other inductive hardware (Connerney et al., 2017). The MAG data is provided in different time resolutions to allow various properties of the planetary field to be explored at different stages of *Juno*'s orbit.

Like the spectra obtained from Juno Waves, the *Juno* MAG data can be utilised to constrain X-ray drivers. With the timing resolution of the field data, potential drivers can be found from the different types of wave activity in the planetary field and

compared to the pulsations found in the X-ray aurora (as examined in Chapter 2). The field model developed from Juno MAG data, JRM09 (Connerney et al., 2018), can also be used to explore the relationship between the gradient of the magnetic field at the poles with the location of the X-rays. Chapter 6 will examine this in more detail and compare with other *in situ* and remote sensing data sets.

3.3 Geostationary Operational Environmental Satellites (GOES)

Chapter 7 focuses on a *Chandra* observation of Saturn, and utilises data from the Geostationary Operational Environmental Satellite (GOES) to monitor solar activity. GOES is a joint NASA and National Oceanic and Atmospheric Administration (NOAA) mission to monitor space and meteorological weather at Earth (Lemen et al., 2004). The first satellite was launched on October 16 1975 and many more have been launched to form a fleet of telescopes over the past 30+ years. At the time of writing, GOES-16, GOES-17 and GOES-18 (or GOES-T launched in March 2022) are currently in operation (Goodman et al., 2013) in a geostationary orbit. One side of GOES is always directed towards the Sun to monitor space weather effects using instruments such as the GOES X-ray Sensor (XRS), part of the Extreme Ultraviolet and X-ray Irradiance Sensor (EXIS) (shown in Figure 3.10). The main focus of XRS (and EXIS) is to monitor solar activity and characterise solar flares. In this thesis, data was used from XRS on GOES-16 to monitor any flaring activity from the Sun. The XRS monitors both soft (1 Å - 8 Å) and hard (0.5 Å - 4 Å) solar X-rays and measures the flux emitted from the Sun. The magnitude of the soft X-ray flux is then used to identify the type of solar flare observed from an A-class (weakest flare: 10^{-8} W m^{-2}) to an X-class flare (strongest flare: $\geq 10^{-4}$ W m^{-2}). The solar data is used to help establish a possible correlation between solar activity and planetary X-ray flux during this time, as found by Bhardwaj et al. (2005c) and Branduardi-Raymont et al. (2010).

When using the GOES data, we take into account the Sun-Earth and Sun-planet-Earth light time to ensure we have the correct time for when the radiation from the flare was detected by GOES and impacted the planet respectively (i.e. as viewed by *Chandra* and/or other remote sensing telescopes like the Hubble Space Telescope (*HST*)). The planet-Sun-Earth angle must also be considered during each of the Chandra observations to get an idea of the direction of any flares found by GOES. If this angle is large, the uncertainty of a solar flare found from any detectors near the Earth-facing side of the Sun impacting the planet will also be large. This will affect any interpretation of results and any interpolation models of solar wind parameters (Tao et al., 2005), especially as there is currently no upstream monitor at either of the gas giants.

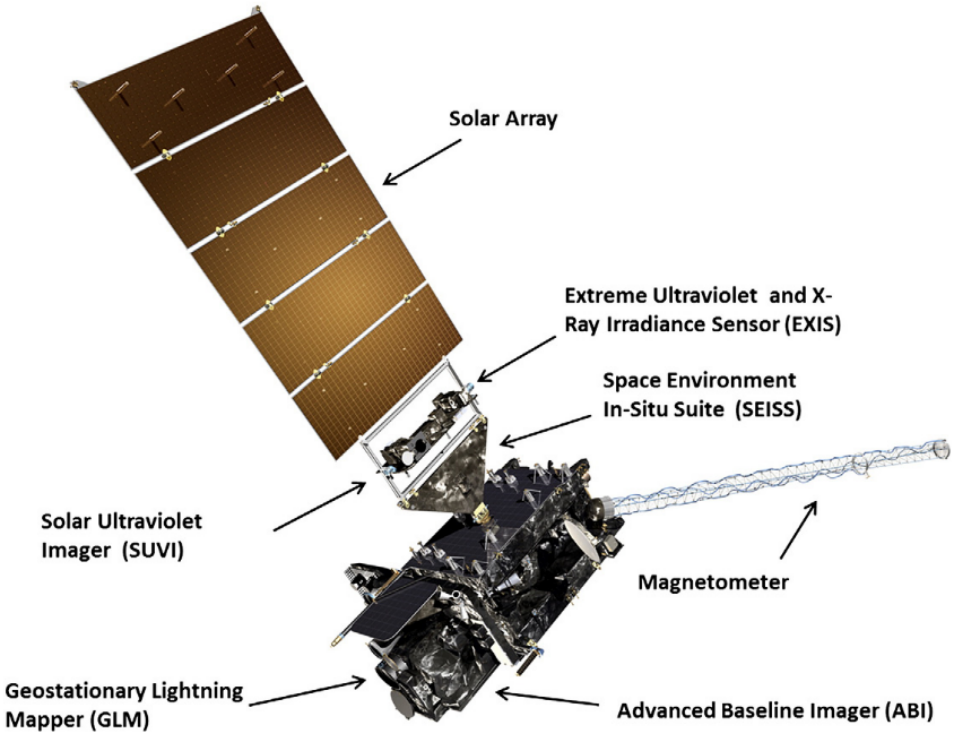

FIGURE 3.10: Schematic of the GOES-R series telescope. The X-ray Sensor (XRS) is part of the Extreme Ultraviolet and X-ray Irradiance Sensor (EXIS) as labelled on the diagram. Image taken from Goodman et al. (2013)

3.4 Hubble Space Telescope (HST)

Chapter 6 compares *Chandra* with *in situ* data from *Juno* and remote sensing data from the Hubble Space telescope (HST) to help identify X-ray "auroral families" as a way to further constrain sources/drivers of different types of magnetospheric dynamics. HST was launched into a low-Earth, geocentric orbit in 1990 to observe and analyse a vast array of objects in the observable universe. *HST* observes Jupiter's far ultra-violet (FUV) and ultra-violet (UV) emissions to help aid our understanding of the gas giant's complex magnetospheric dynamics in tandem with campaigns from *Juno* and other telescopes. The brightest FUV emissions are found within Jupiter's main auroral oval and are observed using the Space Telescope Imaging Spectrograph (STIS) on-board *HST* (Grodent et al., 2003a). As the detector is sensitive to the H_2 Lyman and Werner bands and the strong line emission produced from H Lyman-α, *HST* images of Jupiter are taken when the telescope is in the shadow of Earth. This is to reduce contamination from Lyman-α produced from Earth's geocorona. As a result, each image has a typical exposure time of 45 mins (e.g. the time in takes for *HST* to traverse Earth's shadow). The STIS field of view of $24.7'' \times 24.7''$provides a high spatial resolution of $\sim 0.0025''$, detecting FUV auroral emissions of wavelengths $\sim$ 130 - 170 nm (photon energies $\sim$ 7 - 10 eV) after the longpass filter has been applied.

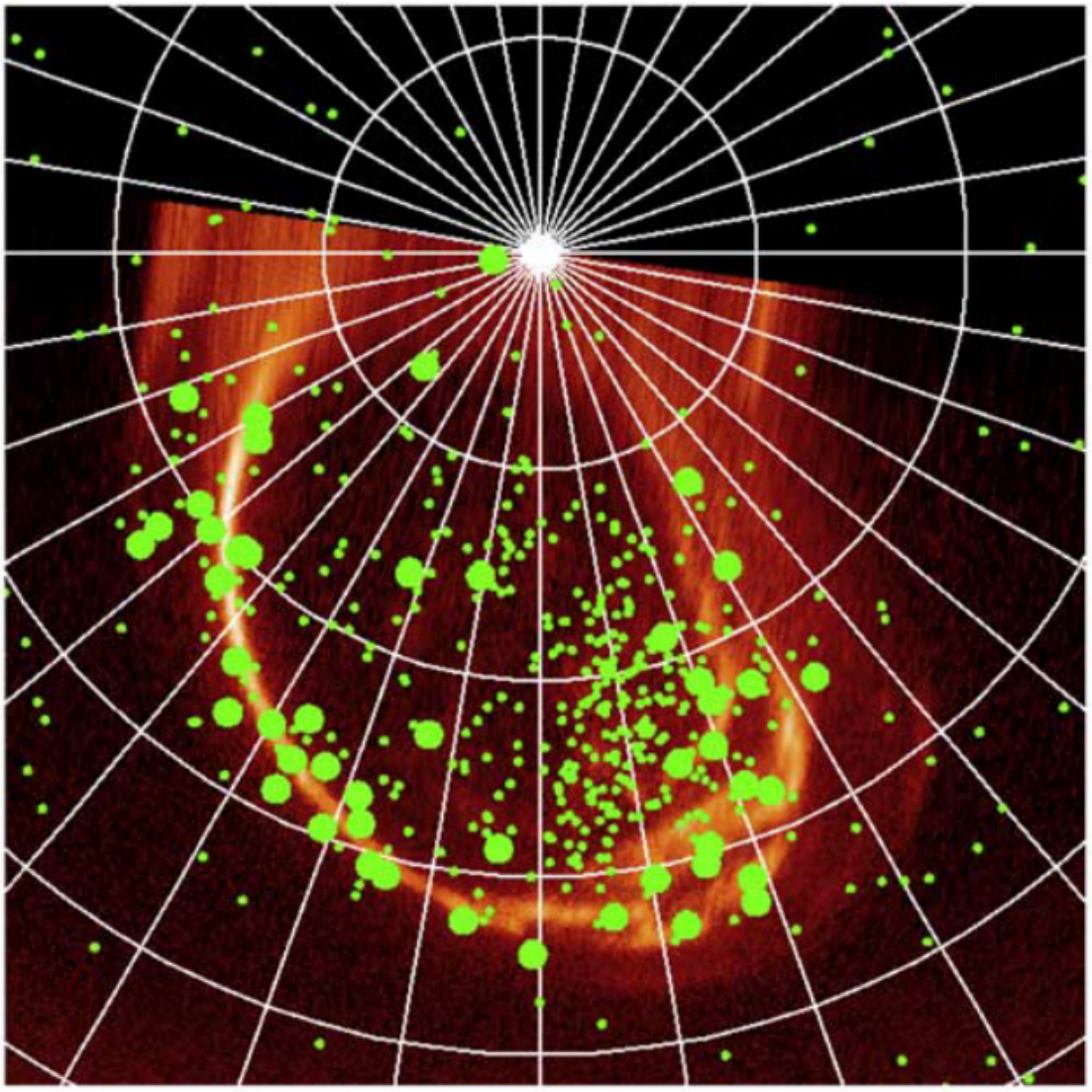

FIGURE 3.11: Polar projection of a *HST* STIS image of the northern auroral emissions taken on February 24 2003. All X-ray photons observed during a simultaneous *Chandra* observation are overplotted (green dots). The hard X-ray photons ($>$ 2 keV) are represented by large green dots and the soft X-rays ($<$ 2 keV) by the small dots. The grid is separated by 10° latitude. The Figure is taken from Branduardi-Raymont et al. (2008).

A series of images can be taken during one *HST* orbit to analyse the dynamic emissions that can occur on and within the main oval. Once the images are cleaned and processed, they can be compared with other data such as time-tagged, X-ray photons from *Chandra* to compare spatial and temporal behaviour of the emissions and the ionospheric location of the emissions. Like *Juno* , comparing to remote sensing data like *HST* provides the X-ray observations with vital magnetospheric context. An example of a *Chandra* - *HST* STIS comparison of the northern auroral region is shown in Figure 3.11 with the soft and hard X-rays identified with small and large green dots respectively. As the images are limited to $\sim$ 45 mins, timing analysis of the jovian HST data needs to be treated conservatively (e.g. to ensure that there are enough cycles of a

detected significant FUV pulsation throughout the observation) and to ensure that comparisons of temporal behaviour between wavelengths is carried out carefully and effectively.

Chapter 4

Chandra Observations of Jupiter's X-ray Auroral Emission during *Juno* Apojove 2017

"Like what you do, and then you will do your best"
- Katherine Johnson, NASA interview in 1966

Inspired by the completion of my first ever PhD study that made me enjoy my research.

4.1 Abstract

As discussed in Section 2.4, the jovian auroral X-rays have been observed and analysed for over 40 years with an unknown driver producing quasi-periodic emissions, the majority of which are concentrated into auroral "hot spots" at the poles. In this chapter we analyse a $\sim$ 10 hour *Chandra* observation from 18:56 on 18 June 2017. The research presented here uses a new Python pipeline (Weigt, 2021), adapted from previous routines used by Gladstone et al. (2002) and Elsner et al. (2005), to analyse the auroral morphology. We also use the timing analysis methods used by Jackman et al. (2018) by incorporating Rayleigh testing, as discussed in Section 2.4.5, with significance testing via Monte Carlo simulations. To infer the conditions of the magnetosphere during this time, we use *in situ Juno* data. Here, the jovian magnetosphere was found to be compressed during the *Chandra* interval. At this time, *Juno* was near its apojove position at a radial distance of $\sim$ 112 R_J from Jupiter, situated on the dawn flank of the magnetosphere heading inbound. *Juno* was near the nominal, or average compressed, magnetopause position as found from the Joy et al.

(2002) model. In this chapter we present new dynamical polar plots showing, for the first time, an extended X-ray "hot spot" in the northern auroral region traversing across the jovian disk as it rotates into view. The results of our mapping allowed us to set a numerical threshold of > 7 photons per 5° System III longitude $\times$ 5° latitude, over $\sim$ a jovian rotation, to define a threshold to allow us to locate and analyse the brightest and most concentrated northern auroral X-ray emissions within the "hot spot". This criterion is used for the remainder of the research presented here. The results of our timing analysis reveal two significant quasi-periodic oscillations (QPOs) in the northern emissions of $\sim$ 37 and $\sim$ 26 minutes, mapping to the dayside magnetopause boundary using the Vogt et al. (2011, 2015) flux equivalence mapping model. There were no significant QPOs in the southern emissions during this time. This chapter will discuss in detail the interpretation of these results to find the potential driver(s) of the X-ray auroral emissions in context of these results.

4.2 Introduction

Section 2.4 examined in great detail the theories and mechanisms behind X-ray auroral production. In this chapter we focus on the morphology, location and pulsations of the soft X-rays (SXRs, photon energy < 2 keV), produced from charge exchange (CX) processes between various precipitating ion species and neutrals in the jovian atmosphere (Cravens et al., 1995; Bhardwaj and Gladstone, 2000; Branduardi-Raymont et al., 2008). The heavy ion precipitation needed for these SXRs can occur either on open field lines connected to the solar wind (i.e. an external source) or on closed field lines mapping to the outer magnetosphere (i.e. an internal plasma source, such as iogenic ions) (Cravens et al., 2003). The CX process on either types of field lines requires strong field-aligned electric fields, capable of producing potentials of $\sim$ 200 kV - 8 MV between the ionosphere and the magnetosphere.

As examined in Section 2.4, the SXRs are found to mainly concentrate in a so-called "hot spot" of emissions near both poles. Each "hot spot" has been observed to emit auroral X-ray emissions with a total power of 1 GW to a few GW and have been observed to exhibit quasi-periodic pulsations during several intervals (e.g., Gladstone et al., 2002; Elsner et al., 2005; Kimura et al., 2016; Dunn et al., 2016, 2017; Jackman et al., 2018). A recent study by Houston et al. (2020) using updated ion models and *in situ* data from *Juno* found that the very energetic precipitating heavy ions (up to $\sim$ few MeV and above in some cases) used in the CX process for SXR production in this region are likely responsible for large proportion of the total X-ray auroral power emitted. As discussed in Section 2.4.3, there have been very few studies and observations focusing on the southern X-ray auroral emissions due to a combination of the viewing geometry of the emissions themselves and the tilt of the planet, as

viewed from Earth, making for unfavourable viewing conditions. Ozak et al. (2010) also noted that, from their extensive modelling of the precipitation of iogenic ions (O and S) at high latitudes fitted to observations, the opacity of the jovian atmosphere may also block outgoing X-rays. Therefore a highly opaque atmosphere coupled with poor viewing geometry will drastically reduce the intensity of the X-rays observed.

The true origin of the SXRs and where they map to in the magnetosphere are also under debate. Previous studies have found X-ray observations where internally driven processes dominate the production of the X-rays (detections of S^{+}, O^{+} and O^{++} from Io flux tubes) and times where the solar wind ions (detections of lighter ions such as carbon) dominate (e.g., Elsner et al., 2005; Branduardi-Raymont et al., 2007a; Dunn et al., 2016; Kimura et al., 2016). A concurrent *XMM-Newton* observation which overlapped with the latter 5 hours of this *Chandra* interval found that the ions were iogenic of nature and therefore most likely internally driven (Wibisono et al., 2020).

Prior studies to our analysis here were looking at observations pre-*Juno* and relied on propagation model to infer the solar wind conditions from Earth-based data in an attempt to infer the driver. As discussed in Chapter 3, we can utilise *Juno in situ* auroral high energy electron and ion data in concert with X-ray observations to help determine the state of the magnetosphere without the need of propagation models which may be highly dependant on the alignment of Jupiter, Sun and Earth. The *in situ* may also help identify the source of the SXRs and therefore the variations we observe. In this chapter, we utilise data from the Jovian Auroral Distributions Experiment (JADE) (McComas et al., 2017) and the Jupiter Energetic Particle Detector Instrument (JEDI) (Mauk et al., 2017) on board *Juno* (Bolton et al., 2017) [details in Chapter 3] to search for magnetopause crossings over a 5 day period, bracketing the *Chandra* interval (Ebert et al., 2017a; McComas et al., 2017; Mauk et al., 2019). The position of these crossings are then used in the Joy et al. (2002) (as described in Section 2.1.1) model to infer a dynamic pressure of the magnetosphere during the observation window, without acquiring large errors on the solar wind parameters that can occur when using propagation models. The errors in the propagation models depend on the Jupiter-Sun-Earth angle and can be up to a few days. We do note however that the method we use here to infer the state of the magnetosphere is very dependant on the location of *Juno* within the jovian system (i.e. need to be close to a boundary in the magnetosphere to identify a potential crossing).

As well as using magnetopause crossings in this research, we take full advantage of he unique polar orbit of *Juno*. This highly eccentric orbit (see Chapter 3) can allow many different magnetospheric processes and auroral drivers to be explored in one orbit, when the instruments are operational, to allows us to get a full picture of the solar wind-ionosphere-magnetosphere coupling at Jupiter. When *Juno* is at or near perijove *Juno* (closest to the planet in its orbit), the main focus of the science payload is to

observe in detail the various processes that produce the auroral emissions, turbulent storms and other phenomena at the poles as *Juno* directly traverses the magnetic field lines along which auroral currents flow. At apojove (furthest from the planet in its orbit) in the early part of the mission, *Juno* is located near the nominal magnetopause position at the dawn flank, allowing likely auroral drivers such as Kelvin-Helmholtz instability (KHI), magnetopause reconnection (Ebert et al., 2017a) and possible cusp reconnection, depending on the local time of *Juno*, (Bunce et al., 2004) to be analysed in greater detail.

As we examined in Chapter 3, the high spatial resolution of *Chandra* combined with the time-tagged nature of the X-ray photon data enable us to spatially select hot spots and study any quasi-periodic oscillations (QPOs) in the X-ray emission. There have been many theories regarding the source of the QPOs in the auroral emissions at different locations in the jovian magnetosphere (e.g., Gladstone et al., 2002; Bunce et al., 2004), as discussed in Section 2.4 in greater detail, with no subsequent observations of the significant $\sim$ 45-min period reported by Gladstone et al. (2002) with the discovery of the northern "hot spot". Rather, a large statistical study by Jackman et al. (2018), and one presented in Chapter 5 (Weigt et al., 2021a) using updated datasets and definitions of the X-ray auroral emissions, found that statistically significant QPOs are relatively rare in the jovian X-ray data, and, where present, periods can differ from observation-to-observation. In some cases, the QPOs can change on timescales less than a Jovian rotation. Dunn et al. (2017) observed that the North and South hot spots can exhibit non-conjugate behaviour and can pulsate independently from each other, during one of the very intervals that both the northern and southern emissions were clearly in view. Chapter 5 identifies a clear spatial dependence of the QPOs within the northern auroral emissions, when analysing the entire *Chandra* catalogue.

In Chapter 3, we discussed how we map the X-ray photons and re-register the brighter pulsating hot spot to its location within the jovian ionosphere in System III coordinates. We combine these results with the flux equivalence mapping model by Vogt et al. (2011, 2015) to map the hot spot emissions (and therefore any QPOs) to their origin within the magnetosphere. This model returns a local time (LT) and radial distance (within uncertainties) at which the ions, and therefore auroral driver, producing currents are thought to originate. Previous mapping attempts by Kimura et al. (2016) and Dunn et al. (2016, 2017) used the VIPAL (Hess et al., 2011a) and Grodent Anomaly (Grodent et al., 2008) field models respectively with the Vogt et al. (2011, 2015) flux equivalence model. In this chapter, we update this mapping with the JRM09 internal magnetic field model, which utilises the *Juno* magnetometer data to improve upon previous models (Connerney et al., 2018). The mapping techniques from both *Chandra* (see Chapter 3) and the magnetospheric mapping model allow us to try and constrain the origin of the X-rays found in Jupiter's pulsating hot spot.

In Section 4.3, we briefly discuss the location of *Juno* during the *Chandra* interval and any other concurrent observing campaigns. The datasets used for this study and Python pipeline used to analyse the *Chandra* data obtained are examined in Chapter 3. Section 4.4 discusses the morphology of the X-ray emissions, the definition of the hot spot, and the timing analysis of the pulsating emissions. Furthermore, the X-rays are mapped using the flux equivalence mapping model by Vogt et al. (2011, 2015), using *Juno* magnetopause crossings from JADE and JEDI, with the latest JRM09 magnetic field model (Connerney et al., 2018) to attempt to isolate the location of their source. Section 4.5 contains a discussion and interpretation of the results.

4.3 Chandra HRC-I observation window

Chandra observed on 18 June 2017 for $\sim$ 10 hours ($\sim$ 1 Jupiter rotation) when *Juno* was close to apojove at $\sim$ 111 R_J on the dawn flank, close to the nominal location of Jupiter's magnetopause. Data from *Chandra* HRC-I are analysed in this study. An *XMM-Newton* observation lasting $\sim$ 24 hours in total and overlapped with the final 5 hours of the *Chandra* observation. Recent findings from this study are in Wibisono et al. (2020). The *Nuclear Spectroscopic Telescope Array (NuSTAR)* also observed Jupiter during this time taking full advantage of *Juno*'s apojove position (Mori et al., 2022). A *Hubble Space Telescope (HST)* observation of the ultraviolet (UV) auroral emissions was taken a few hours before the Chandra interval, as discussed further in Grodent et al. (2018) and Chapter 6.

4.4 Results

4.4.1 Auroral X-ray morphology

Using the pipeline by Weigt (2021) discussed in Chapter 3 to map the auroral X-rays, polar plots were produced to examine the morphology of the auroral X-rays and properties of the hot spot in detail. Figure 4.1 shows (a) the North and (b) South pole, as viewed from above the pole, over an interval of $\sim$ 10 hours from 18:56 on 18 June 2017 to 19 June 2017 05:15. *Chandra* observed a total of 2883 photons from Jupiter with 342 photons detected from the North pole and 180 from the South. The counts at the poles were isolated by a region defined in SAOImageDS9 (Joye and Mandel, 2003) and spatially select regions of the concentrated X-ray emissions. Assuming a photon energy of $\sim$ 0.5 keV (halfway between the sulphur and oxygen emission lines), the auroral power of the northern and southern X-ray emissions were calculated to be $\sim$ 2.6 and 0.7 GW respectively. We exclude the remaining disk counts as this is not the focus of this research. We note that although Jupiter's disk occults X-ray sources and

therefore the any disk emissions are likely real, with the increased gain degradation of HRC (see Chapter 3) the disk emissions are likely to be just a above background. Future studies into the disk emissions will need to account for this effect.

Like previous studies, we find the northern X-ray auroral region to be more intense than its southern counterpart (Dunn et al., 2017; Jackman et al., 2018), over the 0.08 - 10 keV photon energy range of *Chandra* HRC-I. Similar to that found in previous literature, the majority of auroral X-ray emission was found to be localised into a "hot spot" (e.g., Gladstone et al., 2002; Branduardi-Raymont et al., 2004, 2008; Dunn et al., 2016, 2017). However unlike previous studies, the morphology of the northern hot spot X-ray emissions during this interval is found to be more extended poleward in the North at $\sim$160° - 190° S3 longitude and $\sim$ 57° - 76° latitude, using a numerical threshold for photon concentration to find the location of the more intense emissions.

Due to the rotation of the planet, the northern and more diffuse southern X-ray hot spots are observed to traverse the jovian disk when they rotate into view of *Chandra* HRC-I. The soft X-ray (SXR) auroral emissions SXRs from the hot spots are found to be more concentrated in a particular joviographic longitude region. The highest concentrations of X-ray are found in the hot spot regions as shown by the colour bar giving the values of intensity (in units of Rayleighs (R)) with the brightest emissions shown in bright green. Figure 4.2 shows the evolution of the morphology of the northern X-ray emissions over the full *Chandra* observation, split into six $\sim$ 60° sub-solar longitude (SSL) intervals. Each interval has a duration of $\sim$100 minutes. The brighter X-ray region appears in the *Chandra* observations as shown in Figure 4.2a), (b) and (f). All of these intervals show the presence of the extended hot spot emission in the northern auroral region (as highlighted in Figure 4.1a)). When the hot spot rotates fully into view, the majority of the photons detected are found in this region as expected. As shown in the colour bar, the blank white regions on both Figures 4.2 and 4.5 illustrate the regions where *Chandra* observed little-to-no X-ray emissions during this interval. The brightness calculated from the point spread function (PSF) in Figures 4.2 and 4.5, as described in Chapter 3, appears as streaks of emissions on the polar plot. This is because the longitude of the observer (or central meridian longitudes (CML), in this case *Chandra* , changes as Jupiter rotates. This causes the the emissions to "move" across the disk. This effect is highlighted by applying the polar coordinate transformation to the PSF wrapped around Jupiter itself. Such effects are again enhanced in the X-ray emission detected away from the chip's centre, or aim point of the detector. Using the SSL from Earth to Jupiter[1] and the hot spot location found from Figures 4.1a and 4.2, we expect the extended northern auroral emissions to be in view with CML of 60° - 290° (taking $\pm$ 90° to the S3 longitude of the hot spot). The time at which this CML range occurs during the *Chandra* observation is found

[1] from JPL Horizons `https://ssd.jpl.nasa.gov/`

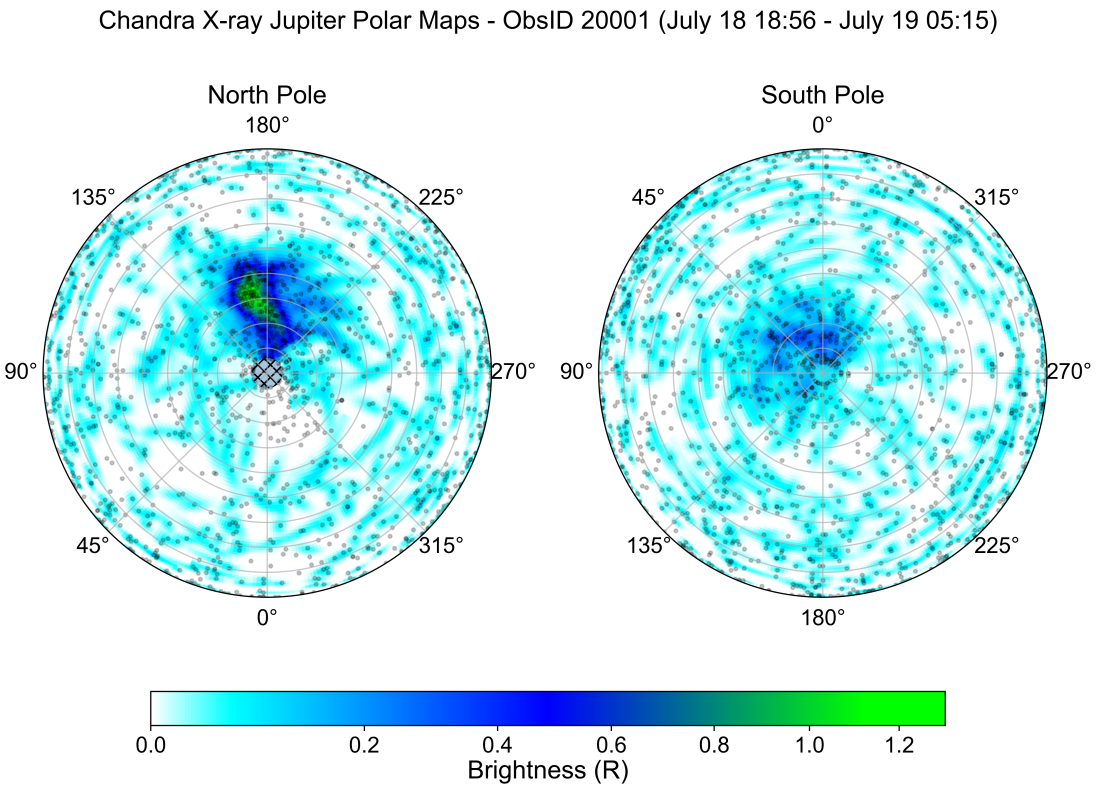

FIGURE 4.1: Planetocentric polar projections of X-ray emissions at an altitude of 400 km above the 1-bar atmosphere of (a) Jupiter's north and (b) south poles as viewed from directly above each pole. The azimuthal angle (represented in joviographic longitude) within the polar plot (in degrees) is labelled around the polar plot. The concentric circles represent 10° latitude increments. The black dots show the location of individual X-ray photons as detected by the *Chandra* -HRC instrument. The brightness of the X-ray emissions is proportional to the photon flux (calculated from the point spread function (PSF)) and is denoted by the colour bar below in units of Rayleighs (R). The areas of the poles which have little to no X-ray emissions are shown in white. Regions out of *Chandra* 's field of view for the full observation window are denoted by the cross-hatched area. Photons over plotted onto regions of no X-ray emission result from photons detected on the limb of Jupiter, resulting in larger errors in position. As these photons are usually observed off-centre on the chip, the positions are difficult to trace back accurately. Figure taken from Figure 1 in Weigt et al. (2020).

from JPL Horizons and is then compared to the intervals shown in Figure 4.2. We therefore find that the hot spot should traverse the disk over a period of $\sim$ 320 mins.

Examining the distribution of photons in Figure 4.1a, we set a threshold of > 7 photons per 5° S3 lon $\times$ 5° lat over $\sim$ 1 jovian rotation to define the more concentrated X-rays in the northern auroral region, including those in the hot spot. We use this threshold for the remainder of this research. We count that photons that lie on the boundary and found to lie within this area (Figure 4.3). This threshold is determined from counting the number of photons within the more concentrated emissions in the X-ray hot spot from previous *Chandra* studies (hot spot locations for Gladstone et al. (2002) $\sim$160° - 180° S3 longitude, $\sim$ 57° - 76° latitude and Dunn et al. (2017) $\sim$155° -

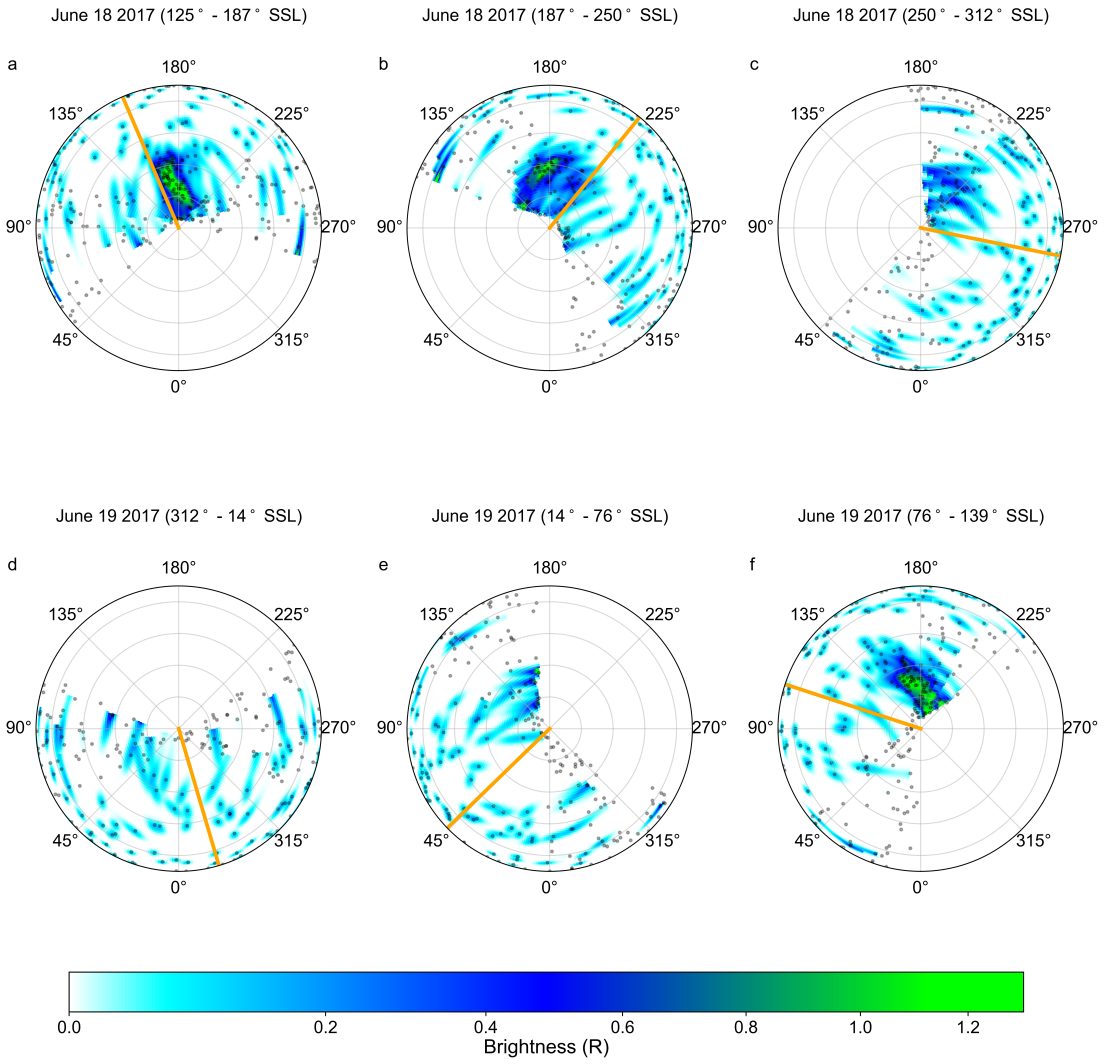

FIGURE 4.2: The full ∼ 10 hour observation of the northern emissions spli into 6 equal ∼ 60° sub-solar longitude (SSL) intervals (each corresponding to ∼ 100 mins of the observation), in a similar format to Figure 4.1a. The SSL midway through each ∼ 100-min interval is indicated by the orange line. The concentric circles represent 20° latitude increments. The northern hot spot emissions are observed in intervals (a), (b) and (f). Figure taken from Figure 2 in Weigt et al. (2020).

180° S3 longitude, ∼ 60° - 75° latitude). The position and density of the photons observed within a 1° S3 lon ×1° lat region from the numerical threshold are also plotted (Figure 4.4), allowing the number of photons to be found and finer structures within the hot spot region to be explored in more detail at higher resolution. Using such a numerical threshold also allows us to confirm the position and morphology of the extended hot spot as shown in Figure 4.1a). We remove any effects from double-counting of the photons lying on the boundary by plotting the positions using a 2D histogram as shown in Figures 4.3 and 4.4. It is clear that, although the X-ray region seems to appear in approximately the same location as found from previous studies, the morphology of the emitting region does not always resemble that of a

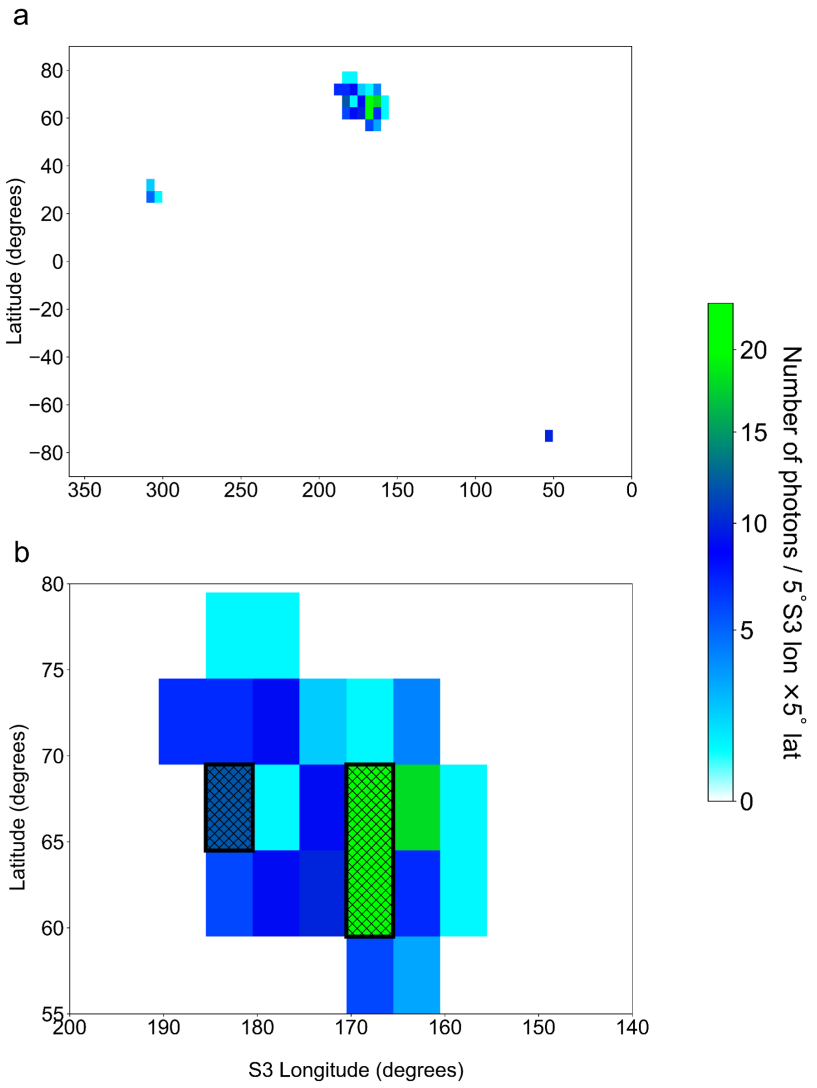

FIGURE 4.3: Cartesian plots of S3 longitude vs. latitude showing the position and number of photons per 5° S3 lon × 5° lat of the (a) full map and (b) the northern X-ray auroral region during the full *Chandra* observation. The threshold used for selecting the brighter X-ray aurora is defined by any emissions containing > 7 photons, using the HRC-I instrument, within an area of 5° × 5° or lying on this boundary. The colours here represent the number of photons within the region of X-ray emission defined by the threshold. (b) shows that the northern hot spot (depicted by the darker blue and green regions) is more extended than what was observed in previous studies (Gladstone et al., 2002; Dunn et al., 2017). The centres of two possible independently driven X-ray regions are highlighted by black cross-hatched rectangles. Figure adapted from Figure 3 in Weigt et al. (2020).

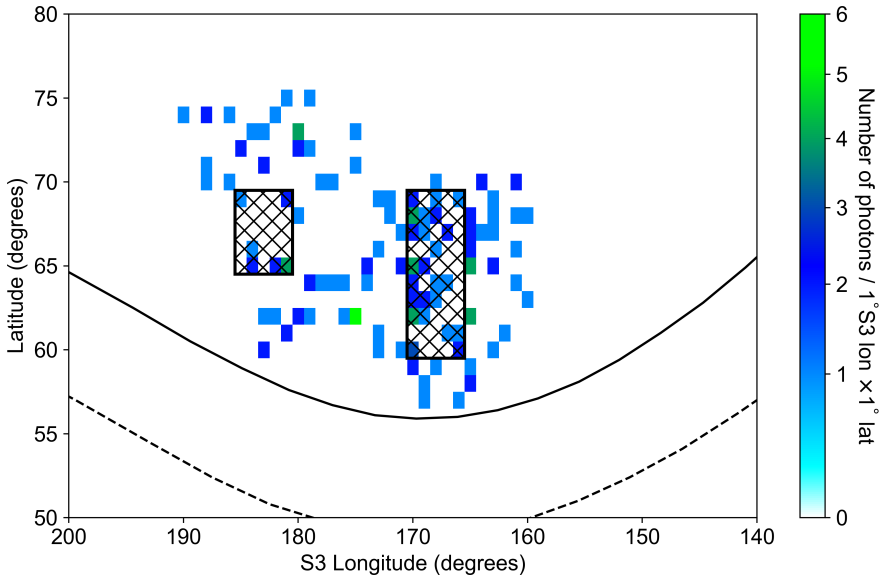

FIGURE 4.4: Identical format to Figure 4.3 highlighting the ionospheric position and number of photons per 1° S3 lon × 1° of the brighter northen X-ray emissions. The Io footprint (black dashed line) and main auroral oval (black solid line) are overplotted (Grodent et al., 2008) to apply context to the magnetospheric location of these emissions. The same threshold as used in Figure 4.3 is used here. The extended hot spot observed in both Figures 4.1 and 4.3 is still present when looking at the mapped data using a higher spatial resolution. Figure taken from Figure 4 in Weigt et al. (2020).

concentrated "spot" of emission. The morphology we observe here suggests that two possible independent X-ray sources may be driving the emissions, highlighted by two distinct regions within the auroral emissions of high photon concentration, separated by a low density boundary. The centres of both regions are highlighted in Figures 4.3 and 4.4 by a black cross-hatched rectangle. The peak concentration of the brighter X-ray source is 23 photons per 5° S3 lon × 5° lat with the centre of the second source ∼ a factor of 2 less dense at 12 photons per 5° S3 lon × 5° lat. This therefore suggests an extended region of X-ray emission may be a result of various or identical processes at different locations in the jovian atmosphere. In order to investigate the numerous X-ray hot spot hypothesis, future studies should perform forward modelling via simulations (e.g., Monte Carlo simulations) to determine what one versus numerous hot spots look like in *Chandra* data.

Figure 4.5 shows how the morphology of the southern auroral emissions evolve during the full *Chandra* observation, split into the same time intervals used in Figure 4.2. The southern X-ray emissions during this time are more diffuse and less intense than the North, resulting in no definitive "hot spot" observed by *Chandra* (as expected from Figure 4.1). Therefore an exact position (in S3 lon, lat) of the southern hot spot emissions could not be determined. The difference in intensity indicates that

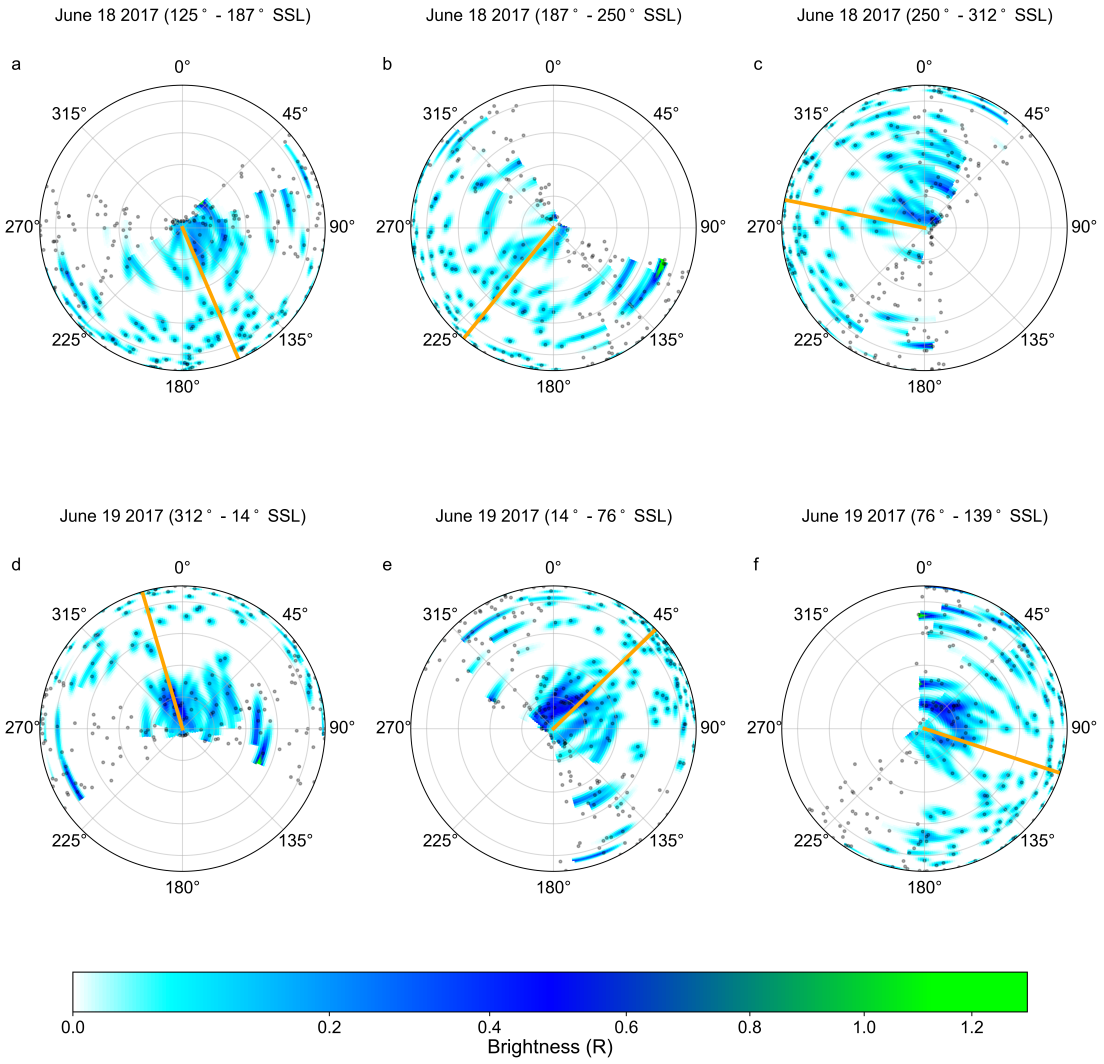

FIGURE 4.5: Identical format to Figure 4.6 except for the South pole. The more diffuse southern hot spot emissions are observed in panels (d), (e) and (f). Figure taken from Figure 5 in Weigt et al. (2020).

the North and South X-ray emission may originate from different locations and/or created by different mechanisms as found by previous studies (e.g., Dunn et al., 2017; Jackman et al., 2018). From the JRM09 magnetic field model by Connerney et al. (2018), in general the magnetic field in the South is found to be weaker and is more dipolar than the internal field at the North, that is more complex due to a magnetic anomaly (Grodent et al., 2008). Chapter 7 will discuss in more detail how the magnetic field may also contribute to the clear asymmetry in intensity. The brighter component of the diffuse hot spot detected by *Chandra* is shown in Figure 4.5d) - (f).

4.4.2 Rayleigh Test results

With the location and morphology of the hot spot identified for this interval, we use timing analysis to find any statistically significant periodic emission in the auroral X-rays. As mentioned in Section 4.4.1, during the $\sim$ 10 hour *Chandra* window on 18 and 19 June, the extended northern emissions rotated into view twice: once at the beginning (0 to 210 mins - North HS1, as labelled in Figure 4.6) and at the end of the interval (500 to 620 mins - North HS2). This is shown clearly from the light curve of the entire observation in Figure 4.6a) where flaring of the X-ray emissions are resolved by *Chandra* . Both intervals, of duration 210 and 120 minutes respectively, are shown in Figures 4.6d) - (f) and Figures 4.6g) - (i). We use a spatial down-select of S3 longitude 150° - 200° and latitude 55° - 80° for both intervals to isolate the photons associated with the extended hot spot region (Figures 4.3 and 4.4).

Figures 4.6a), (d) and (g) show the light curve of X-ray photons from the North polar region with 60s binning (i.e., splitting the time series into minute long observation windows), purely for presentation purposes and not used in the timing analysis. The quantised nature of the X-ray photons is shown clearly in the light curves with many time bins containing no photons at all. The periods where these 0 values occur are true non-detections made by *Chandra* and are not gaps in our dataset(see Jackman et al. (2018) for more details).

To account for the low photon count detected by *Chandra* , we use a Rayleigh test to perform our timing analysis on the X-ray auroral emissions to look for (quasi-)periodicities in the light curve. As discussed in Section 2.4.5 and Jackman et al. (2018), this method is ideal for a low count regime as it requires that the data are unbinned and can account for an irregularly sampled dataset (Brazier, 1994) (e.g. random detection times of time-tagged photons detected by *Chandra*). We believe this method is superior to Fast Fourier Transforms (FFTs) and Lomb-Scargle analysis used elsewhere in the field because it does not require any binning of the data (which can result in missing shorter periods). The Rayleigh technique is particularly suitable for a sparse count regime as we observe in jovian *Chandra* observations as well as on other planets such as Saturn (Chapter 7; Weigt et al. (2021b)) and Uranus (Dunn et al., 2021). The technique is described in greater detail in Section 2.4.5. The statistical significance of any quasi-periodic signals in the *Chandra* light curve can be evaluated when combined with Monte Carlo simulations. This allows us to estimate the likelihood of finding a maximum peak as observed from the data under the null hypothesis (no periodic signal). The Monte Carlo simulations used in this research consist of randomly shuffled fake light curves over the same time interval as the real data. We perform identical Rayleigh analysis on each light curve over the same frequency grid and is carried out for 10,000 different shuffled combinations. The Monte Carlo simulations take into account the fact we inspect many frequencies when searching for

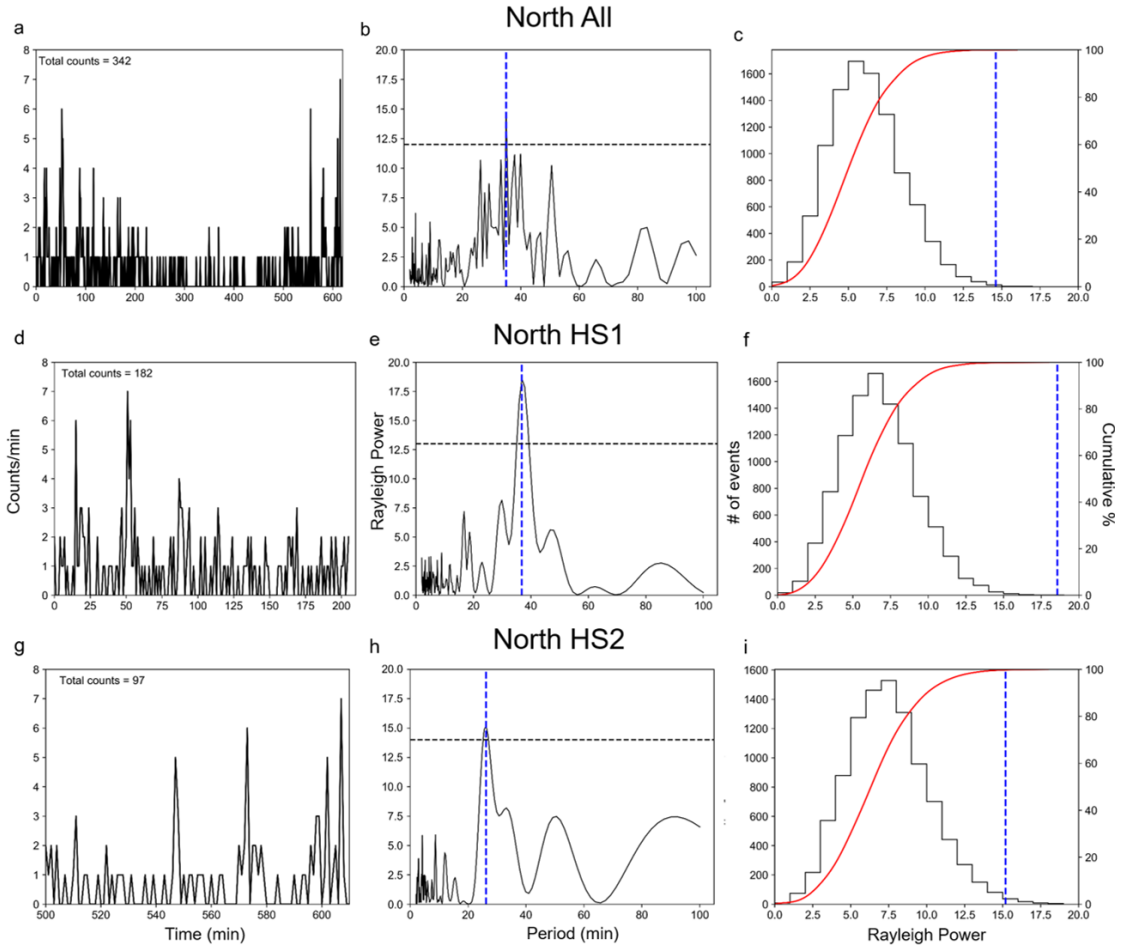

FIGURE 4.6: Results from the Rayleigh test performed on the full light curve [panels (a) to (c)], the first time the extended hot spot is in view [North HS1: panels (d) to (f)] and when it rotated into view again at the end of the *Chandra* interval [North HS2: panels (g) to (i)]. Panels (a), (d) and (g) show a 60-sec smoothed light curve, purely for presentation purposes and not used in our analysis, of time tagged photons in the Northern region of Jupiter from the full observation, North HS1 (0 to 210 mins) and North HS2 (500 to 620 mins) respectively. Panels (b), (e) and (h) show the resulting periodogram (power versus period) from the Rayleigh analysis applied to the light curve used for each interval. The peak power corresponding to the best quasi-period found is indicated by a vertical dashed blue line and the 99th percentile of the power from the 10,000 Monte Carlo simulations by a horizontal black dashed line. This definition is used for all panels shown here. The best periods are found to be $\sim$ 35 mins for the full light curve, $\sim$ 37 mins for HS1 and $\sim$ 26 mins for HS2. Panels (c), (f) and (i) display a histogram of the maximum powers from the Rayleigh analysis of 10,000 light curves generated from the Monte Carlo simulation based on the original input data, randomly shuffled. The solid red line shows the cumulative probability distribution of the maximum powers found from the Rayleigh test. We used an identical Rayleigh test for each region of the light curve (i.e. all assumptions about the frequency grid, number of steps etc. remained the same). Figure taken from Figure 6 in Weigt et al. (2020).

a statistically significant (quasi-)periodic signal. Figures 4.6b), (c), (e), (f), (h), and (i) show the results of the Rayleigh analysis with the Monte Carlo simulations.

Figures 4.6 b), (e) and (h) show the resulting periodogram of the Rayleigh power versus period. The best quasi-period from the light curves and their associated power is indicated by a blue dashed vertical lines. The frequency grid used for the periodogram consist of 150 logarithmically spaced out frequencies and corresponds to a period range between 2 and 100 min. From the *Chandra* observation window and based on the results of previous statistical surveys (e.g., Jackman et al., 2018), we might expect to find frequencies corresponding to periods of ∼8 to ∼46-mins. The logarithmic frequency grid we use in this study ensures that any peaks found in this range will be well defined.

Figures 4.6c), (f) and (i) show histograms generated from our timing analysis of the maximum Rayleigh power found from each of the 10,000 Monte Carlo simulations as a Poisson distribution. The corresponding power from the most significant period is plotted as a vertical dashed-blue line. The cumulative distribution of the histograms is shown by the overlaid red curve. The position of the dashed blue line with respect to the red cumulative distribution curve in these panels shows where the highest power from the *Chandra* input data would lie on any random distribution of photons. The 99th percentile of the 10,000 Monte Carlo simulations is depicted as a horizontal black dashed line in the figures and any quasi-periods detected above this line are considered significant in this research. We use such a strict threshold to compensate for the low count regime of our data. When there are multiple peaks above this 99th percentile (as demonstrated in Figures 4.6 b), the analysis considers the peak with the highest Rayleigh power to be the best (quasi-)period for the interval.

From our Rayleigh analysis of the full light curve (Figures 4.6a) - (c)), we observe a 99.94% significant (p-value 0.0006 or 6 out of 10,000 results from test greater than peak power) quasi-period of $\sim$ 35 min. The light curve (Figure 4.6a) shows that there are pulses from the full light curve when the northern emissions rotate into view. Figure 4.6b shows that there are multiple peaks in the periodogram above the 99th percentile line, indicating the possibility of quasi-pulsations within the signal.

Figures 4.6d) - (f) show the light curve and our Rayleigh analysis for the first 210 mins of the *Chandra* observation (North HS1). The periodogram (Figure 4.6e) shows that a best period of $\sim$ 37 min is found from the North HS1 light curve with a significance of 99.98% (p-value 0.0002 or 2 out of 10,000 results from test greater than peak power). This peak is found to be the only one to extend beyond the threshold. Figures 4.6g) - (i) show the light curve and Rayleigh analysis for the final 120 mins of the interval (North HS2). The periodogram (Figure 4.6h) shows that we find a best period of $\sim$ 26 mins during this interval and is the only one to again extend beyond our threshold. The highest Rayleigh power from both North HS1 and HS2 is far above what we

would typically expect from analysing any random distribution of photons (as shown in Figures 4.6f) and (i)). Therefore, for this *Chandra* observation, we identify two significant best periods for QPOs over a timescale less than a Jupiter rotation. Jackman et al. (2018) found from their large statistical heritage study only one other *Chandra* observation ($\sim$ 11 hour observation from 08:18 8 April 2014) had two significant QPOs using the Rayleigh test but the pulsations were located in the southern hot spot emissions.

The multiple significant periods we find in this study may be a result of an amalgamation of multiple processes within the elongated northern emissions and changing magnetospheric conditions. We note that the significances calculated for both QPOs using the Rayleigh test do not take into account the red noise found in the light curve (as explained in Section 2.4.5). A process that generates a time series in which the periodogram has a significant power that can be fitted by a power-law index > 0 is known as coloured noise. Many colours of noise exist when processing signals however in astronomy, we talk about either white noise (where the periodogram shows no significant signal and the powers are well modelled by a power law index of 0), or red noise (where the power follows a power-law index > 0). It is important to quantify the contribution of the red noise to any power spectra to ensure the real significance of a signal is found. To do this, one can normalise the power spectra by the true underlying spectra (i.e. the expectation value of the power spectra, see, e.g. Vaughan (2005)). For the intervals considered in this paper, the overall power-law index of the periodogram is ~ 0 through the whole frequency range, and therefore red noise is not contaminating our QPO detections (see Jackman et al. (2018) for more details). The location of the origin of the pulsations found in this study is mapped out using the model created by Vogt et al. (2011) and the results are shown in Section 4.4.4.

To further improve and validate the significance of the QPOs found in our timing analysis, we tested the sensitivity of the light curve to frequency using a Jackknife test (Quenouille, 1949, 1956). This is carried out by removing a number of photons from the HS1 and HS2 light curves and running the Rayleigh test again on the modified light curve (Efron and Stein, 1981). All the power spectra are then plotted together and the distance between the minimum and maximum period is found. This provides an estimate of how sensitive the light curve is to frequency. As *Chandra* observes very few photons from Jupiter, the Jackknife test used in this study removed 3 photons each time, ensuring no degeneracy from the selection process. The test for HS1 and HS2 found the time between the lowest and highest best period to be $\Delta P = 0.9809$ and 1.3765 min respectively. For both HS1 and HS2, $> 10^7$ power spectra are generated using the Jackknife test. This small shift in period over this many trials shows that the derived QPO frequencies are quite robust. There was a $\sim$ 5 hour overlap with *XMM-Newton* from June 19 $\sim$ 00:20 - 05:15 where QPOs can be compared. During this interval, *XMM-Newton* found the same QPO at $\sim$ 28 mins further increasing our

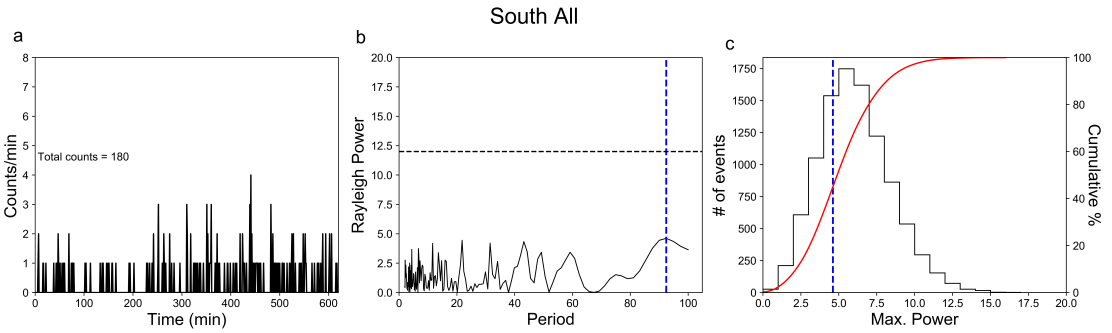

FIGURE 4.7: Our timing analysis for the southern auroral region, using the same Rayleigh test and format as shown in Figure 4.6. Figure taken from Figure 7 in Weigt et al. (2020).

confidence in the significant HS2 signal detected by *Chandra* . *XMM-Newton* continued observing for $\sim$ 16 hours after *Chandra* , and examination of the light curve from that time interval indicates the same QPO is still present for another full rotation (Wibisono et al., 2020). Performing the Rayleigh test discussed in this study on the full *XMM-Newton* light curve, we find a 99.92 % significant $\sim$ 28-min QPO.

Figure 4.7 shows the light curve and results from the same Rayleigh test used to analyse the southern region. As shown in Figure 4.7b, the best quasi period found from the full light curve of the southern region is $\sim$ 92 mins and had a significance of 24.30% (p-value 0.7570 or 7570 out of 10,000 results from test greater than peak power). The large p-values found in the southern region demonstrate that the best periods found from the Rayleigh test are not significant. This is further illustrated in Figure 4.7c, which compares the highest power found with the red cumulative distribution curve. The best period with the highest power from the southern X-ray auroral emissions lie near the peak of what we would typically expect from a random distribution of photons. This therefore suggests that this is not a significant signal and, unlike the northern extended hot spot, there are no significant quasi periods found during the observation.

4.4.3 Accompanying *in situ Juno* data

Around the time of the *Chandra* observation analysed in this research, *Juno* was executing a series of orbits which took its apojove position to $\sim$ 112 R_J on the dawn flank of the jovian magnetosphere, near the nominal magnetopause position. As previously discussed, this allows possible auroral drivers like KHI and magnetopause reconnection to be explored in greater detail. Figure 4.8 shows the JADE data over a 5 day period bracketing the *Chandra* interval. The top panel shows data from the time-of-flight (TOF) mass spectrometer of the ion populations surrounding *Juno* during this interval. The middle panel shows the corresponding electron

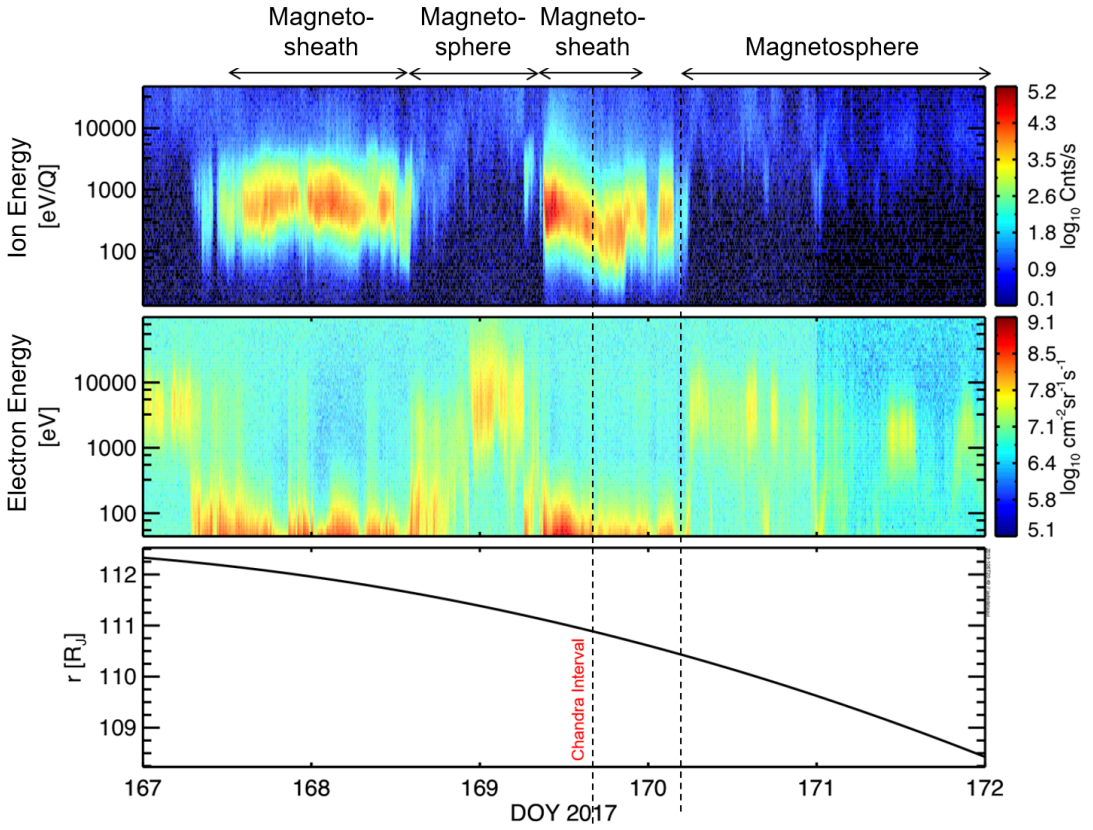

FIGURE 4.8: *Juno* data displayed as spectrograms of the ion time-of-flight (TOF) and electron data taken by JADE. These observations were taken over 5 days while inbound from the apojove position of *Juno*. The top panel shows ion data from the various plasma populations as *Juno* was sampling the magnetosheath and magnetosphere. The middle panel shows the associated electron distributions during this time. The bottom panel confirms the radial distance of *Juno* as it travels towards Jupiter during the 5-day interval. We highlight the *Chandra* interval by vertical dashed lines, corrected for light travel time. The colour bars used in the spectrograms show the count rates (and therefore energy flux) of the electrons and ions detected during this time. The key magnetospheric regions *Juno* flew through during these 5 days are labelled and represented by arrows above the plot. Figure taken from Figure 8 in Weigt et al. (2020).

distributions. The colour bars in both plots represent the count rates (which is proportional to energy flux) for both the electrons and ions detected. The bottom panel shows the radial distance of *Juno* from Jupiter during the observation, in units of Jupiter radii. Arrows at the top of the plot show the region (e.g. magnetosphere, magnetosheath) which *Juno* was sampling at a given time with the *Chandra* observation interval highlighted by dashed vertical lines.

From the JADE data, we define a magnetopause crossing as a steep change in density (or intensity) of the ion plasma population when *Juno* crosses from a region of colder, dense plasma (magnetosheath) to one of hotter, less dense plasma (magnetosphere) and vice versa. In between both regions, *Juno* may cross the boundary layer which looks like a combination of both plasma populations. Figure 4.8 shows that, while

Juno was inbound (heading towards the planet) from apojove, there are several magnetopause crossings prior to the *Chandra* interval. *Juno* was found to cross from the magnetosphere to the magnetopause at $\sim$ 14:30 on day of year (DOY) 167 (16 June) and crossed back into the magnetosphere region at $\sim$ 14:00 on DOY 168. Another crossing out into the magnetosheath was detected by JADE at $\sim$ 09:00 on DOY 169 (18 June), and thereafter *Juno* was found to be in the magnetosheath until nearer the end of the *Chandra* observation window. We also observe a short crossing into the magnetosphere between $\sim$ 00:00 and $\sim$ 01:00 on day 170 within the *Chandra* interval. *Juno* crossed back into the magnetosphere $\sim$ 03:30 with no further crossings detected during the 5 day window. The magnetopause crossings are verified using other *Juno* data in Chapter 6. We also analyse JEDI data during this observation window and found magnetopause crossings at identical times to JADE, confirm the approximate timeline of these events.

With the position of the magnetopause crossing, we use the Joy et al. (2002) model to infer the state of the magnetosphere during the observation window. This particular model is used to find the most probable sub-solar standoff position (as examined in Section 2.1) of the magnetopause boundary. As explained in Section 2.1.1, the Joy et al. (2002) magnetopause and bow shock model provides us with the necessary tools to infer the dynamic pressure of the solar wind upstream of Jupiter and therefore the sub-solar standoff distance from the location of any crossing of the magnetopause boundary. The model uses a combination of multiple spacecraft observations with magnetopause encounters and magnetohydrodynamics (MHD) simulation to predict the most probable position of the magnetopause boundary. More details of the Joy et al. (2002) model are found in Section 2.1.1. Using the closest magnetopause crossing from the JADE data ($\sim$ 111 R_J, 4.4 LT), the Joy et al. (2002) model inferred that the dynamic pressure of the solar wind, P_{dyn}, during this time (DOY 170, $\sim$ 03:00) was 0.319 nPa and the sub-solar stand-off distance, R_{MP}, was 62.52 R_J. Comparing these inferred solar wind parameters to distributions of the solar wind upstream from Jupiter from Jackman and Arridge (2011) and Ebert et al. (2014), shows that the magnetosphere during this time was in a state of compression, well above the 90th percentile of previously observed solar wind dynamic pressures.

4.4.4 Vogt mapping results

To map where in the magnetosphere the hot spot photons and therefore the QPOs originate, the ionospheric position (S3 longitude and latitude) and sub-solar longitude (SSL) of the time-tagged hot spot photons (found using the Weigt (2021) pipeline) are used in a flux equivalence mapping model created by Vogt et al. (2011, 2015) [herein also referred to as the Vogt model, both used interchangeably].

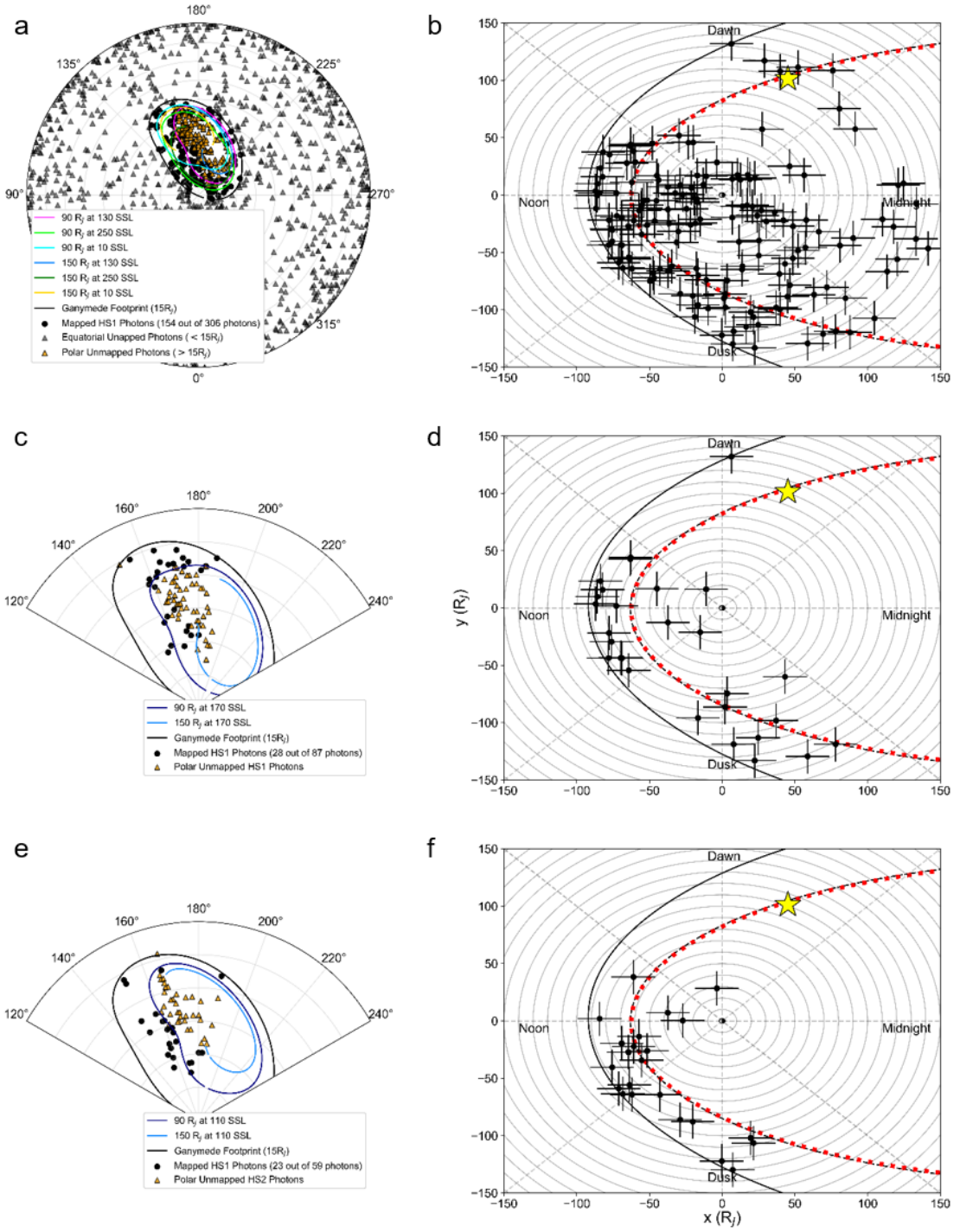

(Caption on next page)

FIGURE 4.9: Planetocentric polar projections of Jupiter's North pole for (a) all auroral photons during the full observation and those associated with the hot spot emissions from (c) HS1 and (e) HS2, as defined in the text. The magnetospheric mapping of the auroral photons in each case are determined from the Vogt et al. (2011, 2015) model shown in panels (b), (d) and (f). Error bars of 15 R_J are used to depict the likely error of the flux equivalence model under compressed magnetospheric conditions. The 15 R_J (black oval), 90 R_J and 150 R_J of the flux equivalence model applied with the JRM09 internal field (Connerney et al., 2018) are plotted in (a), (c) and (e) at various sub-solar longitudes (SSL). Unmapped photons equatorward ($<$ 15 R_J) and poleward ($>$ 15 R_J) are denoted by black and orange triangles respectively. The different colours in panel (a) represent the 90 R_J and 150 R_J contours of various SSLs observed throughout the interval. (c) and (e) show the 90 R_J (navy line) and 150 R_J (light blue line) contours midway through the interval. The location of *Juno* is denoted by the yellow star. The concentric ellipses in (b), (d) and (f) represent the distance form Jupiter in 10 R_J increments. The sub-solar standoff distance inferred from the Joy et al. (2002) magnetospheric model from the *Juno* magnetopause crossings is plotted in red (at 62.52 R_J), as well as the compressed (black dashed line) and expanded boundary limits. Figure taken from Figure 9 in Weigt et al. (2020).

The Vogt model is built from *Galileo* data, and is valid from $\sim$ 15 R_J (Ganymede footprint) to $\sim$ 150 R_J (beyond which there were insufficient data to constrain the model in the jovian magnetotail). The Vogt model and its possible limitations are discussed in greater detail in Chapter 6 where it is used to a greater extent. Figure 4.9a shows the polar plot of both the mapped (black circles) and unmapped equatorial (black triangles) and auroral (orange triangles) photons over the full *Chandra* interval. Figure 4.9b illustrates the associated magnetospheric mappings using the flux equivalence model with the JRM09 field model (Connerney et al., 2018) for all mappable X-ray photons. Rows (c)-(d) and (e)-(f) are in a similar format for the intervals corresponding to the viewing of HS1 and HS2 respectively. The Ganymede footprint (15 R_J; black oval) is overplotted in Figures 4.9 a), (c) and (e). The coloured contours plotted in Figure 4.9 a) show how the magnetic field mapping of the 90 R_J and 150 R_J changes during the full *Chandra* observation at 120° SSL intervals from 130° to 10° SSL during approximately one jovian rotation. At the beginning of the observation (130° SSL), the dayside magnetosphere is on the right hand side of the polar plot and moves clockwise throughout the *Chandra* interval. Figures 4.9 c) and (e) show the position of the magnetic field mapping midway through the hot spot intervals (170° and 110° SSL respectively). As expected photons that have ionospheric positions equatorward of the Ganymede footprint are not mapped by the flux equivalence model. The 90 R_J and 150 R_J contours are indicated in navy and light blue, respectively. Contours mapping to 90 R_J in the equator and beyond are excluded as they correspond to locations in the magnetosphere beyond the Joy et al. (2002) expanded magnetopause limit. The photons shown in grey in Figure 4.9, which we refer to as "unmapped", map to radial distances in the magnetosphere that lie beyond the expanded Joy et al. (2002) magnetopause or the 150 R_J limit of the Vogt model. It is therefore likely that these ionospheric positions are on open field lines. Photons that

have ionospheric positions equatorward of the Ganymede footprint are not mapped by the flux equivalence model as they map to radial distances inside 15 R_J.

Figures 4.9 b), (d) and (f) show the positions of the mapped photons determined from the flux equivalence model within the jovian magnetosphere. The dynamic pressure inferred from the *Juno* magnetopause crossings is used to plot the position of the magnetopause during this time with an inferred sub-solar standoff distance of 62.52 R_J (shown by the red dotted line). Our inferred magnetopause boundary coincides with the sub-solar standoff distance limit in the Joy model for a compressed magnetosphere (0.306 nPa with sub-solar standoff distance $\sim$ 60 R_J: black dashed line). The Joy model limit of an expanded magnetosphere is represented by the solid black line (0.039 nPa with nose standoff distance $\sim$ 90 R_J). The approximate position of *Juno* during the *Chandra* interval is denoted by a yellow star.

Figure 4.9b shows the spread of the mapping throughout the magnetosphere ($\sim$ 50% auroral photons were mappable using the flux equivalence model). The Vogt flux calculation applies a fit to entire catalogue of *Galileo* data collected under all solar wind conditions. Therefore our mapping results represents an "average" magnetospheric state. In our analysis, we include any ionospheric points that map to the magnetospheric positions between the compressed and expanded Joy et al. (2002) magnetopause values (the black dashed and solid lines, respectively, in Figure 4.9). In this research, we interpret these points to map on closed field lines for an expanded magnetosphere/low solar wind dynamic pressure and on open field lines for a compressed magnetosphere/high solar wind dynamic pressure. As the model uses "averaged" solar wind conditions throughout the *Galileo* mission, the most likely state of the jovian magnetosphere throughout the majority of the *Galileo* campaign would be an expanded state or one returning to its equilibrium position. Therefore, the mapping in Figure 4.9 is probably not suited for the highly compressed conditions during the *Chandra* observation interval. As the Vogt model maps photons to points that lie exclusively within the magnetosphere (i.e., on closed field lines), we assume that the points in Figure 4.9 that lie outside the compressed magnetopause would probably actually map to a region near but inside the magnetopause if the compressed conditions were accounted for. From the mapping model however, we are unable to determine quantitatively whether the QPOs found lie on open or closed field lines.

As examined in Section 2.2, during intervals of high solar wind dynamic pressure, as was the case during these observations, we may expect the change in the magnetospheric field geometry to lead to a change in auroral mapping (e.g., Southwood and Kivelson, 2001; Cowley and Bunce, 2003a,b) during intervals of a highly compressed magnetosphere. Such an increase in the solar wind dynamic pressure has been observed to change Jupiter's magnetospheric magnetic field, sufficient enough to shift the auroral mapping of a given point in the magnetosphere

poleward by up to a few degrees (Vogt et al., 2019). Therefore, we estimate a 15 R_J uncertainty in the mapping of our X-ray photons (see Figure 4.9) to account for this effect using the arguments put forward by Vogt et al. (2019). We note that the error we calculate here is a simple estimate and does not include any uncertainties in local time and photon SSL that will affect the flux equivalence model. How the propagation of these errors affects the mapping during different magnetospheric states is yet to be determined.

Figures 4.9 d) and (f) show that the majority of mapped auroral photons, and therefore any associated auroral drivers, from the HS1 (28 out of 87 photons were mapped) and HS2 (23 out of 59 photons were mapped) intervals are found to originate in the noon-dusk magnetosphere, close to the magnetopause boundary within 90 R_J (within errors). The corresponding polar plots, panels (c) and (e), show that the majority of the unmapped photons are found to lie beyond the dayside magnetopause boundary. More specifically, this is the case when the SSL is between 100° and 200°, which occurs for the full HS1 interval and the latter part of the HS2 interval. This may suggest that the origin of some the X-ray emissions, hence many of the unmapped photons, lie on the magnetopause where flux is opened for a short period of time (McComas and Bagenal, 2007). The possibility of an open field line origin for the X-ray emissions is discussed further in Section 4.5. One caveat that supports this hypothesis is taken into account in our analysis: the Vogt model assumes "average" solar wind conditions from the *Galileo* mission, as mentioned before. Therefore many unmapped points close to the 90 R_J contour on the dayside magnetosphere may map to inside, or very close to, the magnetopause. Alternatively, many mapped photons found in this region may actually be on open field lines. At lower SSLs found at the beginning of the HS2 interval, 70° - 100° SSL, some of the unmapped photons are also found to lie on field lines on the nightside beyond 150 R_J. These field lines may be considered opened or closed however insufficient volume of data in this region makes verification of this difficult. The unmapped photons that are found firmly in the middle of the open field area we consider to most likely lie on open field lines. The photons producing the pulsations within the magnetosphere in both intervals are also found to lie in approximately the same locations. This further suggests that the photons responsible for the pulsations in HS1 and HS2 may be a result of a process happening near the dayside magnetopause that varies on timescales less than a Jupiter rotation. Panel (d) shows that the pulsations during the HS1 interval are slightly more spread throughout the magnetosphere than those observed during HS2 (panel (f)) with the pulses mapping to $\sim 11 - 22$ LT compared to the pulses originating mainly in the noon-dusk sector. The pulsations appear to map to spatially localised regions in the magnetosphere as shown by the clustering of mapped photons within the noon-dusk sector present in Figures 4.9 d) and (f).

4.5 Discussion

The results of this research analysing the $\sim$ 10 hour *Chandra* Jupiter observation on 18 June 2017, using a new Python pipeline (Weigt (2021), Chapter 3), reveal an interesting extended morphology of the northern hot spot that has not been studied in great detail before.

4.5.1 Morphology and temporal behaviour of the auroral emissions

The polar plots presented in this research show a clear asymmetry in brightness between the North and South pole. As examined in Section 2.4, Dunn et al. (2017) found that the morphology of the southern X-ray auroral emissions coupled with an unfavourable tilt angle of Jupiter, with respect to the sub-observer latitude, made it very difficult to analyse the South. During this *Chandra* interval however, the full southern region is mapped allowing for direct comparison with the North. The JRM09 magnetic field model (Connerney et al., 2018), derived from *Juno* magnetometer data (Connerney et al., 2017), revealed that the field in the North polar region is non-dipolar and more than twice as strong as the more dipole-like field in the South (Moore et al., 2018). This contrast in magnetic field strength and topology may be a contributing factor to the clear difference in brightness between the poles, as well as the diffuse nature of the X-ray emission observed from the South pole. The different magnetic field magnitude may inject ions into the Jovian ionosphere through a variety of mechanisms. It may be that the stronger magnetic field in the North leads to a stronger mirror force and therefore produces a larger potential drop, capable of accelerating ions to larger energies. Alternatively, it may be that the steeper magnetic field gradients in the North allow drifting particles to enter the loss cone. Given the location of the extended X-ray hot spot relative to the surface magnetic field configuration, we suggest that the former is more likely. Along with the contrast in brightness, the independent nature of the pulsations (observed here and in Dunn et al. (2017)) suggest the emission from the North and South may be from different processes or the same process triggered independently (from a possible time-lag) either side of the magnetopause boundary.

In this research, we find two significant QPOs in the light curve from the North pole when the elongated hot spot is in view (North HS1 and HS2) using a Rayleigh test. Using the same Rayleigh test for the South we found no significant QPOs during this time. As the viewing windows of the hot spot emissions are $\sim$ few hours, due to the location of the emissions, we do note that it is difficult to claim a true "quasi-period" with absolute certainty. This is because we can only observe 2 - 3 cycles of flaring activity during each interval. These flares will still rule out the null hypothesis of the Rayleigh test (that the signal is uniform). We therefore use the term QPO here, and

throughout the remainder of this research, more conservatively to define any significant quasi-pulsations (i.e., $> 99\%$ statistical significance) found within any observation intervals of the auroral X-ray emissions. This is a subtle problem which persists throughout the field of planetary science, and indeed in other areas of astrophysics. Chapter 8 highlights a few methods that can be employed to improve timing analysis in this field. In this particular case study, *XMM-Newton* found the same HS2 QPO simultaneously with *Chandra* improving the significances of our results, using the Rayleigh test and other timing analysis techniques (Wibisono et al., 2020). *XMM-Newton* continued to observe Jupiter for a further ~ 18 hours after the end of the *Chandra* campaign. This dataset is explored in detail in Wibisono et al. (2020). They note that Jupiter continued to pulse with a regular QPO for several Jupiter rotations after this observation, with the North and South exhibiting similar QPOs near the end of the campaign.

4.5.2 Potential sources of ultralow-frequency (ULF) waves

Previous studies looking at the hot spot region (Gladstone et al. (2002); Kimura et al. (2016); Dunn et al. (2016, 2017)) speculate that oscillations may arise from global ULF waves in the magnetic field. The periodic oscillations from ULF waves have been observed throughout the jovian magnetosphere. Manners et al. (2018) propose that all $\sim$ 10-60-min QPOs within the jovian magnetosphere may arise from standing Alfvén waves. This complements the work of Khurana and Kivelson (1989) and Wilson and Dougherty (2000a) who found 10-20-min ULF wave pulsations in the middle magnetosphere. The QPOs we identify here and those found in previous statistical studies (Jackman et al., 2018) lie within the 10-60-min range. This would apply to regions of closed field lines where Alfvénic resonances are present. We discuss potential sources of ULF waves in the regions of interest within the magnetosphere in the remainder of this section.

4.5.2.1 Kelvin Helmholtz Instablities (KHIs)

Dunn et al. (2017) suggest that Kelvin-Helmholtz instabilities (KHIs) observed at Jupiter's magnetopause boundary (Delamere and Bagenal, 2010; Desroche et al., 2012) may be one possible driver to explain the X-ray QPOs and the asymmetric brightening at the poles. The KHIs on a planet's magnetopause boundary allow large quantities of energy, momentum and plasma to be transferred between separate plasma media and may cause reconnection in the twisted field lines (Hasegawa et al., 2004). KHIs on Earth's magnetopause have been found to produce fluctuations in this region as well as compressional ultralow-frequency (ULF) oscillations and field line resonances (on closed field lines), driving standing Alfvén waves in the ionosphere (Mann et al., 2002;

Rae et al., 2005). Previous observations and simulations have found that KHIs often originate on the dawn and dusk flanks of the magnetosphere, where the velocity shear is largest. This has been found to be the case at both Earth and Saturn (Hasegawa et al., 2004; Wilson et al., 2012; Ma et al., 2015) and predominantly on the dusk side at Jupiter from simulations (Zhang et al., 2018). In this study, as shown in Figure 4.9, many of the photons which yield the QPOs are mapped to regions near, or within, the magnetopause boundary on the dusk flank of the magnetosphere. However, with the mapping model not optimised for very compressed magnetospheric conditions, distinguishing between the origin lying on open or closed field lines is difficult.

Dunn et al. (2017) found that the northern and southern X-ray hot spots are non-conjugate and exhibited different temporal behaviour. Using the Vogt mapping model, with a different field model, Dunn et al. (2017) also found that the majority of the northern X-ray photons map onto the dayside magnetopause boundary at noon-dusk. The southern X-ray emissions were found to map to the magnetopause boundary on the dawn-noon sector, indicating that the processes producing the QPOs at the poles may be independent of one another. One possible explanation for this difference in behaviour is rotationally driven magnetic reconnection on the dayside magnetodisk. Guo et al. (2018) report finding such a phenomenon in Saturn's dayside magnetodisk from Cassini charged particle and magnetometer data. This internally driven process could accelerate the high energy ions in the jovian system to the energies required for charge striping and charge exchange to produce the soft X-rays, which dominate the hot spot region. Electrons may also be accelerated via this process and may explain the flaring activity we observe in the aurora (in both X-ray and UV e.g. Bonfond et al. (2016)). Rotationally driven dayside reconnection and reconnection driven by KHIs on the dawn/dusk flanks occur at different local times along the dayside magnetopause boundary. This may be the answer to the observed non-conjugacy of the North and South emissions. For example, the length of the field line may be different for each hemisphere depending on the location of the reconnection site. This may therefore lead to a lagged response when the reconnection occurs, energising the charged particles to the energies required for precipitation.

4.5.2.2 Magnetic reconnection

For open field line regions within the magnetosheath, dawn/dusk flank reconnection may produce the pulsations we observe in the X-rays. The reconnection process in this region of the magnetosphere may be triggered by KHIs on the flank, producing possible field line resonances generating the QPOs we observe (Kimura et al., 2016; Dunn et al., 2016, 2017). Magnetic reconnection along the dawn flank of the magnetosphere has been reported before by Ebert et al. (2017a) where it plays a more significant role within a compressed magnetosphere (i.e. high solar wind dynamic

pressure). However as *Juno* was not on the dusk flank of the magnetosphere, signatures of magnetic reconnection during this time cannot be found. The cusp reconnection model by Bunce et al. (2004) provides a strong argument for the possible origin of strong X-ray emission with 40-50-min QPOs. The significant periods found in this study lie close to this temporal range (in particular the $\sim$ 37-min quasi period from HS1). The X-rays we observe here however only have a maximum brightness of a few Rayleighs (R) as opposed to $\sim$ kR magnitudes predicted by the cusp reconnection model. Therefore, cusp reconnection may provide an answer to the pulsations, estimating an upper limit for the X-ray auroral power and brightness. We observe the expected X-ray auroral power ($\sim$ few GW) predicted by Bunce et al. (2004), but our observed auroral brightness is inconsistent with their model. This inconsistency may be a result of us underestimating the auroral brightness due to the variable throughput of the *Chandra* HRC-I instrument and/or the atmosphere being highly opaque during the *Chandra* interval (Ozak et al., 2010), which is not accounted for in the 2D histograms. Furthermore, several authors argue that dayside reconnection is an ineffective magnetospheric driver within the jovian system (e.g., Delamere and Bagenal, 2010; Desroche et al., 2012; Masters, 2018).

The two different significant quasi periods in the North suggest that the process(es) that cause the flaring activity in the X-rays can change over a timescale less than one jovian rotation. Only a small number of X-ray observations are conducive to searching for variability in quasi-periodicity on the timescales of a few planetary rotations or less. From the Jackman et al. (2018) heritage study, one observation was found ($\sim$ 20 hour observation from 00:21 25th February 2003) where the cadence of the telescope observation allowed the northern and southern hot spots to be viewed separately on consecutive rotations. From the Rayleigh test, they found that the only significant QPO was when the northern hot spot was first in view at $\sim$ 33 mins. The second time the northern hot spot was in view, no significant quasi-periodic signal was found. They found that only one other example ($\sim$ 11 hour observation from 08:18 8th April 2014) exhibited different significant quasi periods in the South over a timescale less than one jovian rotation. Therefore our study is the first to analyse multiple significant QPOs in the northern hot spot, and the conditions for the driver to produce such emission may have been rarely observed. Jackman et al. (2018) also noted that very few of the identified QPOs from previous studies were actually statistically significant using the Rayleigh test.

The quickening of the pulsations during this observation may be a result of the changing conditions of the magnetosphere. If we consider ULF waves to be the source, the changing periodicity of the QPOs would be a result of the changing thickness of the plasma sheet (Manners et al., 2018). During a compression event (similar to that found in the *Juno* data preceding the *Chandra* interval), the plasma sheet is expected to thicken (Southwood and Kivelson, 2001) which in turn, will result in a longer QPO

dependent on the change of thickness (Manners et al., 2018). As the magnetosphere enters the recovery phases after the compression, the thickness of the plasma sheet decreases as does the period of the QPO. However, with the data we have, it is unclear how quickly the plasma will be ejected from the magnetotail to confirm this ULF wave process. The inverse is true if we consider the Bunce et al. (2004) reconnection model.

During a compression event, the field line that the MeV ions travel along into the ionosphere will become shorter, therefore reducing the Alfvén time and generating a quicker QPO. If we assume that the reconnection site is in the same local time along the magnetopause and that the magnetosphere is further compressed between both HS1 and HS2, this may also be an answer to the changing periodicity in this study. However, from the *Juno* JADE and JEDI data, we find the magnetosphere expanding between HS1 and HS2, ruling this mechanism out. From terrestrial observations, the orientation of the Interplanetary Magnetic Field (IMF) and latitude of the reconnection site can also change the topology of the magnetic field and can therefore change the periodicities produced by cusp reconnection processes (Gosling et al., 1990; Fuselier et al., 2012). This may be the case in this study however the limitations with our data prevent us from being able to give a clear answer of the location of possible reconnection sites, if any, close to the mapped photons in the dusk flank.

In the research presented here, we believe that the QPOs observed are more likely caused by ULF waves on the dusk flank of the magnetosphere, produced by possible KHIs. However it is unclear if this is true for all QPOs observed from the X-ray emission as this conclusion is based on one observation. Future work into determining the source of the pulsations may include a comparison between transit times during compression and expansion for both ULF waves and reconnection processes described by (Bunce et al., 2004). *Juno* is expected to be in the dusk sector from 2021, allowing these processes to be explored in detail on the dusk flank of the magnetosphere close to the possible mapped location of the driver we find in this study.

4.5.3 Location of potential drivers in the jovian magnetosphere

The significant number of unmapped photons in both intervals ($\sim$ 68% and $\sim$ 61% for HS1 and HS2 of hot spot photons respectively) may suggest the driver for the X-ray emissions, thus the QPOs, is located on open field lines in a region near but inside the magnetopause during a compression event (similar to Dunn et al. (2016)). This however does not provide an answer for the variability of the driver found in this study. Given the significant number of unmapped hot spot photons combined with the successfully mapped QPOs to the noon-dusk sector, and with *Juno* situated on the dawn flank of the magnetosphere during this time (where only a handful of photons have been mapped to with an error on radial distance due to compressed conditions,

as shown in Figure 4.9), this precludes us from being able to fully determine the auroral driver. If *Juno* 's trajectory was closer to the noon-dusk sector, where the vast majority of photons were mapped to, or crossed field lines connected to the polar position of the X-ray emissions, further analysis of the *in situ* energetic particle data would have been included in our study. The very energetic particles (up to MeV energies) found in the polar auroral region detected by *Juno* are believed to lie on possible open field lines (Ebert et al., 2017b), suggesting that some process producing (or accelerating) these particles must exist. However, some studies suggest that the opened flux may close rapidly under such magnetospheric conditions (McComas and Bagenal, 2007).

The possibility of the source lying along the open-closed field line boundary agrees with results from Dunn et al. (2016). They observed a significant $\sim$ 26-min QPO during the arrival of an interplanetary coronal mass ejection (ICME) at Jupiter (i.e. a compression event). The hot spot was found to be extended and an expansion occurred on field lines that mapped to the region where the magnetopause sub-solar standoff distance was found to move from 92 R_J to 63 R_J (from the Joy et al. (2002) model). Using the equivalence mapping model, Dunn et al. (2016) found the majority of X-ray producing ions originated beyond 60 R_J where most of the carbon/sulphur line emissions were found to originate on open field lines between 50 R_J and 90 R_J (for the case of a compressed magnetosphere). The 26-min QPO was observed to originate on the edge of the hot spot (between 150° and 160° S3 longitude) and was strong in carbon/sulphur emission. The strong carbon/sulphur emission at the edge of the hot spot was speculated to be the source of the brightening in this region. Comparing the Dunn et al. (2016) results to our study, both observe a significant $\sim$ 26-min QPO during an inferred compression event and find that the majority of X-ray producing ions originate $>$ 60 R_J. The observed brightening at the edge of the expanded hot spot region by Dunn et al. (2016) may also suggest that there are multiple independent X-ray sources producing this variable emission (as suggested by Figure 4.3 in this study) during a compression event.

The *Juno* dataset affords us the unique opportunity to have a window on the magnetosphere (or upstream environment) to provide important context for the X-ray observations which has been missing in previous years. From *in situ Juno* data, we can infer the condition of the jovian magnetosphere and have a better understanding of what possible drivers are producing the hot spot emission. When *Juno* is nearer the polar regions, JEDI will allow us to detect and analyse the MeV ions that we expect to underpin the X-ray aurora mechanism. Houston et al. (2020) start to investigate the MeV polar ions in the context of X-ray emissions to help use the *in situ* data to provide a vital contribution on trying to answer the origin of the soft jovian X-rays and their corresponding (quasi-) pulsating driver.

An emergency reset of *HST* meant that a UV observation which was scheduled to overlap with this X-ray campaign did not happen. Thus we unfortunately lost the ability to compare the X-ray QPOs with the UV waveband for this case. The emergency reset itself was possibly triggered by an intense solar event on Jupiter (perhaps associated with the inferred solar wind compression during this interval). Future multi-wavelength campaigns during the *Juno* era should shed light on the relationship between X-ray, UV and other wavebands, and on the distinct physical processes which cause these diverse emissions.

It is clear that further work is required to fully understand the driver of Jupiter's X-rays and future studies will need to make more comparisons with UV and radio data. The processing pipeline and numerical hot spot definition employed in our study combined with *Juno in situ* data can be used to examine any correlations between the varying morphology and intensity of the hot spot with the multitude of different factors that may affect the jovian X-ray emission. These techniques will also allow a more consistent comparison to be made between all the *Chandra* data in great detail. This study provides new information on where the ions originate, although more data are needed to determine where on the field lines the acceleration takes place. Comparisons with factors such as solar activity and magnetospheric state will allow us to determine what conditions produce the different X-ray emission morphologies we have observed and allow us to fully understand the true origin of Jupiter's X-rays.

4.6 Summary

From the expanding catalogue of *Chandra* observations of Jupiter X-rays during a variety of solar wind and magnetospheric conditions, this is the first study analysing an extended northern hot spot emission in great detail during a solar wind compression. Previous works have found a hot spot of emission in both the North and South poles but the intensity and elongation of the northern hot spot during this interval are unique. With accompanying *in situ Juno* data, we can provide the *Chandra* observations with magnetospheric context allowing us to attempt to identify what conditions are needed to produce the various morphologies of the X-ray aurora and find their origin. Our results reveal statistically significant quasi-periodic oscillations from the northern hot spot, with period varying from $\sim$ 26 to 37 minutes during 2 separate viewing windows separated by less than a planetary rotation. These pulsating X-ray photons map to a region close to the dayside magnetopause which points to processes in that region as a likely driver to the X-ray behaviour.

We hope that the work presented here will provide another avenue analysing the morphology and intensity of the hot spot emission using a numerical definition with

more robust timing analysis in the *Juno* era. The combination of these techniques with multi-wavelength remote sensing and *in-situ* data will allow us to finally understand the physics of the drivers producing these dynamic emissions. We look forward to exploring further the conditions that produce the varying morphologies of the hot spot and the range of significant QPOs observed throughout *Chandra* 's ongoing Jupiter campaign.

Chapter 5

Characteristics of Jupiter's X-ray auroral hot spot emissions using Chandra

"We used to think that if we knew one, we knew two, because one and one are two. We are finding that we must learn a great deal more about 'and' "
- Sir Arthur Eddington

Representative of the motivation behind this statistical study and how using a consistent definition is **key**.

5.1 Abstract

Here we expand on the results and definitions from the previous study (Weigt et al., 2020) an apply them to the entire *Chandra HRC-I* catalogue to create the first jovian X-ray auroral first statistical study focusing on the northern emissions. More specifically, this study examines the spatial and temporal behaviour of the so-called 'northern hot spot' (NHS) in an effort to determine the driver of the jovian auroral X-rays. The *Chandra* data that forms our catalogue data used in this analysis spans almost 20 years. We use time-tagged photon data from observations dating back to 18 December 2000 during the *Galileo*-era up to, and including, 8 September 2019, as *Juno* was nearing the end of its prime mission. We use the photon concentration criterion defined in chapter 4, a number density of >7 photons per 5° System III longitude $\times$ 5° latitude over $\sim$ 10 hours (the average duration of the observations over 20 years), to determine the brightest and more concentrated auroral emissions. From this we are able to characterise the typical (i.e. high occurrence rate throughout the observations)

and more extreme i.e. low occurrence rate) behaviour of the NHS emissions from our $\sim$ 20 year dataset. From our catalogue, we calculate the mean power of the NHS to be 1.91 GW with the auroral emissions having an average maximum brightness of 2.02 Rayleighs (R). These auroral emissions are associated with the brightest parts of the jovian X-ray spectrum. For the first time, we identify a statistically significant X-ray auroral region within the more concentrated emissions of the NHS (e.g. a region of the concentrated NHS that appears in all observations of our catalogue), located at the NHS centre. This region has been coined the averaged hot spot nucleus (AHSNuc). We calculate the mean auroral power of the AHSNuc to be of 0.57 GW with an inferred average brightness of $\sim$ 1.2 R. Results from the Vogt et al. (2011, 2015) flux equivalent model throughout our catalogue suggest that the driver, or drivers, of the concentrated NHS emissions associated with the majority of mappable NHS time-tagged photons reside in the pre-dusk to pre-midnight sector of the jovian magnetosphere: the dusk flank boundary. The mapping model also identifies a smaller cluster of mappable photons originating at the jovian noon magnetopause boundary, dominated by mappable AHSNuc photons. These results suggest, as eluded to in previous literature (e.g., Dunn et al., 2017), that multiple magnetospheric sources may be responsible for driving the X-ray auroral emissions. Our timing analysis (including Rayleigh testing with Monte Carlo and Jackknife testing as used in Chapter 4) identifies many, but infrequent, cases of statistically significant quasi-periodic oscillations (QPOs) within the concentrated NHS emissions. These QPOs are found to range from $\sim$ 2.3-min to 36.4-min across the auroral region, with the AHSNuc QPOs dominating the lower limits. These timescales suggest possible associates with ultra-low frequency activity on the magnetopause boundary as found by *Galileo* across a vast range of local times. This study concludes by discussing the possible drivers responsible for the X-ray emissions given their position in the magnetosphere and their timescales, such as dayside reconnection and Kelvin-Helmholtz instabilities.

5.2 Introduction

We have already examined in detail the location and nature of Jupiter's soft X-ray "hot spot" emissions, the most powerful and concentrated of the jovian X-ray auroral emissions, in Chapters 2 and 4. Gladstone et al. (2002), who discovered the northern pulsating "hot spot", postulated that the driver of these highly localised emissions was likely located in the outer magnetosphere, $>$ 30 Jupiter radii (R_J) from the planet. The hot spot was observed to exhibit significant quasi-periodic oscillations (QPOs) of 45-min similar to pulsations identified from jovian radio emissions detected by Ulysses flyby (MacDowall et al., 1993) and bursts of electrons observed from the Cassini flyby (Krimigis et al., 2002). From this discovery, subsequent *Chandra* and

XMM-Newton observations have allowed us to analyse in detail the composition of the ions responsible for soft X-ray (SXR) production and how the hot spot varies both spatially and temporally, as examined in previous chapters. Many studies have found the temporal behaviour of the hot spot SXRs vary from observation-to-observation and exhibit a large range of QPOs (e.g., Chapter 4, Dunn et al., 2016, 2017; Elsner et al., 2005; Gladstone et al., 2002; Jackman et al., 2018; Kimura et al., 2016; Wibisono et al., 2020) and may be correlated with other types of auroral emissions, such as jovian radio emissions (Dunn et al., 2020b). Such a large variation in temporal behaviour makes it difficult to hone in on the auroral driver of these emissions, especially when the observed QPOs change over timescales shorter than a jovian rotation (e.g., Chapter 4 Jackman et al., 2018). A recent study by Yao et al. (2021) suggested the differences in QPOs we observe may be a result of electromagnetic ion cyclotron (EMIC) waves being modulated by electromagnetic waves originating from Jupiter. Therefore the pulsations we observe may be episodic bursts of ion precipitation, confirmed from *in situ* data from *Juno* . Although a very plausible driver, this has yet to be proven for a larger dataset.

The origin of the heavy precipitating ions responsible for SXR production via charge exchange processes with neutrals in the jovian atmosphere is also still up for debate, further complicating matters. Recent modelling by Houston et al. (2020), compared with *in situ Juno* data, identify that these heavy ions contribute the most to the total X-ray auroral power (1 GW to a few GWs), therefore understanding where they come from is vital to aid our understanding of these emissions. Cravens et al. (2003) stated that the aforementioned heavy ions can be composed of species found from the solar wind as they travel down open field anchored to the interplanetary magnetic field (IMF) carried by the solar wind or from an external plasma source, such as Io, on closed field mapping to the outer magnetosphere. However this is made complicated when we observe, for example, iogenic ions in the jovian X-ray auroral emissions during compression events at Jupiter (e.g., Wibisono et al., 2020), where we would expect an external source, such as the solar wind, to have more of an effect. Although many have found the X-ray spectrum was best fitted with iogenic ions (like S and O), many observations have revealed that the spectral fit is improved by including the charge exchange lines associated with solar wind ions (Branduardi-Raymont et al., 2007a; Hui et al., 2010b; Dunn et al., 2020a). As examined in Chapters 2 and 4, the production of X-rays through charge transfer and exchange process requires that the field-aligned electric fields responsible for the coupling of the ionosphere and magnetosphere to produce very high potentials. (Cravens et al., 2003; Bunce et al., 2004). *Juno* observed these high potentials at Jupiter's poles via the Jupiter Energetic Particle Detector Instrument (JEDI) (Mauk et al., 2017) and were identified to be associated with charge stripping of heavy iogenic ions responsible for the SXRs we observe (Clark et al., 2020).

As briefly discussed in Chapter 4, Dunn et al. (2017) studied both the northern and southern hot spots for the first time, during an observation when the tilt of the planet was favourable for both poles to be observed and found that the northern and southern hot spots were non-conjugate. This behaviour was observed from the results of their timing analysis of both auroral regions. The South exhibited a significant 9-11 min QPO in the South with no significant QPOs in the north, suggesting that the driver for both hemispheres may be different. Alternatively, Dunn et al. (2017) suggested that same driver may have been triggered independently, producing a lag in the QPOs and/or the different temporal behaviour observed at the auroral regions. We identify this non-conjugacy of the X-ray auroral emissions in the *Chandra* data during a compression event as examined in Chapter 4. Wibisono et al. (2020) observed identical non-conjugate behaviour during an *XMM-Newton* observation window concurrent with *Chandra*. Outside the *Chandra* window however, the northern and southern auroral regions exhibited the same 23-to 27-min QPO over a $\sim$ 12.5 hours interval (i.e. more than one jovian rotation), agreeing with the conclusions made by Dunn et al. (2017) about potential independent drivers for the auroral regions.

In order to explore in detail how variable the hot spot emissions are both spatially and temporally, we analyse the entire *Chandra* catalogue. We use all these observations in the statistical study presented in this research to determine the typical and extreme behaviours of the auroral hot spot. Identifying such behaviours will enable us to obtain a better understanding of how various magnetospheric effects (e.g. from the varying solar wind or changes to Io activity) has on the X-ray auroral emissions, This analysis will allow these effects to be explored in detail during future X-ray observations of the jovian aurora. In this research, we apply the Weigt (2021) algorithm, as discussed in Chapter 3, and definitions from Chapter 4 to identify any significant regions within the "average" hot spot morphology from comparing the occurrence rate of X-ray emissions across the catalogue. We also map the concentrated X-ray emissions using the Vogt et al. (2011, 2015) flux equivalence mapping to find the likely location of the auroral driver across the catalogue. We also explore the possible limitations and sensitivity of the flux equivalence model to potential errors resulting from the ionospheric position of any mappable photons. Our timing analysis uses the same techniques in Chapter 4 to produce a catalogue of results which we compare to previous statistical studies (e.g., Jackman et al., 2018) and allow us to identify possible spatial dependence of the QPOs (i.e. does the region selection affect the QPO observed? Does the full auroral region pulsate at the same time). This also gives us the capability to check the validity and robustness of our timing analysis.

In Section 5.3, we briefly discuss the full *Chandra* catalogue used in this research. We apply the techniques discussed in Chapter 4 to the $\sim$ 20-year dataset and also use the Weigt (2021) mapping to analyse the morphological behaviour of the emissions. The results from our mapping are discussed in Section 5.4, presenting the average

morphology of the hot spot over the entire *Chandra* campaign for the first time and the associated any statistically significant regions within the concentrated hot spot emissions. The ionospheric location and sub-solar longitude (SSL) of the mappable hot spot emissions are then used in the Vogt et al. (2011, 2015) flux equivalence model to find the most probable location of the auroral driver. In this research, we explore the possible uncertainties of the model in greater detail than what was explained in Chapter 4 to ensure that our interpretations of this very large dataset are fully informed. As mentioned previously, our analysis of the catalogue concluded by our timing analysis of the full dataset with a particular focus on exploring any potential spatial dependence of any identified significant QPOs. Finally Section 5.5 contains a detailed discussion of our interpretation of the results from our large statistical study, exploring in the detail the implications of the behaviours identified from the concentrated northern hot spot emissions.

5.3 Chandra HRC-I catalogue

In this research we use data taken from *Chandra HRC-I* only as it has maximum sensitivity to the pulsed emissions produced from the SXRs. Like before, we utilise the high spatial resolution to map the jovian photons onto Jupiter (see Section 3.1), using the calculated longitude and latitude of the X-ray photons from the Weigt (2021) algorithm. The data from our *Chandra HRC-I* catalogue cover $\sim$ 20 years of observations. The HRC-I instrument has conducted 29 observations in total during this time from 18 December 2000, spanning two solar cycles. The temporal distribution of the observations is shown in Figure 5.1, with the timeline of the *Galileo* and ongoing *Juno* campaigns and flybys performed by *Cassini* and *New Horizons* overplotted.

From these data, 8 observations were spread over multiple campaigns to occur during flybys performed from other spacecraft at Jupiter, or to the predicted arrival of a coronal mass ejection (CME) impacting the jovian magnetosphere. These set of observations is further increased by 21 observations since 2016, planned to coincide during *Juno's* approach to Jupiter and its early orbits. During this time, some *Chandra* observations were planned to coincide with campaigns from other remote sensing observatories to analyse the auroral emissions across the electromagnetic spectrum (e.g. ultraviolet (UV) observations from the Hubble Space Telescope (HST), radio observations from round based telescopes etc.) to fully understand the magnetospheric dynamics at Jupiter. Full details of each observation in our catalogue including: the observation dates and duration; concurrent missions during the *Chandra* interval; geometry of the observer with respect to Jupiter from the sub-solar longitude (SSL) and sub-solar latitude and the visibility of both auroral regions are shown in Table A.1 in Appendix A.1. We note that this extra information is not needed

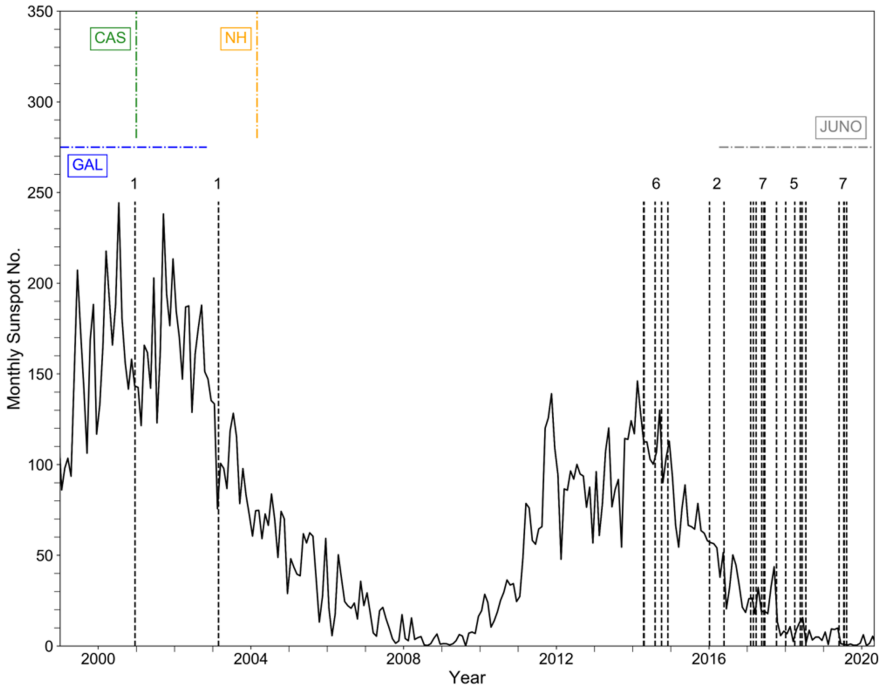

FIGURE 5.1: The sunspot number from 1999 to beginning of 2020 plotted as a function of time is shown in black with individual *Chandra* HRC-I observations, used in this statistical study, represented by dashed vertical black lines (identical format to Figure 3.1). Black labels on top of the *Chandra* lines show the number of HRC-I observations in a given year respectively. The duration of the *Galileo* (GAL) mission is shown by the blue dot-dashed. The ongoing timeline of the *Juno* mission is represented by the grey dot-dashed line. Flybys of both *Cassini* (CAS) and *New Horizons* (NH) are shown by the green and orange dot-dashed lines respectively. *Sunspot number source: WDC-SILSO, Royal Observatory of Belgium, Brussels*

to understand the analysis in the remainder of this chapter but allows sufficient details needed for future comparative studies.

To ensure we analyse the auroral regions in the same place for all 29 observations, we apply a consistent definition across the catalogue for both the northern and southern auroral region. Here we define the northern auroral region as any X-ray emissions poleward of 40° latitude with an System III (S3) longitude of 100° to 240°. The more diffuse southern auroral region makes it very difficult to constrain the emissions in S3 longitude and locate any intense southern emissions, especially when the diffuse emissions are located close to the joviocentric South pole. Therefore we only apply a latitude constraint to the southern emissions, using the region poleward of -60° latitude as our definition here.

As shown in Chapter 4, we observe the northern hot spot to traverse the disk for $\sim$5 hours as the planet rotates. We note that, although most observations from our catalogue are $\geq$10 hours in duration, some have been optimised to look at the northern hot spot in detail and therefore shorter. This is considered in our mapping analysis.

Applying these constraints to our catalogue, we find that 28 out of 29 were useable in our analysis and were successfully mapped using the Weigt (2021) mapping algorithm. The anomalous observation that was unable to be mapped accurately was ObsID 18303, as shown in Table A.1. This was a result of Jupiter being observed off-centre HRC-I, resulting in erroneous photon mapping as the point-spread function (PSF) of the detector increases with distance away from the centre (see Chapter 3).

5.4 Results

The finer sub-structures within the X-ray auroral emissions can be identified and analysed in more detail through the selection of various spatial regions within the auroral emissions and observing the temporal behaviour in each. A recent study by Dunn et al. (2020b) applied this idea to their analysis of a joint *XMM-Newton-Chandra* X-ray campaign during solar minimum in 2007. They compared the X-ray data with *in situ* solar wind data from *New Horizons*, radio data from ground based and remote sensing instruments (like *Juno* Waves) and *HST* UV data. From their analysis, they discovered that the soft X-ray auroral emissions can be split into three different sub-categories from their temporal behaviour: regularly pulsed emission, irregularly pulsed emission and flickering aurora. In this study, our main focus will be analysing those emissions associated with the first two categories. The pulsed behaviours were linked with short-lived flaring (or enhancements) of the X-ray emissions, lasting $\sim$ 1-2 min. Such activity was observed to commence with more concentrated intervals of flaring immediately followed with extended windows of very dim to no emissions. Our analysis will therefore analyse in detail the variations in temporal, spatial and morphological behaviour of the pulsed/flaring emissions and the possible spatial dependence of any significant QPOs we may identify.

5.4.1 Overall morphological characteristics of the X-ray emissions

With the large catalogue of *Chandra* data available to us, we can explore in detail the typical and more extreme conditions of the X-ray auroral emissions. Here we examine polar 2D histograms of all auroral X-ray brightness observed across the catalogue, in a planetographic projection. Figure 5.2 shows the averaged X-ray brightness from 28 observations ($\sim$ 97% of all *Chandra* HRC-I observations). We calculate the average emissions by mapping all time-tagged X-ray photons in our catalogue to their predetermined ionospheric positions, in S3 longitude, latitude, from the Weigt (2021) algorithm. The photon flux found from the point spread function assigned each photon position was then computed in each 1° S3 longitude $\times$ 1° latitude bin (i.e. the typical spatial resolution of our data across the entire catalogue) and then averaged

over the full dataset for each photon in that bin. We use an average observation time of $\sim$ 10.2 hours for the auroral regions at both hemispheres. Figure 5.2 shows the calculated averaged brightness of the X-ray emissions as if observed from above (a) the North and (b) South pole. We overplot the Grodent Anomaly Model (GAM) (Grodent et al., 2008) Ganymede footprint in panel (a). The Io footprint calculated from the Voyager Io Pioneer 4 (VIP4) (Connerney et al., 1998) field model is overplotted plotted in both panels with the VIP4 Ganymede footprint used for the South pole in panel (b). The GAM field contours are only modelled for the North pole. These contours are used, with identical configuration, in all figures herein for northern and southern auroral regions. This provides vital context to the location of the auroral X-ray emissions and their associated magnetic position in the jovian magnetosphere. For example, emissions located close to the Ganymede footprint ($\sim$ 15 R_J from Jupiter) will be associated with magnetic field lines, calculated from the corresponding field model, that map to Ganymede's orbit.

The results presented in Figure 5.2 show a clear asymmetry in the X-ray brightness, indicated by the colour bar, between the northern and southern averaged auroral hot spot [herein referred to as NHS and SHS respectively]. The brightest, and therefore most intense, NHS emissions are found to be concentrated in a tear-drop region. surrounded by diffuse X-ray emissions emission (dark blue) as shown in Figure 5.2. The emissions are observed to have an elongated morphology, extending towards the joviographic pole at S3 longitude of 0°. We observe the more diffuse emissions from our catalogue to be located at longitudes of $\sim$90° - 225° with a more widespread morphology than the most intense NHS emissions. These diffuse NHS emissions extend poleward of the Ganymede footprint (solid) towards the Io footprint (dashed) and further equatorward in regions 225°.

The weaker, more diffuse SHS emissions are observed to be most intense within the Ganymede footprint as shown in Figure 5.2b. The asymmetry we observe across the catalogue may be the result of unfavourable viewing geometry of the southern emissions throughout our dataset (Dunn et al., 2017). We note in our analysis, we observe the same asymmetry in auroral brightness between the poles throughout our catalogue, including 12 observations which had a sub-solar latitude that allowed for equal viewing of the aurora in both hemispheres during the *Chandra* interval. Therefore the viewing geometry of Jupiter as observed from Earth may be a contributing factor to the non-conjugate behaviour we observe but will not be the strongest effect. These results are shown in the Table A.1 in Appendix A and we again emphasise that these results only provide additional information to the key results we present here. The asymmetry we observe in the auroral emissions is more likely a result of the differing characteristics of the magnetic field between both poles, such as strength and field topology, not conisdered in the mapping (Connerney et al., 2018). This asymmetry observed in the magnetic field will have an effect on the current

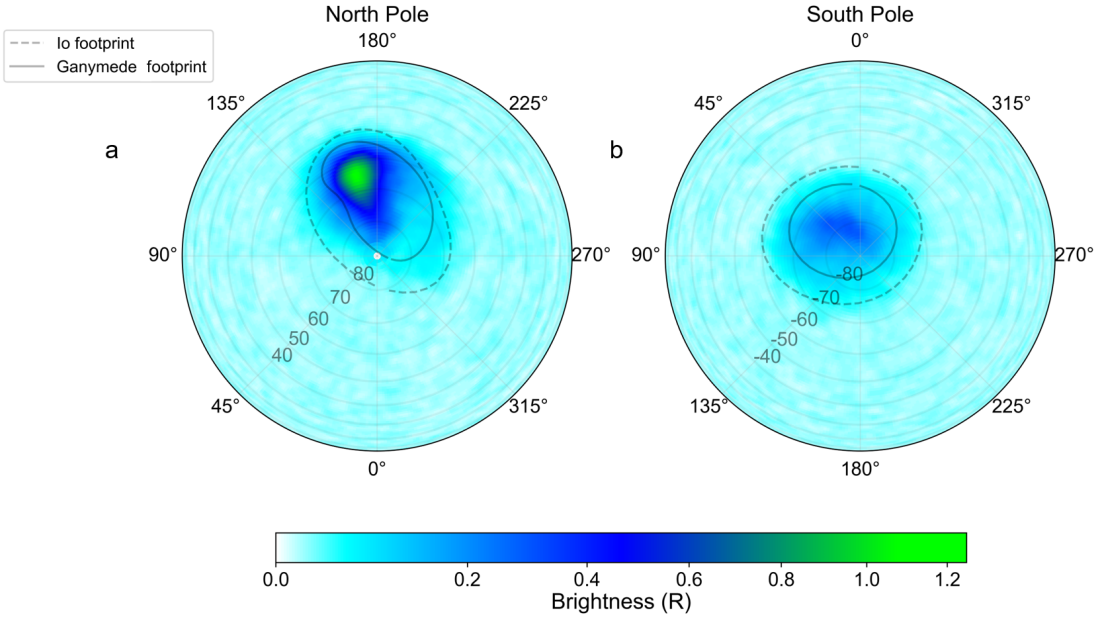

FIGURE 5.2: 2D histograms of averaged X-ray emissions, with a focus on those observed within the auroral regions, of 28/29 observations in our catalogue. The plots are shown using a planetographic polar projection, with the emissions plotted as if they were observed from above (a) Jupiter's north and (b) south joviographic poles. Surrounding both panels are the labelled azimuth angles, as represented by the joviographic longitude. The faded grey-concentric circles indicate increments of 10° latitude. Circles representing all latitudes $\geq |40°|$ are highlighted to provide the reader with context of the location of the emissions in this new projection. The averaged brightness over the catalogue was calculated using the same technique as described in Section 3.1 and Chapter 4 with the colour bar indicating the brightness of the X-ray emissions across Jupiter in units of Rayleighs (R). White regions indicate that very few or no X-ray photons were observed. We overplot the Io footprint from Voyager Io Pioneer 4 (VIP4) (Connerney et al., 1998) Io and the Ganymede footprint from the Grodent Anomaly Model (GAM) (Grodent et al., 2008) Ganymede footprints in panel (a). The footprints shown in panel (b) are both from VIP4. The Io and Ganymede footprints in both panels are shown as the dashed and solid black lines respectively. Figure taken from Figure 1 in Weigt et al. (2021a).

systems that occur at the poles, for instance stronger and more persistent electron currents observed in the South compared to the North (e.g., Kotsiaros et al., 2019). The Weigt (2021) mapping algorithm also does not account for possible atmospheric effects like the opacity of the jovian atmosphere which can block outgoing X-rays from the auroral regions (Ozak et al., 2010). It is therefore difficult to measure these effects from the mapping and X-ray data alone and is not the main focus of the research. We do note that such effects should be highly considered in future auroral studies, to ensure we are not over- or under- estimating the X-ray emissions we observe.

With regards to the overall morphology of the most intense diffuse SHS emissions, we observe them to be located in a more spot-like ($\sim$350° - 60° S3 lon and $\sim$-60° poleward in latitude). Similar to the NHS, we observe the SHS emissions extending just beyond the Ganymede footprint (S3 lon of $\sim$ 45° - 180°). Such spreading of these averaged

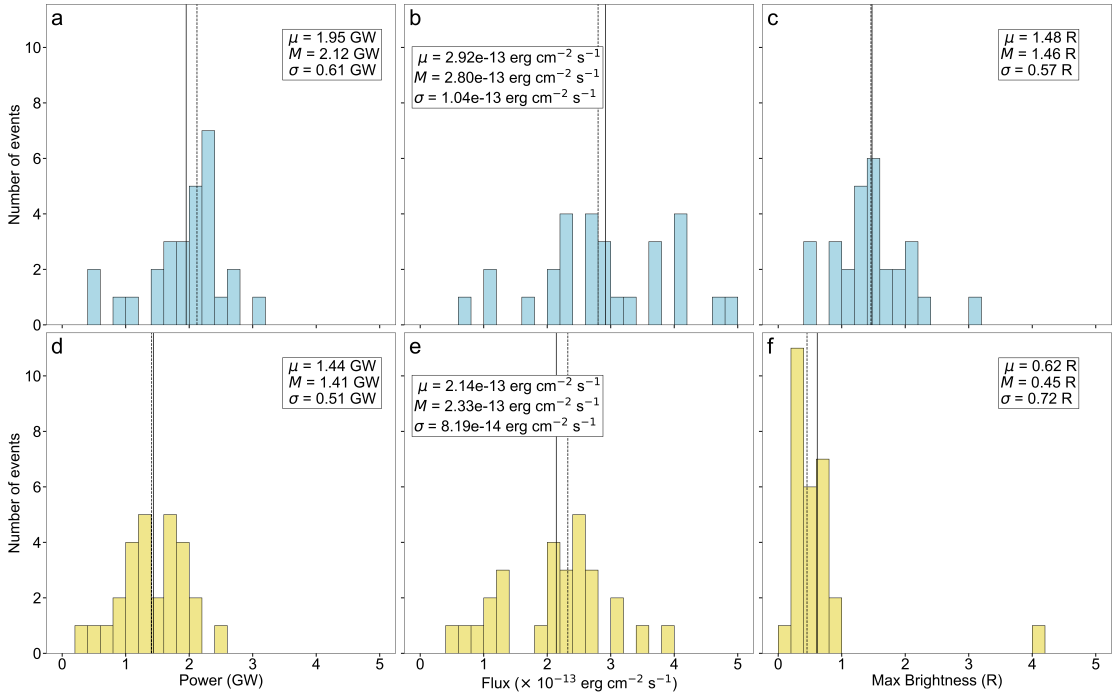

FIGURE 5.3: Distributions of the X-ray auroral power (panels (a) and (d)), associated energy flux ((b) and (e)) and maximum brightness ((c) and (f)) of the auroral emissions across our catalogue of 28 observations. Each parameter has been calculated as if it was observed from *Chandra*, assuming isotropy. The distributions for the northern emissions are shown in the top panels in light blue and the southern emissions shown below in gold. All panels have the calculated mean (μ: solid line), median (M: dashed line), and standard deviation, σ, of the distribution labelled. Figure taken from Figure 2 in Weigt et al. (2021a).

SHS emissions suggests that morphology is highly variable across the observations and/or be a result of the previously discussed poorer viewing conditions, which may affect how accurate we can map the SHS emissions.

The distributions of the calculated average powers, energy flux and maximum brightnesses found for each observation in our catalogue for both the northern and southern emissions are displayed in Figure 5.3. The mean (μ: solid line), median (M: dashed line) and standard deviation (σ) are labelled in each panel. We calculate the median of the distributions to account for the shortest *Chandra* interval in our catalogue ($\sim$ 3-hr observation, ObsID 18676) due to the low exposure time producing unusually high values of auroral brightness in both polar regions (see panels(c) and (f) of Figure 5.3). Similar to Chapter 4, to calculate the auroral flux and power without any energy resolution from *HRC-I*, we assume the peak auroral photon energy to be $\sim$ 0.5 keV. This energy is observed to be halfway between the emissions lines associated with S and O. This assumption has also been used in previous X-ray auroral studies (e.g., Dunn et al., 2016, 2017; Gladstone et al., 2002). We note our energy flux calculation assumes that we measure the X-ray flux as observed from *Chandra* . We account for the varying *Chandra*-Jupiter distance over the catalogue. For the auroral

power and associated energy flux, we assume that the northern and southern auroral regions cover $\sim$ 10% and $\sim$ 5% of the observable jovian disk respectively. When compared to our mapping analysis of the *Chandra* image data, these values represent what is typically observed throughout our catalogue. All additional information from each *Chandra* observation used in our calculations including: photon counts from each auroral region, duration of observation, average angular diameter of Jupiter and *Chandra*-Jupiter distance are shown in Tables A.1 and A.2 in Appendix A.1 and A.2 respectively at the end of the thesis. The powers and energy fluxes we calculate for the southern auroral emissions, dominated by the SHS, are interpreted as lower limits due to the poorer viewing geometry of these emissions throughout the catalogue.

We calculate the mean X-ray auroral power for the northern and southern auroral regions, using our definitions in Section 5.3, from our catalogue to be $\sim$1.95 GW and 1.44 GW respectively (panels (a) and (d) in Figure 5.3) with the full results of each *Chandra* observation (e.g. auroral power, energy flux, brightness etc), presented in Table A.2. Interestingly, studying the statistics of all distributions in Figure 5.3 shows that the standard deviations, σ, for all those associated with the southern emissions are smaller than the corresponding distributions for the North. This shows that the there is less variation in the southern emissions and the associated auroral driver may be less variable than the source responsible for the northern emissions. In other words, plausible evidence to suggest that the auroral drivers for the North and South are different which could explain the more diffuse southern auroral emissions.

As shown in panels (b) and (e) of Figure 5.3, our calculated auroral powers were found to translate to an average flux of 2.92×10^{-13} erg cm^{-2} s^{-1} and 2.14×10^{-13} erg cm^{-2} s^{-1} for the North and South respectively (where 1 erg cm^{-2} s^{-1} = 1×10^{-3} W m^{-2}). The final two panels of this figure show the corresponding mean maximum auroral brightness to be 1.48 R (Rayleighs) and 0.62 R, again highlighting the strong asymmetry of the intensity of the emissions first highlighted by Figure 5.2. As noted previously, there is some variation in the duration of each observation (e.g. some optimised for northern hot spot viewing, some lasting over multiple jovian rotations etc.) throughout the catalogue which can have an affect on our distributions.

The remainder of this study will focus on the northern auroral emissions due to the better viewing geometry and more powerful averaged X-ray emissions observed throughout the catalogue. As there are also many levels to the intensity of the emissions, we are more likely to gauge the differences between typical and more extreme behaviour.

5.4.2 Exploring the persistence of concentrated NHS auroral photons

The average map of the North, as presented in Figure 5.2, provides an overall view of the typical morphology and structure of full auroral region with some idea of the hot spot morphology embedded within these emissions. Here we expand our analysis from these maps by applying a quantitative criteria to locate the more concentrated emissions within the NHS. We apply the methods and numerical criterion defined in Chapter 4 to define the averaged northern hot spot emissions across our catalogue. This criterion is composed of the spatially select region of the northern hot spot emissions we define here in Section 5.3 (S3 lon: 100° - 240°, lat: 40° - 90°) and Weigt et al. (2020)'s numerical threshold for photon concentration at $>$ 7 photons per 5° S3 lon $\times$ 5° lat within the NHS region. From our catalogue, 26/29 observations had emissions that met our criterion as two *Chandra* intervals (ObsID 15670, 18676) had insufficient counts to generate the more concentrated emissions we want to analyse. The results of applying this threshold to the averaged emissions are shown in Figure 5.4 in the form of a 2-D histogram using 3° S3 lon $\times$ 3° lat bins. The Cartesian plot is projected onto a planetographic polar plot, as used previously. We use these plots to identify the typical location of the concentrated emissions within the NHS. Distributions of the S3 lon and lat of the emissions, using 1-D histograms in panel (a), allows us to analyse the width of the average hot spot and identifies the spatial variability within the region (i.e., not a uniform distribution across the NHS). The colour bar shows the percentage of observations that had X-ray emissions mapped to each 3° S3 lon $\times$ 3° lat bin in both plots from 0 - 100% (e.g., an occurrence rate of the X-ray emissions across the catalogue). In our analysis, we have discovered that a fraction of the NHS is always present. This significant region has dimensions $\sim$ 162° - 171° S3 lon and $\sim$ 60° - 66° lat. We show this region of interest by a black cross-hatched region in both panels of Figure 5.4 and herein refer to it as the "averaged hot spot nucleus" or AHSNuc (i.e., a region with photon concentrations above our numerical threshold in 100% of the observations). The AHSNuc is of particular interest as this region may map to the location of a magnetospheric driver that is always switched on.

Figure 5.4 shows that we identify the region of hot spot emissions that often appear in our catalogue (i.e. occurs 70 - 99%) to be $\sim$ 153° - 183° S3 lon and $\sim$ 57° - 72° lat. This region is observed to typically surround the significant AHSNuc region and accompany the central emissions throughout the catalogue due to possible movement of the hot spot. This suggests that the auroral driver generating the more intense NHS emissions is likely to be very variable which can leading to the hot spot changing morphology and position. We observe this further in our analysis with the identification of regions in the NHS that are associated with locations that the hot spot is occasionally observed (i.e an occurrence rate between 30% and 70%). These

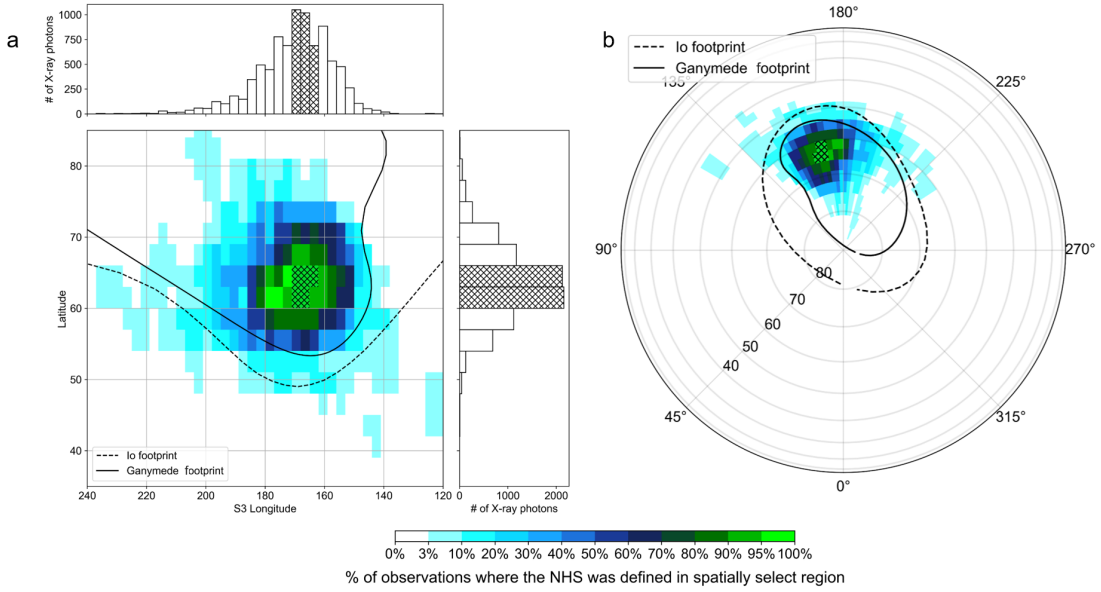

FIGURE 5.4: 2D histograms showing the typical and extreme behaviour of the concentrated NHS emissions throughout the catalogue using a (a) Cartesian (S3 lon vs. lat) and (b) polar planetographic projection. The S3 lon and lat distributions of the NHS photons are shown in panel (a) with 1-D histograms to show the width of the averaged hot spot emissions in more detail. Panel (b) is of identical format to Figure 5.2, with the same Io and Ganymede footprints overplotted (in both panels) to provide context to the position of the auroral driver in the magnetosphere. Both plots, including the 1D histograms, use bins of 3° S3 lon × 3° lat. The colour bar shows the occurrence of X-ray photons in each bin from 26/29 observations in the *Chandra* catalogue that followed the numerical criterion defined in Chapter 4 (Weigt et al., 2020) for photon concentration. The cross-hatched area in both panels highlight the region of statistical significance within the concentrated NHS X-ray emissions that we observe in all 26 observations (i.e., an occurrence rate of 100%). Figure taken from Figure 3 in Weigt et al. (2021a).

emissions located at $\sim 54° - 75°$ latitude and span S3 longitudes $\sim 150° - 195°$, more equatorward than the AHSNuc.

The remaining regions shown in Figure 5.4, $< 30\%$ occurrence, are associated with rare and extreme hot spot behaviour identified from our numerical criterion. These regions are observed to be the most equatorward, beyond the Io footprint in many places, and are the width of our Cartesian grid ($\sim 120° - 237°$ S3 lon). Such regions may be related to auroral drivers only activated under certain conditions, suggesting a fragmented hot spot. The variable morphology of the NHS observed throughout our catalogue is highlighted by the decreasing colour bar from the AHSNuc, clearly revealing the typical and more rare and extreme behaviour of the NHS.

Similar to our analysis in Section 5.4.1, we produce distributions of the X-ray auroral power, flux and maximum brightness of the NHS and AHSNuc throughout the *Chandra* catalogue. The resulting histograms are shown in Figure 5.5 and are of identical format to Figure 5.3. We assume that the emissions from these sub-structures

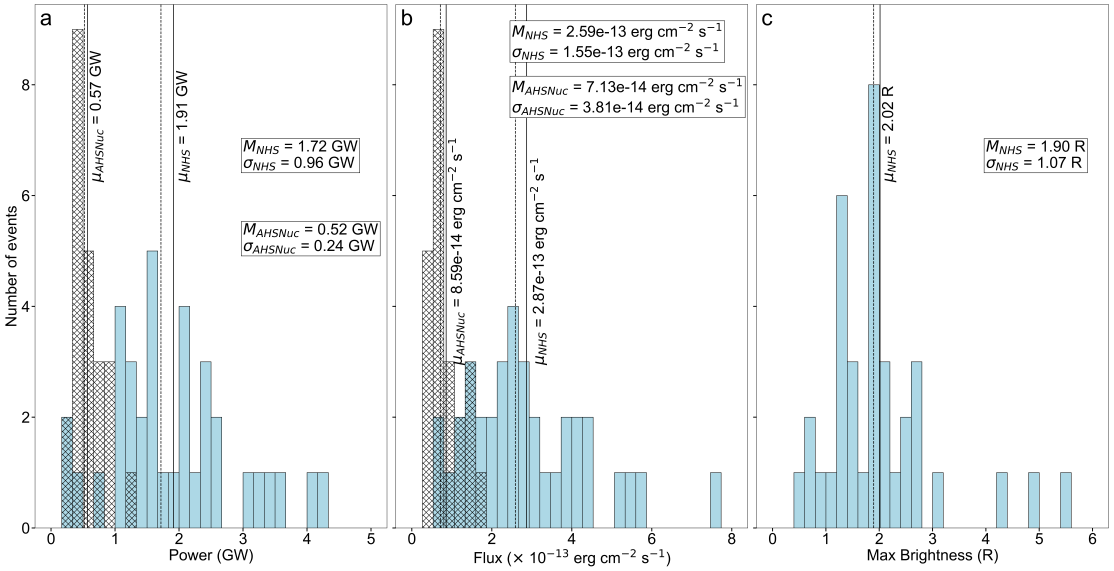

FIGURE 5.5: Distributions of the calculated auroral parameters across the catalogue for the NHS (blue) and AHSNuc (cross-hatched) emissions. Histograms of both regions are of identical format to as Figure 5.3, showing the distributions with labelled statistical information (mean, median and standard deviation) for (a) the average power, (b) energy flux and (c) maximum brightness. We note any overlap of the NHS and AHSNuc distributions are identified as blue-cross-hatched regions of the histograms. The mean for each distribution calculated for the NHS and AHSNuc are represented with the vertical solid line with the value labelled adjacent. The dashed vertical line shows the median of each distribution. As explained in the text, current mapping methods used in this analysis make it difficult to find an accurate max brightness of the AHSNuc, and is therefore not shown in panel (c). This figure is taken from Figure 4 in Weigt et al. (2021a).

cover $\sim$ 7% and $\sim$1% of the jovian disk for the NHS and AHSNuc respectively. This assumption was based on comparing the auroral features of the NHS in Figure 5.4 to the overall averaged northern auroral emissions in Figure 5.2. From our analysis, the distributions presented in Figure 5.5 show the AHSNuc produces $\sim$ one quarter of overall X-ray auroral power of the concentrated emissions of the NHS region (0.56 (AHSNuc) : 1.91 (NHS) GW), corresponding to $\sim$ one third of the auroral energy flux (0.86 : 2.87 $\times$ 10^{-13} erg cm^{-2} s^{-1}). The mean maximum brightness of NHS is observed to be 2.02 R, dominating the brightest portion of the jovian X-ray spectrum. Our analysis suggests that driver responsible for the AHSNuc is likely to be less variable than the one responsible for the overall NHS emissions.The standard deviation of the AHSNuc distribution is smaller than the NHS equivalent, indicative of a smaller spread across the dataset and therefore less variation from the AHSNuc auroral parameters. The different shape between the distributions for the NHS and AHSNuc across each of the calculated auroral parameters suggest that it is likely that multiple drivers may be responsible for the auroral X-ray emissions. Our analysis finds that the AHSNuc behaves differently from the full auroral region and therefore possibly a key feature of the NHS emissions. Future mapping analysis included in X-ray auroral

studies must therefore take the AHSNuc into account. We do note that with more scheduled *Chandra* observation, the statistics of our results will be improved.

Since the location of the AHSNuc is known, We infer the average brightness of the region from the averaged hot spot emissions presented in Figure 5.2a. With our current mapping method, calculating an accurate brightness for a very small area has been proven difficult to obtain. The three intervals 2 - 3σ greater than the calculated mean NHS brightness (ObsID 18678 NHS1, 15671 NHS1 and 18301 NHS1) correspond to the shortest observation time of the NHS in our catalogue. As a result intervals with the shorter exposures times, like the extreme example identified in Figure 5.3, produce more unusual, like erroneous, values for the brightness of the auroral X-rays. The results for all NHS and AHSNuc intervals are shown in Tables A.3 and A.4 in Appendix A.3.

The $\sim$ 20-hour *Chandra* observation taken on 28 February 2017 during *Juno*'s fourth apojove (AJ4), displayed the most extreme viability in NHS auroral morphology. Such a long observation window allows *Chandra* to collect more photon data and therefore a longer interval to observe any variability that may occur on timescales less than a jovian rotation, for many cycles. We observe the more concentrated emissions to span a vast range of longitudes (S3 lon: $\sim$ 120° - 237°) and latitudes (lat: $\sim$ 39° - 75°). The NHS during this time emitted an auroral power of $\sim$ 3.24 GW (Table A.3), $\sim$ 7 times greater than what was observed in a previous observation of equal length: ObsID 2519, 25 February 2003 with calculated auroral power of 0.465 GW. The ObsID 20000 NHS region is also observed to be $\sim$ 4 times larger in longitude. Any seasonal changes that may affect the auroral emissions are likely to be very small as both observations occurred at roughly the same time during the year. This therefore suggests that the radical change in morphological behaviour and auroral power are most likely influenced by a possible change in the jovian magnetospheric conditions due to, for example, changes in the solar wind or with the behaviour of Io (the dominant plasma source in the jovian system).

One other noteworthy observation, again displaying more extreme behaviour of the NHS, is a $\sim$ 7-hr observation (ObsID 22159) taken on 8 September 2019 coinciding with Juno perijove (PJ22). This is one of the many observations optimised for full viewing of the NHS. The NHS emissions are observed to be located within the kink of the GAM Ganymede footprint and are spread equatorward of the Io footprint. The auroral power was calculated to be $\sim$ 2σ greater than the mean power at 4.03 GW. Only one other interval had auroral power exceeding this value: a $\sim$ 11-hr observation (ObsID 18608) taken on 24 May 2016 at 4.24 GW. During ObsID 22159 the NHS emissions were observed to be located in a small region (S3 lon: $\sim$ 135° - 180°; lat: $\sim$ 48° - 66°). The AHSNuc here is observed on the edge of the X-ray auroral emissions, providing plausible evidence to suggest that the driver producing can change the

position as well as the morphology of the auroral emissions, most likely affected by changing conditions. The ObsID 18608 hot spot emissions were mapped to a similar position to those observed during ObsID 22159 with a more stretched morphology. The plots of all the identified extreme cases from our analysis and the remainder of the catalogue are shown in Figure A.3[1] to provide the reader further details, although not required for the interpretation of the results we present here. We note these plots are of identical format to Figure 5.4 except the colour bar shows the number of photons found in each bin of the 2D histogram.

5.4.3 Mapping hot spot photons to their magnetospheric origins

We use the Vogt et al. (2011, 2015) flux equivalence mapping model [herein referred to interchangeably as the Vogt et al. model] to map the origin, and therefore the potential driver, of the concentrated NHS and AHSNuc emissions identified in Figure 5.4. This model relates a region defined in the jovian ionosphere to a potential source region in the equatorial plane. The Vogt et al. model uses an assumption about the location of flux in the jovian magnetosphere: any flux emitted through an area with a given ionospheric position is located in the joviographic equator. This assumption is determined from the plethora of data within the *Galileo* catalogue with a 2D fit (in coordinates of the radial distance and local time (LT) of the spacecraft). Therefore the equatorial flux observed in a given region calculated from the 2D fit applied to the *Galileo* data should be equivalent to the flux through a given area within the ionosphere to which the model identifies a one-to-one mapping. The mapping model is strongly dependent on the position of the Sun's zenith point on Jupiter's surface, more specifically the subsolar longitude (SSL) of the observed photons. WE note this differs slightly from central meridian longitude (CML), which is the observers longitude on the jovian surface as the planet rotates. The inputs of which the Vogt et al. model uses are the time-tagged photons' ionospheric position (in S3 lon and latitude) and their associated SSL. Both are calculated from the Weigt (2021) mapping algorithm. As the flux equivalence model uses mapping based on the jovian magnetic field (e.g., what field line is system is the jovian flux associated with), the choice of field model can have an effect on the mapping. Here we use the internal field from GAM with the model as it was based on UV auroral data and is observed to fits the Ganymede footprint better in the north than VIP4 or VIPAL (Hess et al., 2011b) - excepting Connerney et al. (2018)'s JRM09 model - and is therefore more representative of auroral mapping. The magnetic anomaly or kink in the Ganymede footprint is a consequence of a localised quadrupolar term introduced in the northern auroral region, which agrees with UV observations (Grodent, 2015). Although most

[1] As Figure A.3 is a large PDF taken from Supplementary Information of Weigt et al. (2021a), the plots can be viewed here: https://agupubs.onlinelibrary.wiley.com/action/downloadSupplement?doi=10.1029%2F2021JA029243&file=2021JA029243-sup-0002-Figure+SI-S01.pdf

likely a more nuanced effect on the NHS mapping results, it is important we consider any effects that may affect the modelled magnetospheric position and therefore how we interpret our findings.

We present the statistical mapping results from using the Vogt et al. model with the GAM internal field option on all mappable NHS photons found in our catalogue in Figure 5.6a). The Sun is located to the left of each plot. Identical analysis is performed on the catalogued AHSnuc photons to produce the statistical map shown in Figure 5.6b). To account for larger clusters of photons that may be observed from longer observations, we normalise the photon counts by the exposure time of the observation window presented Figures 5.6c) and (d), where the number of counts are normalised by the length of the observation window. We present our statistical magnetospheric mapping results as 2D histograms showing the number of (panels (a) and (b)) mapped photons (panels (c) and (d)) average number flux in each 10 $R_J \times 1$ hour local time (LT) bin, represent by their associated colour bars. Similar to the Vogt et al. model analysis performed in Chapter 4 , we overplot the Joy et al. (2002) model compressed (subsolar distance $\sim$ 60 R_J; black-dashed line) and expanded ($\sim$ 90 R_J; solid black line) limits for the magnetopause boundary. Our analysis clearly identifies two main populations in driver location found from the Vogt et al. flux equivalence mapping model: a smaller, concentrated population mapped to the noon sector, and a a larger population mapping across most of the dusk magnetosphere (15 LT - 21 LT). This trend still appears in the exposure maps where we have normalised for the exposure time. Most of the mapped events are calculated to be located very close to or on a magnetopause boundary as well as in between both the Joy et al. (2002) limits. The larger population mapped to the dusk magnetosphere, more specifically the pre-dusk to pre-midnight magnetopause boundary, is found to contain $\sim$ 40% of all mappable photons in our *Chandra* catalogue. This suggests that this region in the magnetosphere is potentially the location of the auroral driver of ions needed for SXR production. We do note that the wedge of high photon counts (located at 18 LT, dusk side) observed across all radial distances in this region disappears in the associated exposure map as one observation, ObsID 20000, dominated the counts here. This is he *Chandra* observation that was also identified to have the most extreme hot spot as we examined in Section 5.4.2.

Panels (b) and (d) show that the driver producing the AHSnuc is different from the full NHS and is located between noon and 20 LT. The AHSNuc consists of $\sim$ 7% of all mappable photons in our *Chandra* catalogue and dominates the noon population identified in the other two panels. Our analysis shows the AHSNuc driver is situated between both modelled magnetopause boundaries, suggesting that these auroral emissions may be sensitive to fluctuations in the location of the magnetopause and likely affected by external conditions, for example, changes in the solar wind.

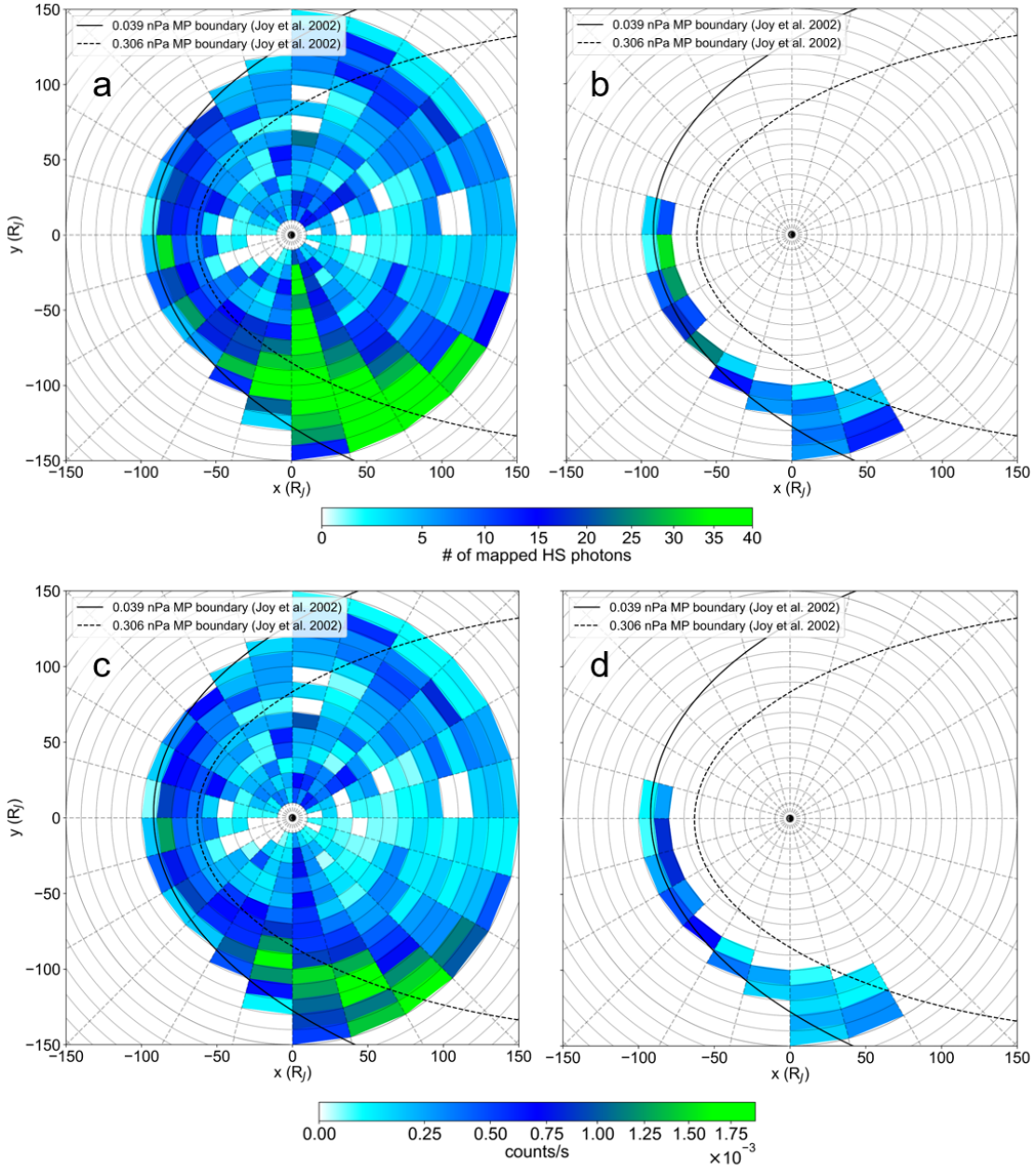

FIGURE 5.6: 2D histograms of our results from the Vogt et al. model with the GAM field model for all mappable (a) NHS and (b) AHSNuc photons for 26/29 observations. The associated exposure maps are displayed in (c) and (d), where we have normalised each photon with the length of the *Chandra* observation window for each event in the catalogue. The mapped magnetospheric positions of the data are binned by 10 R_J (radial distance; outlined by the concentric circles) and 1 hour local time (LT) of 1 hour. We overplot the compressed (black dashed line) and expanded (solid line) magnetopause boundary limits from the Joy et al. (2002) model. The Vogt et al. model mapping is also constrained by these limits. The colour bar represents the (panels (a) and (b)) number of mapped photons and (panels (c) and (d)) the associated average number flux (counts/s) in each bin. Figure taken from Figure 5 in Weigt et al. (2021a).

As the Vogt et al. model is built from mainly *Galileo* data, the mapping is restricted to where in the magnetosphere the spacecraft was able to sample during its campaign. *Galileo* was able to observe the jovian system from Ganymede's orbit ($\sim$15 R_J) out to $\sim$150 R_J, beyond which *Galileo* has insufficient data. The model is also sensitive to fluctuations in the ionospheric position of the photon. To calculate how sensitive the Vogt et al. model is to ionospheric position, we estimate the errors in our magnetospheric by attempting to propagate the uncertainty from each photons' position by applying the same model configuration (Vogt et al. model + GAM field model) to simulated data. We model a grid of simulated photons on Jupiter's northern auroral, each assigned the same SSL (i.e., to initially remove any viewing geometry biases) and apply a 2.5° shift in lat and S3 lon. This was applied to various grids of photons observed with different SSL to determine how this is coupled with photon position. We note the shifts in position are larger than the angular diameter of *Chandra HRC-I*'s PSF and therefore show the the most likely extreme case of error in the photon position, not observed in our catalogue. As shown by many observations of the jovian magnetosphere, the magnetopause is not static, even during comparable timescales of a *Chandra* observation, and therefore our mapping will not be exact. Our current model capabilities, across the whole field, do not account for the time evolution of the jovian magnetosphere as we usually have at most one spacecraft sampling the jovian system at a given time. Therefore our models are very limited. This is accounted for when we interpret our mapping results. It is therefore very likely the the ionospheric position is coupled with changing magnetospheric conditions as well as strongly dependent on the SSL. As discussed in Chapter 4, the flux equivalence model does not provide errors in radial distance and local time for each mapped photon. Since the *Chandra* observation occurred during a compression event, we applied a qualitative error the mapped positions to account for this. In this case however, the errors will be different for each observation and the error propagation calculation will be difficult to carry out given the model does not provide us with any errors. To try and combat this issue, we instead show in Appendix A.4 our results of applying shifts to the ionospheric position to at least show one aspect of the error that needs to be considered with this model (Figure A.1. This is shown in the supplementary material as we can only qualitatively apply this to our interpretations and is not the full error on the mapping.

As discussed in Chapter 4, the *Galieo* data used for the Vogt et al. model is likely to have been taken during more "averaged" magnetospheric conditions. In other words, during the full campaign of *Galileo*, Jupiter's magnetosphere was most likely to be expanded or returning to its equilibrium state leading to compression events not accounted for in the mapping (i.e., time evolution of the system over short timescales) as it is difficult to model. Vogt et al. (2019) observed that such compression events can shift the UV main oval auroral emissions towards Jupiter's magnetic pole at both

hemispheres, leading to a change in magnetospheric mapping of $\sim$ tens of R_J. We note that such effects will likely to not have a strong affect on our statistical study as we take an average over 26 observations but it must be considered for any future mapping analysis.

Like in Chapter 4, we interpret any populations located between both the Joy et al. (2002) model limits and next to the compressed boundary to be situated in a region of flux right on the magnetopause boundary or just outside the jovian magnetosphere. Therefore the various LTs the populations span is likely a result of all the effects we note here that may either shift the auroral position or move the auroral driver in the magnetosphere. We finally show in Appendix A.4 how the choice of field model can change the mapping and therefore our interpretations. We compare mappings with the aforementioned shifts in ionospheric mappings using the GAM and JRM09 field options. Again, we add this to the supplementary material (Figure A.2) as the full scale of the errors have yet to be explored in detail. Although we do note that the the GAM model maps photons closer to the magnetopause boundaries than JRM09, likely resulting from the more emphasised kink of the Ganymede footprint. We still use the GAM model results for our final conclusions here as the model is constrained by the UV auroral emissions. Future studies may want to ensure that their choice of field model is well-informed, especially with the introduction of JRM33 - the latest jovian internal field model using magnetometer data taken from all 33 orbits of *Juno's* main mission (Connerney et al., 2022) - with the latest current sheet model by Connerney et al. (2020) using , to account for the local time dependence of the field.

5.4.4 Searching for quasi-periodic NHS emissions

We use the Rayleigh analysis for jovian auroral X-rays first outlined by Jackman et al. (2018) and implemented in Chapter 4 (Weigt et al., 2020) on our statistical study. We search for any significant quasi-periodic oscillations (QPOs) for each interval the NHS and AHSNuc emissions were observed in our catalogue. Our timing analysis results for all identified QPOs within (a) NHS region and (b) AHSNuc are shown in Figure 5.7. All QPOs with a significance below our 99% significance threshold (p-value (p) > 0.01), from comparisons with 100,000 Monte Carlo simulations, are shown by the grey QPO-distribution. The p-value here has an identical definition to those used in Chapter 4 with the null hypothesis of no periodic signal detected. Any QPOs with calculated statistical significance $\geq 99\%$ ($p \leq 0.01$) are represented as the blue and green distributions for the NHS and AHSNuc respectively. The striped events show QPOs with significance $\geq 99.999\%$ ($p \leq 10^{-5}$) from our analysis. As was the case for the previous histograms presented in this research, all separate results for each interval are displayed in Tables A.5 and A.6 in Appendix A.5.

Here we define an interval to be each time the NHS, and therefore AHSNuc, rotated into view of *Chandra*. From the catalogue, we set this interval to be the time between the arrival times of the time-tagged photons and since we are focusing on the more intense NHS emissions, there is no contributions from the disk or other auroral sources that can make the light curve noisy. We set our interval time to be > 180 min between time-tagged photons striking the detector to allow us to separate NHS intervals to define each time the NHS is in *Chandra's* field of view. To ensure we had enough photons above possible statistical noise to perform our timing analysis, we remove any intervals with counts < 30, in either the NHS or AHSNuc, from our analysis. We present all our results with the relevant interval information (e.g., duration, *Chandra*-Jupiter distance, total counts, count rate) in Tables A.5 and A.6, for the extra information needed for possible future analysis. The remaining information on the table regards the number of mappable photons in both the NHS and AHSNuc. Our analysis identifies that $\sim 90\%$ of observations have $< 50\%$ of total photons being mappable using the Vogt et al. model. This unexpectedly low number of mappable photos may be a result of the drivers being located outside the model constraints ($< 15 R_J$ or > 150 R_J) and/or the mapping errors as discussed in the previous section, with the dominant effect likely from the SSL dependence (e.g., model disregarding many photons with poor viewing conditions, which may dominate most observations).

The duration of the significant QPOs identified in our catalogue are observed to be $\sim$ 3.9 - 36.4 min and $\sim$ 2.3 - 22.4 min for the NHS and AHSNuc respectively. Our analysis suggests that the differences in duration, as well as distributions, between the two regions result from the down-selection of the smaller AHSNuc region from the larger NHS emissions. This also shows that the full NHS region does not pulsate simultaneously with specific sub-structures, such as the AHSNuc, likely to pulsate independently from the full emissions. This is identified to be the case for many intervals in our catalogue of periods show that in many cases the full hot spot auroral region does not pulsate simultaneously and that smaller structures within the hot spot can pulsate independently from the surrounding auroral emissions. The longest significant QPO identified in our catalogue, with $p \leq 10^{-5}$, was observed when the NHS emissions first rotated into view on 18 June 2017 (ObsID 20001), as examined in great detail in Chapter 4. As shown in the AHSNuc distrbution of QPOs in Figure 5.7b), only two QPOs were observed to have duration $> 2\sigma$ of the mean period of 8.25-min. These QPOs were identified from ObsID 22146 (one of the *sim* 7-hr observation optimised for the hot spot) taken on 13 July 2019 and ObsID 20733 NHS2 (the second NHS interval of $\sim$ 11-hr) taken on 1 April 2018, with values of 21.7 and 22.4 mins respectively. Many observations contain QPOs in both the NHS and AHSNuc that produce significant pulsations during the same interval (e.g. ObsID 15669, 18677, 22146). In three instances, the NHS and AHSNuc produce the exact same

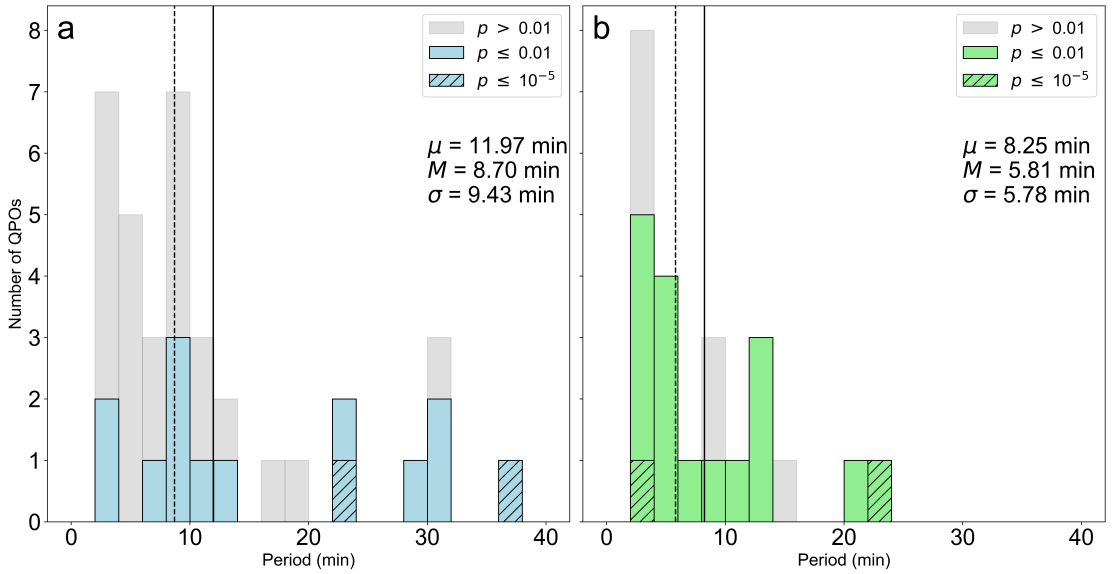

FIGURE 5.7: Resulting distributions of our Rayleigh analysis results for the (a) full NHS and (b) AHSNuc regions in our catalogue. Histograms are in an identical format as those shown in Figures 5.3 and 5.5. Any QPOs with with a statistical significance $< 99\%$ (p-value (p) > 0.01) when tested against our null hypothesis with 100,000 Monte Carlo simulations are shown by the grey distribution present in both panels. The distributions shown in blue and green indicate QPOs with significance $\geq 99\%$ ($p \leq 0.01$).The striped bars represent the most significant QPOs in our catalogue with $p \leq 10^{-5}$ (significance $\geq 99.999\%$) against our null hypothesis. This figure is taken from Figure 6 in Weigt et al. (2021a).

significant QPO (ObsID 16299 NHS2, 20002, 20733 NHS2), suggesting that the main X-ray auroral driver during this time dominated the entire NHS emissions, including those found in the AHSNuc.

In our research, many of the QPOs we observe agree with those previously identified from Jackman et al. (2018)'s statistical study. Jackman et al. (2018) noted that differences observed in the QPO period and their calculated significances are highly sensitive to what is defined as the hot spot region. They applied a simple down-select for the location of the hot spot at both poles based on the time taken for the emissions to traverse the disk. In our analysis we use a more strict spatial criterion for the northern hot spot emissions. Most of the QPOs we identify here are similar to those of Jackman et al. (2018), however many examples display a different quasi-periodicity and significance. This highlights the sensitivity of the QPOs to the spatial selection of the hot spot emissions and therefore likely shows how tightly constrained the driver, or divers, of the quasi-periodic emissions are. From our catalogue, we note no clear correlation between the identified QPOs in the NHS and AHSNuc and the average *Chandra*-Jupiter distance or any other auroral parameters dependent on distance (i.e. flux, power). Therefore, we can rule out distance having an effect on inhibiting any significant QPOs

TABLE 5.1: Table of *Chandra* ObsID, hot spot interval and results of the Jackknife test performed on statistically significant QPOs found in the NHS. All observations with $\Delta P > 5$ min from either Jackknife test are highlighted in bold text. Table taken from Table 1 Weigt et al. (2021a).

ObsID	Region	JK1[a] (ΔP (mins))	JK2[b] (ΔP (mins))
15669	NHS2	0.000	0.000
15671	**NHS2**	**19.742**	**19.921**
15672	NHS2	0.063	0.063
16299	**NHS2**	**0.000**	**9.803**
16300	NHS	0.000	0.223
18608	NHS1	0.000	0.000
18609	NHS	0.000	0.000
18677	NHS	0.237	0.473
20000	NHS3	0.000	0.000
20001[†]	NHS1	0.570	0.852
20002	NHS	0.000	0.000
20733[†]	NHS2	0.000	0.175
22146	NHS	0.000	0.000
22148	NHS	0.000	0.000

[a]Results from Jackknife test removing 1 photon.
[b] Results from Jackknife test removing 2 photons.
[†] Hot spot intervals with a 99.999% sig. QPO.

TABLE 5.2: Table of Chandra ObsID, hot spot interval and results of the Jackknife test performed on statistically significant QPOs found in the AHSNuc. Table taken from Table 2 in Weigt et al. (2021a).

ObsID	Region	JK1[a] (ΔP (mins))	JK2[b] (ΔP (mins))
15669	**AHSNuc**	**7.236**	**7.236**
15671	**AHSNuc2**	**19.388**	**19.564**
15672	**AHSNuc2**	**0.291**	**9.777**
16299	**AHSNuc**	**0.106**	**9.826**
18302	AHSNuc	0.000	3.198
18608	AHSNuc2	0.000	0.041
18677	AHSNuc	0.049	0.049
18678	**AHSNuc**	**11.398**	**11.398**
20001	AHSNuc1	0.072	4.182
20002[†]	AHSNuc	0.000	0.622
20733	**AHSNuc1**	**0.065**	**64.1806**
20733[†]	AHSNuc2	0.351	0.702
22146	AHSNuc	0.171	0.512
22147	AHSNuc	0.034	0.034
22148	AHSNuc	4.048	4.048
22151	**AHSNuc**	**0.000**	**5.681**
22159	**AHSNuc2**	**8.013**	**8.013**

Note. Identical format to Table 5.1

To further improve the statistical significance of the QPOs found here, we test the sensitivity of each of the light curves to the measured frequency of the signal. We do this by performing a Jackknife test (Quenouille, 1949, 1956) on the signals, by removing a number of photons from each of the light curves. We then run the identical Rayleigh analysis (e.g., using an identical frequency space, same number of steps as described in Chapter 4) on each new light curve (Efron and Stein, 1981). As carried out in Chapter 4, we then plot all the new power spectra together and calculate time interval between the minimum and maximum period, ΔP. The smaller the ΔP value, the less sensitive the light curve is to frequency and therefore provides as with a quantity to remove less robust QPOs from the timing catalogue. The variable throughput of the *Chandra* instruments means that very few photons make it to the detector. Therefore, the Jackknife test used in our statistical study removed a maximum of two random photons each time while removing degeneracy from the selection process. We present the results of our Jackknife testing for the removal of a single photon (JK1) and two photons (JK2) in Tables 5.1 and 5.2 for all QPOs with a significance above our 99% threshold. The first column in the Jackknife testing tables gives the corresponding *Chandra* ObsID for each observation. The remaining columns provide information on the region (NHS or AHSNuc) and interval during the observation window (i.e. NHS2 = NHS observed or rotated into view of *Chandra* for the 2nd time and similar nomenclature for AHSNuc) as well as the results from JK1 and JK2. Any hot spot intervals with a measured $\Delta P > 5$ min are bold text showing that, although statistically significant from the initial Rayleigh analysis, we interpret as not robust and highly sensitive to frequency. Therefore these periods are removed from our timing catalogue, bringing the number of significant QPOs from 14 to 12 for the NHS and 17 to 9 for QPOs within the AHSNuc. We note that the light curves found for the AHSNuc are composed of far fewer photons and are therefore will be more sensitive to frequency. However, Jackknife testing does not consider the coherence (i.e. how sinusoidal) of the signal resulting in signals with larger coherence will have a smaller ΔP. This results in some of the QPOs removed may still be robust but may not be in sinusoidal envelope and therefore penalised by the test. Future temporal studies of the jovian X-ray aurora will need to account for the coherence of the QPO signal to remove the biases produced from such tests. We do note however that this is non-trivial to implement in our current timing analysis.

The range of QPOs identified in our catalogue are likely associated with a variety of possible drivers. The large range in significant quasi-periodicities suggest that the possible X-ray auroral driver, or drivers, may be linked with ultra-low frequency (ULF) activity along the magnetopause boundary. Manners et al. (2018) identified pulsations of length $\sim$ 5-60 min from standing Alfvén waves in *Galileo* magnetometer throughout Jupiter's magnetosphere. From the identified magnetospheric location associated with the AHSNuc emissions, the driver of these emissions may be linked

with pulsed dayside reconnection on the magnetopause. Modelling conducted by Bunce et al. (2004) identified that dayside cusp reconnection processes are likely to generate pulsations of ∼30-50-min and are far more active when the jovian magnetosphere is compressed. Cusp reconnection may therefore be a likely driver for larger QPOs located on the dayside magnetopause boundary found in our catalogue.

From our timing and mapping analysis, we suggest that multiple auroral drivers are likely responsible for X-ray production along the noon-dusk flank magnetopause boundary. This hypothesis is supported by the distributions shown in Figures 5.6 and 5.7. These suggest that multiple drivers, exhibiting either semi-permanent or sporadic behaviour, are the main contributors to driving the X-ray auroral emissions in the northern auroral region.

5.5 Discussion

5.5.1 Characteristics and polar conjugacy of auroral X-ray emissions

Our analysis presented in in Section 5.4.1 clearly identify an asymmetry in the auroral X-ray brightness and morphology between the northern and more diffuse southern auroral emissions across our catalogue. This has been observed in research examined here as well as previous case studies (e.g., Chapter 4 Dunn et al., 2017; Weigt et al., 2020) and, as discussed previously, is likely a result of an amalgamation of possible effects including unfavourable viewing geometry of the southern region (Dunn et al., 2017); different field configuration at the poles (Connerney et al., 2017, 2018) as well as possible opacity effects produced by the jovian atmosphere (Ozak et al., 2010). *Juno* observed the magnetic field at the North pole to be twice as strong as that observed at the South with a non-dipolar topology (Moore et al., 2018). The topology of the southern magnetic field is observed to be dipolar. Such a difference in magnetic field strength and configuration may lead to a preference for ion precipitation in the North over the South, explaining the differences we observe in our research. Recent *Juno* observations by Kotsiaros et al. (2019) found that South hosts more persistent and powerful electron currents which may inhibit the ion injections into the ionosphere required for X-ray production. One other possible explanation is that a stronger mirror force will be generated in a non-dipolar field in the North than the dipolar case observed in the southern auroral region. As a result, the stronger mirror force will produce the large potential drop, creating the ideal site for ion acceleration. More ions in the North will be trapped and likely gain the the larger energies needed for ion precipitation,necessary for auroral soft X-ray production (Cravens et al., 2003; Houston et al., 2020) as observed here with the most intense extended tear-drop morphology in the NHS. The weaker mirror force in the South will therefore lead to

fewer ions being trapped and accelerated to the required energies for precipitation. This may therefore explain the dimmer and more diffuse emissions in the South.

A recent study by Dunn et al. (2020b) identified three sub-categories of the X-ray auroral emissions from a joint *Chandra-XMM Newton* campaign in 2007: hard X-ray (HXR: energies $>$ 2 keV) bremsstrahlung, coinciding with the UV main emission; regular and irregular pulsed SXR emissions and dim flickering emissions which vary on short timescales. Spectral analysis from *XMM-Newton* identified the ions producing the SXR emissions were iogenic in origin, agreeing with recent findings from Wibisono et al. (2020). They also observed that the brightest X-ray auroral emissions were found to coincide with expansions of the jovian magnetosphere with a more patchy and extended morphology across the northern auroral region. During a compression, the auroral emissions were concentrated into a more localized bright auroral region at S3 lon. $\sim$160° - 180°. Our analysis presented in Section 5.4.1 agrees with the Dunn et al. (2020b) analysis with the averaged northern emissions observed to be more elongated in nature across our *Chandra* catalogue. The averaged NHS emissions, Figure 5.4, also highlight the spatial variability of the NHS emissions, likely reflecting the different the different magnetospheric conditions at Jupiter. The brightest NHS emissions, located within the tear-drop region identified in Figure 5.2, is observed in approximately the same location as the X-ray *core region* discovered by Kimura et al. (2016) during a 2014 UV-X-ray campaign. Therefore it is likely this brightest tear-drop region may be a recurring structure/characteristic of the northern auroral X-ray emissions.

Previous case studies analysing the X-ray hot spot emissions have occurred during compressions of the jovian magnetosphere (e.g., Chapter 4 Dunn et al., 2016; Wibisono et al., 2020). Dunn et al. (2016) observed localized brightenings within the northern auroral emissions, as also identified later by Dunn et al. (2020b), and a more extended morphology, as examined in great detail in Chapter 4 (Weigt et al., 2020), during different compression events. Wibisono et al. (2020) also identified that, contrary to expectation, the X-ray emissions were dominated by precipitating iogenic ions as opposed to solar wind ions during the compression. However findings from Kimura et al. (2016) identified that the core region count rate was positively correlated with the solar wind velocity and not the auroral morphology. Therefore the flux within this bright auroral core may respond to the magnetosphere's response to changing solar wind dynamic pressure as opposed to the solar wind affecting the auroral emissions directly (i.e., lack of solar wind ions observed). The variable morphologies we observe in the northern x-ray auroral emissions (as examined in this study and the Dunn et al. (2020b) sub-categories) is therefore likely a result of changing dynamic pressure and changes with the jovian magnetospheric response to external changes

5.5.2 Morphological variability and origins of the concentrated NHS emissions

Our analysis in Section 5.4.2 examines, for the first time, the more typical and extreme behaviour of the NHS emissions as shown in bur polar project 2D histograms. Here we discover a statistically significant auroral structure within the NHS emissions present in all of the *Chandra* catalogue, using our numerical thresholding: the AHSNuc. This sub-structure is observed to be less variable than the full NHS emission across the full catalogue (Figure 5.5) and maps to the noon magnetopause boundary. This provides further evidence of the hot spot being more segmented than previous thought (e.g., Chapter 4, Dunn et al., 2016). This also highlights that it is likely the auroral emissions are driven from multiple drivers as opposed to one single one, eluded to by the classic hot spot picture. We also note that power and brightness of this region is non-uniform across the catalogue, again eluding to the idea that internal and/or external changes to the jovian system, like variations in the solar wind dynamic pressure, may affect the AHSNuc itself as well as any surrounding emissions in a similar manner to the averaged X-ray auroral emissions.

The more typical behaviour observed from the NHS emissions (occurrences of $> 70\%$ in our) are found to be confined to an ellipse of dimensions $\sim 15^{\circ}$ (semi-major axis) and $\sim 7.5^{\circ}$ (semi-minor axis), with centre at (168° S3 lon, 65° lat). In this auroral region, the occurrence of X-ray photons is found to vary with a gradual gradient at higher S3 longitudes situated away from the AHSNuc, suggesting a movement of localised brightening of the intense NHS emissions that can occur during a compression event (e.g., Dunn et al., 2016, 2020b). The most extreme NHS behaviour (occurrences $\leq 20\%$) surrounds the boundary of the ellipse that defines typical NHS behaviour. As suggested by Dunn et al. (2020b), the more expanded regions of the NHS emissions may be a response to jovian magnetosphere expansions from low solar wind dynamic pressure. Therefore our analysis suggests, within the accuracy of our mapping, very few *Chandra* observations occurred in tandem with an expansion event.

Our results from the Vogt et al. (2011, 2015) flux equivalence model with the Grodent Anomaly Model (GAM) (Grodent et al., 2008) field model are presented in Figure 5.6. We identify two ion populations, and therefore driver locations, along the noon-dusk magnetopause boundary when we use the mappable NHS photons as an input to the model: one large population in the pre-dusk to pre-midnight sector on the dusk flank which dominates the majority of mappable photons and a smaller, more concentrated cluster at noon. The dominant dusk flank ion population identified here agrees with previous literature using the Vogt et al. model, with various internal field options, to examine the magnetospheric origin of the NHS emissions (e.g., Chapter 4, Kimura et al., 2016; Dunn et al., 2017), all suggesting that the auroral driver may be related with Kelvin-Helmholtz instabilities (KHIs) on the dusk flank. KHIs generated on the

magnetopause boundary are observed to be responsible for energy, momentum and plasma transfer between the turbulent plasma in the magnetosheath and the less dense magnetosphere. This phenomena has already been observed at the jovian magnetopause boundary (Delamere and Bagenal, 2010; Desroche et al., 2012), where the velocity shear between the flow generated by the solar wind flow and plasma in the magnetosheath flow is greatest. Simulations of the complex jovian magnetic field suggest that KHIs are likely to dominate on the dusk side magnetopause boundary (Zhang et al., 2018) contradictory to the expectation that velocity shears should be greatest in the pre-noon sector where the plasma flows (of the solar wind and sheath) move in opposite directions. KHIs have also been observed at Saturn (e.g., Masters et al., 2012; Delamere et al., 2013)). From these observations, they theorised that the dawn-dusk asymmetry of KHIs observed in the magnetosphere may be a result of fast-growing KHIs at the dawn sector being harder to interpret from the spacecraft data in comparison than the slow-growing KHIs observed at the dusk boundary (Ma et al., 2015). This is consistent with our analysis here using the Vogt et al. model.

We compare our Vogt et al. results with those from a statistical study by Manners and Masters (2020) analysing ultra-low frequency (ULF) activity in the jovian magnetosphere from *Galileo* data. We find that equatorial conjugate positions of both populations identified in our study are consistent with the locations of the most occurrences of ULF wave activity. Manners and Masters (2020) observed the most active ULF wave active regions to be near the noon sector at a radial distance of $\sim$ 40 - 100 R_J (e.g., outer magnetosphere) and the dusk-midnight sector at of $\sim$ 20 - 120 R_J, mainly confined to the magnetopause boundary. The generated ULF wave power was observed to be anti-correlated with distance, with the weakest wave power located in the outer magnetosphere. The outer magnetosphere is believed to be the location of the majority of the X-ray ($>$ 60 R_J; Dunn et al. (2016)). In the terrestrial magnetosphere, KHIs on the magnetopause boundary trigger ULF wave activity (Hasegawa et al., 2004), which can therefore lead to possible reconnection within the KHI vortices (Nykyri and Otto, 2001). Our analysis therefore suggests that X-ray auroral drivers may be linked to possible ULF wave activity in the jovian magnetosphere due to the drivers of both likely residing in the same magnetospheric locations.

5.5.3 Timescales of possible noon and dusk flank X-ray drivers

As discussed throughout this research, much of the literature surrounding jovian X-ray auroral emissions suggest that the auroral driver is likely situated on the magnetopause boundary. In the noon region of the jovian magnetosphere, Bunce et al. (2004) suggested a high-latitude cusp reconnection model may be responsible for driving the X-ray emissions, producing $\sim$30- to 50-min QPOs. Their model calculates that cusp reconnection would contribute to $\sim$ few Rayleighs (R) of the X-ray

brightness/intensity up to a few kR (kilo-Rayleighs). We do observe the lower limit of the cusp model brightness in the AHSNuc in this research, which maps to the noon magnetopause boundary, and comparable X-ray auroral power to the values predicted by the Bunce et al. (2004) model. Therefore cusp reconnection may be a likely candidate for the noon driver we observe in this research. The upper limit of auroral X-ray intensity predicted by the model may be greater than what we observe here however we note our flux (and power) calculations do not account for the poor throughput of HRC-I and/or any opacity effects in the jovian atmosphere (Ozak et al., 2010). Therefore, we suggest that the AHSNuc is likely driven by cusp reconnection and the temporal variability we observe in the identified significant QPOs may be associated with reconnection activity on the noon magnetopause boundary, linked to solar wind flow.

Other types of magnetic reconnection on the noon sector may also contribute to driving the AHSNuc emissions. For example at Saturn, Guo et al. (2018) observed signatures of reconnection driven by the planet's rotation from *Cassini* magnetometer and charged particle data while the spacecraft was in the kronian plasmasheet. Guo et al. (2018) observed multiple reconnection sites along the plasmasheet and a secondary "magnetic island", suggesting that this type of reconnection is not in a steady-state. With the rapid rotation of Jupiter, a similar reconnection mechanism is likely to occur in Jupiter's magnetosphere and may be provide the reason of the identified noon population also located planetward of the magnetopause boundary on the equatorial plane. *Juno* has observed signatures of magnetic reconnection on the jovian dawn flank magnetopause, where *Juno* performed its orbit insertion (Ebert et al., 2017a). Reconnection in this region is believed to contribute more to the magentospheric dynamics of the jovian system during intervals of compression events (Huddleston et al., 1997). This therefore suggests that both cusp and rotationally driven reconnection process may be a likely candidate as an auroral driver for the noon ion population responsible for producing the AHSNuc.

Many previous studies in the literature have suggested a link between the quasi-periodic soft X-ray auroral emissions and global ULF waves in the jovian magnetic field (e.g., Gladstone et al., 2002; Dunn et al., 2017; Yao et al., 2021). ULF waves have been observed by various spacecraft throughout Jupiter's magnetosphere (e.g., Khurana and Kivelson, 1989; Wilson and Dougherty, 2000b) producing pulses within 10- to 60-min, the significant QPO range proposed by Manners et al. (2018) for standing Alfvén waves. The Manners et al. (2018) ULF period range is very similar to the results produced from recent, more complicated models designed specifically to simulate field line resonances within the jovian magnetosphere (Lysak and Song, 2020).

The standing Alfvén waves are likely to be a by-product of KHIs occurring on the magnetopause boundary. The cusp and rotationally driven-ike "drizzle" reconnection processes we examine here may produce linear sinusoidal KHI waves or *surface waves*. In the terrestrial ionosphere, surface waves drive standing Alfvén waves on field lines (Mann et al., 2002; Rae et al., 2005) and therefore provide a mechanism to transport ULF wave activity from Jupiter's outer magnetosphere planetwards towards the to the ionosphere, gaining power as it propagates as found by Manners and Masters (2020). Observations and simulated data of the jovian magnetosphere suggest that surface waves on the dusk flank boundary may be advected from the dayside boundary, at LT < 10, as the waves propagate in the direction of increasing velocity shear (Zhang et al., 2018; Manners and Masters, 2020). As the velocity shear increases, the KHI waves become more unstable and evolve to a non-linear KHI wave with rolled vortices and larger amplitudes. First suggested by Dungey (1955), non-linear waves are usually, or predicted to be, observed in KH-unstable regions located on the dawn and dusk magnetopause (i.e., regions of greatest velocity shear) where the KHI is likley to grow. As observed in Earth's magnetosphere, the orientation of the magnetic field carried by the solar wind, the interplanetary magnetic field (IMF), cna influence the thickness and location of the magnetosphere's KH-unstable (Farrugia et al., 1998; Foullon et al., 2008). Due to the vast size of the jovian magnetosphere, few studies and observations have been conducted regarding possible locations of KH-unstable regions at Jupiter. A recent study by Masters (2018) suggested that the jovian magnetosphere will be dominated by viscous-like effects, including KHIs growing in KH-unstable regions, over reconnection-type effects compared to the terrestrial magnetosphere. This is further evidence to suggest the possible correlation we observe here between X-rays and ULF may indeed exist in the jovian magnetosphere. In its current extended science mission, *Juno* will move towards the dawn-midnight magnetosphere where dusk flank activity can be analysed in greater detail.

Although recent, and more updated, global simulations of the jovian field by Zhang et al. (2021) revealed further complexity to Jupiter's magnetic field. Their simulations agreed with previous literature, showing that the rate of reconnection on the dayside of the jovian atmosphere is too slow to generate a fully open polar cap as observed at Earth, on timescales of a jovian rotation. Instead the majority of the jovian "polar cap" is associated with magnetic flux that extends from the planet's interior to the outer magnetosphere, piling up at the dawn flank due to the fast differential rotation of the plasma in this region pushes the filed towards noon. Such an unusual configuration will affect the auroral morphology we observe, across multiple wavelengths, at Jupiter and may provide an explanation for how dynamic the auroral emissions are and how numerous magnetospheric drivers may be responsible for energising the ions needed for the X-ray auroral emissions.

Manners and Masters (2020) identified significant ULF QPOs linked with standing Alfvén waves, spanning $\sim$ 5-60 min across all local times from their extensive study of heritage jovian magnetometer data. The *Galileo* spacecraft sampled the jovian magnetosphere over a large range of local times with most of its dwelling time in the dusk-dawn sector. The QPOs indented from the heritage magnetometer dataset are comparbale with the range of significant QPOs observed in our analysis. Studies of Saturn's magnetosphere have found quasi-pulsations of $\sim$ 35 - 50-min from KHI waves identified from *Cassini* magnetometer data in the dawn and dusk flank of the kronian magnetopause boundary (Cutler et al., 2011; Masters et al., 2009). Since the quasi-pulsations are within the ULF periodicity range, Manners and Masters (2020)'s idea of weaker, low-amplitude ULF wave energy building up in the dusk flank due to advection of ULF waves from the noon sector may be a plausible mechanism that can be applied to the jovian magnetosphere. How ULF wave energy can modulate local ion populations in the magnetosphere to energise and pitch-angle scatter ions into the loss cone is still up for debate. The KHIs along the dusk flank magnetopause may be responsible for the various auroral morphologies categorised by Dunn et al. (2020b). As examined in Chapter 2, compression events cause the jovian magnetopause stand-off distance to shrink and move closer to the planet. As a result, the dusk flank also shrinks leading to the production of fewer but more powerful KHI waves. These waves are likely to drive the ULF wave activity on the magnetopause boundary and produce the more concentrated and localised X-ray brightening we observe here. During expanded magentospheric conditions, the more patchy auroral X-rays we observe may result from more vortices being produced, across a larger magnetopause boundary, generating less powerful KHI waves. Therefore this suggests that the "hot spot" emissions are likely produced from multiple processes not just a single spot region. We suggest that using such nomenclature, like "hot spot", may be unsuitable and misleading to describe the jovian auroral X-ray emissions.

The mapping and timing analysis we present in our statistical study suggest that multiple drivers along the noon-dusk magnetopause boundary, including, but not limited to, cusp/dayside reconnection and KHIs may be responsible for the auroral X-ray emissions. The drivers we identify in our research on the noon-dusk magnetopause boundary may be linked to possible ULF wave activity when compared to the location and significant pulsations highlighted by Manners and Masters (2020)'s statistical study. The link between the auroral X-rays and ULF activity (i.e low amplitude ULF waves advected to the nightside?) is still not fully understood. In this research we have hopefully provided the foundations to explore this unknown region in more detail in future observations, especially when *Juno*'s extended mission takes it further towards the dusk flank magnetosphere. This will allow us explore ULF wave activity on the dusk flank in more detail and how it is connected to the pulsation X-ray aurora we observe in both hemispheres.

5.6 Summary

We present the first *Chandra* statistical study of its kind, analysing $\sim$ 20 years worth of data spanning multiple solar cycles, to analyse typical and extreme behaviour of the so-called "hot spot" emissions. The analysis we present here includes mapping and timing analysis to identify any statistical significances in the spatial and temporal behaviour of the emissions. We identify the AHSNuc, a region of concentrated X-ray auroral emissions that is present throughout the catalogue, using the numerical criterion for photon concentration defined in Chapter 4, that maps to the noon magnetopause boundary. The largest population of mappable photons reside in the dusk flank boundary, dominating our magnetospheric mapping results. These results suggest that the northern auroral X-rays are driven from multiple drivers which are associated with possible ULF wave activity on the magnetopause boundary. Our analysis suggests that the likely drivers capable of accelerating the ions to energies required for precipitation are dayside reconnection and KHIs along the magnetopause boundary, possibly linked with ULF wave activity. We frame the results from our catalogue with previous key studies analysing the northern auroral X-ray emissions and provide the foundations for future studies.

We hope that the research presented here helps narrow down the list of possible X-ray auroral drivers using a consistent definition of the NHS emissions. The idea of a single driver producing one auroral "hot spot" seems less likely from the conclusions made in our analysis. *Juno*'s extended science mission will take the spacecraft through dusk-midnight sector, with far better coverage of the southern magnetosphere. Therefore a similar statistical study can be conducted for the southern auroral emissions with comparisons made between the poles. From there, we can observe and understand how the X-rays behave on a global scale and how the possible drivers generate the asymmetries we observe between the northern and southern auroral emissions.

Chapter 6

Identifying jovian X-ray auroral families: tying the morphology of X-ray emission to associated magnetospheric dynamics

"Ok, one last time. These are small, but the ones out there are far away. Small... Far away... Ah forget it."
- Dermont Morgan (Father Ted), 1996

Recommended and inspired by Sarah Badman. Watch this Father Ted clip[1] (https://www.youtube.com/watch?v=MMiKyfd6hA0) for more context and a small breather.

6.1 Abstract

Many recent studies have found that using the single "hot spot" nomenclature may not be representative of the jovian X-ray auroral emissions. The variability in both the temporal and morphological behaviour of the X-ray aurora suggest the possibility of more than one potential magnetospheric driver. These drivers are likely located on the noon and dusk flank magnetopause boundary. In this study we aim to explore this idea further by separating the concentrated X-ray emissions within the northern auroral region into physics-informed 'X-ray auroral families'. We apply this analysis to the catalogue of high spatial resolution observations by Chandra during the *Juno* -era. We define the following families: *X-ray noon*, *dusk*, *polar region*, *dawn* and the

[1] Morgan et al., 1996: *Father Ted*: Season 2, Episode 1: 'Hell'

low latitude extension (LLE) region. The X-ray polar region encompasses both the X-ray noon and dusk ionospheric regions, poleward of the auroral main oval; X-ray dawn is found to overlap a portion of the main oval emissions and the LLE region is found to coincide with a likely active site for particle injections found by the *Hubble Space Telescope (HST)*. We compare the distribution of auroral photons within each of the X-ray families to magnetospheric dynamics found from previously defined ultra-violet (UV) auroral families (Grodent et al., 2018) and *Juno* data to determine the state of the magnetosphere during each *Chandra* window. We identify two likely categories of X-ray morphology from our family definitions: fully polar aurora and low latitude emissions (e.g. when LLE photon distribution $>$ 10% of all auroral emissions). The preliminary results we present here suggest that the non-uniform distribution of X-ray auroral photons across the regions, within a central meridian longitude (CML) range of 80° - 250°, is more likely associated with the switching on/off of magnetospheric drivers opposed to viewing geometry effects. We also find that the majority of events exhibiting fully polar aurora occurs during or just after a compression event, identified by *Juno* and UV *HST* data. Therefore combining both the X-ray and UV families allows us to simplify complex auroral behaviour, making logical connections between the emissions and provides us with a possible proxy to monitor solar wind/magnetospheric conditions when an upstream monitor is absent. Further analysis is outlined to help improve our X-ray families and verify their use as a robust method to predict the likely magnetospheric conditions during the observation window.

6.2 Introduction

As examined at great length in Sections 2.2 and 2.4, the jovian auroral emissions are very complex and are highly variable in their morphological and temporal behaviour. The X-ray emissions still remain the most elusive of the observable aurora with, as discussed in Sections 2.4, many recent studies trying to understand the highly sophisticated driver(s) capable of energising the ions to such an extent to allow charge stripping and charge exchange to take place in the jovian ionosphere for soft X-ray (SXR: $<$ 2 keV) production (e.g., Chapter 5, Dunn et al., 2020a,b). The SXRs are produced from precipitating MeV ions originating in the outer magnetosphere and are sometimes observed to be coincident with flaring UV emissions within the UV active polar region (Dunn et al., (2022), in prep.). The HXRs result from bremsstrahlung emissions from precipitating electrons, with the auroral emissions observed to sometimes coincide with the UV main oval (e.g., Branduardi-Raymont et al., 2008; Dunn et al., 2017). This suggest that the precipitating electrons responsible for the HXR and UV main oval auroral emissions are likely to originate in the same region of the middle magnetosphere. Recent and ongoing studies are investigating how the

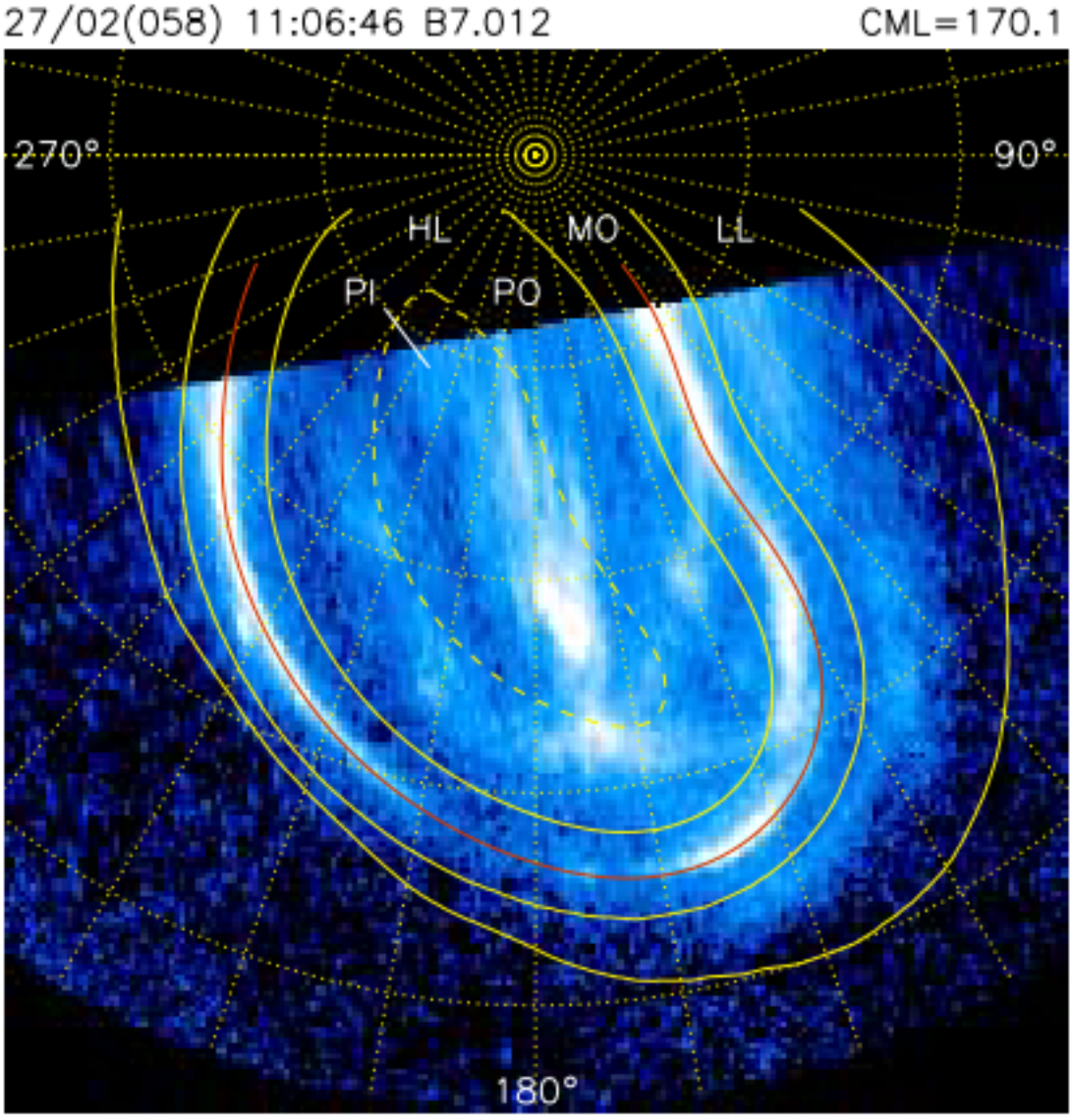

FIGURE 6.1: Planetocentric polar projection of the UV northern auroral emissions observed by HST on 27 February 2007. The projection is plotted on a 10° × 10° S3 longitude-latitude gird (outlined by the dotted yellow line). The log colour scale used is saturated at 500 kR. The dashed yellow lines outline the polar inner (PI) and outer (PO) regions. The low-latitude (LL), high-latitude (HL) are labelled on the projection. The main oval (MO) is outlined by the red contour. Figure taken from Figure 1 in Nichols et al. (2009).

X-rays are connected to other auroral emissions in the EM spectrum via plasma waves such as electromagnetic ion cyclotron (EMIC) waves for precipitating ions (e.g., Yao et al., 2021). Other studies have looked at how the auroral hard X-rays (HXR: > 2 keV), likely produced from electron bremsstrahlung in the middle magnetosphere, are correlated with the more intense UV auroral emissions (e.g., Wibisono et al., 2021). We continue this ongoing effort to determine the X-ray auroral drivers in this research by sorting the X-rays into morphological categories based on their ionospheric position.

Previous studies analysing the jovian UV aurorae from the *Hubble Space Telescope (HST)* have isolated various regions within the auroral emissions to explore the variation across them. Nichols et al. (2009) identified three auroral components within the UV northern emissions from two 2007 *HST* campaigns: (1) the main oval (MO), (2) low-latitude (LL) aurorae and (3) high-latitude (HL) auroral emissions. These regions are outlined and labelled on the HST image taken on 27 February 2007 as shown in Figure 6.1. From these isolated regions, they calculated the auroral power (through observation and visibility modelling) and compared to predicted solar wind conditions propagated from Earth to investigate the most likely cause of variation. Their results showed that generally the auroral power from the polar regions (low- and high- latitude auroral emissions) were uncorrelated with that of the main oval unless a dawn storm or enhancements due to a compression occurred. During a dawn storm, the main oval and high-latitude auroral emissions were found to be enhanced while compression events caused the main oval emissions to become more narrow, enhanced and seem to be shifted slightly poleward from their typical location. They found that in these intervals all other emissions were faint with the exception of distinct, bright arcs in the post-noon sector of the polar emissions.

More recently Grodent et al. (2018) characterised 118 *HST* images during *Juno* orbits 3 to 7 (from 30 November 2016 up to and including 18 July 2017), using six new definitions of "UV auroral families" to help provide a simplified description of the complex dynamics observed in the UV auroral emissions. These new definitions allowed different morphologies to be compared to establish logical, plausible connections to identify the responsible auroral driver and allowed a more detailed quantitative way to analyse variations of spatial behaviour. The Grodent et al. (2018) auroral family definitions are summarised as follows:

1. ***'Q'* (Quiet)**: very low auroral power (< 1 TW) in a more expanded and broad main oval or main emission (ME) region and as well as dimmer auroral emissions in equatorial regions (e.g., the Io footprint (IFP)). The jovian magnetosphere can be assumed to be mainly unperturbed.

2. ***'N'* (Narrow)**: very narrow and expanded ME (width $\sim$ 200 - 300 km) with average auroral power. This suggests a quiet magnetosphere with a slow increase in mass loading (i.e. magnetospheric activity increasing due to moderate acceleration of plasma and a slight enhancement of the field aligned currents (FACs) related to the ME through corotation - see Section 2.2).

3. ***'U'* (Unsettled)**: the intermediate stage between *Q* and *N*. ME relatively wide but fainter at dawn and narrower in the afternoon sectors.

4. ***'I'* (strong Injections)**: strong enhancements at $\sim 140^\circ$ - 170° S3 longitude, equatorward of the ME (i.e. low-latitude emissions) with a corner-shape

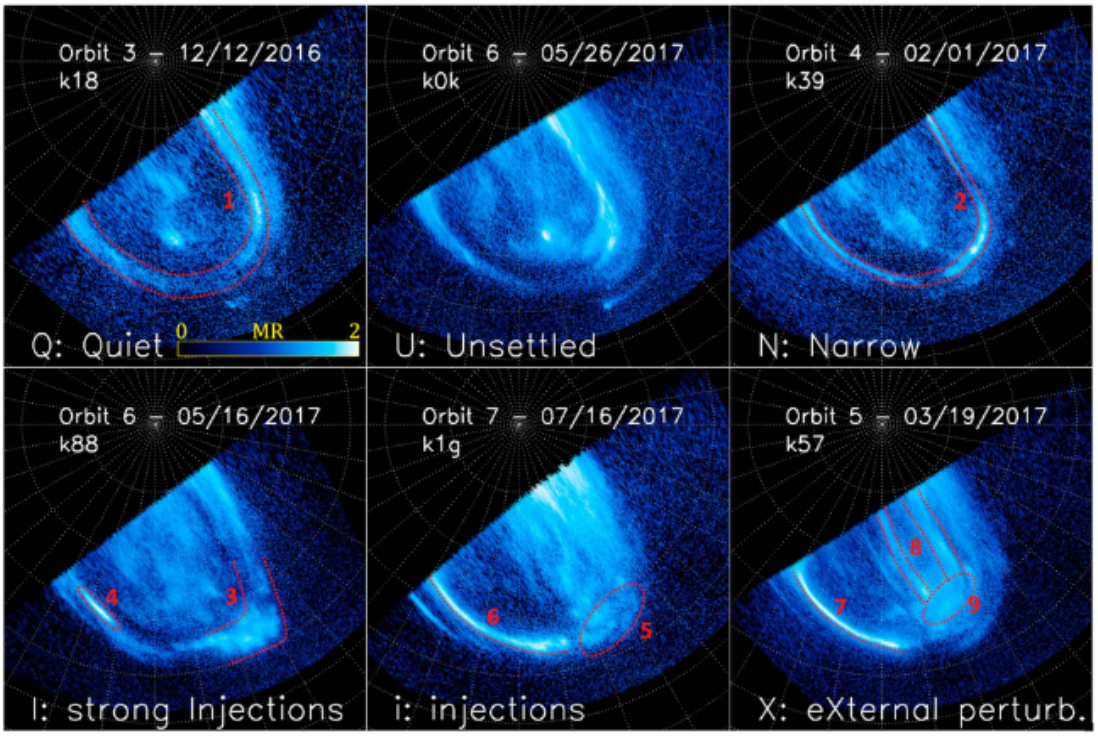

FIGURE 6.2: Polar projections of the identified auroral structures (highlighted by red-dashed lines, ellipses and number from 1 - 9) corresponding to each UV auroral family (Q, U, N, I, i and X). Each auroral family corresponds represents the magnetospheric dynamics, potentially influenced from internal and external drivers, responsible for producing such emissions. Each UV auroral family is discussed in more detail in Grodent et al. (2018). Figure taken from Figure 3 from Grodent et al. (2018).

morphology. This feature relates to dynamics in the inner jovian magnetosphere are can be found to coincide with possible dawn storms.

5. ***'i'* ([moderate] injections)**: very similar morphology to *I* with an overall lower brightness of the equatorial auroral. This family can be interpreted as an early/late stage of *I*.

6. ***'X'* (eXternal perturbation)**: very strong and contracted ME with large enhancements at dawn with bright and narrow morphology in the afternoon sector. Poleward region exhibits bright, pulsing patches and arcs parallel to ME. This type of family is likely associated with responses to the interplanetary medium (IM) surrounding the jovian magnetosphere (e.g. a compression region). Equatorward emissions are dimmer as inner magnetosphere is less responsive to external fluctuations.

Figure 6.2 shows an example of how the auroral families were identified and labelled in the *HST* data during *Juno* orbits 3 - 7, based on various identifiable features and behaviours within the UV northern auroral emissions. All Grodent et al. (2018) auroral definitions are shown in Figure 6.2 with the defining features highlighted with

red dashed lines, ellipses and numbers "1 - 9". For example, the corner of emissions labelled as "3" overplotted on the '*I*' (strong injections) family is typical to this morphology.

Grodent et al. (2018) observed that auroral emissions corresponding to the *U* family occurred most often (29.5% of 118 *HST* images) and were identified to be connected to the *Q* family due to slight changes in brightness of the ME. The connection was only interrupted by episodes of injection events (*I*, *i*) which were observed to precede or follow the *N* family. The moderate injections, *i*, were identified after auroral structures associated with compressions of the IM (*X*). The disturbances from IM compressions can trigger episodic injections of trapped particles in the middle magnetosphere, as observed by Louarn et al. (2014) from Galileo particle and radio measurements.

In this study we utilise the techniques used for the UV auroral emissions to isolate and define specific auroral structures and apply them to the concentrated northern X-ray emissions in an attempt to find a link between X-ray morphology and magnetospheric dynamics. We use concurrent *HST* data to help provide vital magnetospheric context to the *Chandra* observations, using the Grodent et al. (2018) auroral definitions, and model the visibility of the X-ray auroral families we define here, similar to Nichols et al. (2009) (Sections 6.4.1 and 6.4.2). We then compare the magnetospheric dynamics found from the X-ray-UV data and compare with the magnetospheric conditions identified from the *Juno* spacecraft (Bolton et al., 2017), using radio and magnetometer data. This allows us to determine the state of the jovian magnetosphere and to compare against the solar wind predictions of the Tao et al. (2005) 1D MHD solar wind propagation model (Section 6.4.3). Similar to the logic applied by Grodent et al. (2018), the goal of this study is to simplify the complex morphological variations of the X-ray aurora, allowing plausible connections to be made between the auroral emissions and magnetospheric dynamics. Linking our X-ray families with the UV equivalent may allow us to infer the state of the jovian magnetosphere in the absence of upstream solar wind data.

6.3 Contemporaneous remote sensing UV and X-ray observations with Juno Waves and MAG data

We use the catalogue of *Chandra* HRC-I (High Resolution Camera) observations described in Chapter 5 taken during the *Juno* main mission from 24 May 2016, when *Juno* was on approach to Jupiter upstream of the solar wind, up to and including 8 September 2019. These observations include those taken during Juno approach (in the solar wind), while Juno was at apojove (near the dawn magnetopause), during several perijoves and intervals when *Juno* was inside the jovian plasmasheet. We then correct

the *Chandra* observations using the McEntee (2021) updated mapping algorithm to ensure that we have accounted for the time-dependent degradation of the *Chandra* HRC-I[2] instrument while removing any contaminant background (more details found in McEntee at al. (2022)). As we are focusing on the more concentrated X-ray auroral emissions rather than the more diffuse disk emissions, which can be difficult to distinguish from the background, the change in count rate from the Weigt et al. (2021a) catalogue is minimal and does not change the interpretation of the results. We do note that accounting for the instruments increasing degradation is crucial for future observations and must be taken into account in future studies during the *Juno* extended mission (especially when mapping X-ray emissions to the jovian disk).

To help provide essential magnetospheric context to the X-ray auroral emissions, we use *HST* observations concurrent with *Chandra* data. We analyse 17 *Chandra* observations during the *Juno*-era, 14 of which have *HST* Space Telescope Imaging Spectrograph (STIS) data $\pm$ 1 day from the *Chandra* window, to allow the magnetospheric conditions to be analysed in detail. These 14 *HST* observations focus on the northern auroral emissions of which components within the UV aurora have been identified using the Grodent et al. (2018) definitions. All observations used in this research are shown in Table 6.1. To compare with contemporaneous *Juno* data, both the *Chandra* and *HST* intervals have been corrected for the Juno-Earth light-travel time, taken from ephemeris data[3]. The specifications of both remote sensing instruments' are discussed in Chapter 3.

We then compare these observations to remote sensing radio data from *Juno* Waves (Kurth et al., 2017) and *in situ* data from the magnetometer (*Juno* MAG Connerney et al., 2017) to confirm the magnetospheric state during these intervals and potentially identify any internal drivers (e.g. such as particle injection signatures). As shown in Appendix A.1 and described in Section 3.2, *Juno* was executing an eccentric polar orbit which allows it to sample the inner, middle and outer magnetosphere during its 53-day orbit. Chandra observations were taken coinciding with different stages of Juno's *in situ* exploration of the Jupiter system including perijoves, apojoves and plasmasheet crossings. This also gives us the opportunity to look at *in situ* data during these various stages to analyse the different auroral drivers located at various sites within the jovian magnetosphere. We take this into account when interpreting these data as processes within regions drive the jovian magnetosphere, and therefore the auroral emissions. The specifications of the *Juno* instrument suite are also described in detail in Chapter 3.

[2]See Section 7.7 - 7.10 in https://cxc.harvard.edu/proposer/POG/html/chap7.html for more details

[3]Ephemeris data associated with the solar system can be found here: https://ssd.jpl.nasa.gov/horizons/app.html#/

TABLE 6.1: Table of concurrent *Chandra* and *HST* observations throughout the *Juno* era. Date and time of each observation, identified UV auroral families from current literature using the Grodent et al. (2018) definition and predicted solar wind dynamic pressure from the Tao et al. (2005) with average Jupiter-Sun-Earth angle are shown. Bold entries highlight observations associate with possible eXternal perturbation (X) structures.

Observation start date (dd/mm/yyyy)	**Chandra ObsID**	**Observation interval (Juno time; light corrected)**		**HST UV northern auroral family* from literature**			**Predicted mean solar wind† P_{dyn} (nPa)**	**Mean Jupiter-Sun-Earth angle (°)**
		Chandra	**HST**	**G18[a]**	**MP22[b]**	**D22[c]**		
24/05/2016	18608	09:39 - 20:41	17:03 - 17:47	-	U	Q/N	0.007	∼ 57.7
			20:14 - 20:58	-	U	U	0.007	∼ 57.7
01/06/2016	18609	10:47 - 21:49	14:13 - 14:57	-	U	Q/N	0.130	∼ 64.5
			17:24 - 18:08	-	U	Q/N	0.081	∼ 64.8
02/02/2017	18301	09:14 - 18:19	16:17 - 16:57	-	i	i	0.010	∼ -79.6
28/02 (CXO); 01/03/2017 (HST)[d]	20000[d]	11:58 - 07:34	14:37 - 15:16	i	i	-	0.024	∼ -53.1
18/05 - 19/05/2017	18302	23:48 - 10:10	04:27 - 05:07	N	N	N	0.111	∼ 19.2
			06:03 - 06:43	N	N	N	0.137	∼ 19.3
18/06/2017[d]	**20001[d]**	**17:55 - 04:06**	**08:31 - 09:13**	**X**	**i**	**-**	**0.008**	**∼ 47.7**
01/04/2018	**18678**	**09:59 - 21:06**	**09:59 - 10:17**	-	**X**	**-**	**0.154**	**∼ - 58.6**
23/05 - 24/05/2018	18679	23:22 - 10:21	09:02 - 09:32	-	U	Q	0.040	∼ -3.1
06/09/2018	**18680**	**19:50 - 06:56**	**04:22 - 05:02**	-	**i**	**X**	**0.053**	**∼ 97.1**
29/05/2019	22159	02:50 - 12:34	12:18 - 12:56	-	i	-	0.011	∼ -32.4
15/07/2019	22148	12:21 - 19:13	14:06 - 14:44	-	U	N	0.067	∼ 10.6
			15:41 - 16:17	-	U	Q	0.070	∼ 10.6
16/07/2019	22149	08:07 - 15:00	10:43 - 11:21	-	N/i	N	0.040	∼ 11.2
18/07/2019[d]	22150[d]	19:40 - 01:32	14:10 - 14:49	-	i	-	0.011	∼ 13.6
08/09/2019	**22151**	**08:01 - 14:46**	**14:24 - 15:02**	-	**X/i**	**-**	**0.300**	**∼ 64.0**

* UV families as described in Grodent et al. (2018)

† Predicted values from Tao et al. (2005) model during the *HST* interval(s).

[a] UV families identified from Grodent et al. (2018)

[b] UV families identified from Moral-Pombo et al., (2022, in prep.)

[c] UV families identified from Dunn et al. (2022)

[d] observations not concurrent but occurred ± 1 day from *Chandra* interval

6.4 Results

Following studies that have identified different regions with the UV emissions associated with different potential drivers (e.g., Grodent et al., 2018), we apply similar logic to the X-ray northern auroral emissions from the *Chandra* catalogue described in Chapter 5, with a focus on select observations taken during the *Juno* -era. Here we use the families defined from UV emissions from concurrent *HST* data to provide vital magnetospheric context to the concentrated northern X-ray emissions. We then model the visibility from each X-ray family, using the area of the region defined in S3 longitude and latitude, as they rotate into view of *HST* -STIS. The visibility was defined here as the number of visible STIS pixels associated with each X-ray region during one jovian rotation. We assume that the emissions across the area of the defined X-ray families used in the model were uniform. *HST* -STIS was used for this model as it has a superior spatial resolution to *Chandra* .

6.4.1 Identifying X-ray auroral families

As analyzed in the statistical study presented in Chapter 5 (Weigt et al., 2021a), it is clear that the northern X-ray emissions exhibit very variable morphological and temporal behaviours over a jovian rotation, with only a very small region of X-rays appearing consistently across the entire $\sim$ 20 year *Chandra* HRC-I dataset: the averaged hot spot nucleus (AHSNuc). The AHSNuc was found to mainly map to the noon magnetopause boundary, infrequently exhibiting robust quasi-periodic oscillations (QPOs) of $\sim$ 2.3 - 22.4-min that were suggested to be associated with possible ultra-low frequency (ULF) wave activity. We show the AHSNuc in an example of a 2D histogram of mapped concentrated X-rays, using the numerical criterion for photon concentration defined in Chapter 4 (Weigt et al., 2020), as a black cross-hatched region in Figure 6.3. The colour bar shows the photon flux of the X-rays (counts s^{-1}) and the 1D histograms show the latitude and S3 longitude distribution of the X-ray emissions. The X-ray auroral families we define here, over a central meridian longitude (CML) range of 80° - 250° (see Section 6.4.2 for more details), are *X-ray noon* (red; System 3 longitude (S3 lon): 155° - 190°, latitude (lat): 58° - 68°), *X-ray dusk* (purple; poleward of noon, S3 lon: 155° - 190°, lat: 70° - 80°), *X-ray dawn* (grey; equatorward of noon and extends to higher longitudes, S3 lon: 180° - 230°, lat: 51° - 75°), the *Low Latitude Extension (LLE) region* (gold; equatorward of noon at lower longitudes, S3 lon: 143° - 177°, lat: 45° - 61°) and the *X-ray polar region* (striped; S3 lon: 155° - 190°, lat: 58° - 80°) which envelopes both the noon and dusk families. The AHSNuc is found to lie within X-ray noon. Together they form the physics-informed X-ray auroral families used in the remainder of this study, each potentially corresponding to various drivers throughout the jovian magnetosphere. The statistical

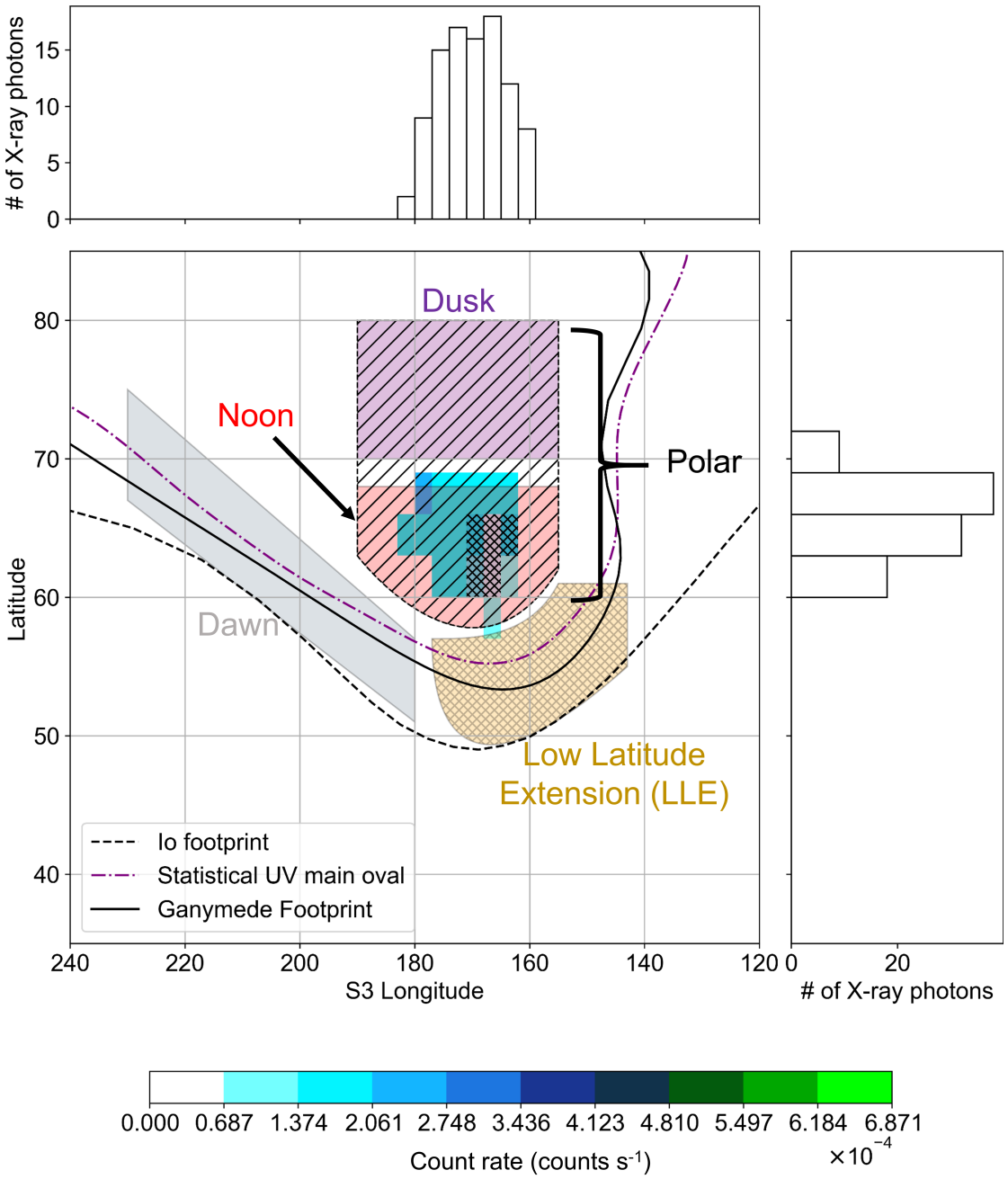

FIGURE 6.3: A Cartesian plot of the X-ray mapping for an example *Chandra* observation (ObsID 18301) on 2 February 2017 analysed in this research with the location of the labelled physics-informed auroral families as described in the text. The concentrated X-ray auroral emissions (2D histogram: binned by 3° S3 lon × 3° lat) given by the colour bar. The statistical UV main oval (e.g., Nichols et al. (2017); Swithenbank-Harris et al. (2019)), Io and Ganymede footprints from the Grodent Anomaly Model (GAM) (Grodent et al., 2008) and Weigt et al. (2021a) significant auroral region (cross-hatched), mapping to the noon magnetosphere, are overplotted. The X-ray emissions mapped and analysed for this research are selected from a 10800 ± 1080 s interval, covering a CML range of 80° - 250° (i.e. optimum visibility for each region as shown in Figure 6.4).

UV main oval and Io and Ganymede magnetic footprints are also plotted to provide context of the location of these regions within the magnetosphere.

As discussed in Chapter 2.2.3 the UV auroral emissions, and in particular those that are located at the poles, are very complex and have yet to be fully understood. As shown in Figure 6.3, the X-ray polar region is poleward of the UV main oval and is likely to be co-located with the UV polar active region (at X-ray noon) and part of the swirl region (e.g., likely situated at both X-ray noon and dusk, Grodent et al., 2003a). As examined in Chapter 2.2.3, the polar active region is the most dynamic of the UV polar emissions, producing flares and bright arc sub-structures of a few hundred kilo-Rayleigh (kR) lasting in the order of a few minutes and associated with powerful dayside reconnection (e.g., high-latitude cusp reconnection, Bunce et al., 2004) due to interactions between the solar wind and the jovian magnetosphere. Such signatures suggest this noon region is linked to a Dungey-like process, as described in Chapter 5, responsible for the transport of plasma and energy on the dayside magnetosphere (Grodent et al., 2003a; Cowley et al., 2003). The UV swirl region, located poleward of the polar active region, is found to be more patchy and turbulent, likely associated with open field lines linked to a Dungey-like return flow (e.g., Pallier and Prangé, 2001; Cowley et al., 2003). The swirl region also coincides with an infrared feature associated with stagnant flows called the fixed Dark Polar region (f-DPR) (Stallard et al., 2003), further validating a Dungey-like process suggested by Cowley et al. (2003).

The X-ray dawn region is found to coincide with a portion of the main oval and the Io footprint to help associate possible dawn storms, injections of hot plasma from the middle magnetosphere (e.g., as examined in Chapter 2.2.3, Gerard et al., 1994; Kimura et al., 2017), with bright X-ray populations. As discussed in Chapter 2.4, recent work by Wibisono et al. (2021) found the intensity of the hard X-rays (HXRs) to increase during the presence of a dawn storm with no presence from the more poleward soft X-rays (SXRs). *XMM-Newton* can separate the energies of the SXRs and HXRs due to the energy resolution of the imaging spectrometer which cannot be done with *Chandra* HRC-I. The more poleward region of X-ray dawn is likely to overlap with the UV dark polar region (DPR) which contains very little UV emissions and is found to contract and expand as Jupiter rotates, mapping to the outer magnetosphere (Pallier and Prangé, 2001; Grodent et al., 2003a). The DPR has been found to be the likely location of empty flux tubes, emptied via Vasyliūnas-like reconnection in the tail which then rotate to the dayside magnetosphere (see Vasyliūnas, 1983, and Chapter 2.2 for more details). As this is a region of essentially empty flux tubes, it is therefore no surprise that there are very little UV emissions here. Recent work by Dunn et al. (2022) [herein referred to as D22 - see Table 6.1] found that the DPR is also present within the X-ray northern auroral emissions. D22 show from observations and simulated data that very few or no X-ray photons to be located in the DPR. They confirm this

conclusion form their Monte Carlo simulations which state that likelihood of X-rays being emitted from the DPR is very small. This includes possible scattering of solar X-ray photons in the jovian upper atmosphere that can be detected from Chandra.

The final X-ray auroral family is the LLE region, equatorward of the polar emissions. As discussed further in Section 6.4.3, concentrated auroral photons in this region do not appear often. In the UV emissions, this region is found to be possibly associated with active particle injections from the middle magnetosphere driven by reconnection events and dipolarizations of the jovian magnetic field (e.g., Dumont et al., 2014, 2018; Yao et al., 2020). Such injection events are found to occur alongside dawn storms, suggesting disturbances of the middle magnetosphere at a range of local times. For the remainder of this chapter, we will associate the described phenomena found in the UV data with the X-rays located in each auroral family allowing us to provide context to our dataset. We will then use data from *Juno* and identifications of UV structures from *HST* data to help decipher potential drivers for the emissions in each region and link them to potential morphologies of the X-ray auroral emissions.

6.4.2 Visibility and distribution of auroral photons across the X-ray auroral families

As stated in many previous studies analysing the jovian X-ray auroral emissions, the tilt of Jupiter as viewed from the observer can lead to issues of viewing geometry of the planet when using remote sensing data (e.g., Dunn et al., 2017; Weigt et al., 2020, 2021a). As the magnetic field at the South pole is more dipolar, this tilt of the planet affects these emissions the most when viewed from Earth. However we cannot completely neglect such effects when viewing the northern emissions as the longitude of the observer, or CML, can change what part of the emissions are observed. To resolve such issues, we utilise the higher spatial resolution of the *HST* -STIS instrument compared to *Chandra* to model the visibility of the each X-ray auroral family, using the area of the region defined in S3 longitude and latitude, as they rotate into view of *HST* -STIS. We use the number of visible pixels of each X-ray region as it rotates into view as a proxy to gauge the visibility of our X-ray families as viewed by an observer at Earth. In other words, we analyse how much an effect the tilt of the planet has when observing fixed regions (in S3 lon and lat) on Jupiter from any Earth-based instrument.

We then model the visibility from each X-ray family, using the area of the region defined in S3 longitude and latitude, as they rotate into view of *HST* -STIS. The visibility was defined here as the number of visible STIS pixels associated with each X-ray region during one jovian rotation. We assume that the emissions across the area

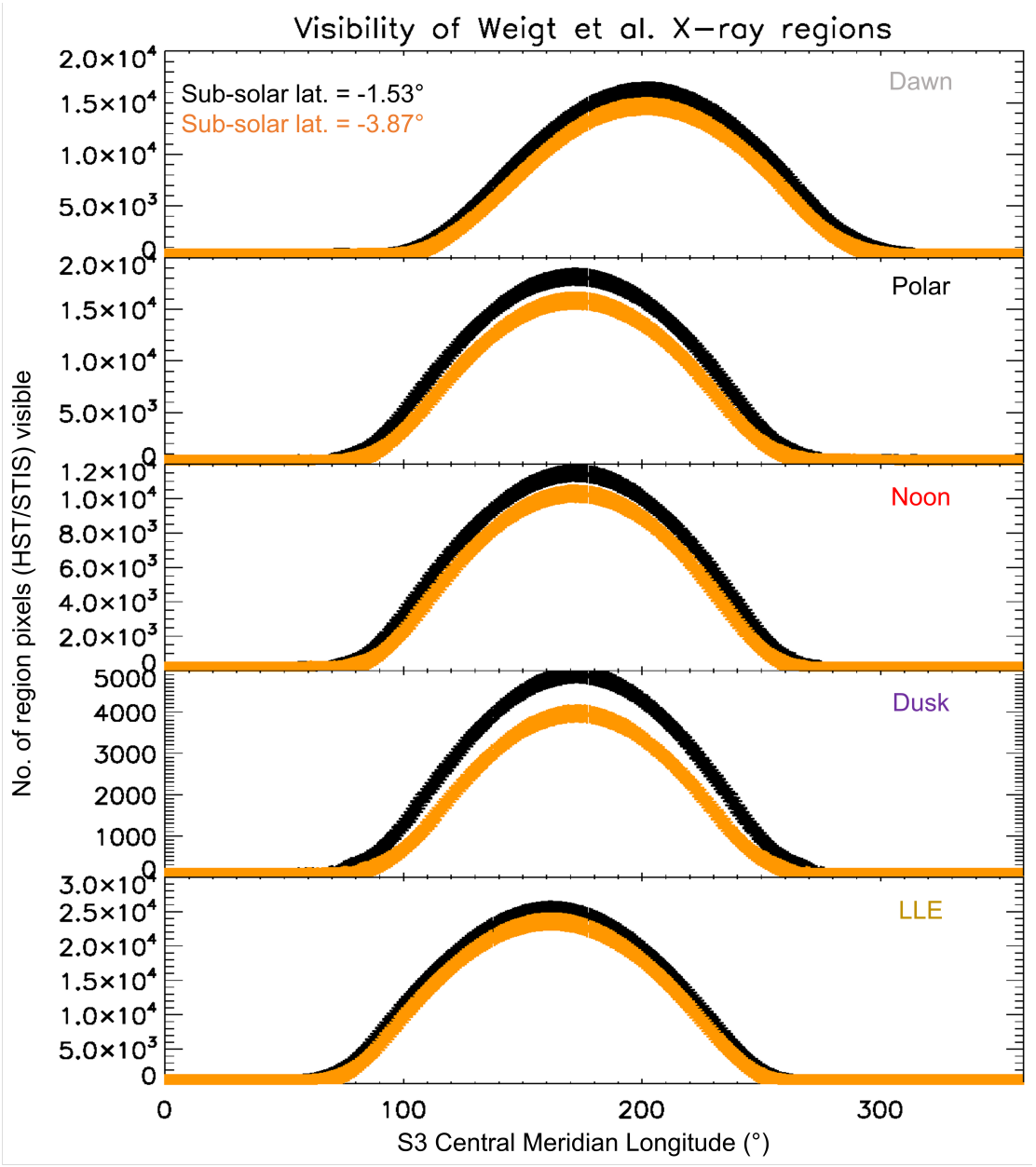

FIGURE 6.4: Plots showing the modelled visibility for a full jovian rotation of each northern auroral region as observed from STIS on board *HST* for the smallest (black: sub-solar latitude = -1.53°) and largest (orange: -3.87°) planetary tilt as viewed from Earth (sub-solar latitude) during the *Juno* main science mission. Each family is labelled with identical colouring used in Figure 6.3.

of the defined X-ray families used in the model were uniform. *HST* -STIS was used for this model as it has a superior spatial resolution to *Chandra* .

We adapt the method by Nichols et al. (2009) used to measure the normalized power of different isolated components of polar and main auroral emissions over two *HST* campaigns in 2007, using the Advanced Camera for Surveys (ACS) Solar Blind Channel (SBC) with an average resolution of ~ 0.032 arcsec pixel^{-1} . Here, we apply this algorithm to the regions described in the previous section, using the ionospheric position and size of each region as viewed by *HST* -STIS with similar resolution to ACS/SBC[4] (~ 0.025 arcsec pixel^{-1}). Figure 6.4 shows the results of our visibility modelling over a full jovian rotation (e.g. full CML coverage) for the highest (orange crosses) and lowest (black crosses) sub-solar latitude during the *Juno* main mission for all X-ray auroral families. The sub-solar latitude relates to how tilted Jupiter is away from the observer, resulting in the peak for both cases being different. The location of peak visibility in all panels is associated with the optimum CML of which the full region is in view and is therefore related to the ionospheric position of the X-ray family. The width of the peak gives an indication of the size of the region of interest. As shown in Figure 6.4, the location and width of the modelled peak visibility for the polar, noon and dusk regions (labelled with the same colours corresponding to the regions in panel (a)) are very similar as expected as all regions span the same S3 longitude range. The main discrepancies are associated with the amplitude of the peak with the dusk region having the fewest number of visible pixels resulting from the region being more poleward and more difficult to view with *HST* -STIS (see Grodent, 2015, for more details) and therefore more sensitive to sub-solar latitude. We note X-ray noon is also affected by sub-solar latitude to an extent but the number of visible pixels still remain above $\sim 1.0 \times 10^4$ during the more hindered viewing geometry. Since the polar region is the accumulation of visible pixels from both X-ray noon and dusk, the modelled visibility curve is a combination of both regions. The dawn region spans greater longitudes and surrounds the polar emissions, following a portion of the dawn main oval leading to the peak visibility shifting to higher CMLs. As the shape of X-ray dawn region is longer in size (i.e. spans a greater range of longitudes) and is more equatorward than the X-ray polar region, the peak of the visibility curve is broader and less sensitive to the tilt of the planet. Finally, similar to X-ray dawn, the LLE region is more equatorward than the polar emissions and therefore the visibility is less sensitive to the tilt of the planet. The LLE region spans the smallest range of longitudes out of the X-ray families which is reflected by the width of the visibility curve. Although none of these results are particularly surprising, this is the first time the visibility of the X-ray auroral emissions has been modelled in this way.

[4]Section 2.5 from https://www.stsci.edu/files/live/sites/www/files/home/hst/documentation/_documents/stis/stis_ihb_cycle25.pdf

The distribution of auroral X-ray photons within each of the auroral families for each *Chandra* observation are shown as a stacked bar chart in Figure 6.5, with the ObsIDs in order of observation start date (as shown in Table 6.1) throughout the duration of *Juno's* main mission. Each region is represented by the same colours used in panel (a) with the example indicated by a yellow arrow. The mean number of total auroral photons populating the X-ray families, μ, is given by a horizontal dashed line with a value 93.45%. In other words, $\sim$ 93% of northern X-ray auroral emissions are likely to be located within the described X-ray regions. Observations were the sum of the components are $<$ 100%, as shown in Figure 6.5, indicate that concentrated emissions were also mapped to regions outside the X-ray auroral families. The X-ray emissions used in the stacked bar chart, and mapped using the 2D histogram in panel a), are from 10800 $\pm$ 1080 s (3 $\pm$ 0.3 hours) intervals, spanning a CML range of 80° - 250° including the peak visibility of all regions. As many of the X-ray observations have different exposure times, this ensures we are removing any observation bias as the same portion of all northern auroral emissions is observed in each of the *Chandra* campaigns. As shown by the highlighted example in Figure 6.5 and four other observations (ObsID 20001, 20002 (no *HST* intervals during this time), 18678 and 18679; details of the observations in Table 6.1), all the northern auroral emissions are located within the X-ray polar region, dominated by X-ray noon photons. During these intervals there were no dawn or LLE region photons detected despite these regions being in view of *Chandra* at the time. However, many other observations have auroral photons located in this range within the same viewing and timing restraints. This therefore suggests that the potential drivers that cause emissions in these regions may be "switched off". Further evidence of this is shown by the observations that had a higher population of LLE photons ($>$ 10% of total photons) with no X-ray dusk emissions (ObsID 18608, 18677, 22148, 22150 and 22151). This suggests that during these intervals, the concentrated X-ray emissions were located equatorward of the main oval and displaying more extreme morphological behaviour when compared to the averaged map of northern auroral emissions in Chapter 5 (Weigt et al. (2021a): Figure 5.4), shown by the low occurrence rate of the X-ray emissions (using the same latitude/S3 longitude binning). The most extreme example, ObsID 22151 (8 September 2019), is a very rare case of the majority of the auroral emissions mapping to beyond the polar region.

From Figure 6.5, it is clear we can split distinct behaviours into two categories: (1) fully polar emissions (i.e. X-ray polar population = 100% of all auroral emissions) and (2) low latitude emissions (i.e. LLE photon population $>$ 10%). The observations that exhibit intermediate behaviour between both categories may be interpreted as a "transition interval" between the two. We do however need to compare the mapping of these morphologies with *HST* and *Juno* data to verify such a state. The key result we present here is that the lack of uniformity across the Figure 6.5 shows that the

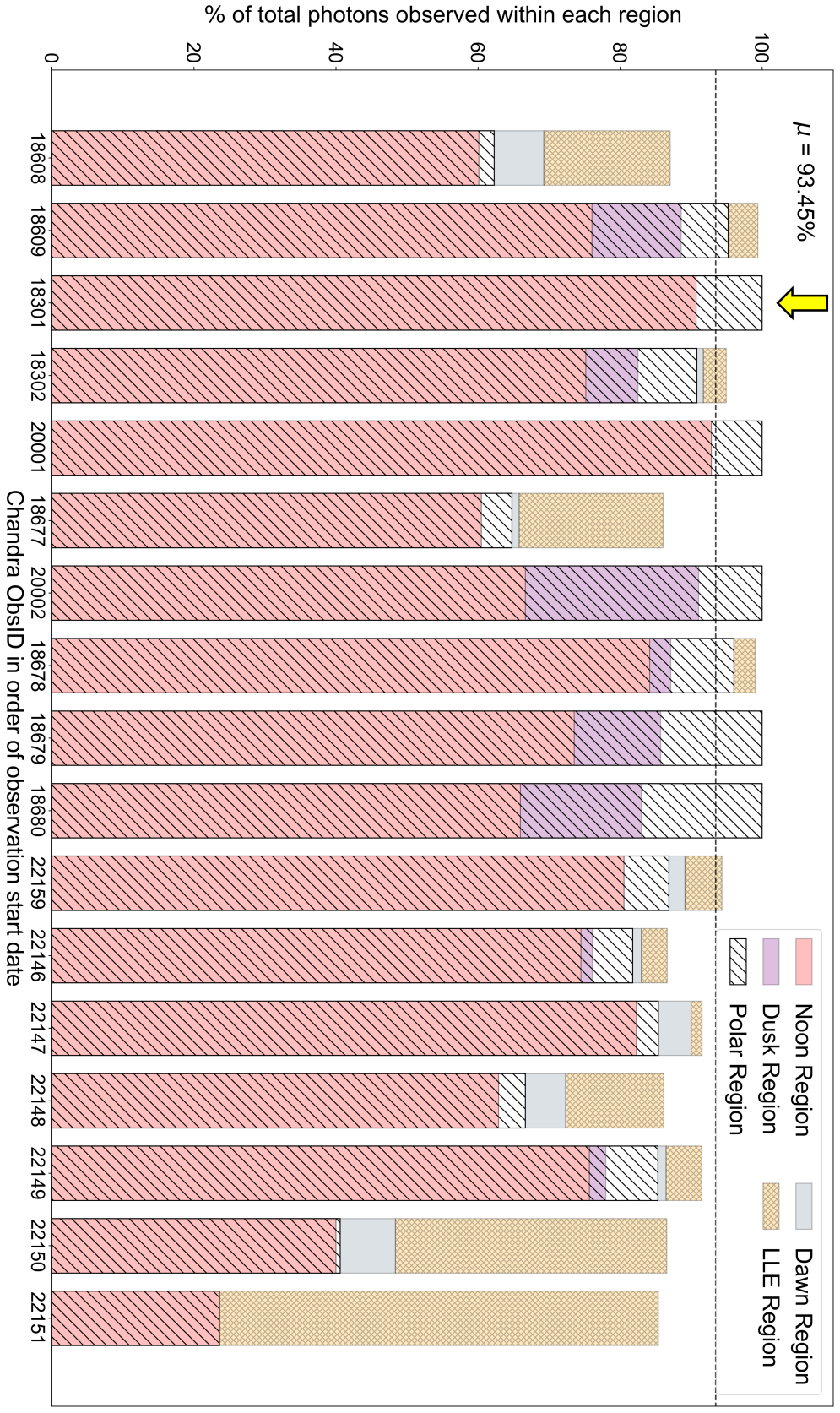

FIGURE 6.5: Stacked bar chart showing the distribution of all concentrated X-ray auroral emissions in each auroral family for each *Chandra* observation (in order of date: Table 1) during the *Chandra* observation. The mean, μ, is given and indicated by the horizontal line. Like Figure 6.3, the X-ray emissions analysed from a 10800 $\pm$ 1080 s interval, covering a CML range of 80° - 250°. The example shown in Figure 6.3 is indicated by the yellow arrow.

viewing geometry has little influence when observing the northern concentrated X-ray auroral emissions. This suggests that the switching on/off of potential magnetospheric drivers likely dominate. The remainder of this section will compare these results with concurrent *HST* and *Juno* observations to link any of the auroral behaviours and morphologies to possible magnetospheric and/or external processes.

6.4.3 Using *in situ* and remote sensing diagnostics to infer magnetospheric state

In order to understand the state of the jovian magnetosphere during the *Chandra* interval and constrain the driver(s) responsible for variable X-ray aurora, we combine predicted solar wind conditions from the 1D MHD propagation model by Tao et al. (2005) with data from the *Juno* fluxgate magnetometer (*Juno* MAG) and the radio antennas (*Juno* Waves). The purpose of the model is to infer solar wind compressions or rarefactions (which contracts or expands the jovian magnetosphere) to infer the state of the jovian magnetosphere, within a maximum error of $\pm$ 2 days given the alignment of the Sun, Earth and Jupiter We also compare the predicted UV auroral families during the interval to the *Juno* data to verify the auroral behaviour and morphology. The aim here is to combine the UV and X-ray predicted morphologies with predicted solar wind conditions as a possible proxy for magnetospheric conditions when there is no upstream *in situ* data.

Figure 6.6 shows the results of the Tao et al. (2005) 1D MHD solar wind propagation model combined with *Juno* MAG and Waves data, covering 4 days centred on the *Chandra* observation taken on 16 June 2017 (ObsID 20001 - see Table 6.1 and Chapter 4 for more details). The *Chandra* (CXO) and *HST* intervals are highlighted in orange and grey respectively in all panels. Panels (a) and (b) show the predicted solar wind dynamic pressure (P_{dyn}) and associated Jupiter-Sun-Earth (JSE) angle respectively, evolving over time. We only consider JSE angles $< |60°|$ (highlighted in cyan) to ensure that the errors of the model are within $\pm$ 2 days. Panels (c) and (d) show the *Juno* MAG data in spherical components, transformed from Cartesian coordinates (B_r: blue, B_θ: black, B_ϕ: red) and the total field strength ($|B|$) measured by the *Juno* MAG data, in units of nanotesla (nT), within the Tao model errors (dashed grey vertical lines: shown in all panels). Finally panel (e) shows the concurrent *Juno* Waves data with the colour bar showing the electric spectral density of the radio emissions. The *Juno* ephemeris data during this interval is displayed at the bottom, showing its position in Jupiter's System 3 frame. The purple lines represent *Juno* making inbound (dashed: *Juno* moving from magnetosheath to magnetosphere plasma) and outbound (dotted: *Juno* moving from magnetosphere to magnetosheath) crossings of the magnetopause boundary as identified from *Juno* JADE data shown in Chapter 4 (Weigt et al., 2020).

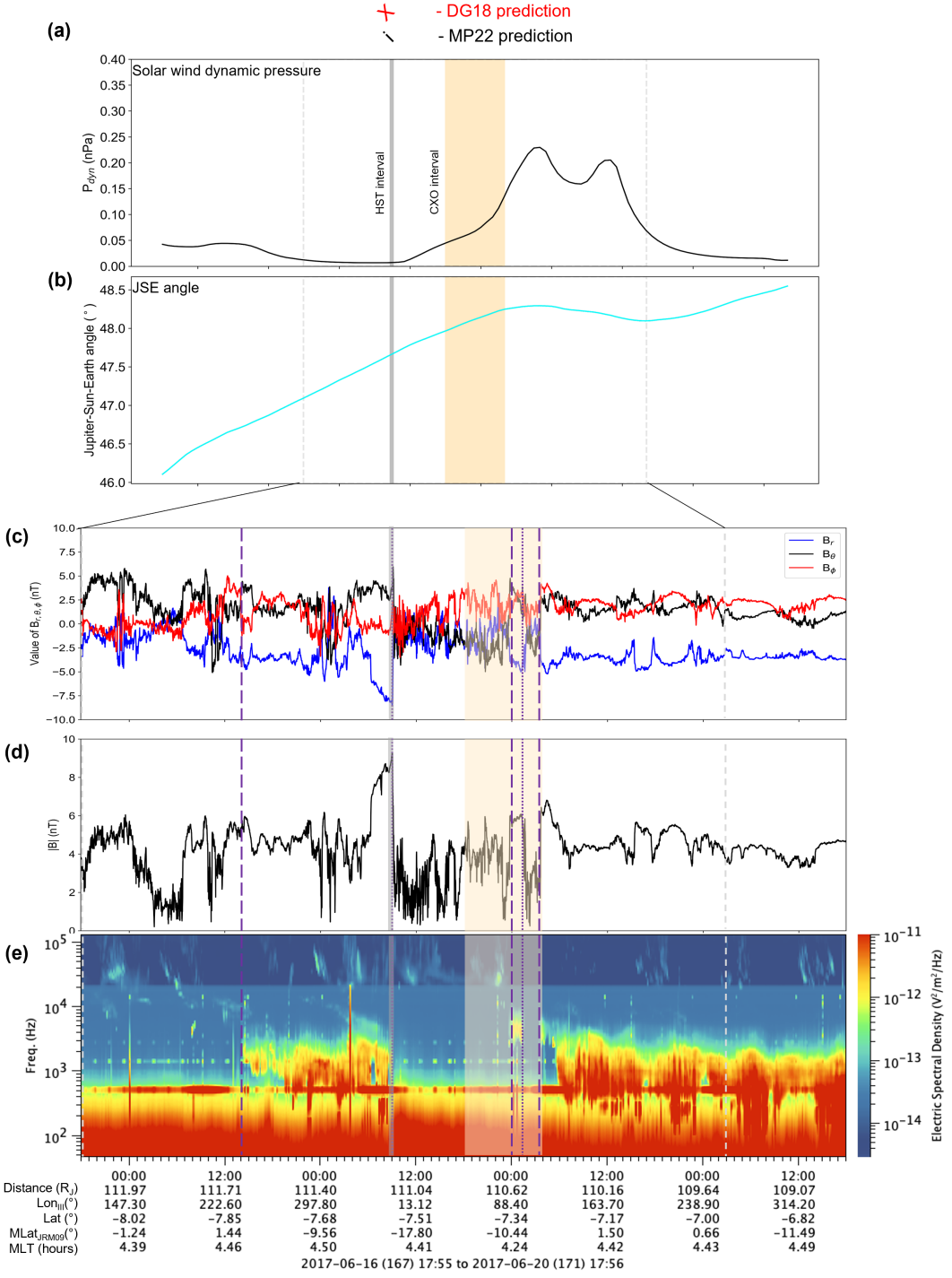

(Caption on next page)

FIGURE 6.6: Multi-panelled plot combining the results from the Tao et al. (2005) 1D MHD solar wind propagation model with *Juno* MAG and Waves, covering 4 days centring the *Chandra* observation (orange area) taken on 16 June 2017 (ObsID 20001 - see Table 6.1 for more details). Panels (a) and (b) show the predicted solar wind dynamic pressure (P_{dyn}) and associated Jupiter-Sun-Earth (JSE) angle respectively, evolving over time with the *Chandra* (CXO) and *HST* interval (grey area) shown in all panels. The angle represented in cyan shows periods of time when the value is $< |60°|$. Panels (c) and (d) show the *Juno* MAG data in spherical components (B_r: blue, B_θ: black, B_ϕ: red) and the total field strength ($|B|$) measured by the *Juno* MAG data, in units of nanotesla (nT), within the Tao model errors (dashed grey vertical lines: shown in all panels). Panel (e) shows the concurrent *Juno* Waves data, measuring the electric spectral density of the radio emissions. The *Juno* ephemeris data during this interval is displayed at the bottom, showing its position in Jupiter's System 3 frame (in radial distance from Jupiter, R_{J}, and magnetic local time (MLT; hours)) and its position projected onto Jupiter's surface (S3 longitude (Lon_{III}; degrees), latitude (Lat; degrees) and magnetic latitude found from the JRM09 field model ($\text{MLat}_{\text{JRM09}}$; degrees)). The purple lines represent *Juno* making inbound (dashed) and outbound (dotted) crossings of the magnetopause boundary as identified form *Juno* JADE data as described in Chapter 4. The identified UV auroral family using the Grodent et al. (2018) definitions, as shown in Table 6.1, are at the top of panel (a). DG18 = Grodent et al. (2018) prediction; MP22 = Moral-Pombo et al. (2022, in prep.) prediction [herein reffered to as MP22].

The magnetopause crossings correspond to a compressed magnetosphere during the *Chandra* interval, as found from the Joy et al. (2002) model inferring a P_{dyn} of 0.391 nPa. Figure 6.6 shows that Tao model predicted a series of shocks to the jovian magnetosphere within model error, during a relatively reasonable alignment. The magnetopause crossings are confirmed in the *Juno* data (as shown in panels (c) - (e)) with a sharp change in the total magnetic field strength and its spherical components. The character of the magnetic field also changes during a crossing as it is noisier in the magnetosheath than in the magnetosphere. To infer the magnetopause boundary crossings, one can look at the Waves data, and in particular the appearance/disappearance of the non-thermal trapped continuum emissions (as done by Hospodarsky et al. (2017)). These emissions, observed between $\sim$ 10 Hz - 10 kHz, located in the jovian magnetospheric cavity where the emission frequency exceeds that of the surrounding plasma frequency (Equation 1.4) (e.g., Gurnett and Scarf, 1983). When in the magnetosheath, the trapped continuum emissions are blocked by the denser sheath plasma due to refraction effects of the emission frequency at the magnetopause boundary. These emissions appear again when *Juno* enters the more rarefied magnetospheric plasma. These transitions in electric spectral density also align with the identified *Juno* crossings. Finally, during the series of compressions Grodent et al. (2018) found that the UV auroral emissions exhibited features associated with the *X*-family, suggesting that the magnetosphere was being affected by an interplanetary compression region. When comparing these results to Figure 6.5, the X-ray auroral emissions were found to be fully polar, dominated by X-ray noon. This may therefore suggest that the auroral emissions remain poleward and more concentrated during intervals of compressions. This example was used as a "proof of

concept" as the location of *Juno* , near its apojove position at the magnetopause boundary, allows identifying the magnetospheric response to changing solar wind conditions in the *in situ* data is clearest during its orbit. Further analysis of the *Juno* Waves data will allow us to identify if there was a global magnetospheric response to the compressions (e.g. the activation of radio sources, Louarn et al. (1998)).

Figure 6.7 shows an example when *Juno* is near perijove during the *Chandra* interval (ObsID 18678: 1 April 2018), making it difficult to infer the state of the magnetosphere due to the very strong field as you approach Jupiter (panels (c) and (d)). From this position we have limited ability from the *in situ* measurements to infer the upstream conditions (unlike at apojove when magnetopause boundary crossings can give us snapshots of magnetospheric size and inferred upstream dynamic pressure). The Tao model suggests that there is, again, a series of solar wind compressions during the *Juno* perijove interval. Moral-Pombo et al. (2022, in prep.) [herein referred to as MP22 - see Table 6.1] found the UV auroral morphology was associated with the *X*-family, agreeing with the predicted results. As shown in panel (e), the spectrogram is dominated by high frequency periodic emissions (up to $\sim$ 10 kHz as bursts of high electric spectral density), making it difficult to disentangle sources associated with state of the jovian magnetosphere and verify the model results. We do however highlight a region of potential activity, as the dotted black box in Figure 6.7, in the magnetic field associated with a possible dipolarization of the field when *Juno* is crossing the plasmasheet. A dipolarization occurs when the magnetic field line which *Juno* travels across changes from a stretched to a more dipolar configuration after a tail reconnection event, producing an anomalous feature in the $B\phi$ component. The plasmasheet crossing is shown by the sharp transition in electric spectral density, where the denser plasmasheet blocks the periodic emissions via refraction effects (similar to before). Such dipolarizations of the field have been found to be associated with injection events found from *HST* UV observations (e.g., Yao et al., 2020). When comparing Figure 6.7 to Figure 6.5, the auroral emissions found in ObsID 18678 exhibited a more transitional morphology, with the majority of emissions located in the X-ray polar region with a small portion of the emissions located in the LLE region. This suggests that the *Chandra* data may identify a possible injection event which may precede or follow a compression event, which has already been observed in the UV auroral emissions (Grodent et al., 2018). As this is a preliminary result, more analysis is required to verify the magnetometer data being associated with particle injections. If this is found to be true, this would be the first instance of particle injections being observed and mapped in the X-ray auroral emissions.

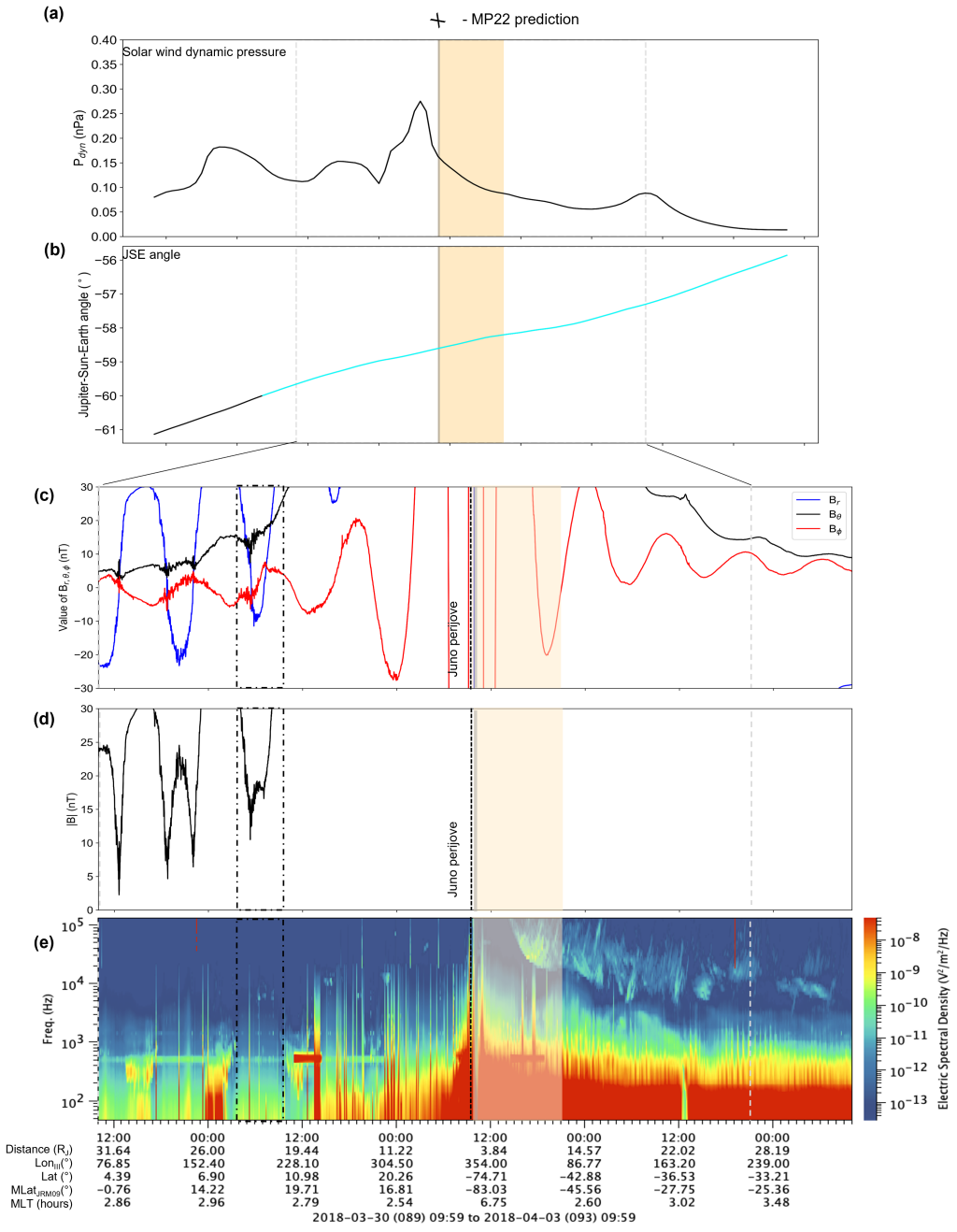

FIGURE 6.7: Multi-panelled plot for ObsID 18678 (1 April 2018) in identical format to Figure 6.6. The interval of the *Juno* perijove is shown by the black dashed line. Dotted black box highlights interval of potential dipolarization of the magnetic field (mainly in B_ϕ) associated with injection events in the UV aurora. The Grodent et al. (2018) UV family identified by MP22 is shown at the top of panel a).

6.5 Discussions and Future Work

The preliminary results presented in this section show some evidence that using the families defined from the UV and X-ray emissions may be a good indicator of magnetospheric conditions. This will be particularly useful when analysing auroral observations during the portion of *Juno's* orbit which situates the spacecraft in the plasmasheet, making it difficult to observe magnetospheric features associated with compression regions in the interplanetary medium. We do however present a case study here (ObsID 18678) during a possible injection interval (as shown by the change of behaviour in the B_ϕ component of the magnetic field) which may be related to a compression event predicted from the Tao model. The *Juno* data here require more analysis to verify activity in the middle magnetosphere during this time although it is clear that the UV-X-ray families show some evidence of moderate injections with the small LLE region population in the X-ray aurora and the relationship between the *X* and *i* UV families. As found from previous *HST* campaigns, particle injections events related to the dipolarization of the field can be accompanied by bright dawn storm emissions (Yao et al., 2020). We do note that, although no X-ray auroral emissions appeared in the X-ray dawn in this example, there are many observations which had concentrated emissions in both the X-ray dawn and LLE regions, with predicted *X* or *i* UV auroral families as shown in Table 6.1 and Figure 6.5 (e.g. ObsID 22159, 22149, 22150 and 22151). Further analysis will look into these observations in more detail to verify: (1) if a dawn storm was present during these times looking at the *HST* images in more detail and (2) if we can identify any signatures of injection events from the *HST* and *Juno* data. This would be beneficial to the ongoing effort to analyse the hard X-rays (HXRs) in the jovian aurora in more detail (e.g., Mori et al., 2022). We do note that some UV dawn storms do not fully develop into a bright auroral feature and that magnetospheric injections do not necessarily have an auroral counterpart.

As mentioned in Section 2.4, Wibisono et al. (2021) observed that the intensity of the hard X-ray emissions (up to 10 keV), often located along the main oval, increased in the presence of a dawn storm while the more poleward soft X-rays (SXRs: see Chapter 5) were unaffected. This showed that there is a direct X-ray-UV connection during bright dawn storms. However due to the poorer spatial resolution of *XMM-Newton*, the emissions were unable to be mapped. The technique outlined here will therefore make it possible to identify locations of auroral X-ray emissions potentially linked to dawn storms (i.e. concentrated photons in the X-ray dawn region), allowing us to see how they evolve over time and if they are correlated with those found from UV data from *HST* and *Juno* . Similar to the UV families, this will allow us to separate and examine the magnetospheric drivers responsible for the X-ray aurora.

As well as providing motivation to investigate injection events in more detail, the results presented in this study show that the auroral morphology may provide a useful proxy of solar wind conditions during a possible compression event. From the five observations that exhibit fully polar emissions, three (ObsID 18301, 20001, 18680) coincided with a predicted solar wind compression and/or produced UV auroral emissions associated with the *X*-family or the linked *i*-family (as presented in Table 6.1 and in Figure 6.6). ObsID 20002 (6 August 2017) does not appear in Table 6.1 as there was no *HST* observation $\pm$ 1 day from the *Chandra* window however initial analysis of magnetopause crossings made by *Juno* suggest that the magnetosphere was compressed during this time, as found by the Joy et al. (2002) model. During these observations, the X-ray noon population dominates suggesting that the likely driver from these emissions lies on the noon magnetopause boundary, as examined in Chapter 5. In the context of magnetospheric dynamics, magnetic reconnection would occur more frequently on the noon magnetosphere during periods of high P_{dyn} solar wind either at high latitudes in the cusps (e.g., Bunce et al., 2004) or at multiple smaller sites with more drizzle-like reconnection (e.g., Guo et al., 2018). Three of these intervals (ObsID 20001, 20002, 18678) were also found to exhibit very significant quasi-period oscillations (QPOs) between 2- and 4- minutes within the AHSNuc region (e.g. in the centre of X-ray noon), further suggesting that there was potentially a dominant noon driver. Again, more analysis to verify these assumptions is needed but it is clear this study sets the foundations for more in depth exploration of the noon drivers associated with the X-ray auroral emissions which clearly play a somewhat significant role in the production of the emissions.

The other outlying observation, ObsID 18679 (23 May 2018), had concentrated northern auroral emissions with maximum intensity $\sim$ 50% dimmer than the average found in Chapter 5. As shown in Appendix A.2, the X-rays observed were found to be the weakest throughout *Chandra* HRC's 20-year campaign. The UV auroral families associated with this observation found quiet and unsettled conditions (*Q*- and *U*-family) which are indicative of a more quiet and relatively unperturbed magnetosphere. Therefore through a combination of interpretation of the UV-X-ray auroral families, the fully polar aurora may either suggest intervals of a more compressed magnetosphere when *HST* identifies an *X*-family or intervals when the X-ray auroral emissions are fairly weak due to quiet magnetospheric conditions. The latter point is more difficult to verify as there are instances found in this research when the magnetosphere is quiet yet the X-ray auroral morphology is not fully polar. Such observations exhibit intermediate behaviour between fully polar and low latitude emissions, or a "transition interval", in their X-ray auroral morphology (e.g. LLE distribution is present at $<$ 10% with emissions still within X-ray noon), such as ObsID 18609 (1 June 2016) when *Juno* was on approach to Jupiter. It is clear that for such cases further analysis of the *Juno* remote sensing data, such as the Waves

instrument, and other datasets to determine whether the *Chandra* intervals occurred after a solar wind compression and during a period of relaxation (e.g. to account for the idea of the auroral emissions starting to ”shift” more equatorward) is required.

From the results presented in Sections 6.4.1 and 6.4.2, our key results suggest that there are likely numerous drivers, not necessarily the same, responsible for the concentrated X-ray auroral emissions. With the modelled visibility of the regions, the lack of emissions we observe in a given region is more likely associated with the switching on/off of drivers as opposed to visibility. Each region was still visible throughout the *Juno* era during the greatest planetary tilt, when viewed from Earth, with the distribution of auroral photons changing throughout X-ray dusk is expected to be affected the most by the changing sub-solar latitude. However as shown by our use of constraining the CML and exposure time of each observation, the region is still visible throughout, emphasising our argument for the dominant effect being the switching on/off of potential drivers.

Future studies may define X-ray auroral families for the more diffuse southern auroral region. Comparisons between both poles will allow the conjugacy of the driver to be evaluated in greater detail and aid the ongoing effort to understand the clear North-South asymmetry present across many wavelengths. As mentioned in Section 2.4, a very recent study by Mori et al. (2022) found the first significant detection of HXRs in the 3 - 20 keV range, produced from non-thermal bremsstrahlung. They found that the hard, non-thermal bremsstrahlung X-rays were $\sim$ twice as bright in the southern auroral region than the North, consistent with more persistent and stronger electron currents in the South found by recent *Juno* observations (Kotsiaros et al., 2019). A future study categorising the southern X-ray emissions by comparing the brightest UV emissions with the observed non-thermal bremsstrahlung, and comparing to the northern auroral emissions, would be key to understand the observed non-conjugate behaviour. Previous studies have also found that the very intense UV emissions should also be a site for electron bremsstrahlung at the gas giant planets (e.g. Ness and Schmitt, 2000; Ness et al., 2004b). This will help understand why the observations suggest there is a preference for ion X-ray aurora dominating in the North and electron X-ray aurora in the South. With *Juno's* extended mission providing wider coverage of the South pole and the southern regions of the jovian magnetosphere, we will have more data to look at the electron precipitation in greater detail.

Another possible avenue for this research may be to overlay the internal field contours from JRM09 (Connerney et al., 2022, or the more recent JRM33 field model, which maps the internal field of the planet using data covering *Juno's* 33 orbits during its main science mission,) to find a possible relationship between magnetic field strength and topology with the distributions we find here. This is beyond the scope of this

thesis but it is clear the studies aiming to categorise and simplify very complex behaviour, such as this one and the UV case by Grodent et al. (2018), allows such further analysis to be carried out and is essential for the progression of the field.

Chapter 7

Searching for Saturn's X-rays during a rare Magnetotail Crossing using Chandra

"If I have seen further than others, it is by standing upon the shoulders of giants"
- Issac Newton

Inspired by the title of my successful *Chandra* DDT proposal to observe Saturn: *On the Shoulders of Gas Giants*. Recommend this excerpt from *On the Shoulders of Giants* by Peter Graham if you want to feel powerful while reading this chapter: https://www.youtube.com/watch?v=zOlF8j0OOws

7.1 Abstract

The orbit of Saturn is such that the planet passes through the jovian 'flapping' magnetotail every 19 years. In this research, we report the first ever Chandra X-ray observations of the kronian emissions planned to coincide with this rare planetary alignment. These observations were carried out to analyse Saturn's magnetospheric response as it transitions to this unique and poorly understood parameter space. Here, we analyse our three Director's Discretionary Time (DDT) observations looking at Saturn's X-ray response using *Chandra*'s *High Resolution Camera (HRC-I)*. Our DDT observations were planned for 19, 21 and 23 November 2020 with the aim to find potential kronian auroral and/or disk emissions. The conditions of the kronian magnetosphere are inferred from looking at contemporaneous soft X-ray solar flux data, with the Chandra intervals, from the *Geostationary Operational Environmental*

Satellite (GOES) and ultraviolet (UV) auroral emissions observed from the *Hubble Space Telescope (HST)*. We note that the large Saturn-Sun-Earth angle during these intervals would imply that most flares observed from the Earth-facing side of the Sun would not have impacted Saturn, similarly to the logic applied regarding the solar wind propagation model in Chapter 6. We report here no significant detection of Saturn's disk or auroral emissions throughout the Chandra DDT campaign. We calculate the 3σ upper band energy flux of Saturn, as observed from Chandra, during this time to be 0.9 - 3.04 $\times$ 10^{-14} erg cm^{-2} s^{-1} (where 1 erg cm^{-2} s^{-1} = 1 $\times$ 10^{-3} W m^{-2}). Our value is in agreement with fluxes found in previous literature from modelled spectra of the kronian disk emissions. We conclude this chapter by discussing the implications of the non-detection of Saturn during this rare planetary alignment and how it is imperative that the next generation of X-ray telescope, like *Athena* and the *Lynx* mission concept, continue to observe Saturn with their more updated instrumentation with greater spatial and spectral resolution coupled with very enhanced sensitivity to help us finally solve the mysteries behind Saturn's apparently elusive X-ray aurora.

7.2 Introduction

As discussed in Chapter 2, the magnetospheres of Jupiter and Saturn are considered to be the two largest coherent structures in our Solar System with most of the plasma supplied by their moons with their size determined from a variable interaction with the upstream solar wind (e.g., Blanc et al., 2015; Bolton et al., 2015). The magnetotail of Jupiter is so vast that it extends beyond Saturn's orbit at an average distance of 9.5 au (Kurth et al., 1982; Lepping et al., 1982), and contains a wide variety of plasma populations with different structures and velocities (McComas et al., 2007). Lepping et al. (1983) calculated that Jupiter's magnetotail appears to "flap" over an approximate 2-3 day cadence. They stated that the structure and movement of the jovian magnetotail are both determined from the variable solar wind dynamic pressure surrounding the jovian system. Measurements from both *Voyager* missions found that the tail consisted of more rarefied plasma with a density of $\sim$ 10^{-3} - 10^{-5} cm^{-3} (Gurnett et al., 1979; Lepping et al., 1983; Kurth et al., 1982). This is several orders of magnitude smaller than the denser plasma observed from typical solar wind conditions sampled close to the Saturn system ($\sim$0.01 - 0.5 cm^{-3}; Lepping et al. (1983)). As a result of their analysis the shape of the tail is predicted to resemble a "sausage string". This tail geometry is produced from solar wind with higher dynamic pressure generating the narrower structures of the tail, or the 'link' between sausages, and weaker pressure for the expanded regions, the sausage shape itself. This is similar to the logic applied to the solar wind creating the bimodal size of the jovian magnetosphere as examined in Section 2.1.

Every $\sim$ 19-20 years, the alignment of the gas giant planets is such that Saturn is located in Jupiter's wake. This leads to Saturn's magnetosphere being alternately immersed in the solar wind and the more rarefied plasma located deep within the jovian tail. Due to the vast size of the jovian system, the phenomenon of "overlapping" or intertwined planetary magnetospheres in the solar system is unique to the gas giants. The last observation of this planetary alignment we planned our observations around here was recorded by the *Voyager 2* flyby of Saturn in 1981. During this time, the evidence for Saturn's immersion in the jovian tail was measured from the radio data, with almost complete dropouts of the Saturn Kilometric Radiation (SKR) observed (Desch, 1983). SKR emissions are detected within a frequency range of a few kHz to 1200 kHz on the dawn-noon sector of Saturn's auroral zone (or auroral region) (Lamy et al., 2009) and, like other planetary radio emissions (e.g. auroral kilometric radiation at Earth and the jovian radio emissions briefly examined in Chapter 6), are likely generated from accelerated beams of electrons in the auroral emissions via the cyclotron maser instability (CMI) (Zarka, 1998). The CMI is an instability related to the interactions between waves and particles for which resonance is reached when the Doppler-shifted angular frequency of the wave in the electron frame is equivalent to the relativistic gyro-frequency of the electrons in resonance (e.g., Treumann, 2006). For this CMI to occur in the magnetosphere, accelerated electrons need to present and the plasma needs to be low density. Further studies analysing the SKR (e.g., Reed et al., 2018) identified that these emissions can be used as a remote diagnostic tool to infer and predict the magnetospheric conditions at Saturn. This was due to the timescale of many previously observed SKR events that were observed to correlate with those associated with possible auroral drivers such as changing solar wind conditions (i.e. the dynamic pressure or) magnetotail reconnection. Desch (1983) observed during the *Voyager 2* flyby that the SKR emissions returned to a nominal level of intensity when Saturn transitioned back into the wake of the solar wind. Therefore they concluded that these dropouts were a signature of intervals when Saturn was immersed in the jovian magnetotail. These intervals were then used as a useful tracer for the apparent flapping motion of Jupiter's vast magnetotail. During these observations however, there were no campaigns designed to monitor Saturn's auroral emissions in both ultraviolet (UV) or X-ray wavelengths. Therefore the global kronian magnetospheric response to rare external conditions was not fully captured.

As examined extensively in Chapter 2, the magnetospheric responses of the gas giants to external (e.g. the solar wind) and various internal drivers (e.g., rapid rotation of the planet, moon-planet interactions; Bagenal, 1992) have been studied extensively using auroral measurements in the UV (e.g., Nichols et al., 2010, 2016), infrared (IR; e.g., Badman et al., 2011; Stallard et al., 2008b,a) and radio (e.g. Kurth et al. (2005), Lamy et al. (2009)) wavelengths. The magnetospheric processes at the gas giants are found to be highly dynamic and complex in all wavebands, generated very varied auroral

responses (see detailed reviews by Bhardwaj and Gladstone (2000) and Badman et al. (2015) for an overview of each of these processes).

As discussed in Section 2.4, the drivers of the X-ray auroral emissions at the gas giants are the most mysterious when compared to other auroral emissions at different wavelengths. Auroral X-ray emissions have been postulated to be present within the kronian auroral region since the very first observation of its magnetosphere, by the *Voyager* spacecraft (Opp, 1980; Sandel et al., 1982), and the detection of its powerful high latitude UV auroral emissions (Broadfoot et al., 1981). Similar to Jupiter, the location and observed spectrum of the UV auroral emissions implied that they were driven by precipitating electrons (energies $\sim$ 10s keV; Carbary and Krimigis, 1983) and that X-ray bremsstrahlung emissions would occur alongside the most powerful UV emissions. The first X-ray campaign of Saturn to detect any X-ray emissions from the planet was conducted by the *Einstein Observatory* on 17 December 1979 (Gilman et al., 1986). This observation was prompted by the discovery of X-ray auroral emissions at Jupiter's poles (Metzger et al., 1983). The $\sim$ 11ks observation of Saturn observed no significant X-ray emissions. Gilman et al. (1986) therefore concluded that electron bremsstrahlung processes were likely to be the main driver responsible for auroral X-ray production in the kronian system. They calculated a predicted 3σ upper limit for the kronian X-ray flux at Earth, using these assumptions, to be 1.7×10^{-13} erg cm^{-2} s^{-1}. This value was compared with the expected energy flux detected at Earth from a non-relativistic thick target bremsstrahlung model based on previous UV observations (Sandel et al., 1982) of 8×10^{-16} erg cm^{-2} s^{-1}. The model assumes that the thick-target bremsstrahlung is observed at higher latitudes. The first significant detection of kronian X-ray emissions was observed by *ROSAT* on 30 April 1991. This observation was part of a campaign to detect X-ray emissions at both the gas and ice giants (Uranus and Neptune) (Ness and Schmitt, 2000). Ness and Schmitt (2000) calculated that the upper limits of the jovian X-ray luminosity surpassed what was observed from the other 3 planets. These remaining planets were calculated to have a very similar X-ray power. *ROSAT* observed the X-ray flux of Saturn to be $\sim$ one order of magnitude more intense than the modelled X-ray bremsstrahlung flux from Gilman et al. (1986). They postulated that the observed flux increase may be associated with a higher electron flux background detected than previous observations or a possible indicator of multiple X-ray mechanisms at Saturn, including potential X-ray bremsstrahlung processes.

With a new generation of telescopes, subsequent X-ray campaigns with *XMM-Newton* on 10 September 2002 (Ness et al., 2004a) and *Chandra* on 14 April 2003 (Ness et al., 2004b) discovered X-ray emissions from the kronian disk via elastic scattering of solar X-rays from upper atmosphere, similar to that observed from Jupiter. Further *Chandra* campaigns taken during January 2004, which was observed to coincide with an M6-class solar flare, discovered that the disk X-ray flux was correlated with solar

activity. The disk X-ray flux was observed to increase by ~ 5 times when the flare arrived at Saturn (Bhardwaj et al., 2005c). They stated that scattering mechanisms responsible for the kronian X-ray disk emissions would require the disk to have a high X-ray albedo (Ness et al., 2004b). Bhardwaj et al. (2005b) discovered that an atomic oxygen Kα fluorescence line (as explained in Section 2.3) dominated the X-ray spectrum of Saturn's rings at 0.53 keV. This provided evidence for another X-ray mechanism on Saturn. Branduardi-Raymont et al. (2010) re-analysed previous X-ray campaigns as well as two observations from a 2005 *XMM-Newton* campaign and discovered that Saturn's disk emissions correlated with solar activity (e.g. followed the 11-year solar cycle). These results verified what was found in previous literature and discovered the oxygen fluorescence line dominating the ring region spectrum varied differently from the X-ray disk emissions. A *Chandra* ACIS campaign planned to coincide with the predicted arrival of a potential solar wind shock in April-May 2011 (Branduardi-Raymont et al., 2013). Contemporaneous *in situ Cassini* data during the planned *Chandra* intervals verified the arrival and impact of a solar wind shock at Saturn, as predicted from solar wind propagation models. Branduardi-Raymont et al. (2013) observed X-ray emissions associated with scattering of solar X-rays in the upper atmosphere, as resolved using the energy spectrum of ACIS, during an episodic flaring of solar X-rays. They observed no significant X-ray auroral emissions on Saturn, similar to previous attempts. They therefore concluded that in order for a significant auroral signal to be produced from the X-ray emissions, more powerful solar wind shocks may be required to accelerate the particles (electrons or ions) to the required energies to produce a signal above *Chandra's* the detector background and therefore threshold of detectability.

As examined in Section 2.4, if there is a kronian equivalent to a mechanism producing X-ray bremsstrahlung similar to Jupiter, we would expect to observe X-ray photons with energies > 2 keV (e.g. jovian hard X-rays). Branduardi-Raymont et al. (2008) observed these emissions to sometimes coincide with the UV main auroral oval and suggested a link between the precipitating electrons responsible for the UV and hard X-ray emissions. The dominant X-rays in the jovian spectra, and discussed at great length throughout this research, are the soft X-ray emissions. The emissions are located poleward of the UV main oval and are produced via charge exchange and transfer processes between ions and neutrals in the atmosphere. There may be a kronian equivalent with ions from the torus produced by Enceladus, Saturn's dominant internal plasma source. However there has been so substantial evidence of a jovian-like mechanism for X-ray production occurring at Saturn. Although as speculated by previous studies, these emissions and the X-ray bremsstrahlung component may be too dim to be observed with current X-ray telescope capabilities (Hui et al., 2010a).

In this research, we report the first Chandra Director's Discretionary Time (DDT) specifically designed to observe a planet's magnetospheric response during a rare planetary alignment. As mentioned before, this is only possible to observe when Saturn is inside the jovian magnetotail. Here we analyse data from *Chandra*'s High Resolution Camera (HRC-I), assuming that the kronian magnetosphere will experience far more powerful fluctuations than typical solar wind shocks as Saturn transitions from a very low-density plasma in Jupiter's tail to the denser solar wind. The *Voyager 2* data also observed very low dynamic pressures of $\sim 10^{-4}$ nPa (Lepping et al., 1983) when Saturn was immersed in the tail. This is significantly lower than the more typical observed range of $\sim$ 0.01 - 0.1 nPa (e.g. Jackman and Arridge (2011)) produced from the solar wind. We predict that these intervals of very low dynamic pressure when Saturn is in the jovian magnetotail, will cause the kronian magnetosphere to expand larger to what has been typically observed. The X-ray analysis in this study will allow us to see how this extreme external environment will affect the kronian magnetosphere as we expect the shocks between the solar wind and more rarefied tail will be far more powerful than what we typically observe at Saturn. We compare our X-ray observations with data from *Geostationary Operational Environmental Satellite (GOES)* (Lemen et al., 2004) to monitor the solar activity and find any potential solar flares that may impact Saturn. The uncertainty of a flare impacting the Saturn is dependent on the Saturn-Sun-Earth angle.

7.3 Observations and Data Analysis

7.3.1 Chandra DDT observations

In this research we analyse three $\sim$ 10 ks *Chandra* HRC-I DDT observations of Saturn (ObsID 24845, 24846 and 24847). This campaign was planned to take place during mid-November 2020. The sub-solar latitude at Saturn was $\sim 20^{\circ}$, allowing *Chandra* to observe the North pole and the rings which were obscuring the South pole. With this tilt, the North pole is more exposed to the solar wind environment. Table 7.1 displays the start date, duration, apparent diameter of Saturn, heliocentric and Chandra-Saturn distance are for each of the three observations in our DDT campaign. The observations were planned to be conducted in $\sim$ 2-day cadence to account for the motion of Jupiter's magnetotail as predicted by (Lepping et al., 1983). Saturn should therefore also be immersed in the jovian magnetotail every 2-3 days. All the observations in this study were corrected for the movement of Saturn across the chip, as discussed in Chapter 3.1. In order to determine what plasma environment Saturn is located in (magnetotail or solar wind), we look at the auroral dynamics in UV images observed by Hubble Space Telescope (HST) during a simultaneous campaign to analyse the UV auroral behaviour is this unique parameter space [P.I. J. Nichols]. As the HST

TABLE 7.1: Chandra DDT observations of Saturn throughout November 2020. Table taken from Weigt et al. (2021b).

ObsID	Observation Start Date (UT) dd/mm/yyyy (HH:MM)	Duration (ks)	Apparent diameter	Heliocentric distance (AU)	Chandra-Saturn distance (AU)
24845	19/11/2020 (11:27)	10.0	15.90″	9.99	10.45
24846	21/11/2020 (12:09)	10.01	15.85″	9.99	10.48
24847	23/11/2020 (22:44)	9.89	15.80″	9.99	10.52

observations are still undergoing analysis to determine the location of Saturn, we do not present them here.

As discussed in Chapter 3.1, the contaminant build-up on ACIS now severly inhibits the detection of X-rays below 1 keV. Like the jovian X-ray spectrum, we expect the peak X-ray photon energy to also be located here. Therefore, similar to the Jupiter observations examined in detial in Chapters 4 - 6, our Saturn observations were conducted with the *Chandra* HRC-I with no energy resolution. Therefore it is difficult to differentiate between the various processes potentially responsible for X-ray production at Saturn. Our main focus of this campaign was to utilise the high spatial resolution of HRC-I to separate observed kronian auroral and disk X-ray, similar to Jupiter. As described in Chapter 3.1, we can use the Weigt (2021) pipeline to potentially map the time-tagged photons observed from Saturn.

7.3.2 Simultaneous GOES data

Here we use data from GOES 16 satellite [herein referred to as GOES] to find the correlation between solar activity and kronian X-ray disk during thr *Chandra* windows, as observed by Bhardwaj et al. (2005c) and Branduardi-Raymont et al. (2010). Details of how we use the X-ray monitor on GOES to track solar flux are given in Chapter 3.3.

When using the GOES data, we account for light travel time from Sun-Earth and Sun-Saturn-Earth. This ensures we have the correct observation time for when the solar flare was first detected by GOES and then travelled to Saturn respectively (i.e. as viewed by the Earth-based remote sensing instruments like *Chandra* and *HST*). We corrected the light curves in this way for each of the Chandra DDT observations. The Saturn-Sun-Earth angle is also considered during each observation to find the likelihood of impact at Saturn and the direction of any flares found by GOES. When the angle is large (e.g. large deviation from perfect alignment of Saturn, Sun and Earth at 0°), the uncertainty of a solar flare detected from any spacecraft on or near the Earth-facing side of the Sun travelling to Saturn will also be large.

7.4 Results

7.4.1 Low X-ray count analysis

Based on previous observations of Saturn, we expect a low-count regime when analysis our data. Here we adopt the algorithm used by Dunn et al. (2021) to find the first significant detection of X-rays from Uranus. We first divide the full detector into a

grid of cells, or boxes, the size of the Saturn's apparent diameter (i.e. Saturn's disk) during the observation. This helps us calculate the significance of our Saturn photon counts within the red circle region, overplotted onto the gird, shown in Figure 7.1, with diameter $\sim 16''$(e.g. the largest angular diameter of Saturn during the DDT campaign). The position of the Saturn region is determined from its RA and DEC from ephemeris data[1]. With these parameters, we create the Saturn region using SAOImageDS9 (Joye and Mandel, 2003) for the example shown in Figure 7.1, ObsID 24847. This is example is used as the greatest number of photon counts (blue dots) were detected during this interval. The number of photon counts within the Saturn region, as shown in the inset, are then compared to the counts on the remainder of the chip, which forms our background during the observation. We note that Figure 7.1 shows a small portion of the chip, to allow the position of Saturn to be visualised in more detail. The centre or aim-point of the detector is situated in the middle of the image. The aim-point is surrounded by a navy-dashed $16'' \times 12''$ box associated with an errors due to possible drifts of the effective aim-point centre. We note here the error in the pointing will have a very little effect on our observations as the Saturn region is close to the centre, well within the errors. The point spread function (PSF) of HRC is shown by a black-dashed circle to represent the spatial resolution we use for our analysis against the size of Saturn's disk .

Saturn was undetectable throughout our November campaign due to the kronian emissions being indistinguishable from the particle background. Using the low count algorithm, each observation showed no significant detection above the background of the detector (e.g. signal observed was $< 3\sigma$ detection from the background counts, where σ is the standard deviation). This was the case for both kronian auroral and disk X-rays. The resulting distributions of our analysis for all photons counts across the chip within each Saturn-sized box relative to the counts detected within our Saturn region for our full campaign are shown in Figure 7.2a), (c) and (e). Here we note that each DDT observation had a similar distribution of photons across the chip, with the number of observed Saturn counts situated at or near peak of the distribution (C_S: as shown by the black-dashed line). This shows that for each of our observations the signal-to-noise ratio (SNR) was too low and therefore results in Saturn being indistinguishable from the photon background. As presented in Table 7.2 and our distributions of the photon counts, the mean background or Field of View ($FoV\ \mu$) across the entire HRC-I chip were comparable to counts we detect within our defined Saturn region. The total number of Saturn-sized boxes or cells defined across the chip, N_{Box}, the $FoV\ \mu$, the percentage of N_{Box} that had a photon count number smaller than C_S and the number of standard deviations C_S is from the $FoV\ \mu$ are all labelled in the top three panels of Figure 7.2. We note that the calculated background count for each

[1] https://ssd.jpl.nasa.gov/horizons/app.html#/

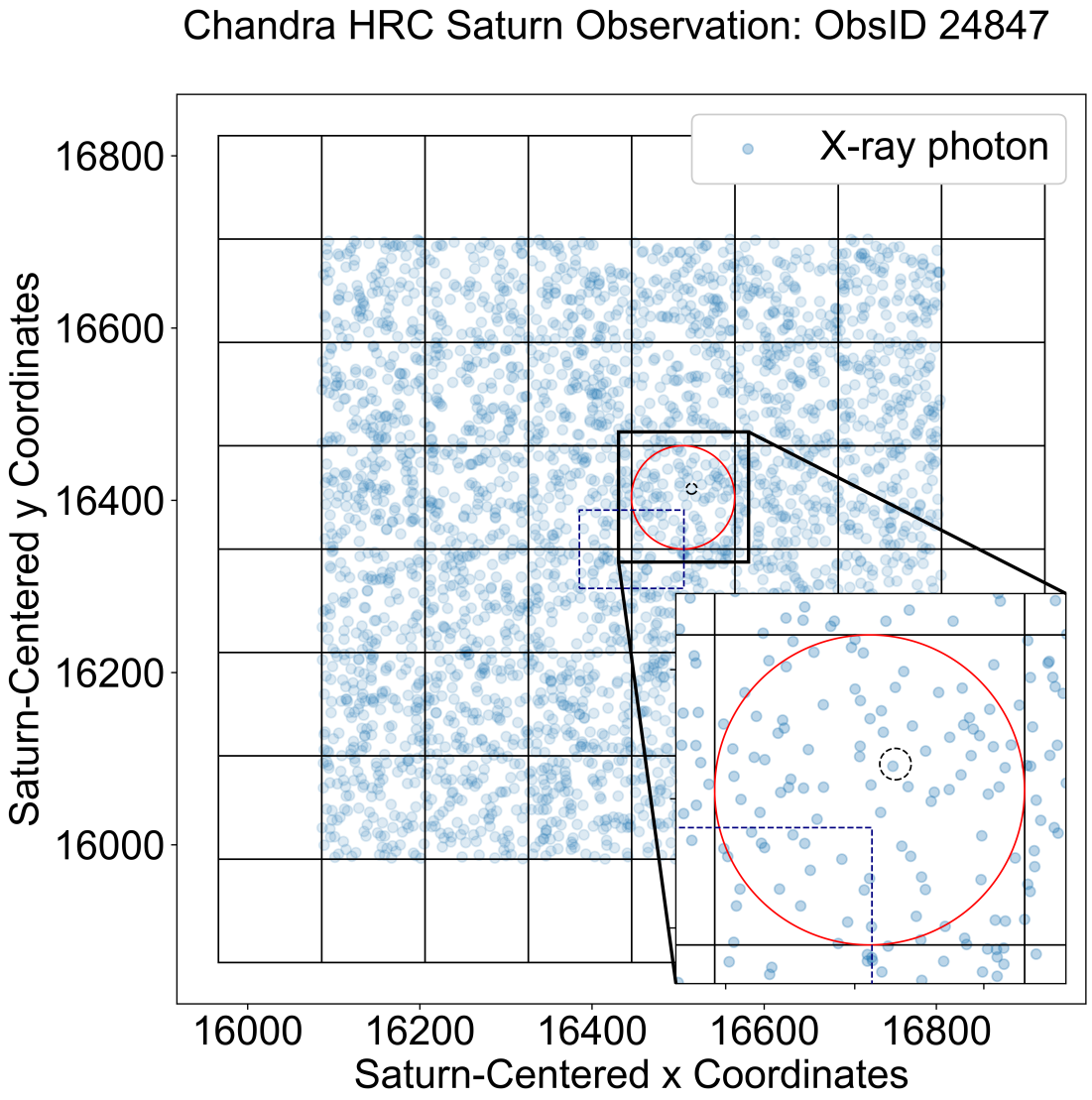

FIGURE 7.1: Positions of all detected X-ray photons (blue dots) from ObsID 24847 on a fraction the HRC-I chip closest to the centre. The navy-dashed box (of size $16'' \times 12''$) indicates the error associated with the effective aim-point centre of the detector, assumed to be at the centre of this image. The black-dashed circle depicts the size of the PSF. We split the chip into a grid with each cell (or box) the same width as Saturn's disk during each observation, using the angular diameter of the planet from ephemeris data. We apply this for the full chip beyond the region shown here. Saturn is located to be near the centre of the chip, as shown by the red circle, after its position is corrected. We then count the number of photons in each box across the chip and then compare with those located within the Saturn region to find the significance of the X-ray detection of the disk. The inset in the bottom right corner shows a zoomed image of the Saturn region in more detail. The positions of the photons on the chip grid are in planetocentric (i.e. Saturn centered) coordinates. The identical algorithm and grid was used for all 3 observations. Figure taken from Figure 1 in Weigt et al. (2021b).

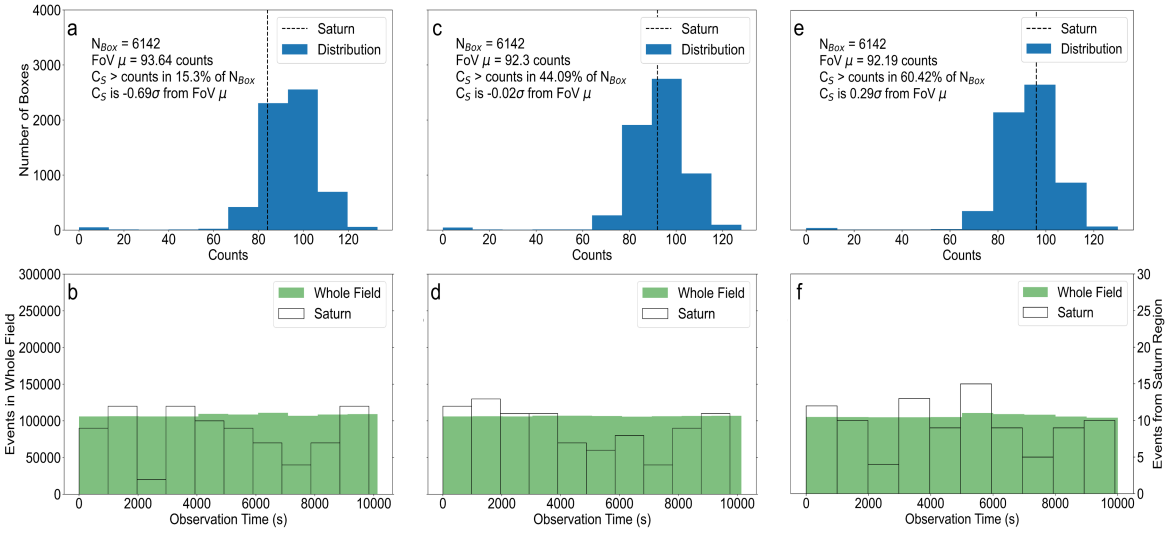

FIGURE 7.2: Resulting histograms of our analysis showing the distribution of counts within each Saturn-disk sized grid box (Figure 7.1) relative to the counts observed in the Saturn region for (a) ObsID 24845, (c) 24846 and (e) 24847. The corresponding histograms showing the distribution of photon counts over the observation interval within the Saturn region (transparent distribution, with y-axis on the right) and the whole distribution across the entire chip (green) are shown in panels (b), (d) and (f) for all DDT observations respectively. The black-dashed line in the overlaid on full chip distribution of photon counts signify the number of counts detected within the Saturn region, C_S. Key values and statistics of the distributions are labelled in panel a) including: the total number of Saturn-disk sized boxes the generate the grid across the entire chip (N_{Box}); the Field of View mean across the chip ($FoV\ \mu$) or background counts; the percentage of N_{Box} that had a count number smaller than C_S and the number of standard deviations (σ) C_S was from the $FoV\ \mu$. Figure taken from Figure 2 in Weigt et al. (2021b).

observation agrees with the expected instrumental background during this time[2]. We present the total number of Saturn photon counts and the calculated net counts, using $C_S - FoV\ \mu$, for observations in our campaign in Table 7.2. In this research we assume that the statistics used in our analysis are Poissonian since we are in a low count regime and account for the low SNR of the kronian X-rays we observe. From this we calculate the resulting error on the net counts found from ObsID 24847 to be 13.71 cts. As mentioned previously, this observation had the highest number of Saturn counts detected during the campaign. We apply identical assumptions to the remaining DDT observations with the results also displayed in Table 7.2.

To identify any possible time variability associated with the light curve at Saturn's position, we look at the time series in the Saturn region and compare to that found for the full distribution across the chip. Previous analysis of similar light curves associated with the full jovian X-ray spectrum show possible correlation between disk

[2]Full details can be found: https://cxc.cfa.harvard.edu/proposer/POG/html/HRC.html#tth_sEc7.10.3. Typical background rate of event files after processing $\sim 3 \times 10^{-5}$ counts s^{-1} arsec^{-2}. Area of each Saturn cell is 256 arcsec^2 with each observation lasting 10 ks (or 1×10^4 s). We therefore expect a background of $3 \times 10^{-5} \times 1 \times 10^4 \times 256 \sim 90$ background photons per observation, consistent with our analysis.

X-rays and solar X-ray activity (e.g., Bhardwaj et al., 2005a; Dunn et al., 2020a); auroral X-rays which dominate the spectrum which are usually concentrated into distinct hot spots in the north and south (e.g., Chapters 4 and 5, Gladstone et al., 2002; Dunn et al., 2017) as well as infrequent significant quasi-periodic flaring of the auroral regions (e.g., Chapter 5, Jackman et al., 2018). For our Saturn campaign, our analysis shows that the light curve across the full HRC chip is approximately flat for all three observations with the portion associated with Saturn's position again not significant above the detector background (e.g., more evidence of low SNR).

As our analysis lies within in a low count regime with using data with low SNR, we calculate the predicted 3σ upper limit of the kronian disk emissions for all observations during our campaign. Since this is the first X-ray auroral campaign of its kind linked to the unique planetary alignment of Jupiter and Saturn which occurs every $\sim$ 19 years, this is our first opportunity to predict X-ray powers for this unique scenario and compare them with measurements from previous studies in a more typical parameter space. We calculate the true mean for the predicted upper limit using the average value determined from the parameter associated with the range of net counts. This was applied to all observations in our campaign. Our energy flux calculation assumes a photon energy of $\sim$ 0.5 keV as computed by Branduardi-Raymont et al. (2010) as a robust average for the flux associated with Saturn's disk emissions. We make this assumption to account for the absence of energy resolution on HRC-I. A similar approach has been applied in previous studies focusing on the jovian emissions (e.g., Chapters 4 and 5, Gladstone et al., 2002; Dunn et al., 2017). We calculate an upper limit for Saturn's disk power by multiplying the fluxes by $4\pi\ d^2$, where d is the average *Chandra* -Saturn distance (see Table 7.1). The 3σ upper limit of Saturn's disk power of our best observation during the campaign, ObsID 24847, is 0.95 GW, with an associated energy flux upper limit of 3.04×10^{-14} erg cm^{-2} s^{-1}. In this calculation we assume that the net counts observed are from Saturn if it is emitting isotropic X-ray emissions (from either the disk or auroral regions). The low SNR and high background throughout the DDT campaign lead to the larger errors calculated in the net counts. The high background is likely to originate from high energy galactic cosmic ray photons, which are observed to be of the same level as our source counts. The upper limits of power and flux are calculated for all observations in our campaign and are displayed in Table 7.2.

7.4.2 Observing simultaneous GOES flux

As there is no spacecraft currently in orbit at Saturn or close to the kronian magnetosphere, there is no *in situ* monitor to sample the solar wind and/or kronian system conditions. Therefore we have to infer the conditions of the system throughout our campaign from other remote sensing measurements.Bhardwaj et al. (2005a) and

TABLE 7.2: Results from the Dunn et al. (2021) low count algorithm for each Chandra DDT observation with 3σ upper limit power and flux estimates. Table taken from Weigt et al. (2021b).

ObsID	**Counts in Saturn region (C_S)**	**Mean Background Counts ($FoV\ \mu$)**	**Net Counts** $\left(\pm\sqrt{(C_S + FoV\ \mu)}\right)$	**3σ upper limit[a] Disk power (GW)**	**3σ upper limit[a] Disk Flux[b]**	**Mean GOES soft X-ray flux ($\times$ 10^{-7} Wm^{-2})**
24845	84	94	-10 $\pm$ 13.34	0.28	0.90	0.83
24846	92	92	0 $\pm$ 13.56	0.76	2.48	3.17
24847	96	92	4 $\pm$ 13.71	0.95	3.04	6.93

[a] calculated 3σ upper limit as all observations were non-detections.
[b] upper limit of X-ray disk flux has units $\times 10^{-14}$ erg cm^{-2} s^{-1}

other previous X-ray studies analysing the kronian emissions (e.g., Bhardwaj et al., 2005c; Branduardi-Raymont et al., 2010) used data from solar observatories to infer the conditions at Saturn. As found from these studies, the expectation is that the kronian disk power should be correlated with solar activity. Such solar activity can be tracked using GOES measurements of the solar X-ray flux. When a flare is detected from the observable solar surface emissions across the electromagnetic spectrum, including the solar X-ray flux, are measured to be enhanced when the measured from solar observatories (e.g., Fletcher et al., 2011). In this research we use measurements of the soft solar X-ray flux (wavelengths 1Å- 8Å; where $1Å = 10^{-10}$ m) from the X-ray detector on board GOES as an indicator for solar activity throughout the DDT campaign. We display the calculated mean GOES solar X-ray flux for each observation in Table 7.2.

As discussed in Chapter 6, comparing our *Chandra* data with auroral observations detected in other wavelengths can also help us to infer the state of the magnetosphere during our observation window. During our observations, there was an ongoing *Hubble Space Telescope (HST)* UV campaign [P.I J. Nichols] from 29 October until 23 November 2020 with the same aim as our set of observations except monitoring Saturn's auroral UV response within this unique parameter space. There were 2 *HST* observations from the campaign within 2 days of our DDT observations (22 November $\sim$ 08:20 UT and 23 November $\sim$ 05:00 UT, $\sim$ 18 hours before ObsID 24847). Initial analysis of the HST observations suggest that the main driver responsible for the UV auroral emissions was different between both observations. This was identified from the change in morphological behaviour from a spiral-like structure, forming Saturn's equivalent to a UV main oval, to a concentrated brightening of emissions near Saturn's North pole enveloped by half the UV main oval. Such a dramatic change in the UV auroral morphology may be an indicator of the magnetospheres response to changing external conditions over short timescales.

Figure 7.3 illustrates the GOES soft X-ray flux evolving over time with the aforementioned *HST* (dashed black lines) intervals and our *Chandra* DDT observations (shaded orange regions) overplotted. The GOES time series is shown for (a: top panel) the entire month of November and (b: bottom panel) an inset displaying the week containing the *Chandra* observations. The data gap from 5 - 16 November represents the time period where no GOES data was available. Figure 7.3 shows that GOES observed the solar soft X-ray flux to gradually increase from around 20 November to 23 November where it seems to plateau at a greater average solar. Evidence of this is also represented in Table 7.2 with our calculated mean solar X-ray fluxes increasing throughout our *Chandra* campaign. This higher soft X-ray flux floor is maintained for the rest of November. As shown in the zoomed inset of the GOES data encompassing our DDT observations, GOES detects a possible C-class flare that may have impacted Saturn just before ObsID 24847. We correct the GOES time series for Sun-Earth and

Sun-Saturn-Earth light travel times to account for when the flare arrives at GOES (light time (lt) $\sim$ 8.2 min) and when it arrives at the kronian system as viewed from Earth by *Chandra* and *HST* ($lt \sim 170$ min). This was applied to all intervals and data shown in Figure 7.3. However, we note that the Saturn-Sun-Earth angles, taken from ephemeris data, during our DDT campaign were determined to be $\sim 72^{\circ}$ - 89°. As discussed in Chapter 6, such a large angle would imply that any flares detected GOES would unlikely to have impacted Saturn due to the very high propagation errors. We find the X-ray flux of the C-class flare to be $\sim 4 \times 10^{-6}$ W m^{-2} (or 4×10^{-3} erg cm^{-2} s^{-1}). Although as the alignment of Saturn-Sun-Earth implies that the flare is unlikely to have impacted Saturn, we do observe the mean solar flux to increase after the flare throughout the remainder of November (including our DDT campaign). As noted in previous literature analysing the disk X-ray emissions from the gas giants, not all solar photons impacting the upper atmosphere of the planet will be scattered back, and therefore producing the disk X-ray emissions we observe, due to the X-ray albedo of the planet (e.g., Bhardwaj et al., 2005a; Ness et al., 2004a,b). The albedo is an indicator of the reflectivity of the planet measured on how much sunlight is reflected back into space. For the case of the disk emissions in this research, we focus on the solar X-ray contribution of the observed sunlight. For Saturn the X-ray albedo is determined to be $> 5.7 \times 10^{-4}$ (e.g., Bhardwaj et al., 2005a; Ness et al., 2004a,b). This is slightly higher than what is calculated for Jupiter ($\sim 5 \times 10^{-4}$). This therefore implies that Saturn's upper atmosphere resembles that of slightly opaque, diffuse mirror for any incoming solar X-rays produced by the Sun. Due to its albedo, the upper atmosphere will be scattering back ~ 1 in a few thousand photons. From these numbers we would therefore expect Saturn's disk emissions to be observed, as has been the case in previous literature, and would also expect the increase in solar flux (and therefore an increase in solar X-ray photons) to allow significant detection from *Chandra* HRC-I of at least Saturn's disk emissions.

7.5 Discussion and Conclusions

This research analyses the first *Chandra* HRC-I DDT campaign aimed to observe X-ray emissions from Saturn to monitor its magnetospheric response during a rare planetary alignment with Jupiter, unique to these two planets in our solar system. We find a non-detection of Saturn in X-rays (both disk and auroral emissions) throughout our campaign. We note that our campaign coincided with the early rising phase of the current solar cycle. During this time, the Sun emits low solar X-ray flux, with expected sporadic flaring and ejections of faster solar wind streams on shorter timescales (e.g., Ataç and Özgüç, 2001; Burlaga et al., 2001; Xystouris et al., 2014). During our campaign, the observed soft solar X-ray flux from GOES was found to only peak above 10^{-6} Wm^{-2} during one of our three observations (ObsID 24847; see Figure 7.3).

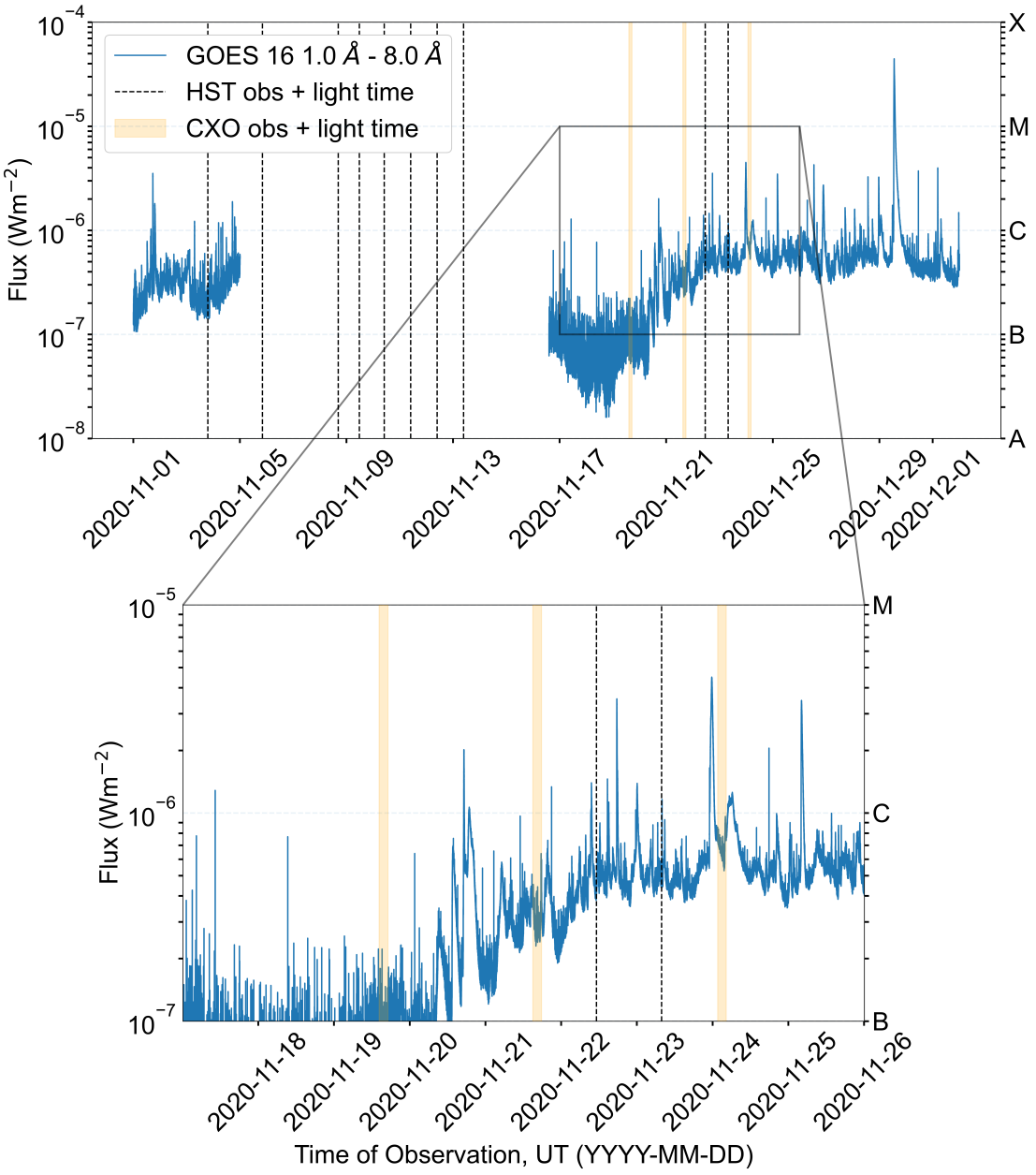

FIGURE 7.3: Time series of soft solar X-ray flux in logspace as detected from GOES 16 for (a) the entirety of November and (b) the week centring the Chandra observations. We note there was no GOES data available between 5 and 16 November. Observation intervals from both *HST* (black dashed line) and *Chandra* (shaded orange regions) are overplotted in both panels. We account for the Sun-Earth and Sun-Saturn-Earth light times were used to account for the flare being observed by GOES, when it arrived at Saturn and then viewed by *Chandra* and *HST* respectively. The ObsID 24847 example throughout this research is shown in both panels by the final shaded area. The estimated arrival time of the C-class flare is found to impact Saturn just prior to or coincide with ObsID 24847. The C-class flare has flux of $\sim 4 \times 10^{-6}$ W m^{-2}; the peak solar flux observed throughout the Chandra campaign. The C-class flare impacted Saturn after a steady increase of average solar flux throughout the month of November as shown in panel (a). Figure taken from Figure 3 in Weigt et al. (2021b).

This peak solar flux was observed immediately after a C-class flare and is likely related to a more global disturbance in response to the flare. The low solar X-ray fluxes observed from GOES and poor alignment of Saturn-Sun-Earth throughout the campaign, we expect the disk emissions to be dim with little response to the the solar activity. This is due to an amalgamation of fewer solar photons being elastic scattered in the kronian upper atmosphere as well as very little activity occurring on the observable solar surface that is Earth facing. We do note however that solar flares can be produced from active regions facing away from the Earth and therefore would not be detected from GOES. However, from the analysis presented in Figure 7.2 showing a flat distribution in the time series and non-significant kronian X-ray detection due to low SNR, this seems unlikely to be the case here. Although the weak solar flux would contribute to the non-detection of Saturn's disk amongst the detector background as fewer solar photons would lead to the chip being dominated by high energy galactic cosmic rays. As eluded to in Chapter 6, the continuing degradation of HRC-I will also have an affect when observing dimmer X-ray emissions[3]. From our analysis, we do note that the observation with the greatest number of counts detected within the Saturn region (C_S), ObsID 24847, is associated with the highest observed mean GOES flux. This observation, although still a non-detection, agrees with conclusions made from previous studies that detected a possible correlation between Saturn's disk emissions and solar activity measured by the soft solar X-ray flux (e.g., Bhardwaj et al., 2005c).

The predicted 3σ upper limit of the energy flux we calculate here using our assumptions, at 0.90 - 3.04 $\times$ 10^{-14} erg cm^{-2} s^{-1}, is observed to be within those found from modelled spectra of previously observed significant kronian X-ray disk emissions. Branduardi-Raymont et al. (2010) calculated the kronian energy flux between 0.2 and 2 keV (i.e. the jovian soft X-ray range associated with the aurora) to be $\sim$ 0.30 - 1.00 $\times$ 10^{-14} erg cm^{-2} s^{-1}. Like the observations we present here, the *Chandra* intervals coincided with GOES measurements of the solar soft X-ray flux exceeding 10^{-6} Wm^{-2}, like we observe here for one of our intervals. Our predicted energy fluxes are calculated to be an order of magnitude weaker than those calculated by Gilman et al. (1986) for modelled non-relativistic, thick-target bremsstrahlung at 1.7 $\times$ 10^{-13} erg cm^{-2} s^{-1}, from a $\sim$ 11ks observation (i.e. similar exposure time to what we present here). These values are also taken from the 3σ upper limit. When compared to the energy fluxes calculated from Ness and Schmitt (2000), our values matched their predictions for Saturn soft X-ray flux if detected at 1.9 $\times$ 10^{-14} erg cm^{-2} s^{-1} and their 95% confidence upper limit flux for possible bremsstrahlung emissions at 1.3 $\times$ 10^{-14} erg cm^{-2} s^{-1}. Therefore the predicted fluxes calculated in this research are consistent with previous results. We note that no spectral data were available throughout our campaign. Similar to the limitations of

[3]See Section 7.7 - 7.10 in https://cxc.harvard.edu/proposer/POG/html/chap7.html

HRC-I with Jupiter, as explained in Chapter 3, the energy resolution is very limited due to the kronian X-rays activating the lower pulse height amplitude channels associated with very soft X-ray emissions. As a result our estimated flux and power include photons with energies exceeding 2 keV, previously used as an upper bound for the spectral models used by Branduardi-Raymont et al. (2010). Our results are therefore consistent with previous observations from previous campaigns, such as *ROSAT* (Ness and Schmitt, 2000), but without any energy filtering due to the limited spectral resolution of the instrument. As our predicted fluxes agree with previous literature, we suggest that there should be more future campaigns planned to observe Saturn again during this unique and poorly understood parameter space. The next planetary alignment will be coincident with the launch and science operations of the next generation of X-ray telescopes with higher sensitivity such as *Athena* (Barret et al., 2016) and the mission concept *Lynx* (Gaskin et al., 2019), currently being reviewed for the 2020 Astrophysics Decadal Survey.

With the new fleet of X-ray telescopes comes updated optics and energy resolution, improving the capabilities of X-ray telescopes. For example, at 1 keV the collecting area of both *Athena* (~ 1.5 m^2) and the *Lynx* concept (~ 2.3 m^2) is ~ 20 - 30 times greater than that found on *Chandra* (~ 0.08 m^2). The improved collecting area will allow for far deeper exploration of space by increasing the threshold of detectability, allowing fainter sources to be observed above the statistical noise and background of the instrument. The large collecting area of *Lynx* coupled with a very high spatial resolution ($< 0.5''$) allows fainter X-ray sources to be observed, analysed and mapped in greater detail. *Athena's* spatial resolution ($\sim 5''$) will be inadequate to map the X-ray emissions like *Chandra* , as we show throughout this thesis. However, the spectral resolution of *Athena's X-ray Integral Field Unit (X-IFU)* surpasses that of *High Definition X-ray Imager* on board *Lynx* (~ 70 eV - 150 eV at energies 0.3 - 5.9 keV) and our current capabilities with ACIS (~ 130 eV - 280 eV at energies 1.49 - 5.9 keV) (Falcone et al., 2019) at ~ 2.5 eV up to energies of 7 keV (Barret et al., 2016). *Athena's* extremely high energy resolution will provide us with the capabilities to probe deeper into the kronian X-ray emissions as well as that observed from other planets, such as Uranus (Dunn et al., 2021). With the improved sensitivity and capabilities of future X-ray telescopes, future studies can perform a deeper and more thorough search for X-ray aurorae at Saturn allowing us to further constrain the disk emissions. This will also allow us to monitor the response of the kronian magnetosphere to this poorly understood parameter space. We will be able to explore the magnetospheric response of other planets as well, providing a greater understanding of the X-ray drivers within our Solar System. We do note that to fully utilise these improved capabilities, future observations will need to ensure that they are planned with an optimised exposure time.

The aim of our campaign was to determine whether the powerful shocks generated from Saturn transition from a less dense plasma environment in the jovian magnetotail to the denser solar wind plasma would be to provide the energy required to generate X-ray aurora on Saturn. This is because that, during transitions from the magnetotail to the solar wind, we expect the kronian magnetosphere to be impacted with more powerful shocks than what is typically observed when Saturn is exposed to changing solar wind regimes (i.e. a more typical parameter space). This will result in the magnetosphere to change state, or compress, more rapidly than the typical plasma environment Saturn is usually located within, releasing more energy in the process. Like Jupiter, the dominant plasma source is internal and is in form of heavy ions produced from one of its moons. For the case of Saturn, the constituents of the heavy ions consist mainly of H_2O^+, OH^+ and O^+ produced the most active icy moon Enceladus (e.g., Hui et al., 2010a). This campaign provided us with the unique opportunity to probe and try to understand the extremes of the parameter space at the kronian system from a water-rich kronian magnetosphere, in a typical state, enveloped in the solar wind, to a magnetosphere completely immersed in the vast jovian magnetotail containing very little plasma relative to its size (and therefore more rarefied than the solar wind). However, the non-detections of any significant kronian emissions presented in our analysis suggests more extreme and variable external conditions generating more powerful magnetospheric compressions are still insufficient to energise heavy ions to the required MeV energies required for auroral X-ray production, assuming a similar mechanism as observed for the jovian emissions (e.g., as discussed throughout this thesis: Section 2.4 and Chapters 4 - 6). Hui et al. (2010a) suggested that field potentials at the poles of Saturn are too weak to allow charge stripping of magnetospheric plasma to occur or accelerate solar wind ions to energies required for the production of X-ray ion aurora (Cravens et al., 2003; Clark et al., 2020). Therefore a mechanism for soft X-ray production similar to Jupiter may not be possible at Saturn, although there may be a preference for electron dominated X-ray emissions (e.g. bremsstrahlung) in a more dipolar field as shown by a recent study by Mori et al. (2022). The more dipolar southern region at Jupiter was found to generate harder X-rays than the more complex field at the North pole. The field topology at the South pole of Jupiter is similar to that found on Saturn (i.e. a dipolar field) and may favour strong electron currents (as observed at Jupiter from *Juno* , Kotsiaros et al., 2019). Future observations including *NuSTAR* may help answer some of these questions.

As mentioned previously, the two *HST* intervals that overlapped with our campaign (within 2 days before ObsID 24847) observed a dramatic change in morphology. The UV emissions were first dominated by a spiral-like morphology within the main oval, as observed on 22 November 22, and then transitioned to a different morphology with more concentrated emissions at the North pole. The latter UV morphology was

observed hours before the Chandra interval. Previous literature suggest that the spiral morphology of Saturn's UV auroral emissions is associated with episodic precipitation of hot plasma during periods of rapid reconnection in the kronian magnetotail and reconnection on the dayside magnetosphere (Cowley et al., 2004; Jackman et al., 2004). These reconnection events were found to be steady but unbalanced during these times. As discussed in Chapter 6 for the case of Jupiter, dayside reconnection is likely associated with a shock events from the interplanetary medium, compressing the magnetosphere. This has also been observed at Saturn from possible shocks produced from more powerful and dynamic solar wind conditions (e.g., Badman et al., 2016). The rate of dayside reconnection is likely to vary with changing solar wind dynamic pressure. Cowley et al. (2005) suggested that one likely cause of more localised brightening of emissions in the kronian polar auroral is from a dawn storm. Similar to Jupiter, such dawn storm emissions are a result of intense auroral emissions generated from reconnection in Saturn's tail promoted by compression events. However we cannot verify any unusual X-ray emissions at Saturn's north pole after the HST interval due to our insignificant detection.

We present in this research first X-ray campaign o its kind, designed to specifically monitor the magnetospheric response of a planet in a highly unusual parameter space. With the analysis conducted here, we hope the foundations for further exploration into this rare planetary alignment, which occurs every $\sim$ 20 years, using the next generation of X-ray observatories with improved sensitivity to fainter sources coupled with greater spectral resolution. We will then be able to calculate tighter observational constraints on the kronian auroral luminosity in all possible parameter spaces and monitor in greater the detail how the magnetosphere responds. This will aid us to solve the mystery behind Saturn's absent X-ray aurora.

Chapter 8

Summary and Future Work

"And now the end is near, And so I face the final curtain..."
- Frank Sinatra, *My Way*[1], 1969
[English lyrics written by Paul Anka]

8.1 Summary

The year 2022 marks over 40 years since the jovian auroral X-ray emissions were first discovered by the *Einstein Observatory* (Metzger et al., 1983). Since then, with the development of more sophisticated X-ray cameras and spectrographs on-board a fleet of telescopes, we have been able to spatially resolve and map the photons onto the planet to a degree of accuracy and extract the jovian X-ray spectrum with the most intricate detail to help aid our understanding of the elusive X-ray driver or drivers. The research presented in this thesis contributed to this ongoing effort by exploring the morphology and timing analysis of the jovian X-ray auroral emissions in great detail over $\sim$ 20 years worth of data, separating the aurora into physics-informed regions to determine the driver(s) of the variable emissions and identifying any key, significant regions of interest.

In Chapter 4 (Weigt et al., 2020) we focused on one particular observation by *Chandra* while *Juno* was at apojove. In this study we analysed how a solar wind compression affects the jovian X-ray driver as well as exploring the possibility of kronian auroral emissions occurring during a rare and extreme planetary alignment. Using the Vogt et al. (2011, 2015) flux equivalence model to provided us with ionosphere-magnetosphere mapping to locate potential drivers capable of energising ions to $\sim$ a few MeV (Houston et al., 2020) needed for the charge stripping and exchange processes to take place. The mapping model was used in context with the

[1]For one last sing-song: https://www.youtube.com/watch?v=qQzdAsjWGPg

aforementioned case study, X-ray observation taken in tandem with an identified solar wind compression from *Juno* on 18 June 2017, and the entire *Chandra* HRC-I dataset of jovian X-rays (2000 - 2019). The case study allowed us to utilise the mapping model with our Rayleigh test and Monte Carlo simulation (timing analysis) to map and isolate significant quasi-periodic oscillations (QPOs) to analyse their evolution during a jovian rotation. In this instance, during the 18 June 2017 observation we found a significant QPO at $\sim$ 37-min when the northern auroral emissions first rotated into view which changed to $\sim$ 26-min later in the observation. The latter QPO was simultaneously observed by *XMM-Newton*, further increasing its significance. Both QPOs mapped to the dayside magnetopause, suggesting possible time evolution of the driver. The auroral morphology was found to be more elongated equatorward, as found previously by Dunn et al. (2016), who had also observed a $\sim$ 26-min QPO during a compression event caused by an interplanetary coronal mass ejection.

In Chapter 5 (Weigt et al., 2021a) we applied the flux equivalence model to the full 20-year *Chandra* dataset of the northern auroral region, we found two potential locations for the X-ray auroral driver: the noon and dusk flank magnetopause boundary. Comparing to ultra-low frequency (ULF) wave activity found by *Galileo*, these driver regions may be associated with standing Alfvén wave activity from possible cusp or drizzle-like reconnection on the dayside (e.g., Bunce et al., 2004; Guo et al., 2018); the unusual crescent-shape "polar cap" configuration (Zhang et al., 2021) or Kelvin-Helmholtz Instabilities (KHIs) on the dusk flank magnetosphere (e.g., Masters, 2018; Manners and Masters, 2020) as predicted by the magnetic field line mapping from Zhang et al. (2018). From our timing analysis using Rayleigh testing and Monte Carlo simulation, we found the distribution of QPOs to be different for the statistically significant noon region, AHSNuc, and the full northern auroral emissions suggesting multiple drivers linked to possible ULF wave activity along the magnetopause boundary. All QPOs were found to be between $\sim$ 2.3 - 36.4-min, similar to the ULF wave oscillations found by Manners and Masters (2020) from the entire *Galileo* mission.

In Chapter 6 we created physics-informed auroral regions for the northern X-ray emissions to allow us to associate morphological features with magnetospheric drivers. The identification of multiple drivers in chapter 5 puts into question the "hot spot" nomenclature used throughout the literature; the auroral families of the X-ray emissions allowed us to explore this hypothesis further. We found that potential drivers switch on/off at different times during the *Juno* -era, with a fully polar X-ray auroral morphology likely associated with solar wind compressions as confirmed from UV auroral classifications from *HST* and *Juno* magnetometer and radio data, as eluded to by the 18 June 2017 case study. We also show that a low-latitude extension (LLE) is likely associated with possible particle injection in the jovian middle magnetosphere although further analysis of the *Juno* and *HST* data is needed to verify

this. We address the potential issues of viewing geometry by modelling our regions as viewed by the *Hubble Space Telescope HST* over a full jovian rotation. All regions should be visible throughout each observation although we note that the tilt of Jupiter, as viewed from the observer, has an effect on the peak visibility. As we analyse the *Chandra* data over identical timing and viewing constraints (to avoid observation bias), our preliminary results suggest that visibility effects are minimal and the lack of uniformity of the auroral photon distributions across the observations suggest that magnetospheric drivers are likely switching on/off in response to internal and/or external effects. Understanding how the auroral emissions change and evolve with solar wind dynamics will allow us to determine more characteristics about the unknown auroral driver. The analysis presented in this thesis therefore concludes that the most plausible source of the pulsating emissions occurs on the magnetopause boundary. It is likely that emissions are related to ULF wave activity from comparisons of the flux equivalence mapping and timing analysis, with the morphology of the aurora changing with solar wind conditions.

Finally, in Chapter 7 (Weigt et al., 2021b) we explored the unique parameter space of Saturn being in a rare planetary alignment with Jupiter, potentially immersing itself in the jovian magnetotail. Several previous X-ray studies have failed to observe significant X-ray emissions from Saturn's auroral regions and argued that the sensitivity of current X-ray instruments were insufficient. Such studies did however predict that bremsstrahlung emissions should be present simultaneously with very bright UV emissions, assuming a similar mechanism to Jupiter (e.g. Ness and Schmitt, 2000; Ness et al., 2004b). We obtained telescope time to observe X-rays, for the first time, in this unique parameter space. No significant detection was found, and we argue with the new fleet of telescopes, such as Athena and Lynx, with highly sensitive spatial and spectral resolution, the extremely soft auroral X-ray spectra may be resolved for the first time.

In this thesis we have utilised the *Chandra* data to help us obtain more details surrounding the elusive auroral driver(s) of the X-ray emissions using various mapping and timing analysis techniques. In the Future Work section, we examine: (1) how the auroral families can be expanded to generate a catalogue of labelled observations for future projects; (2) how we can utilise the timing analysis techniques demonstrated here and in other fields to allow a coherent comparison of auroral pulsations between datasets of different length and (3) how we can use *in situ* *Juno* data to help us estimate solar wind conditions at Jupiter as well as being a ground truth to perform metrics on widely used solar wind propagation models.

8.2 Future Work

With our current X-ray telescope capabilities, the potential for future work on jovian auroral X-ray emissions is vast. We have only scratched the surface of the Chandra, XMM-Newton and possible future NuSTAR datasets. The remainder of this chapter will briefly discuss future avenues the research examined here could take to improve how we analyse and label the current datasets, as well as using Juno *in situ* to further improve solar wind estimations and how we look at magnetospheric dynamics to finally identify possible drivers for the X-ray auroral emissions.

8.2.1 Labelled catalogues of physics-informed auroral families

As discussed in Chapter 6, defining auroral morphological families allows us to analyse links with associated magnetospheric dynamics and quantify many spatial variations across the full auroral region. As shown in Figure 6.2, Grodent et al. (2018) labelled *HST* data during *Juno* orbits 3 - 7 based on various identifiable features and behaviours within the UV main aurora, polar active region and regions just equatorward of the main aurora. The Grodent et al. (2018) northern auroral families are defined as: Q = quiet, U = unsettled, N = Narrow, I = strong injections, i = injectons and X = eXternal perturbations, all shown in Figure 6.2 with the defining auroral features highlighted with red dashed lines, ellipses and numbers "1 - 9". More details of the auroral families can be found in Grodent et al. (2018) and in Chapter 6.

This image segmentation can be carried out for auroral and disk emissions across many wavelengths, not just X-ray and UV auroral emissions, from various maps and spectrograms using current methods to correct and clean images prior to analysis (McEntee, 2021) and to map and select specific features using a polygon selector (Guio and Achilleos, 2009; Empey et al., 2021). Previous studies have implemented image segmentation to identify and analyse structures within the auroral emissions (e.g., Guio and Achilleos, 2009), but a complete catalogue of fully labelled auroral images across multiple wavelengths has yet to be created. Using these techniques, we can combine labelled structures associated with auroral emissions and magnetospheric dynamics to build a complete multiwavelength catalogue, from contemporaneous observations. This catalogue could be used for comparative studies to analyse possible correlations between multiple wavelengths to determine the X-ray auroral driver or can be used as a training set for future machine learning projects (e.g. to find specific auroral structures from the big data sets associated with various solar wind/magnetospheric conditions). One example of such a study is by Nichols et al. (2019) who used principal component analysis (PCA) to identify repeated structures which varied within the UV auroral morphology. From their analysis using density-based spatial clustering algorithms with additional noise, they found that the

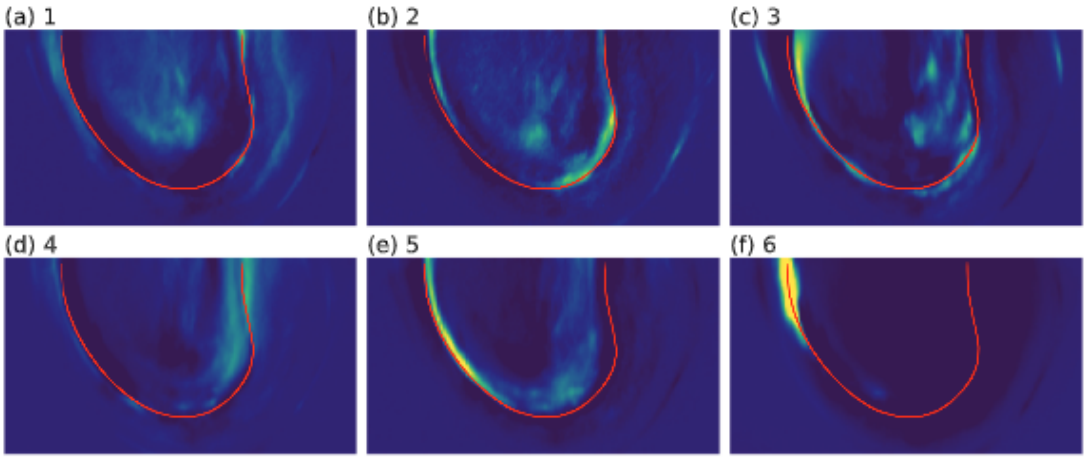

FIGURE 8.1: Figure showing the six auroral classes found from the principal component analysis performed by Nichols et al. (2019). Class (5) and (6) are found to be associated with solar wind compressions and dawn storms respectively. Image taken from Figure 6 in Nichols et al. (2019).

auroral components can be grouped into six repeated auroral classes, as shown in Figure 8.1. They found one class associated with solar wind compression, (5), and another with dawn storms, (6).

Similar machine learning studies using a more detailed auroral catalogue will identify common structures found within multiple wavelengths. For example, the link between dawn storms and the hard X-rays in the auroral emissions have been observed by Wibisono et al. (2021), however were unable to be mapped due to the low spatial resolution of XMM-Newton detectors. Such machine learning projects could identify UV dawn storm emissions associated with specific X-ray regions, isolating the structures and allowing for in depth analysis of the associated magnetospheric drivers for both the dawn storms and the hard X-rays. This would be beneficial to the field due to the continued degradation of the *Chandra* instrument, affecting the energy resolution at the observed peak wavelength of the X-ray auroral emissions (as discussed in Chapter 3).

8.2.2 Optimising timing analysis methods

As well as generating a catalogue of auroral morphology with associated magnetospheric dynamics, another one can be generated to focus on the temporal behaviour of the auroral emissions. The temporal behaviour of jovian aurora have been studied across many different wavelengths (e.g., Kimura et al., 2011; Jackman et al., 2018) to help understand the complex auroral drivers in the jovian magnetosphere. In the Juno era we now have a significant catalogue of contemporaneous UV and X-ray emission with quasi-continuous radio data from *Juno* . One revolutionary project would be to combine *in situ* and remote sensing data

to quantify the conditions under which quasi-periodic oscillations (QPOs) are observed, and link these to appropriate driving mechanisms (e.g. as found from the spatial behaviour).

The datasets from *HST* , *Chandra* and *Juno* data, such as from the Waves instrument (radio), are, or can be processed, to be time-tagged. As discussed in this research, this means that the detector records the time of arrival of the photon or particle during the observation. We can therefore construct a time-series of the arrival times to examine temporal behaviour of the aurora using various techniques such as Rayleigh testing and Monte Carlo Simulation (Chapter 2 - 6) to find any significant pulsations from potentially sparse, unbinned data.

With some previous studies analysing jovian auroral temporal behaviour, the statistical testing used to look at (quasi-)pulsations did not account for the number of cycles the signal appears during the observation window; the frequency grid used to search for QPOs, or consider the statistical noise that could lead to false significances. This therefore leads to vast differences in significance thresholds that may not be appropriate for the size of the dataset. A catalogue of timing behaviour will combat these issues by finding QPOs across multiple wavelengths using consistent significance testing and develop optimised techniques to compare data of different window sizes, for example *Chandra* (10 hours) with *HST* (45 minutes). One potential technique can involve examining the coherence of any signals over longer times (i.e., consecutive 45-min HST orbits), stitching together neighbouring observations to see if the coherence of the signal remains for a few more cycles. When comparing such datasets. it is important to quantify how QPOs can be judged significant when working in a very low count regime (e.g. often the case for auroral X-rays). Such methods can be adapted and improved from expertise outside of the field of planetary science such as solar and X-ray binary physics, where measuring temporal behaviour and significance is a key component of their research.

8.2.3 Improving current solar wind propagation models

With the lack of upstream solar wind monitors at the gas giants, many studies have used various 1D solar wind propagation models, linearly interpolating the conditions observed in geospace (e.g., Tao et al., 2005; Zieger and Hansen, 2008), with large arrival time errors ($\pm$ 2 days). Both methods come with significant uncertainties which are not well constrained. One potential avenue would be to calculate performing metrics on these models and testing them against *in situ* solar wind data from Juno, allowing the robustness and output accuracy to be assessed and compared for the first time. This is essential to ensure external shocks from the solar wind can be predicted with greater accuracy in the absence of an upstream monitor. Metric testing

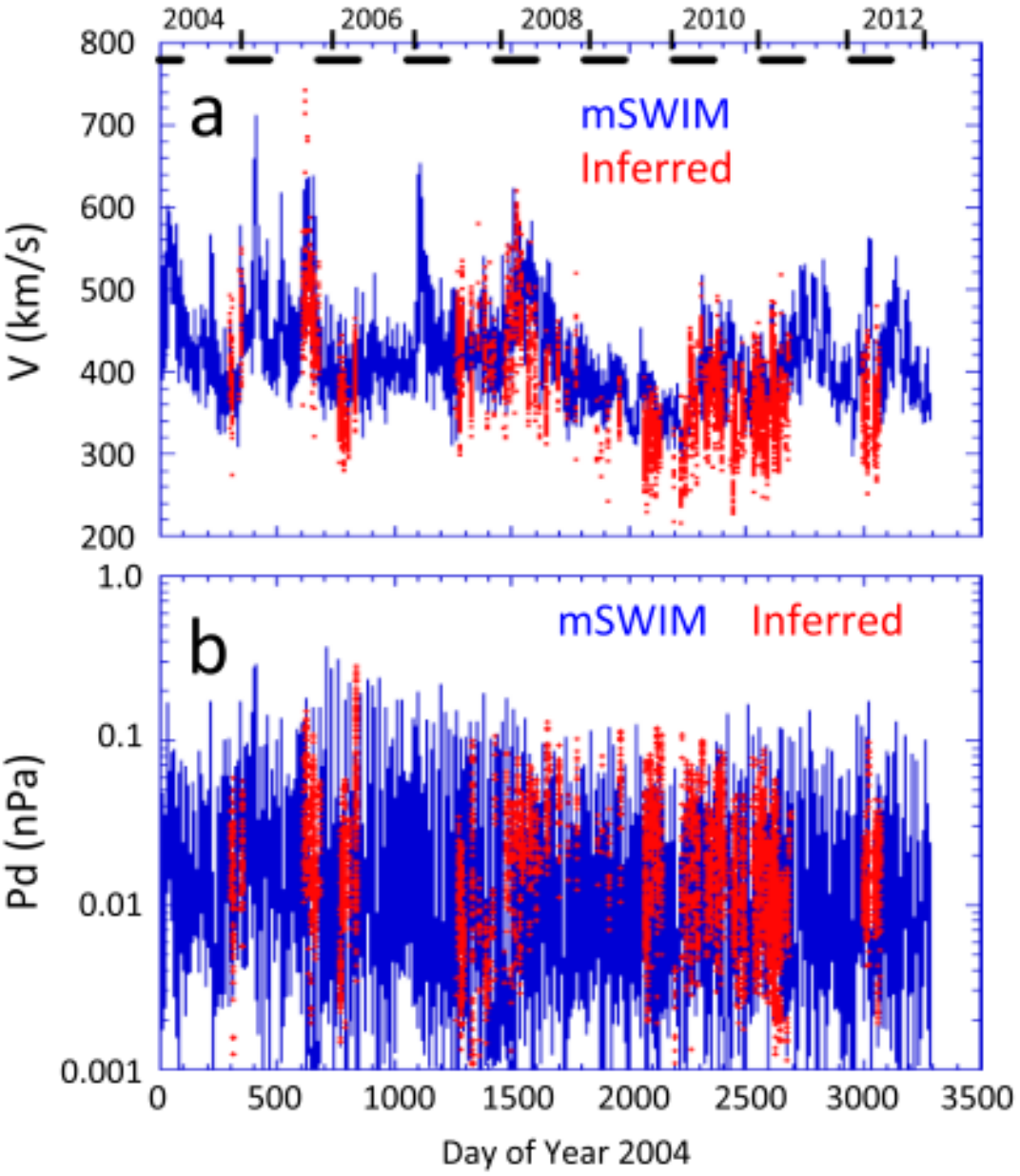

FIGURE 8.2: Time variation of the (a) solar wind speed and (b) dynamic pressure inferred from Casinni magnetosheath measurements (red) and the mSWiM model (blue) from January 1 2004. The solar wind parameters are plotted with aas a function of time. Black bars indicate times when the Jupiter-Sun-Earth angle $< 75°$ when the mSWiM model would be most accurate (see Thomsen et al. (2017) fore more details). Figure taken from Figure 4 in Thomsen et al. (2017).

these models can draw from state-of-the art techniques currently used in space and terrestrial weather forecasting to quantify the robustness of solar wind estimates through methods like skill score calculation, using the *in situ* Juno data as a ground truth.

Another way to utilise the vast amount of Jupiter magnetosheath data from Juno is to build on a technique by Thomsen et al. (2017) from Saturn, not yet applied to Jupiter,

to calculate robust local estimates of solar wind parameters, specifically the velocity and dynamic pressure, used to infer the state of the magnetosphere. This analytical method would again provide a useful tool to compare *in situ* conditions with the predicted arrival times. Thomsen et al. (2017) compare their analytical results for Saturn with the mSWiM MHD model (Zieger and Hansen, 2008) to validate their method (see Figure 8.2). They found the inferred measurements of the solar wind velocity and dynamic pressure were lower than the predicted values although the temporal variations found from shocks were captured well and fell within the arrival time prediction. Applying this to the Juno data will allow the time evolution of compression effects on auroral X-ray structures (identified from the auroral families) and their associated magnetospheric drivers to be analysed in greater detail. Such a tool would also be very useful to understand how both the temporal and spatial morphology of the X-ray emissions in both hemispheres are affected and evolve under different magnetospheric conditions.

As clearly presented in this thesis, the analysis of X-ray emissions at the gas giants is still a relatively new field in planetary science today although producing new and exciting results, changing our perspective on how the jovian magnetosphere operates. It is clear that there are still many unanswered key questions however the quest for discovery and understanding is still ongoing. This is made possible through collaborations with the *Juno* spacecraft and other remote sensing telescopes, which we hope continues with the introduction of *Athena* and *Lynx* (if selected) and other future missions. As with all new fields, the coming years will be important and exciting in order to fully establish the planetary X-ray field with huge potential for further science to be explored and new discoveries to be made.

Appendix A

Chapter 5: Supplementary Information

The figures and tables here showcase the analysis discussed in Chapter 5 to the entire catalogue and are used to emphasise the main results. We show how the errors within the mapping model and using a different internal field model can affect our interpretations of the driver. We also present heat maps of all the concentrated X-rays found within the numerical threshold, showing the location of the AHSNuc within the auroral structure for all observations analysed.

As Figure A.3 consists of a $\sim$ 25 page long PDF document, the link to access the plots are found as a footnote in Chapter 5.4.2 in the thesis chapter. For completeness, the link is also provided here: https://agupubs.onlinelibrary.wiley.com/action/downloadSupplement?doi=10.1029%2F2021JA029243&file=2021JA029243-sup-0002-Figure+SI-S01.pdf. A longer caption for each of the tables listed in Appendix A are given at the start of each section.

A.1 Chandra HRC-I catalogue

Table A.1: List of all Chandra HRC-I observations of Jovian X-ray emissions from 2000 – 2019 (all observations at the time of writing). Column 1 gives the unique identity number given to each observation. The following columns give the observation start date and time, the duration of the entire observation in kiloseconds (ks) or hours, the range of sub-solar longitudes observed (SSL), the sub-observer latitude, the hot spot visibility and counts of the North and South auroral regions respectively and any concurrent observations. We note the following acronyms are used for concurrent flybys and remote sensing data: CAS = Cassini (flyby), HST = Hubble Space Telescope, UI = Ulysses (flyby), XMM = XMM-Newton, SUZ = Suzaku, SPR = Hisaki, NuS = NuSTAR, IR = Ground based Infra

TABLE A.1: Table of all Chandra HRC-I observations from 2000-2019.

ObsID	Obs Date (UTC time) dd/mm/yyyy (HH:MM)	Total Obs. Duration ks (hours)	Range of observed Sub-solar Longitude (SSL) during obs. (°)	Sub-observer Latitude* (°)	Auroral Visibility** (Total counts)		Concurrent Obs.
1862	18/12/2000 (09:53)	∼36 (10 hours)	14 - 72	3.51	N (196)	S (90†)	CAS, GAL, HST?
2519	25/02/2003 (00:21)	∼72 (20 hours)	357 - 92	0.16	N (261)	S (276)	UI, GAL, XMM
15671	08/04/2014 (08:18)	∼40 (11 hours)	201 - 279	1.78	N (568)	S (276†)	XMM
16299	10/04/2014 (01:09)	∼40 (11 hours)	252 - 347	1.77	N (530)	S (172†)	
15672	12/04/2014 (22:09)	∼40 (11 hours)	233 - 311	1.76	N (444)	S (261†)	XMM
15669	15/04/2014 (20:43)	∼40 (11 hours)	273 - 348	1.75	N (414)	S (243†)	XMM, SUZ, SPR
16300	17/04/2014 (12:19)	∼40 (11 hours)	269 - 315	1.74	N (336)	S (220†)	XMM, SUZ, SPR
15670	20/04/2014 (02:19)	∼40 (11 hours)	351 - 19	1.73	N (230)	S (209†)	XMM, SUZ, SPR
18608	24/05/2016 (10:21)	∼40 (11 hours)	185 - 249	-1.75	N (626)	S (417)	J-U, XMM, HST
18609	01/06/2016 (11:31)	∼40 (11 hours)	351 - 40	-1.74	N (452)	S (482)	J-U
18301	02/02/2017 (09:56)	∼36 (10 hours)	227 - 254	-3.40	N (455)	S (561)	J-PJ4, HST, OPT, IR, RAD
20000	28/02/2017 (12:38)	∼72 (20 hours)	277 - 4	-3.50	N (1208)	S (1122)	J-AJ4
18676	27/03/2017 (15:42)	∼9.5 (3 hours)	234 - 239	-3.49	N (94)	S (91†)	J-PJ5, HST, IR, RAD
18302	19/05/2017 (00:27)	∼40.4 (11 hours)	227 - 294	-3.19	N (746)	S (537)	J-PJ6, NuS, HST, OPT, RAD
20001	18/06/2017 (18:37)	∼36 (10 hours)	125 - 152	-3.02	N (434)	S (390)	J-AJ6, XMM, HST, NuS, OPT, IR
18677	10/07/2017 (21:11)	∼40.4 (11 hours)	287 - 335	-2.96	N (578)	S (436†)	J-PJ7, XMM, NuS, HST, OPT, IR, RAD
20002	06/08/2017 (01:55)	∼36 (10 hours)	44 - 84	-2.95	N (472)	S (337†)	J-AJ7
18678	31/03/2018 (23:10)	∼40.4 (11 hours)	119 - 151	-3.87	N (571)	S (564)	J-PJ12, OPT, IR, RAD
20733	01/04/2018 (10:38)	∼40 (11 hours)	171 - 213	-3.87	N (726)	S (634)	J-PJ12, HST, OPT, IR, RAD
18679	23/05/2018 (23:59)	∼40.4 (11 hours)	287 - 325	-3.78	N (558)	S (478)	J-PJ13, HST, IR
18303	15/07/2018 (07:05)	∼40.4 (11 hours)	-	-	-	-	J-PJ14, XMM, HST, OPT, IR,
18680	06/09/2018 (20:38)	∼40.4 (11 hours)	119 - 133	-3.33	N (482)	S (466†)	J-PJ15, HST, IR
22159	29/05/2019 (03:26)	∼36 (10 hours)	55 - 110	-3.16	N (757)	S (491)	PJ-20, HST, OPT, IR
22146	13/07/2019 (01:26)	∼25 (7 hours)	44 - 96	-3.08	N (515)	S (324†)	J-PLAS, XMM
22147	13/07/2019 (21:08)	∼25 (7 hours)	171 - 191	-3.08	N (473)	S (276†)	J-PLAS, XMM
22148	15/07/2019 (12:58)	∼25 (7 hours)	62 - 86	-3.07	N (462)	S (291†)	J-PLAS, XMM
22149	16/07/2019 (08:44)	∼25 (7 hours)	51 - 93	-3.07	N (577)	S (306†)	J-PLAS, XMM, HST
22150	18/07/2019 (20:17)	∼25 (7 hours)	58 - 97	-3.07	N (610)	S (309)	J-PLAS, XMM, HST
22151	08/09/2019 (23:00)	∼25 (7 hours)	58 - 89	-2.88	N (512)	S (314†)	J-PJ22, XMM, HST

* Latitude of Jupiter's centre as observed by Chandra from the beginning of the observation window

** Which auroral region (North (N) and/or South (S)) was being viewed by Chandra during this time. Found qualitatively by viewing the image data and comparing with the sub-observer latitude. The total number of counts for the N/S auroral regions as defined in Sections 5.3 and 5.4 are also shown. A more negative sub-observer latitude allows the South to be observed more clearly. Opacity effects of the atmosphere are not taken into account.

† Counts determined from southern auroral region defined in Section 5.3 but with poor viewing geometry during observation.

Note. ObsID 18303 could not be analysed using the algorithm and therefore excluded from further analysis.

A.2 Properties of the auroral regions

Table A.2: List of all auroral powers, flux and brightness of Chandra HRC-I observations of the North and South emissions. Column 1 gives the unique identity number given to each observation. The next two columns give the average angular dimeter of Jupiter (arcsec) and the average Chandra-Jupiter distance (AU) during the observation. The remaining columns give the calculated average auroral power (GW), flux ($\times 10^{-21}$ erg cm^{-2} s^{-1}) and brightness (Rayleighs = R) of the North and South emissions throughout our catalogue. We note that the results of ObsID 18676 may be affected by the small duration of the observation.

TABLE A.2: Table of all auroral powers, flux and brightness of Chandra HRC-I observations of the North and South emissions.

Obs ID	Av. angular diameter (arcsec)	Chandra-Jupiter Distance (AU)	Av. North Power (GW)	Av. South Power (GW)	Av. North flux[a]	Av. South flux[a]	Av. North Brightness (R)	Max. North Brightness (R)	Av. South Brightness (R)	Max. South Brightness (R)
1862	47.80	4.13	0.548	0.245	1.142	0.510	0.018	0.532	0.013	0.331
2519	44.66	4.44	0.413	0.435	0.744	0.784	0.013	0.558	0.021	0.384
15669	36.81	5.36	1.766	1.042	2.186	1.290	0.047	1.446	0.042	0.643
15670	36.28	5.43	0.967	0.878	1.166	1.059	0.023	0.479	0.017	0.245
15671	37.59	5.25	2.155	1.065	2.780	1.374	0.056	1.598	0.031	0.481
15672	37.14	5.32	1.850	1.061	2.324	1.333	0.042	1.311	0.032	0.609
16299	37.37	5.28	2.260	0.744	2.883	0.949	0.057	2.103	0.024	0.295
16300	36.60	5.40	1.425	0.925	1.737	1.128	0.035	1.052	0.029	0.368
18301	39.20	5.02	1.937	2.421	2.734	3.416	0.052	1.594	0.070	0.792
18302	42.03	4.70	2.309	1.653	3.718	2.660	0.075	2.299	0.038	0.430
18608	38.11	5.19	2.375	1.628	3.135	2.149	0.048	1.700	0.043	0.578
18609	37.21	5.31	1.829	1.912	2.306	2.412	0.049	1.543	0.043	0.576
18676[†]	44.02	4.48	1.143	1.195	2.025	2.117	0.026	3.122	0.038	4.190
18677	36.35	5.43	2.394	1.792	2.887	2.162	0.053	1.910	0.028	0.197
18678	42.58	4.63	1.701	1.681	2.822	2.788	0.042	1.243	0.052	0.427
18679	44.55	4.43	1.531	1.309	2.774	2.372	0.043	1.342	0.036	0.285
18680	34.32	5.75	2.220	2.161	2.387	2.324	0.041	1.000	0.028	0.272
20000	42.15	4.68	2.071	1.924	3.362	3.124	0.042	0.990	0.058	0.839
20001	38.76	5.09	1.708	1.548	2.344	2.125	0.043	1.310	0.034	0.347
20002	33.84	5.83	2.548	1.797	2.665	1.880	0.057	2.155	0.027	0.214
20733	42.67	4.61	2.164	1.893	3.622	3.168	0.053	1.715	0.052	0.477
22146	44.57	4.42	2.272	2.178	4.134	3.963	0.044	1.885	0.042	0.854
22147	44.57	4.43	2.259	1.332	4.094	2.414	0.039	1.131	0.036	0.618
22148	44.39	4.45	2.091	1.295	3.754	2.326	0.040	0.882	0.037	0.618
22149	44.30	4.46	2.629	1.367	4.699	2.443	0.052	1.473	0.045	0.764
22150	44.11	4.47	2.778	1.394	4.943	2.480	0.040	1.273	0.036	0.792
22151	38.14	5.18	3.133	1.906	4.152	2.526	0.039	1.578	0.020	0.245
22159	45.73	4.31	2.190	1.426	4.193	2.729	0.058	2.152	0.041	0.350

[a] X-ray flux has units $\times 10^{-13}$ erg cm^{-2} s^{-1}

[†] The small exposure time of ObsID 18676 lead to the unusual maximum brightness for both North and South. We plot both sets of statistics of the catalogue in Figure 2 to account for this unusual observation.

A.3 Properties of the NHS and AHSNuc

Tables A.3 and A.4: List of all auroral powers, flux and brightness of Chandra HRC-I observations of the NHS (Table A.3) and AHSNuc emissions (Table A.4). Column 1 gives the Chandra ObsID for each observation. The following columns gives the region and interval during the observing window (i.e. NHS2 = NHS observed for the 2nd time) and the results of the power, flux and brightness for each region. The AHSNuc table does not include the brightness of the auroral region (as explained in Section 5.4.2).

TABLE A.3: Table of all auroral powers, flux and brightness of Chandra HRC-I observations of the NHS.

Obs ID	Region	Av. NHS Power (GW)	Av. NHS flux [a]	Av. NHS Brightness (R)	Max. NHS Brightness (R)
1862	NHS	0.306	0.638	0.015	0.537
2519	NHS1	0.333	0.606	0.013	1.409
2519	NHS2	0.465	0.847	0.022	1.421
15669	NHS2	1.938	2.399	0.046	1.391
15671	NHS1	1.436	1.853	0.045	4.893
15671	NHS2	2.404	3.101	0.071	1.867
15672	NHS2	2.069	2.600	0.040	1.303
16299	NHS2	3.029	3.863	0.062	2.081
16300	NHS	1.131	1.379	0.039	1.221
18301	NHS1	1.539	2.172	0.040	5.562
18301	NHS2	1.786	2.520	0.045	1.867
18302	NHS	3.503	5.638	0.081	2.692
18608	NHS1	0.813	1.073	0.021	0.646
18608	NHS2	4.239	5.596	0.053	2.645
18609	NHS	1.649	2.079	0.050	1.732
18677	NHS	3.370	4.064	0.053	1.930
18678	NHS1	1.554	2.577	0.040	4.244
18678	NHS2	1.633	2.708	0.015	2.155
18679	NHS2	1.477	2.676	0.050	2.377
18680	NHS1	1.268	1.363	0.037	2.464
18680	NHS2	1.049	1.128	0.039	2.083
20000	NHS2	3.241	5.262	0.047	1.216
20000	NHS3	2.633	4.274	0.036	0.702
20001	NHS1	1.184	1.625	0.039	1.355
20001	NHS2	1.137	1.561	0.028	2.595
20002	NHS	2.414	2.526	0.058	1.913
20733	NHS1	2.571	4.302	0.057	1.940
20733	NHS2	2.027	3.392	0.048	1.907
22146	NHS	2.051	3.733	0.040	1.889
22147	NHS	1.186	2.145	0.037	1.090
22148	NHS	1.587	2.850	0.040	0.874
22149	NHS	2.118	3.785	0.050	1.453
22150	NHS	2.273	4.046	0.038	1.268
22151	NHS	2.404	3.186	0.038	1.902
22159	NHS1	1.070	2.047	0.025	3.140
22159	NHS2	4.027	7.709	0.060	2.790

Note. Chandra ObsID corresponding to observations found in Table A.1
The following column gives the region and interval during the observing window (i.e. NHS2 = NHS observed for the 2nd time).
[a] X-ray flux has units $\times 10^{-13}$ erg cm^{-2} s^{-1}

TABLE A.4: Table of all auroral powers, flux and brightness of Chandra HRC-I observations of the AHSNuc.

Obs ID	Region	Av. AHSNuc Power (GW)	Av. AHSNuc flux[a]
1862	AHSNuc	0.206	0.429
15669	AHSNuc2	0.571	0.707
15671	AHSNuc2	0.530	0.683
15672	AHSNuc2	0.434	0.545
16299	AHSNuc2	0.877	1.119
16300	AHSNuc	0.394	0.481
18302	AHSNuc	0.710	1.142
18608	AHSNuc2	1.194	1.577
18609	AHSNuc	0.357	0.451
18677	AHSNuc	0.833	1.005
18678	AHSNuc1	0.461	0.765
20000	AHSNuc2	0.529	0.859
20001	AHSNuc1	0.520	0.713
20002	AHSNuc	0.487	0.509
20733	AHSNuc1	0.801	1.340
20733	AHSNuc2	0.423	0.708
22146	AHSNuc	0.947	1.723
22147	AHSNuc	0.360	0.653
22148	AHSNuc	0.389	0.699
22149	AHSNuc	0.537	0.960
22150	AHSNuc	0.403	0.718
22151	AHSNuc	0.290	0.384
22159	AHSNuc2	0.829	1.587

[a] X-ray flux has units $\times 10^{-13}$ erg cm^{-2} s^{-1}
Same nomenclature as Table A.3

A.4 Exploring potential sources of error in the Vogt et al. flux eqiuvalence model

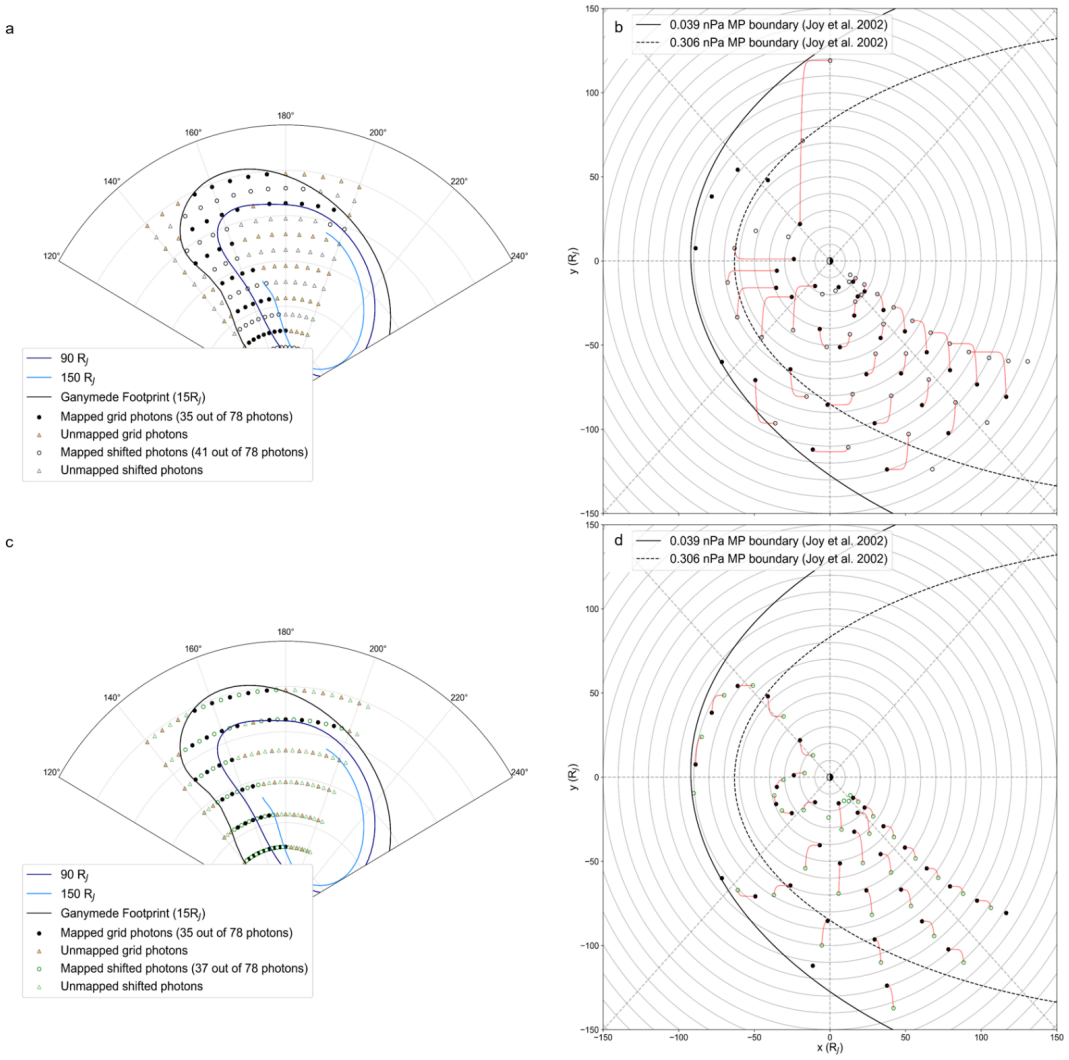

FIGURE A.1: Polar plots of Jupiter's north pole of a 5° S3 lon × 5° lat grid with shifted photons of (a) 2.5° lat and (c) 2.5° S3 lon. This allows us to try and estimate the error in mapping by propagating through the possible uncertainty in the ionospheric position of the X-ray photons. The 15 R_J (black line), 90 R_J (navy line), and 150 R_J (light blue line) of the flux equivalence model using the Grodent Anomaly Model (GAM) are plotted in (a) and (c) at 180° subsolar longitude (SSL). Unmapped photons equatorward (< 15 R_J) and poleward (> 15 R_J) are denoted by triangles: orange for the original grid photons in both panels; white triangles with (a) black outline for the latitude shifted grid and (c) green outline for the longitude shifted grid. The origins of the photons in both grids are calculated using the Vogt et al. (2011, 2015) model shown in panels (b) and (d) for the latitude and S3 longitude shift respectively. Mapped photons in all panels are represented by circles of similar colour scheme to the unmapped points. Both panels are of a similar format to Figure 4b). The red lines between unshifted and shifted photons represent the change in radial distance and LT as a consequence of the possible uncertainty of ionospheric position has on the mapping.

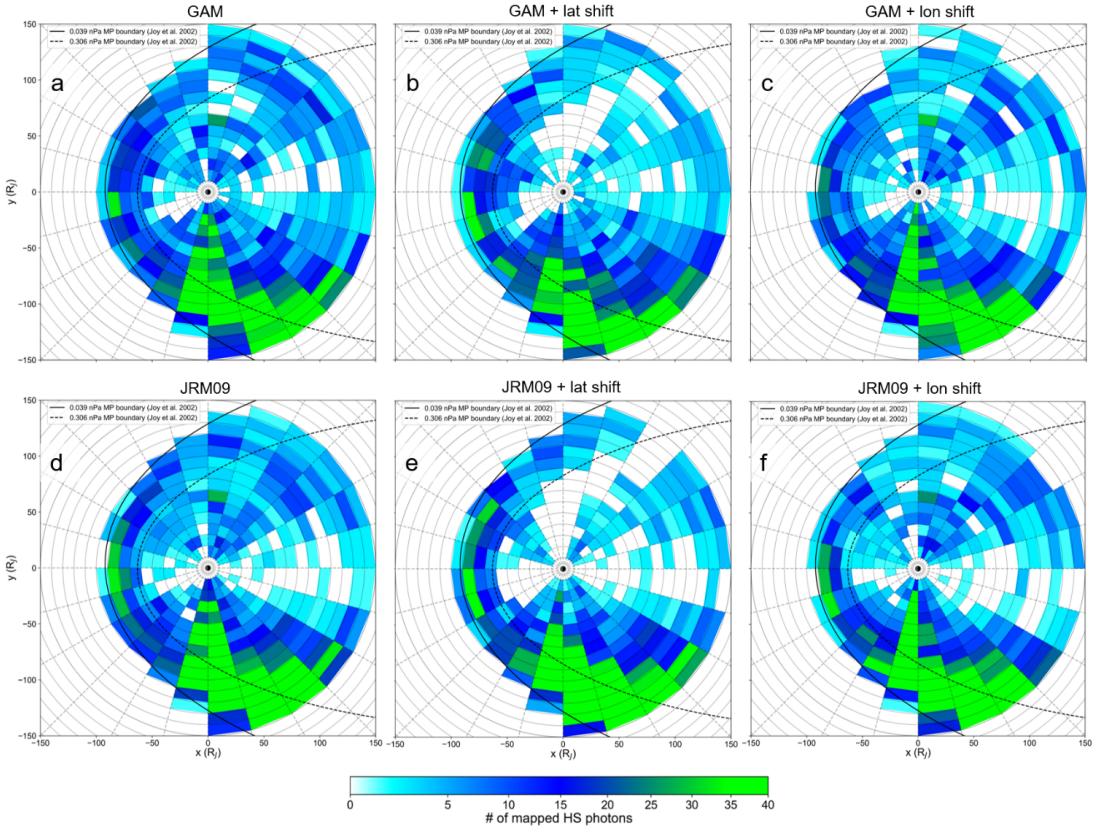

FIGURE A.2: Figure in the same format as Figure 5.6a), showing how the (a) original flux equivalence mapping using the Grodent Anomaly Model (GAM) is affected by a (b) latitude and (c) longitude shift in ionospheric position. The JRM09 field model counterparts are shown in (d)-(f). By comparing GAM and JRM09, the main populations of mapped NHS photons lie in the same radial distance and local time (LT) sectors. The main difference between both field models is shown at noon, where GAM maps more photons towards the magnetopause boundaries and therefore evens beyond the expanded Joy et al. boundary. The latitude (b,e) and longitude (c,f) for both field models are found to mainly affect the populations at noon, close to the AHSNuc driver (Figure 5.6b)), and midnight.

A.5 Rayleigh test results

Table A.5: Table showing all the results from the Rayleigh test for each time the NHS was in view of Chandra HRC-I throughout the entire catalogue. Observations with quasi-periods above the significance threshold of 99.0% (p-value $\leq 1 \times 10^{-2}$) are shown in bold. Nomenclature and format are identical to Tables A.3 and A.4.

Table A.6: Table showing all the results from the Rayleigh test for each time the NHS was in view of Chandra HRC-I throughout the entire catalogue. Observations with quasi-periods above the significance threshold of 99.0% (p-value $\leq 1 \times 10^{-2}$) are shown in bold. Nomenclature and format are identical to Tables A.5.

TABLE A.5: Table of Rayleigh test results for all NHS regions in the catalogue.

ObsID	Region	Duration (min)	Chandra-Jupiter Distance (AU)	Total Counts	Counts/min	Photons mapped	% mapped	Sig. percentile	Sig. p-value	Best period (min)
1862	NHS	319.36	4.13	61	0.191	0	0.00	95.901	4.099×10^{-2}	19.889
2519	NHS1	242.15	4.42	44	0.182	1	2.27	75.148	2.485×10^{-1}	6.742
2519	NHS2	279.78	4.42	71	0.254	2	2.82	91.134	8.866×10^{-2}	11.763
15669	**NHS2**	**358.95**	**5.36**	**258**	**0.719**	**59**	**22.87**	**99.478**	5.220×10^{-3}	**9.519**
15671	NHS1	129.67	5.25	72	0.555	23	31.94	94.271	5.729×10^{-2}	11.580
15671	**NHS2**	**330.43**	**5.25**	**307**	**0.929**	**59**	**19.22**	**99.826**	1.740×10^{-3}	**22.725**
15672	**NHS2**	**364.61**	**5.32**	**284**	**0.779**	**200**	**70.42**	**99.965**	3.500×10^{-4}	**8.011**
16299	**NHS2**	**341.24**	**5.28**	**395**	**1.158**	**167**	**42.28**	**99.011**	9.890×10^{-3}	**13.759**
16300	**NHS**	**343.58**	**5.40**	**142**	**0.413**	**50**	**35.21**	**99.731**	2.690×10^{-3}	**28.526**
18301	NHS1	64.54	5.02	42	0.651	12	28.57	28.905	7.110×10^{-1}	2.267
18301	NHS2	177.45	5.02	134	0.755	21	15.67	94.502	5.498×10^{-2}	9.297
18302	NHS	336.81	4.70	569	1.689	228	40.07	86.631	1.337×10^{-1}	4.555
18608	**NHS1**	**161.72**	5.19	**52**	**0.322**	**43**	**82.69**	**99.989**	1.100×10^{-4}	**3.864**
18608	NHS2	278.52	5.19	467	1.677	94	20.13	96.775	3.225×10^{-2}	5.809
18609	**NHS**	**338.65**	**5.31**	**211**	**0.623**	**50**	**23.70**	**99.09**	9.100×10^{-3}	**8.074**
18677	**NHS**	**311.22**	**5.43**	**379**	**1.218**	**54**	**14.25**	**99.778**	2.220×10^{-3}	**30.135**
18678	NHS1	255.12	4.63	197	0.772	101	51.27	94.594	5.406×10^{-2}	2.530
18678	NHS2	138.04	4.63	112	0.811	25	22.32	87.36	1.264×10^{-1}	2.321
18679	NHS2	295.61	4.43	237	0.802	19	8.02	88.416	1.158×10^{-1}	2.937
18680	NHS1	88.12	5.75	36	0.409	33	91.67	92.919	7.081×10^{-2}	4.520
18680	NHS2	286.99	5.75	97	0.338	40	41.24	92.3	7.700×10^{-2}	9.977
20000	NHS2	388.78	4.68	613	1.577	452	73.74	98.234	1.766×10^{-2}	8.397
20000	**NHS3**	**391.99**	**4.68**	**502**	**1.281**	**271**	**53.98**	**99.208**	7.920×10^{-3}	**7.407**
20001	**NHS1**	**203.32**	**5.09**	**99**	**0.487**	**23**	**23.23**	**99.999**	1.000×10^{-5}	**36.374**
20001	NHS2	111.21	5.09	52	0.468	4	7.69	98.669	1.331×10^{-2}	31.587
20002	**NHS**	**318.47**	**5.83**	**241**	**0.757**	**22**	**9.13**	**99.691**	3.090×10^{-3}	**3.925**
20733	NHS1	189.30	4.61	244	1.289	106	43.44	90.427	9.573×10^{-2}	7.011
20733	**NHS2**	**226.31**	**4.61**	**230**	**1.016**	**37**	**16.09**	**>99.999**	$<1.000 \times 10^{-5}$	**22.371**
22146	**NHS**	**303.06**	4.42	**339**	**1.119**	**59**	**17.40**	**99.903**	9.700×10^{-4}	**10.215**
22147	NHS	326.03	4.43	210	0.644	100	47.62	98.979	1.021×10^{-2}	13.127
22148	**NHS**	**292.75**	**4.45**	**250**	**0.854**	**50**	**20.00**	**99.817**	1.830×10^{-3}	**30.611**
22149	NHS	366.77	4.46	416	1.134	95	22.84	98.808	1.192×10^{-2}	4.312
22150	NHS	346.47	4.47	420	1.212	154	36.67	98.026	1.974×10^{-2}	17.822
22151	NHS	316.38	5.18	302	0.955	114	37.75	60.934	3.907×10^{-1}	9.010
22159	NHS1	141.82	4.31	87	0.613	44	50.57	91.594	8.406×10^{-2}	3.925
22159	NHS2	216.03	4.31	499	2.310	77	15.43	93.534	6.466×10^{-2}	5.947

Note. Observations with quasi-periods above the significance threshold of 99.0% (p-value $\leq 1 \times 10^{-2}$) are shown in bold. Column 1 gives the Chandra ObsID corresponding to observations found in Table S1. The following column gives the region and interval during the observing window (i.e. NHS2 = NHS observed for the 2nd time). The following columns give the duration and average Chandra-Jupiter distance of the hot spot interval, total counts, count rate and number and percentage of photons mapped with the Vogt et. al flux equivalence model. The final columns give the outs of the Rayleigh analysis for the peak power as: (i) the significance from the Monte Carlo simulation as a percentile; (ii) corresponding *p-value* and (iii) the best QPO associated with the peak power found.

TABLE A.6: Table of Rayleigh test results for all AHSNuc regions in the catalogue.

ObsID	Region	Duration (min)	Chandra-Jupiter Distance (AU)	Total Counts	Counts/min	Photons mapped	% mapped	Sig. percentile	Sig. p-value	Best period (min)
1862	AHSNuc	241.18	4.13	31	0.129	0	0.00	97.345	2.66×10^{-2}	9.594
15669	**AHSNuc2**	**311.70**	**5.36**	**66**	**0.212**	**5**	**7.58**	**99.456**	5.44×10^{-3}	**2.285**
15671	**AHSNuc2**	**317.40**	**5.25**	**65**	**0.205**	**9**	**13.85**	**99.989**	1.10×10^{-4}	**11.222**
15672	**AHSNuc2**	**318.20**	**5.32**	**52**	**0.163**	**11**	**21.15**	**99.418**	5.82×10^{-3}	**12.233**
16299	**AHSNuc2**	**310.30**	**5.28**	**104**	**0.335**	**22**	**21.15**	**99.908**	9.20×10^{-4}	**13.545**
16300	AHSNuc	256.75	5.40	37	0.144	3	8.11	92.27	7.73×10^{-2}	15.117
18302	**AHSNuc**	**280.48**	**4.70**	**96**	**0.342**	**5**	**5.21**	**99.928**	7.20×10^{-4}	**5.809**
18608	**AHSNuc2**	**215.92**	**5.19**	**102**	**0.472**	**15**	**14.71**	**99.814**	1.86×10^{-3}	**5.287**
18609	AHSNuc	288.88	5.31	39	0.135	2	5.13	98.707	1.29×10^{-2}	3.715
18677	**AHSNuc**	**278.93**	**5.43**	**84**	**0.301**	**9**	**10.71**	**99.962**	3.80×10^{-4}	**6.185**
18678	**AHSNuc1**	**196.29**	**4.63**	**45**	**0.229**	**7**	**15.56**	**99.678**	3.22×10^{-3}	**3.601**
20000	AHSNuc2	221.53	4.68	57	0.257	22	38.60	97.913	2.09×10^{-2}	3.804
20001	**AHSNuc1**	**145.04**	**5.09**	**31**	**0.214**	**2**	**6.45**	**99.445**	5.55×10^{-3}	**2.321**
20002	**AHSNuc**	**275.37**	**5.83**	**42**	**0.153**	**3**	**7.14**	**99.999**	1.00×10^{-5}	**3.925**
20733	**AHSNuc1**	**141.98**	**4.61**	**57**	**0.401**	**19**	**33.33**	**99.482**	5.18×10^{-3}	**8.266**
20733	**AHSNuc2**	**198.06**	**4.61**	**72**	**0.364**	**8**	**11.11**	>99.999	$<1.00 \times 10^{-5}$	**22.371**
22146	**AHSNuc**	**191.78**	**4.42**	**99**	**0.516**	**10**	**10.10**	**99.985**	1.50×10^{-4}	**21.681**
22147	**AHSNuc**	**286.16**	**4.43**	**56**	**0.196**	**6**	**10.71**	**99.915**	8.50×10^{-4}	**4.346**
22148	**AHSNuc**	**229.08**	**4.45**	**48**	**0.210**	**5**	**10.42**	**99.684**	3.16×10^{-3}	**2.694**
22149	AHSNuc	257.22	4.46	74	0.288	3	4.05	72.879	2.71×10^{-1}	9.899
22150	AHSNuc	246.49	4.47	53	0.215	13	24.53	93.057	6.94×10^{-2}	3.329
22151	**AHSNuc**	**286.55**	**5.18**	**33**	**0.115**	**8**	**24.24**	**99.48**	5.20×10^{-3}	**4.627**
22159	**AHSNuc2**	**199.79**	**4.31**	**95**	**0.475**	**5**	5.26	99.032	9.68×10^{-3}	13.868

Table format and nomenclature are identical to Table A.5

References

N. Achilleos, C. S. Arridge, C. Bertucci, C. M. Jackman, M. K. Dougherty, K. K. Khurana, and C. T. Russell. Large-scale dynamics of Saturn's magnetopause: Observations by Cassini. *Journal of Geophysical Research (Space Physics)*, 113(A11): A11209, November 2008. .

H. Alfvén. Existence of Electromagnetic-Hydrodynamic Waves. *Nature*, 150(3805): 405–406, October 1942. .

R. C. Allen, C. P. Paranicas, F. Bagenal, S. K. Vines, D. C. Hamilton, F. Allegrini, G. Clark, P. A. Delamere, T. K. Kim, S. M. Krimigis, D. G. Mitchell, T. H. Smith, and R. J. Wilson. Energetic Oxygen and Sulfur Charge States in the Outer Jovian Magnetosphere: Insights From the Cassini Jupiter Flyby. *Geophysical Research Letters*, 46(21):11709–11717, 2019. ISSN 19448007. .

Tamer Ataç and Atila Özgüç. Flare index during the rising phase of solar cycle 23. *Solar Physics*, 198(2):399–407, 2001. ISSN 00380938. .

S. V. Badman, G. Provan, E. J. Bunce, D. G. Mitchell, H. Melin, S. W.H. Cowley, A. Radioti, W. S. Kurth, W. R. Pryor, J. D. Nichols, S. L. Jinks, T. S. Stallard, R. H. Brown, K. H. Baines, and M. K. Dougherty. Saturn's auroral morphology and field-aligned currents during a solar wind compression. *Icarus*, 263:83–93, 2016. ISSN 10902643. . URL http://dx.doi.org/10.1016/j.icarus.2014.11.014.

Sarah V. Badman, Chihiro Tao, Adrian Grocott, Satoshi Kasahara, Henrik Melin, Robert H. Brown, Kevin H. Baines, Masaki Fujimoto, and Tom Stallard. Cassini VIMS observations of latitudinal and hemispheric variations in Saturn's infrared auroral intensity. *Icarus*, 216(2):367–375, 2011. ISSN 00191035. . URL http://dx.doi.org/10.1016/j.icarus.2011.09.031.

Sarah V. Badman, Graziella Branduardi-Raymont, Marina Galand, Sébastien L G Hess, Norbert Krupp, Laurent Lamy, Henrik Melin, and Chihiro Tao. Auroral Processes at the Giant Planets: Energy Deposition, Emission Mechanisms, Morphology and Spectra. *Space Science Reviews*, 187(1-4):99–179, 2015. ISSN 0038-6308. . URL http://dx.doi.org/10.1007/s11214-014-0042-xhttp://link.springer.com/10.1007/s11214-014-0042-x.

F. Bagenal. Plasma conditions inside IO's orbit: Voyager measurements. *Journal of Geophysical Research*, 90(A1):311–324, January 1985. .

Fran Bagenal. Giant planet magnetospheres. *Annual Review of Earth and Planetary Sciences*, 20:289–328, 1992.

Didier Barret, Thien Lam Trong, Jan-Willem den Herder, Luigi Piro, Xavier Barcons, Juhani Huovelin, Richard Kelley, J. Miguel Mas-Hesse, Kazuhisa Mitsuda, Stéphane Paltani, Gregor Rauw, Agata RoŻanska, Joern Wilms, Marco Barbera, Enrico Bozzo, Maria Teresa Ceballos, Ivan Charles, Anne Decourchelle, Roland den Hartog, Jean-Marc Duval, Fabrizio Fiore, Flavio Gatti, Andrea Goldwurm, Brian Jackson, Peter Jonker, Caroline Kilbourne, Claudio Macculi, Mariano Mendez, Silvano Molendi, Piotr Orleanski, François Pajot, Etienne Pointecouteau, Frederick Porter, Gabriel W. Pratt, Damien Prêle, Laurent Ravera, Etienne Renotte, Joop Schaye, Keisuke Shinozaki, Luca Valenziano, Jacco Vink, Natalie Webb, Noriko Yamasaki, Françoise Delcelier-Douchin, Michel Le Du, Jean-Michel Mesnager, Alice Pradines, Graziella Branduardi-Raymont, Mauro Dadina, Alexis Finoguenov, Yasushi Fukazawa, Agnieszka Janiuk, Jon Miller, Yaël. Nazé, Fabrizio Nicastro, Salvatore Sciortino, Jose Miguel Torrejon, Hervé Geoffray, Isabelle Hernandez, Laure Luno, Philippe Peille, Jérôme André, Christophe Daniel, Christophe Etcheverry, Emilie Gloaguen, Jérémie Hassin, Gilles Hervet, Irwin Maussang, Jérôme Moueza, Alexis Paillet, Bruno Vella, Gonzalo Campos Garrido, Jean-Charles Damery, Chantal Panem, Johan Panh, Simon Bandler, Jean-Marc Biffi, Kevin Boyce, Antoine Clénet, Michael DiPirro, Pierre Jamotton, Simone Lotti, Denis Schwander, Stephen Smith, Bert-Joost van Leeuwen, Henk van Weers, Thorsten Brand, Beatriz Cobo, Thomas Dauser, Jelle de Plaa, and Edoardo Cucchetti. The Athena X-ray Integral Field Unit (X-IFU). In Jan-Willem A. den Herder, Tadayuki Takahashi, and Marshall Bautz, editors, *Space Telescopes and Instrumentation 2016: Ultraviolet to Gamma Ray*, volume 9905 of *Society of Photo-Optical Instrumentation Engineers (SPIE) Conference Series*, page 99052F, July 2016. .

K. W. Behannon, L. F. Burlaga, and N. F. Ness. The Jovian magnetotail and its current sheet. *Journal of Geophysical Research*, 86(A10):8385–8401, September 1981. .

Anil Bhardwaj and G Randall Gladstone. Auroral emissions of the giant planets. *Reviews of Geophysics*, 38(3):295–353, 2000. ISSN 87551209. .

Anil Bhardwaj, G. Branduardi-Raymont, R. F. Elsner, G. R. Gladstone, G. Ramsay, P. Rodriguez, R. Soria, Jr H. Waite, and T. E. Cravens. Solar control on Jupiter's equatorial X-ray emissions: 26-29 November 2003 XMM-Newton observation. *Geophysical Research Letters*, 32(3):1–5, 2005a. ISSN 00948276. .

Anil Bhardwaj, Ronald F Elsner, J. Hunter Waite, Jr., G Randall Gladstone, Thomas E Cravens, and Peter G Ford. The Discovery of Oxygen Kα X-Ray Emission from the

Rings of Saturn. *The Astrophysical Journal*, 627(1):L73–L76, jul 2005b. ISSN 0004-637X. . URL https://iopscience.iop.org/article/10.1086/431933.

Anil Bhardwaj, Ronald F Elsner, J. Hunter Waite, Jr., G Randall Gladstone, Thomas E Cravens, and Peter G Ford. Chandra Observation of an X-Ray Flare at Saturn: Evidence of Direct Solar Control on Saturn's Disk X-Ray Emissions. *The Astrophysical Journal*, 624(2):L121–L124, may 2005c. ISSN 0004-637X. . URL https://iopscience.iop.org/article/10.1086/430521.

M. Blanc, R. Kallenbach, and N. V. Erkaev. Solar system magnetospheres. *Space Science Reviews*, 116(1):227–298, 2005. .

M. Blanc, D. J. Andrews, A. J. Coates, D. C. Hamilton, C. M. Jackman, X. Jia, A. Kotova, M. Morooka, H. T. Smith, and J. H. Westlake. Saturn Plasma Sources and Associated Transport Processes. *Space Science Reviews*, 192(1-4):237–283, 2015. ISSN 15729672. . URL http://dx.doi.org/10.1007/s11214-015-0172-9.

S. J. Bolton, J. Lunine, D. Stevenson, J. E. P. Connerney, S. Levin, T. C. Owen, F. Bagenal, D. Gautier, A. P. Ingersoll, G. S. Orton, T. Guillot, W. Hubbard, J. Bloxham, A. Coradini, S. K. Stephens, P. Mokashi, R. Thorne, and R. Thorpe. The Juno Mission. *Space Science Reviews*, 213(1-4):5–37, 2017. ISSN 0038-6308. . URL http://dx.doi.org/10.1007/s11214-017-0429-6http://link.springer.com/10.1007/s11214-017-0429-6.

Scott J. Bolton, Fran Bagenal, Michel Blanc, Timothy Cassidy, Emmanuel Chané, Caitriona Jackman, Xianzhe Jia, Anna Kotova, Norbert Krupp, Anna Milillo, Christina Plainaki, H. Todd Smith, and Hunter Waite. Jupiter's Magnetosphere: Plasma Sources and Transport, 2015. ISSN 15729672.

B. Bonfond, D. Grodent, J. C. Gérard, A. Radioti, V. Dols, P. A. Delamere, and J. T. Clarke. The Io UV footprint: Location, inter-spot distances and tail vertical extent. *Journal of Geophysical Research: Space Physics*, 114(7):1–12, 2009. ISSN 21699402. .

B. Bonfond, D. Grodent, S. V. Badman, J. C. Gérard, and A. Radioti. Dynamics of the flares in the active polar region of Jupiter. *Geophysical Research Letters*, 43(23): 11,963–11,970, 2016. ISSN 19448007. .

B. Bonfond, Z. H. Yao, G. R. Gladstone, D. Grodent, J.-C. Gérard, J. Matar, B. Palmaerts, T. K. Greathouse, V. Hue, M. H. Versteeg, J. A. Kammer, R. S. Giles, C. Tao, M. F. Vogt, A. Mura, A. Adriani, B. H. Mauk, W. S. Kurth, and S. J. Bolton. Are Dawn Storms Jupiter's Auroral Substorms? *AGU Advances*, 2(1):1–14, 2021. ISSN 2576-604X. .

Bertrand Bonfond, Zhonghua Yao, and Denis Grodent. Six Pieces of Evidence Against the Corotation Enforcement Theory to Explain the Main Aurora at Jupiter. *Journal of Geophysical Research (Space Physics)*, 125(11):e28152, November 2020. .

G. Branduardi-Raymont, R. F. Elsner, G. R. Gladstone, G. Ramsay, P. Rodriguez, R. Soria, and J. H. Waite. First observation of Jupiter by XMM-Newton. *Astronomy*, 337(1149):331–337, 2004. ISSN 00046361. .

G. Branduardi-Raymont, A. Bhardwaj, R. F. Elsner, G. R. Gladstone, G. Ramsay, P. Rodriguez, R. Soria, J. H. Waite, and T. E. Cravens. Latest results on Jovian disk X-rays from XMM-Newton. *Planetary and Space Science*, 55(9):1126–1134, 2007a. ISSN 00320633. .

G. Branduardi-Raymont, A. Bhardwaj, R. F. Elsner, G. R. Gladstone, G. Ramsay, P. Rodriguez, R. Soria, J. H. Waite, and T. E. Cravens. A study of Jupiter's aurorae with XMM-Newton. *Astronomy and Astrophysics*, 463(2):761–774, 2007b. ISSN 0004-6361. . URL http://arxiv.org/abs/astro-ph/0611562{%}0Ahttp://dx.doi.org/10.1051/0004-6361:20066406.

G. Branduardi-Raymont, R. F. Elsner, M. Galand, D. Grodent, T. E. Cravens, P. Ford, G. R. Gladstone, and J. H. Waite. Spectral morphology of the X-ray emission from Jupiter's aurorae. *Journal of Geophysical Research: Space Physics*, 113(2):1–11, 2008. ISSN 21699402. .

G. Branduardi-Raymont, A. Bhardwaj, R. F. Elsner, and P. Rodriguez. X-rays from Saturn: A study with XMM-Newton and Chandra over the years 2002-05. *Astronomy and Astrophysics*, 510(1):1–9, 2010. ISSN 00046361. .

G. Branduardi-Raymont, P. G. Ford, K. C. Hansen, L. Lamy, A. Masters, B. Cecconi, A. J. Coates, M. K. Dougherty, G. R. Gladstone, and P. Zarka. Search for Saturn's X-ray aurorae at the arrival of a solar wind shock. *Journal of Geophysical Research: Space Physics*, 118(5):2145–2156, 2013. ISSN 21699402. .

K. T. S. Brazier. Confidence intervals from the Rayleigh test. *Monthly Notices of the Royal Astronomical Society*, 268(3):709 – 712, 1994. .

A. L. Broadfoot, M. J.S. Belton, P. Z. Takacs, B. R. Sandel, D. E. Shemansky, J. B. Holberg, J. M. Ajello, S. K. Atreya, T. M. Donahue, H. W. Moos, J. L. Bertaux, J. E. Blamont, D. F. Strobel, J. C. McConnell, A. Dalgarno, R. Goody, and M. B. McElroy. Extreme ultraviolet observations from Voyager 1 encounter with Jupiter. *Science*, 204(4396):979–982, 1979. ISSN 00368075. .

A. L. Broadfoot, B. R. Sandel, D. E. Shemansky, J. B. Holberg, G. R. Smith, D. F. Strobel, J. C. McConnell, S. Kumar, D. M. Hunten, S. K. Atreya, T. M. Donahue, H. W. Moos, J. L. Bertaux, J. E. Blamont, R. B. Pomphrey, and S. Linick. Extreme ultraviolet observations from voyager 1 encounter with Saturn. *Science*, 212(4491):206–211, 1981. ISSN 00368075. .

E. J. Bunce, S. W.H. Cowley, and T. K. Yeoman. Jovian cusp processes: Implications for the polar aurora. *Journal of Geophysical Research: Space Physics*, 109(A9):1–26, 2004. ISSN 21699402. .

L. F. Burlaga, R. M. Skoug, C. W. Smith, D. F. Webb, T. H. Zurbuchen, and Alysha Reinard. Fast ejecta during the ascending phase of solar cycle 23: ACE observations, 1998-1999. *Journal of Geophysical Research: Space Physics*, 106(A10):20957–20977, 2001. ISSN 21699402. .

J. Caldwell, B. Turgeon, and X. M. Hua. Hubble Space Telescope Imaging of the North Polar Aurora on Jupiter. *Science*, 257(5076):1512–1515, September 1992. .

J. F. Carbary and S. M. Krimigis. Energetic Particle Microsignatures of Saturn'S Satellites. *Journal of Geophysical Research*, 88(A11):8947–8958, 1983. ISSN 01480227. .

R. C. Carrington. Description of a Singular Appearance seen in the Sun on September 1, 1859. *Monthly Notices of the Royal Astronomical Society*, 20:13–15, November 1859. .

Francis F. Chen. *Introduction*, pages 1–18. Springer International Publishing, Cham, 2016. ISBN 978-3-319-22309-4. . URL https://doi.org/10.1007/978-3-319-22309-4_1.

G. Clark, B. H. Mauk, P. Kollmann, C. Paranicas, F. Bagenal, R. C. Allen, S. Bingham, S. Bolton, I. Cohen, R. W. Ebert, W. Dunn, D. Haggerty, S. J. Houston, C. M. Jackman, E. Roussos, A. Rymer, and J. H. Westlake. Heavy Ion Charge States in Jupiter's Polar Magnetosphere Inferred From Auroral Megavolt Electric Potentials. *Journal of Geophysical Research: Space Physics*, 125(9):1–12, 2020. ISSN 2169-9380. .

J. T. Clarke, H. W. Moos, S. K. Atreya, and A. L. Lane. Observations from earth orbit and variability of the polar aurora on Jupiter. *Astrophysical Journal, Part 2 - Letters to the Editor*, 241:L179–L182, November 1980. .

J T Clarke, J Ajello, G Ballester, L Ben Jaffel, J Connerney, J-C Gérard, G R Gladstone, D Grodent, W Pryor, J Trauger, and J H Waite. Ultraviolet emissions from the magnetic footprints of Io, Ganymede and Europa on Jupiter. *Nature*, 415(6875): 997–1000, 2002. ISSN 0028-0836. . URL http://www.ncbi.nlm.nih.gov/pubmed/11875560.

John T. Clarke, Lotfi Ben Jaffel, and Jean-Claude Gérard. Hubble Space Telescope imaging of Jupiter's UV aurora during the Galileo orbiter mission. *Journal of Geophysical Research*, 103(E9):20217–20236, September 1998. .

J. E. P. Connerney, M. H. Acuña, N. F. Ness, and T. Satoh. New models of Jupiter's magnetic field constrained by the Io flux tube footprint. *Journal of Geophysical Research: Space Physics*, 103(A6):11929–11939, 1998. ISSN 2169-9402. .

J. E. P. Connerney, S. Timmins, M. Herceg, and J. L. Joergensen. A jovian magnetodisc model for the juno era. *Journal of Geophysical Research: Space Physics*, 125, 10 2020. ISSN 2169-9380. . URL https://onlinelibrary.wiley.com/doi/10.1029/2020JA028138.

J. E. P. Connerney, S. Timmins, R. J. Oliversen, J. R. Espley, J. L. Joergensen, S. Kotsiaros, P. S. Joergensen, J. M. G. Merayo, M. Herceg, J. Bloxham, K. M. Moore, A. Mura, A. Moirano, S. J. Bolton, and S. M. Levin. A New Model of Jupiter's Magnetic Field at the Completion of Juno's Prime Mission. *Journal of Geophysical Research: Planets*, 127(2), feb 2022. ISSN 2169-9097. . URL https://onlinelibrary.wiley.com/doi/10.1029/2021JE007055.

J. E.P. Connerney, M. Benn, J. B. Bjarno, T. Denver, J. Espley, J. L. Jorgensen, P. S. Jorgensen, P. Lawton, A. Malinnikova, J. M. Merayo, S. Murphy, J. Odom, R. Oliversen, R. Schnurr, D. Sheppard, and E. J. Smith. The Juno Magnetic Field Investigation. *Space Science Reviews*, 213(1-4):39–138, 2017. ISSN 15729672. . URL http://dx.doi.org/10.1007/s11214-017-0334-z.

J. E.P. Connerney, S. Kotsiaros, R. J. Oliversen, J. R. Espley, J. L. Joergensen, P. S. Joergensen, J. M.G. Merayo, M. Herceg, J. Bloxham, K. M. Moore, S. J. Bolton, and S. M. Levin. A New Model of Jupiter's Magnetic Field From Juno's First Nine Orbits. *Geophysical Research Letters*, 45(6):2590–2596, 2018. ISSN 19448007. .

S. W. H. Cowley and E. J. Bunce. Origin of the main auroral oval in Jupiter's coupled magnetosphere-ionosphere system. *Planetary and Space Science*, 49(10-11):1067–1088, August 2001. .

S. W. H. Cowley, E. J. Bunce, T. S. Stallard, and S. Miller. Jupiter's polar ionospheric flows: Theoretical interpretation. *Geophysical Research Letters*, 30(5):1220, March 2003. .

S. W H Cowley, E. J. Bunce, and J. M. O'Rourke. A simple quantitative model of plasma flows and currents in Saturn's polar ionosphere. *Journal of Geophysical Research: Space Physics*, 109(A05212), 2004. ISSN 21699402. .

S. W. H. Cowley, S. V. Badman, S. M. Imber, and S. E. Milan. Comment on "Jupiter: A fundamentally different magnetospheric interaction with the solar wind" by D. J. McComas and F. Bagenal. *Geophysical Research Letters*, 35(10):L10101, May 2008. .

S. W.H. Cowley, S. V. Badman, E. J. Bunce, J. T. Clarke, J. C. Gérard, D. Grodent, C. M. Jackman, S. E. Milan, and T. K. Yeoman. Reconnection in a rotation-dominated magnetosphere and its relation to Saturn's auroral dynamics. *Journal of Geophysical Research: Space Physics*, 110(A2):1–19, 2005. ISSN 21699402. .

S.W.H. Cowley and E.J. Bunce. Modulation of Jovian middle magnetosphere currents and auroral precipitation by solar wind-induced compressions and expansions of

the magnetosphere: initial response and steady state. *Planetary and Space Science*, 51 (1):31–56, 2003a. ISSN 00320633. .

S.W.H. Cowley and E.J. Bunce. Modulation of Jupiter's main auroral oval emissions by solar wind induced expansions and compressions of the magnetosphere. *Planetary and Space Science*, 51(1):57–79, 2003b. ISSN 00320633. .

T. E. Cravens, E. Howell, J. H. Waite, and G. R. Gladstone. Auroral oxygen precipitation at Jupiter. *Journal of Geophysical Research*, 100(A9):17153, 1995. ISSN 0148-0227. .

T. E. Cravens, J. H. Waite, T. I. Gombosi, N. Lugaz, G. R. Gladstone, B. H. Mauk, and R. J. MacDowall. Implications of Jovian X-ray emission for magnetosphere-ionosphere coupling. *Journal of Geophysical Research: Space Physics*, 108(A12):1–12, 2003. ISSN 21699402. .

T. E. Cravens, J. Clark, A. Bhardwaj, R. Elsner, J. H. Waite, A. N. Maurellis, G. R. Gladstone, and G. Branduardi-Raymont. X-ray emission from the outer planets: Albedo for scattering and fluorescence of solar X rays. *Journal of Geophysical Research: Space Physics*, 111(7):1–11, 2006. ISSN 21699402. .

Thomas E. Cravens and Ahilleas N. Maurellis. X-ray emission from scattering and fluorescence of solar x-rays at Venus and Mars. *Geophysical Research Letters*, 28(15): 3043–3046, 2001. ISSN 00948276. .

J. C. Cutler, M. K. Dougherty, E. Lucek, and A. Masters. Evidence of surface wave on the dusk flank of Saturn's magnetopause possibly caused by the Kelvin-Helmholtz instability. *Journal of Geophysical Research: Space Physics*, 116(10):1–9, 2011. ISSN 21699402. .

Peter Debye and Erich Hückel. Zur theorie der elektrolyte. i. gefrierpunktserniedrigung und verwandte erscheinungen *"[The theory of electrolytes. I. Freezing point depression and related phenomenon"*. *Physikalische Zeitschrift*, 24(185): 305, 1923.

P. A. Delamere and F. Bagenal. Solar wind interaction with Jupiter's magnetosphere. *Journal of Geophysical Research: Space Physics*, 115(10):1–20, 2010. ISSN 21699402. .

P. A. Delamere, R. J. Wilson, S. Eriksson, and F. Bagenal. Magnetic signatures of Kelvin-Helmholtz vortices on Saturn's magnetopause: Global survey. *Journal of Geophysical Research: Space Physics*, 118(1):393–404, 2013. ISSN 21699402. .

Michael D. Desch. Radio Emission Signature of Saturn Immersions in Jupiter'S Magnetic Tail. *Journal of Geophysical Research*, 88(A9):6904–6910, 1983. ISSN 01480227. .

M. Desroche, F. Bagenal, P. A. Delamere, and N. Erkaev. Conditions at the expanded Jovian magnetopause and implications for the solar wind interaction. *Journal of Geophysical Research: Space Physics*, 117(7):1–18, 2012. ISSN 21699402. .

M. Dumont, D. Grodent, A. Radioti, B. Bonfond, and J.-C. Gérard. Jupiter's equatorward auroral features: Possible signatures of magnetospheric injections. *Journal of Geophysical Research: Space Physics*, 119(12):A07000, dec 2014. ISSN 2169-9380. . URL http://doi.wiley.com/10.1029/2006JA011892https://onlinelibrary.wiley.com/doi/abs/10.1002/2014JA020527.

M. Dumont, D. Grodent, A. Radioti, B. Bonfond, E. Roussos, and C. Paranicas. Evolution of the Auroral Signatures of Jupiter's Magnetospheric Injections. *Journal of Geophysical Research: Space Physics*, 123(2015):1–13, 2018. ISSN 21699380. . URL http://doi.wiley.com/10.1029/2018JA025708.

J. W. Dungey. Electrodynamics of the Outer Atmosphere. In *Physics of the Ionosphere*, page 229, January 1955.

J. W. Dungey. Interplanetary magnetic field and the auroral zones. *Physical Review Letters*, 6(2):47–48, 1961. .

W. R. Dunn, G. Branduardi-Raymont, L. C. Ray, C. M. Jackman, R. P. Kraft, R. F. Elsner, I. J. Rae, Z. Yao, M. F. Vogt, G. H. Jones, G. R. Gladstone, G. S. Orton, J. A. Sinclair, P. G. Ford, G. A. Graham, R. Caro-Carretero, and A. J. Coates. The independent pulsations of Jupiter's northern and southern X-ray auroras. *Nature Astronomy*, 1 (11):758–764, 2017. ISSN 23973366. . URL http://dx.doi.org/10.1038/s41550-017-0262-6.

W. R. Dunn, G. Branduardi-Raymont, V. Carter-Cortez, A. Campbell, R. Elsner, J.-U. Ness, G. R. Gladstone, P. Ford, Z. Yao, P. Rodriguez, G. Clark, C. Paranicas, A. Foster, D. Baker, R. Gray, S. V. Badman, L. C. Ray, E.J. Bunce, B. Snios, C. M. Jackman, I. J. Rae, R. Kraft, A. Rymer, S. Lathia, and N. Achilleos. Jupiter's X-ray Emission During the 2007 Solar Minimum. *Journal of Geophysical Research: Space Physics*, 125(6):e2019JA027219, jun 2020a. ISSN 2169-9380. . URL https://onlinelibrary.wiley.com/doi/abs/10.1029/2019JA027219.

W. R. Dunn, R. Gray, A. D. Wibisono, L. Lamy, C. Louis, S. V. Badman, G. Branduardi-Raymont, R. Elsner, G. R. Gladstone, R. Ebert, P. Ford, A. Foster, C. Tao, L. C. Ray, Z. Yao, I. J. Rae, E. J. Bunce, P. Rodriguez, C. M. Jackman, G. Nicolaou, J. Clarke, J. Nichols, H. Elliott, and R. Kraft. Comparisons Between Jupiter's X-ray, UV and Radio Emissions and In-Situ Solar Wind Measurements During 2007. *Journal of Geophysical Research: Space Physics*, 125(6):e2019JA027222, jun 2020b. ISSN 2169-9380. . URL https://onlinelibrary.wiley.com/doi/abs/10.1029/2019JA027222.

W. R. Dunn, J.-U. Ness, L. Lamy, G. R. Tremblay, G. Branduardi-Raymont, B. Snios, R. P. Kraft, Z. Yao, and A. D. Wibisono. A Low Signal Detection of X-Rays From Uranus. *Journal of Geophysical Research: Space Physics*, 126(4), 2021. ISSN 2169-9380. . URL https://onlinelibrary.wiley.com/doi/10.1029/2020JA028739.

W. R. Dunn, D. M. Weigt, D. Grodent, Z. H. Yao, D. May, K. Feigelman, B. Sipos, D. Fleming, S. McEntee, B. Bonfond, G. R. Gladstone, R. E. Johnson, C. M. Jackman, R. L. Guo, G. Branduardi-Raymont, A. D. Wibisono, R. P. Kraft, J. D. Nichols, and L. C. Ray. Jupiter's X-ray and UV Dark Polar Region. *Geophysical Research Letters*, 4, 2022. ISSN 0094-8276. . URL https://onlinelibrary.wiley.com/doi/10.1029/2021GL097390.

William R. Dunn, Graziella Branduardi-Raymont, Ronald F. Elsner, Marissa F. Vogt, Laurent Lamy, Peter G. Ford, Andrew J. Coates, G. Randall Gladstone, Caitriona M. Jackman, Jonathan D. Nichols, I. Jonathan Rae, Ali Varsani, Tomoki Kimura, Kenneth C. Hansen, and Jamie M. Jasinski. The impact of an ICME on the Jovian X-ray aurora. *Journal of Geophysical Research A: Space Physics*, 121(3):2274–2307, 2016. ISSN 21699402. .

R. W. Ebert, F. Allegrini, F. Bagenal, S. J. Bolton, J. E.P. Connerney, G. Clark, G. A. DiBraccio, D. J. Gershman, W. S. Kurth, S. Levin, P. Louarn, B. H. Mauk, D. J. McComas, M. Reno, J. R. Szalay, M. F. Thomsen, P. Valek, S. Weidner, and R. J. Wilson. Accelerated flows at Jupiter's magnetopause: Evidence for magnetic reconnection along the dawn flank. *Geophysical Research Letters*, 44(10), 2017a. ISSN 19448007. .

R. W. Ebert, F. Allegrini, F. Bagenal, S. J. Bolton, J. E.P. Connerney, G. Clark, G. R. Gladstone, V. Hue, W. S. Kurth, S. Levin, P. Louarn, B. H. Mauk, D. J. McComas, C. Paranicas, M. Reno, J. Saur, J. R. Szalay, M. F. Thomsen, P. Valek, S. Weidner, and R. J. Wilson. Spatial Distribution and Properties of 0.1–100 keV Electrons in Jupiter's Polar Auroral Region. *Geophysical Research Letters*, 44(18), 2017b. ISSN 19448007. .

Robert W. Ebert, Fran Bagenal, David J. McComas, and Christopher M. Fowler. A survey of solar wind conditions at 5 AU: a tool for interpreting solar wind-magnetosphere interactions at Jupiter. *Frontiers in Astronomy and Space Sciences*, 1(September):1–13, 2014. .

E. Echer, W. D. Gonzalez, F. L. Guarnieri, A. Dal Lago, and L. E. A. Vieira. Introduction to space weather. *Advances in Space Research*, 35(5):855–865, January 2005. .

B. Efron and C. Stein. The Jackknife Estimate of Variance. *The Annals of Statistics*, 9(3): 586–596, 1981. ISSN 0090-5364. . URL http://projecteuclid.org/euclid.aos/1176345976http://projecteuclid.org/euclid.aos/1176348654http://projecteuclid.org/euclid.aos/1176345462.

R. F. Elsner, N. Lugaz, J. H. Waite, T. E. Cravens, G. R. Gladstone, P. Ford, D. Grodent, A. Bhardwaj, R. J. MacDowall, M. D. Desch, and T. Majeed. Simultaneous Chandra X ray Hubble Space Telescope ultraviolet, and Ulysses radio observations of Jupiter's aurora. *Journal of Geophysical Research: Space Physics*, 110(A1):1–16, 2005. ISSN 21699402. .

Aaron Empey, Corentin K. Louis, and Caitriona M. Jackman. Space labelling tool, November 2021. URL https://doi.org/10.5281/zenodo.5636922.

A. Eviatar and G. L. Siscoe. Limit on rotational energy available to excite Jovian aurora. *Geophysical Research Letters*, 7(12):1085–1088, December 1980. .

Abraham D. Falcone, Ralph P. Kraft, Marshall W. Bautz, Jessica A. Gaskin, John A. Mulqueen, and Doug A. Swartz. Overview of the high-definition x-ray imager instrument on the Lynx x-ray surveyor. *Journal of Astronomical Telescopes, Instruments, and Systems*, 5(2), 2019. ISSN 23318422. .

C. J. Farrugia, F. T. Gratton, L. Bender, H. K. Biernat, N. V. Erkaev, J. M. Quinn, R. B. Torbert, and V. Dennisenko. Charts of joint Kelvin-Helmholtz and Rayleigh-Taylor instabilites at the dayside magnetopause for strongly northward interplanetary magnetic field. *Journal of Geophysical Research: Space Physics*, 103(A4):6703–6727, 1998. ISSN 2169-9402. .

Joel A Fedder and John G Lyon. The Earth's magnetosphere is 165 R_E long: Self-consistent currents, convection, magnetospheric structure, and processes for northward interplanetary magnetic field. *Journal of Geophysical Research*, 100(A3): 3623–3635, 1995. ISSN 01480227. .

L. Fletcher, B. R. Dennis, H. S. Hudson, S. Krucker, K. Phillips, A. Veronig, M. Battaglia, L. Bone, A. Caspi, Q. Chen, P. Gallagher, P. T. Grigis, H. Ji, W. Liu, R. O. Milligan, and M. Temmer. An observational overview of solar flares. *Space Science Reviews*, 159(1-4):19–106, 2011. ISSN 00386308. .

C. Foullon, C. J. Farrugia, A. N. Fazakerley, C. J. Owen, F. T. Gratton, and R. B. Torbert. Evolution of Kelvin-Helmholtz activity on the dusk flank magnetopause. *Journal of Geophysical Research: Space Physics*, 113(11):1–22, 2008. ISSN 21699402. .

S. A. Fuselier, K. J. Trattner, S. M. Petrinec, and B. Lavraud. Dayside magnetic topology at the Earth's magnetopause for northward IMF. *Journal of Geophysical Research: Space Physics*, 117(8):1–14, 2012. ISSN 21699402. .

Jessica A. Gaskin, Douglas A. Swartz, Alexey A. Vikhlinin, Feryal Özel, Karen E. E. Gelmis, Jonathan W. Arenberg, Simon R. Bandler, Mark W. Bautz, Marta M. Civitani, Alexandra Dominguez, Megan E. Eckart, Abraham D. Falcone, Enectali Figueroa-Feliciano Mark D. Freeman, Hans M. Günther, Keith A. Havey Jr., Ralf K.

Heilmann, Kiranmayee Kilaru, Ralph P. Kraft, Kevin S. McCarley, Randall L. McEntaffer, Giovanni Pareschi, William R. Purcell, Paul B. Reid, Mark L. Schattenburg, Daniel A. Schwartz, Eric D. Schwartz Sr., Harvey D. Tananbaum, Grant R. Tremblay, William W. Zhang, and John A. Zuhone. Lynx X-Ray Observatory: an overview. *Journal of Astronomical Telescopes, Instruments, and Systems*, 5(02):1, may 2019. ISSN 2329-4124. . URL https://www.spiedigitallibrary.org/journals/Journal-of-Astronomical-Telescopes-Instruments-and-Systems/volume-5/issue-02/021001/Lynx-X-Ray-Observatory-an-overview/10.1117/1.JATIS.5.2.021001.full.

J. C. Gerard, D. Grodent, R. Prange, J. H. Waite, G. R. Gladstone, V. Dols, F. Paresce, A. Storrs, L. Ben Jaffel, and K. A. Franke. A Remarkable Auroral Event on Jupiter Observed in the Ultraviolet with the Hubble Space Telescope. *Science*, 266(5191): 1675–1678, December 1994. .

Daniel J. Gershman, Gina A. DiBraccio, John E.P. Connerney, George Hospodarsky, William S. Kurth, Robert W. Ebert, Jamey R. Szalay, Robert J. Wilson, Frederic Allegrini, Phil Valek, David J. McComas, Fran Bagenal, Steve Levin, and Scott J. Bolton. Juno observations of large-scale compressions of Jupiter's dawnside magnetopause. *Geophysical Research Letters*, 44(15), 2017. ISSN 19448007. .

Daniel J. Gershman, John E.P. Connerney, Stavros Kotsiaros, Gina A. DiBraccio, Yasmina M. Martos, Adolfo F.-Viñas, Vincent Hue, George Clark, Fran Bagenal, Steve Levin, and Scott J. Bolton. Alfvénic fluctuations associated with Jupiter's auroral emissions. *Geophysical Research Letters*, page 2019GL082951, 2019. ISSN 0094-8276. . URL https://onlinelibrary.wiley.com/doi/abs/10.1029/2019GL082951.

P. Gibbon. Introduction to Plasma Physics. In Bernhard Holzer, editor, *Proceedings of the 2014 CAS-CERN Accelerator School: Plasma Wake Acceleration, Geneva, Switzerland, November 2014*, volume 001, pages 51–66, 2016. .

D. A. Gilman, K. C. Hurley, F. D. Seward, H. W. Schnopper, J. D. Sullivan, and A. E. Metzger. An upper limit to X-ray emission from Saturn. *The Astrophysical Journal*, 300(9):453, jan 1986. ISSN 0004-637X. . URL http://adsabs.harvard.edu/doi/10.1086/163820.

I. Gingell, S. J. Schwartz, J. P. Eastwood, J. L. Burch, R. E. Ergun, S. Fuselier, D. J. Gershman, B. L. Giles, Y. V. Khotyaintsev, B. Lavraud, P. A. Lindqvist, W. R. Paterson, T. D. Phan, C. T. Russell, J. E. Stawarz, R. J. Strangeway, R. B. Torbert, and F. Wilder. Observations of Magnetic Reconnection in the Transition Region of Quasi-Parallel Shocks. *Geophysical Research Letters*, 46(3):1177–1184, February 2019. .

G. R. Gladstone, J. H. Waite, D. Grodent, W. S. Lewis, F. J. Crary, R. F. Elsner, M. C. Weisskopf, T. Majeed, J.-M. Jahn, A. Bhardwaj, J. T. Clarke, D. T. Young, M. K. Dougherty, S. A. Espinosa, and T. E. Cravens. A pulsating auroral X-ray hot spot on Jupiter. *Nature*, 415(6875):1000–1003, feb 2002. ISSN 0028-0836. . URL http://www.nature.com/articles/4151000a.

G. Randall Gladstone, Steven C. Persyn, John S. Eterno, Brandon C. Walther, David C. Slater, Michael W. Davis, Maarten H. Versteeg, Kristian B. Persson, Michael K. Young, Gregory J. Dirks, Anthony O. Sawka, Jessica Tumlinson, Henry Sykes, John Beshears, Cherie L. Rhoad, James P. Cravens, Gregory S. Winters, Robert A. Klar, Walter Lockhart, Benjamin M. Piepgrass, Thomas K. Greathouse, Bradley J. Trantham, Philip M. Wilcox, Matthew W. Jackson, Oswald H.W. Siegmund, John V. Vallerga, Rick Raffanti, Adrian Martin, J. C. Gérard, Denis C. Grodent, Bertrand Bonfond, Benoit Marquet, and François Denis. The Ultraviolet Spectrograph on NASA's Juno Mission. *Space Science Reviews*, 213(1-4):447–473, 2017. ISSN 15729672. . URL http://dx.doi.org/10.1007/s11214-014-0040-z.

C. K. Goertz and R. J. Strangeway. Plasma waves. In Kivelson, Margaret G. and Russell, Christopher T., editor, *Introduction to Space Physics*, chapter 12, pages 356–399. Cambridge University Press, 1995.

Steven J. Goodman, Richard J. Blakeslee, William J. Koshak, Douglas Mach, Jeffrey Bailey, Dennis Buechler, Larry Carey, Chris Schultz, Monte Bateman, Eugene McCaul, and Geoffrey Stano. The GOES-R Geostationary Lightning Mapper (GLM). *Atmospheric Research*, 125-126:34–49, 2013. ISSN 01698095. . URL http://dx.doi.org/10.1016/j.atmosres.2013.01.006.

J T Gosling, M F Thomsen, S J Bame, T G Onsager, and C. T. Russell. The electron edge of low latitude boundary layer during accelerated flow events. *Geophysical Research Letters*, 17(11):1833–1836, oct 1990. ISSN 00948276. . URL http://doi.wiley.com/10.1029/GL017i011p01833.

Thomas Greathouse, Randy Gladstone, Maarten Versteeg, Vincent Hue, Joshua Kammer, Rohini Giles, Michael Davis, Scott Bolton, Steven Levin, John Connerney, Jean Claude Gérard, Denis Grodent, Bertrand Bonfond, Emma Bunce, and Marissa F. Vogt. Local Time Dependence of Jupiter's Polar Auroral Emissions Observed by Juno UVS. *Journal of Geophysical Research: Planets*, 126(12):1–13, 2021. ISSN 21699100. .

David J. Griffiths. *Introduction to Electrodynamics*. Prentice Hall, 1999.

D. Grodent, J. T. Clarke, J. Kim, J. H. Waite, and S. W. H. Cowley. Jupiter's main auroral oval observed with HST-STIS. *Journal of Geophysical Research (Space Physics)*, 108(A11):1389, November 2003a. .

D. Grodent, J. T. Clarke, J. H. Waite, S. W.H. Cowley, J. C. Gérard, and J. Kim. Jupiter's polar auroral emissions. *Journal of Geophysical Research: Space Physics*, 108(A10):1–9, 2003b. ISSN 21699402. .

Denis Grodent. A Brief Review of Ultraviolet Auroral Emissions on Giant Planets. *Space Science Reviews*, 187(1-4):23–50, 2015. ISSN 15729672. . URL http://dx.doi.org/10.1007/s11214-014-0052-8.

Denis Grodent, Bertrand Bonfond, Jean Claude Gérard, Aikaterini Radioti, Jacques Gustin, John T. Clarke, Jonathan Nichols, and John E.P. Connerney. Auroral evidence of a localized magnetic anomaly in Jupiter's northern hemisphere. *Journal of Geophysical Research: Space Physics*, 113(9):1–10, 2008. ISSN 21699402. .

Denis Grodent, B. Bonfond, Z. Yao, J. C. Gérard, A. Radioti, M. Dumont, B. Palmaerts, A. Adriani, S. V. Badman, E. J. Bunce, J. T. Clarke, J. E.P. Connerney, G. R. Gladstone, T. Greathouse, T. Kimura, W. S. Kurth, B. H. Mauk, D. J. McComas, J. D. Nichols, G. S. Orton, L. Roth, J. Saur, and P. Valek. Jupiter's Aurora Observed With HST During Juno Orbits 3 to 7. *Journal of Geophysical Research: Space Physics*, 123(5): 3299–3319, 2018. ISSN 21699402. .

P. Guio and N. Achilleos. The VOISE algorithm: A versatile tool for automatic segmentation of astronomical images. *Monthly Notices of the Royal Astronomical Society*, 398(3):1254–1262, 2009. ISSN 00358711. .

R. L. Guo, Z. H. Yao, N. Sergis, Y. Wei, D. Mitchell, E. Roussos, B. Palmaerts, W. R. Dunn, A. Radioti, L. C. Ray, A. J. Coates, D. Grodent, C. S. Arridge, P. Kollmann, N. Krupp, J. H. Waite, M. K. Dougherty, J. L. Burch, and W. X. Wan. Reconnection Acceleration in Saturn's Dayside Magnetodisk: A Multicase Study with Cassini . *The Astrophysical Journal*, 868(2):L23, 2018. ISSN 2041-8213. . URL http://dx.doi.org/10.3847/2041-8213/aaedab.

D. A. Gurnett and F. L. Scarf. Plasma waves in the jovian magnetosphere. In A. J.Editor Dessler, editor, *Physics of the Jovian Magnetosphere*, Cambridge Planetary Science Old, page 285–316. Cambridge University Press, 1983. .

D. A. Gurnett, W. S. KURTH, and F. L. SCARF. Plasma Wave Observations Near Jupiter: Initial Results from Voyager 2. *Science*, 206(4421):987–991, nov 1979. ISSN 0036-8075. . URL https://www.sciencemag.org/lookup/doi/10.1126/science.206.4421.987.

H Hasegawa, M Fujimoto, T-D Phan, H Rème, A Balogh, M W Dunlop, C Hashimoto, and R Tandokoro. Transport of solar wind into Earth's magnetosphere through rolled-up Kelvin-Helmholtz vortices. *Nature*, 430(7001):755–758, 2004. ISSN 0028-0836. .

S. L.G. Hess, B. Bonfond, P. Zarka, and D. Grodent. Model of the Jovian magnetic field topology constrained by the Io auroral emissions. *Journal of Geophysical Research: Space Physics*, 116(5):1–19, 2011a. ISSN 21699402. .

S. L.G. Hess, B. Bonfond, P. Zarka, and D. Grodent. Model of the Jovian magnetic field topology constrained by the Io auroral emissions. *Journal of Geophysical Research: Space Physics*, 116(5):1–19, 2011b. ISSN 21699402. .

T. W. Hill. Inertial limit on corotation. *Journal of Geophysical Research*, 84(A11): 6554–6558, November 1979. .

T. W. Hill. The Jovian auroral oval. *Journal of Geophysical Research*, 106(A5):8101–8108, May 2001. .

R. Hodgson. On a curious Appearance seen in the Sun. *Monthly Notices of the Royal Astronomical Society*, 20:15–16, November 1859. .

M. Horanyi, T. E. Cravens, and Jr. Waite, J. H. The precipitation of energetic heavy ions into the upper atmosphere of Jupiter. *Journal of Geophysical Research*, 93(A7): 7251–7271, July 1988. .

G. B. Hospodarsky, W. S. Kurth, S. J. Bolton, F. Allegrini, G. B. Clark, J. E.P. Connerney, R. W. Ebert, D. K. Haggerty, S. Levin, D. J. McComas, C. Paranicas, A. M. Rymer, and P. W. Valek. Jovian bow shock and magnetopause encounters by the Juno spacecraft. *Geophysical Research Letters*, 44(10):4506–4512, 2017. ISSN 19448007. .

S. J. Houston, T. E. Cravens, D. R. Schultz, H Gharibnejad, W. R. Dunn, D. K. Haggerty, A. M. Rymer, B. H. Mauk, and N. Ozak. Jovian Auroral Ion Precipitation: X-Ray Production From Oxygen and Sulfur Precipitation. *Journal of Geophysical Research: Space Physics*, 125(2):2019JA027007, 2020. ISSN 2169-9380. . URL https://onlinelibrary.wiley.com/doi/10.1029/2019JA027007.

D. E. Huddleston, C. T. Russell, G. Le, and A. Szabo. Magnetopause structure and the role of reconnection at the outer planets. *Journal of Geophysical Research A: Space Physics*, 102(A11):24289–24302, 1997. ISSN 01480227. .

W. J. Hughes. The magnetopause, magnetotail and magnetic reconnection. In Kivelson, Margaret G. and Russell, Christopher T., editor, *Introduction to Space Physics*, chapter 9, pages 227–287. Cambridge University Press, 1995.

Yawei Hui, Thomas E. Cravens, Nataly Ozak, and David R. Schultz. What can be learned from the absence of auroral X-ray emission from Saturn? *Journal of Geophysical Research: Space Physics*, 115(A10), oct 2010a. ISSN 01480227. . URL http://doi.wiley.com/10.1029/2010JA015639.

Yawei Hui, David R. Schultz, Vasili A. Kharchenko, Anil Bhardwaj, Graziella Branduardi-Raymont, Phillip C. Stancil, Thomas E. Cravens, Carey M. Lisse, and Alexander Dalgarno. Comparative analysis and variability of the Jovian X-ray spectra detected by the Chandra and XMM-Newton observatories. *Journal of Geophysical Research: Space Physics*, 115(A7):1–19, 2010b. .

A. J. Hundhausen. The solar wind. In Kivelson, Margaret G. and Russell, Christopher T., editor, *Introduction to Space Physics*, chapter 4, pages 91–128. Cambridge University Press, 1995.

C. M. Jackman and C. S. Arridge. Solar Cycle Effects on the Dynamics of Jupiter's and Saturn's Magnetospheres. *Solar Physics*, 274(1-2):481–502, 2011. ISSN 00380938. .

C. M. Jackman, N. Achilleos, E. J. Bunce, S. W.H. Cowley, M. K. Dougherty, G. H. Jones, S. E. Milan, and E. J. Smith. Interplanetary magnetic field at ~ 9 AU during the declining phase of the solar cycle and its implications for Saturn's magnetospheric dynamics. *Journal of Geophysical Research: Space Physics*, 109(A11), 2004. ISSN 21699402. .

C. M. Jackman, C. Knigge, D. Altamirano, R. Gladstone, W. Dunn, R. Elsner, R. Kraft, G. Branduardi-Raymont, and P. Ford. Assessing Quasi-Periodicities in Jovian X-Ray Emissions: Techniques and Heritage Survey. *Journal of Geophysical Research: Space Physics*, 123(11):9204–9221, 2018. ISSN 21699402. .

F. Jansen, D. Lumb, B. Altieri, J. Clavel, M. Ehle, C. Erd, C. Gabriel, M. Guianazzi, P. Gondoin, R. Much, R. Munoz, M. Santos, N. Schartel, D. Texier, and G. Vacanti. XMM-Newton spacecraft and operations. *Astronomy and Astrophysics*, 365:L1–L6, 2001. .

S. P. Joy, M. G. Kivelson, R. J. Walker, K. K. Khurana, C. T. Russell, and T. Ogino. Probabilistic models of the Jovian magnetopause and bow shock locations. *Journal of Geophysical Research: Space Physics*, 107(A10):1–17, 2002. ISSN 21699402. .

W.A Joye and E. Mandel. New Features of SAOImage DS9. *Astronomical Data Analysis Software and Systems XII*, 295:489, 2003. URL `http://www.aspbooks.org/a/volumes/article{_}details/?paper{_}id=27026`.

K. K. Khurana and M. G. Kivelson. Inference of the angular velocity of plasma in the Jovian magnetosphere from the sweepback of magnetic field. *Journal of Geophysical Research*, 98(A1):67–80, January 1993. .

Krishan K. Khurana and Margaret G. Kivelson. Ultralow frequency MHD waves in Jupiter's middle magnetosphere. *Journal of Geophysical Research*, 94(A5):5241, 1989. ISSN 0148-0227. .

Krishan K. Khurana and Hannes K. Schwarzl. Global structure of Jupiter's magnetospheric current sheet. *Journal of Geophysical Research (Space Physics)*, 110 (A7):A07227, July 2005. .

Krishan K. Khurana, Margaret G. Kivelson, Vytenis M. Vasyliunas, Norbert Krupp, Joachim Woch, Andreas Lagg, Barry H. Mauk, and William S. Kurth. The configuration of Jupiter's magnetosphere. In Fran Bagenal, Timothy E. Dowling, and William B. McKinnon, editors, *Jupiter. The Planet, Satellites and Magnetosphere*, volume 1, pages 593–616. Cambridge University Press, 2004.

T. Kimura, R. P. Kraft, R. F. Elsner, G. Branduardi-Raymont, G. R. Gladstone, C. Tao, K. Yoshioka, G. Murakami, A. Yamazaki, F. Tsuchiya, M. F. Vogt, A. Masters, H. Hasegawa, S. V. Badman, E. Roediger, Y. Ezoe, W. R. Dunn, I. Yoshikawa, M. Fujimoto, and S. S. Murray. Jupiter's X-ray and EUV auroras monitored by Chandra, XMM-Newton, and Hisaki satellite. *Journal of Geophysical Research A: Space Physics*, 121(3):2308–2320, 2016. ISSN 21699402. .

T. Kimura, J. D. Nichols, R. L. Gray, C. Tao, G. Murakami, A. Yamazaki, S. V. Badman, F. Tsuchiya, K. Yoshioka, H. Kita, D. Grodent, G. Clark, I. Yoshikawa, and M. Fujimoto. Transient brightening of Jupiter's aurora observed by the Hisaki satellite and Hubble Space Telescope during approach phase of the Juno spacecraft. *Geophysical Research Letters*, 44(10):4523–4531, 2017. ISSN 19448007. .

Tomoki Kimura, Fuminori Tsuchiya, Hiroaki Misawa, Akira Morioka, Hiromasa Nozawa, and Masaki Fujimoto. Periodicity analysis of Jovian quasi-periodic radio bursts based on Lomb-Scargle periodograms. *Journal of Geophysical Research: Space Physics*, 116(3):1–10, 2011. ISSN 21699402. .

M. G. Kivelson and D. J. Southwood. Dynamical consequences of two modes of centrifugal instability in Jupiter's outer magnetosphere. *Journal of Geophysical Research: Space Physics*, 110(A12):A12209, December 2005. .

Margaret G. Kivelson. Physics of Space Plasmas. In Kivelson, Margaret G. and Russell, Christopher T., editor, *Introduction to Space Physics*, chapter 2, pages 27–57. Cambridge University Press, 1995.

Margaret G. Kivelson and Fran Bagenal. Planetary Magnetospheres. In McFadden, Lucy-Ann A. and Weissman, Paul R. and Johnson T. V., editor, *Encyclopedia of the Solar System*, chapter 28, pages 519–540. Academic Press, 2007.

Stavros Kotsiaros, John E.P. Connerney, George Clark, Frederic Allegrini, G. Randall Gladstone, William S. Kurth, Barry H. Mauk, Joachim Saur, Emma J. Bunce, Daniel J. Gershman, Yasmina M. Martos, Thomas K. Greathouse, Scott J. Bolton, and Steven M. Levin. Birkeland currents in Jupiter's magnetosphere observed by the

polar-orbiting Juno spacecraft. *Nature Astronomy*, 3(10):904–909, 2019. ISSN 23973366. . URL http://dx.doi.org/10.1038/s41550-019-0819-7.

Stamatios M Krimigis, Donald G Mitchell, Douglas C Hamilton, Jannis Dandouras, Thomas P Armstrong, Scott J Bolton, Andrew F Cheng, George Gloeckler, K C Hsieh, Edwin P Keath, Norbert Krupp, Andreas Lagg, Louis J. Lonzerotti, Stefano Livi, Barry H. Mauk, Richard W. McEntire, Edmond C. Roelof, Berend Wilken, and Donald J. Williams. A nebula of gases from Io surrounding Jupiter. *Nature*, 415 (6875):994–996, 2002. ISSN 00280836. .

N Krupp, J Woch, A Lagg, B Wilken, S Livi, and D. J. Williams. Energetic particle bursts in the predawn Jovian magnetotail. *Geophysical Research Letters*, 25(8): 1249–1252, apr 1998. ISSN 00948276. . URL http://doi.wiley.com/10.1029/98GL00863.

N. Krupp, A. Lagg, S. Livi, B. Wilken, J. Woch, E. C. Roelof, and D. J. Williams. Global flows of energetic ions in Jupiter's equatorial plane: First-order approximation. *Journal of Geophysical Research*, 106(A11):26017–26032, November 2001. .

N. Krupp, V. M. Vasyliunas, J. Woch, A. Lagg, K. K. Khurana, M. G. Kivelson, B. H. Mauk, E. C. Roelof, D. J. Williams, S. M. Krimigis, W. S. Kurth, L. A. Frank, and W. R. Paterson. Dynamics of the Jovian magnetosphere. In Fran Bagenal, Timothy E. Dowling, and William B. McKinnon, editors, *Jupiter. The Planet, Satellites and Magnetosphere*, volume 1, pages 617–638. Cambridge University Press, 2004.

Irena Kupo, Yuri Meekler, and Aharon Eviatar. Detection of Ioinzed Sulfur in the Jovian Magnetosphere. *Astrophysical Journal*, 13(2):258–283, 1976.

W. S. Kurth, J D Sullivan, D A Gurnett, F. L. Scarf, H S Bridge, and E. C. Sittler. Observations of Jupiter's distant magnetotail and wake. *Journal of Geophysical Research*, 87(A12):10373, 1982. ISSN 0148-0227. . URL http://doi.wiley.com/10.1029/JA087iA12p10373.

W. S. Kurth, D. A. Gurnett, J. T. Clarke, P. Zarka, M. D. Desch, M. L. Kaiser, B. Cecconi, A. Lecacheux, W. M. Farrell, P. Galopeau, J.-C. Gérard, D. Grodent, R. Prangé, M. K. Dougherty, and F. J. Crary. An Earth-like correspondence between Saturn's auroral features and radio emission. *Nature*, 433(7027):722–725, feb 2005. ISSN 0028-0836. . URL http://www.nature.com/articles/nature03334.

W. S. Kurth, G. B. Hospodarsky, D. L. Kirchner, B. T. Mokrzycki, T. F. Averkamp, W. T. Robison, C. W. Piker, M. Sampl, and P. Zarka. The Juno Waves Investigation. *Space Science Reviews*, 213(1-4):347–392, 2017. ISSN 15729672. . URL http://dx.doi.org/10.1007/s11214-017-0396-y.

L. Lamy, B. Cecconi, R. Prangé, P. Zarka, J. D. Nichols, and J. T. Clarke. An auroral oval at the footprint of Saturns kilometric radio sources, colocated with the UV aurorae. *Journal of Geophysical Research: Space Physics*, 114(10):1–13, 2009. ISSN 21699402. .

James R Lemen, Dexter W. Duncan, Christopher Edwards, Frank M Friedlaender, Bruce K Jurcevich, Mons D Morrison, Larry A Springer, Robert A Stern, Jean-Pierre Wülser, Marilyn E Bruner, and Richard C Catura. The Solar X-ray Imager for GOES. *Proceedings of SPIE Vol. 5171 (Telescopes and Instrumentation for Solar Astrophysics)*, 5171:65–76, 2004. ISSN 0277786X. .

R. P. Lepping, L. F. Burlaga, M. D. Desch, and L. W. Klein. Evidence for a distant (>8,700 RJ) Jovian magnetotail: Voyager 2 observations. *Geophysical Research Letters*, 9(8):885–888, 1982. ISSN 19448007. .

R. P. Lepping, M D Desch, L. W. Klein, E. C. Sittler, J D Sullivan, W S Kurth, and K W Behannon. Structure and other properties of Jupiter's distant magnetotail. *Journal of Geophysical Research: Space Physics*, 88(A11):8801–8815, nov 1983. ISSN 01480227. . URL http://doi.wiley.com/10.1029/JA088iA11p08801.

Malcolm S. Longair. *High Energy Astrophysics*. Cambridge University Press, 2011.

C. T. S. Lorch, L. C. Ray, C. S. Arridge, K. K. Khurana, C. J. Martin, and A. Bader. Local Time Asymmetries in Jupiter's Magnetodisc Currents. *Journal of Geophysical Research (Space Physics)*, 125(2):e27455, February 2020. .

Philippe Louarn, A. Roux, S. Perraut, W. Kurth, and D. Gurnett. A study of the large-scale dynamics of the jovian magnetosphere using the galileo plasma wave experiment. *Geophysical Research Letters*, 25(15):2905–2908, 1998. ISSN 00948276. .

Philippe Louarn, Christopher P. Paranicas, and William S. Kurth. Global magnetodisk disturbances and energetic particle injections at Jupiter. *Journal of Geophysical Research: Space Physics*, 119(6):4495–4511, June 2014. .

C. K. Louis, R. Prangé, L. Lamy, P. Zarka, M. Imai, W. S. Kurth, and J. E.P. Connerney. Jovian Auroral Radio Sources Detected In Situ by Juno/Waves: Comparisons With Model Auroral Ovals and Simultaneous HST FUV Images. *Geophysical Research Letters*, 46(21):11606–11614, 2019. ISSN 19448007. .

R. L. Lysak and Y. Song. Field Line Resonances in Jupiter's Magnetosphere. *Geophysical Research Letters*, 47(18), 2020. ISSN 19448007. .

X Ma, B Stauffer, P A Delamere, and A Otto. Asymmetric Kelvin-Helmholtz propagation at Saturn's dayside magnetopause. *Journal of Geophysical Research: Space Physics*, 120(3):1867–1875, mar 2015. ISSN 21699380. . URL http://doi.wiley.com/10.1002/2014JA020746.

R. J. MacDowall, M. L. Kaiser, M. D. Desch, W. M. Farrell, R. A. Hess, and R. G. Stone. Quasiperiodic Jovian Radio bursts: observations from the Ulysses 1. MacDowall, R. J. et al. Quasiperiodic Jovian Radio bursts: observations from the Ulysses Radio and Plasma Wave Experiment. Planet. Space Sci. 41, 1059–1072 (1993).Radio and Plasma Wave Ex. *Planetary and Space Science*, 41(11-12):1059–1072, 1993. ISSN 00320633. .

I. R. Mann, I. Voronkov, M. Dunlop, E. Donovan, T. K. Yeoman, D. K. Milling, J. Wild, K. Kauristie, O. Amm, S. D. Bale, A. Balogh, A. Viljanen, and H. J. Opgenoorth. Coordinated ground-based and Cluster observations of large amplitude global magnetospheric oscillations during a fast solar wind speed interval. *Annales Geophysicae*, 20(4):405–426, 2002. ISSN 09927689. .

H Manners and A Masters. The Global Distribution of Ultra-Low-Frequency Waves in Jupiter's Magnetosphere. *Journal of Geophysical Research: Space Physics*, 2020. ISSN 2169-9380. . URL https://doi.org/10.1002/essoar.10503411.1https://onlinelibrary.wiley.com/doi/10.1029/2020JA028345.

H. Manners, A. Masters, and J. N. Yates. Standing Alfvén Waves in Jupiter's Magnetosphere as a Source of ˜ 10- to 60-Min Quasiperiodic Pulsations. *Geophysical Research Letters*, 45(17):8746–8754, sep 2018. ISSN 00948276. . URL http://doi.wiley.com/10.1029/2018GL078891.

A. Masters. A More Viscous-Like Solar Wind Interaction With All the Giant Planets. *Geophysical Research Letters*, 45(15):7320–7329, 2018. ISSN 19448007. .

A. Masters, N. Achilleos, C. Bertucci, M. K. Dougherty, S. J. Kanani, C. S. Arridge, H. J. McAndrews, and A. J. Coates. Surface waves on Saturn's dawn flank magnetopause driven by the Kelvin-Helmholtz instability. *Planetary and Space Science*, 57(14-15): 1769–1778, 2009. ISSN 00320633. . URL http://dx.doi.org/10.1016/j.pss.2009.02.010.

A. Masters, J. P. Eastwood, M. Swisdak, M. F. Thomsen, C. T. Russell, N. Sergis, F. J. Crary, M. K. Dougherty, A. J. Coates, and S. M. Krimigis. The importance of plasma β conditions for magnetic reconnection at Saturn's magnetopause. *Geophysical Research Letters*, 39(8):1–6, 2012. ISSN 00948276. .

B. H. Mauk, D. K. Haggerty, S. E. Jaskulek, C. E. Schlemm, L. E. Brown, S. A. Cooper, R. S. Gurnee, C. M. Hammock, J. R. Hayes, G. C. Ho, J. C. Hutcheson, A. D. Jacques, S. Kerem, C. K. Kim, D. G. Mitchell, K. S. Nelson, C. P. Paranicas, N. Paschalidis, E. Rossano, and M. R. Stokes. The Jupiter Energetic Particle Detector Instrument (JEDI) Investigation for the Juno Mission. *Space Science Reviews*, 213(1-4):289–346, 2017. ISSN 15729672. .

B.H. Mauk, I.J. Cohen, D.K. Haggerty, G.B. Hospodarsky, J.E.P. Connerney, B.J. Anderson, F. Bagenal, R.W. Ebert, S.J. Bolton, J.L. Burch, S.M. Levin, R.B. Torbert,

S.K. Vines, and J.H. Westlake. Investigation of mass/charge-dependent escape of energetic ions across the magnetopauses of Earth and Jupiter. *Journal of Geophysical Research: Space Physics*, pages 1–29, 2019. ISSN 21699380. . URL http://doi.wiley.com/10.1029/2019JA026626.

Ahilleas N. Maurellis, Thomas E. Cravens, G. Randall Gladstone, J .Hunter Waite, and Loren W. Acton. Jovian X-ray emission from solar X-ray scattering. *Geophysical Research Letters*, 27(9):1339–1342, 2000. ISSN 00948276. .

D. J. McComas and F. Bagenal. Jupiter: A fundamentally different magnetospheric interaction with the solar wind. *Geophysical Research Letters*, 34(20):1–5, 2007. ISSN 00948276. .

D. J. McComas, F. Allegrini, F. Bagenal, F. Crary, R. W. Ebert, H. Elliott, A. Stern, and P. Valek. Diverse Plasma Populations and Structures in Jupiter's Magnetotail. *Science*, 318(5848):217–220, oct 2007. ISSN 0036-8075. . URL https://www.sciencemag.org/lookup/doi/10.1126/science.1147393.

D. J. McComas, N. Alexander, F. Allegrini, F. Bagenal, C. Beebe, G. Clark, F. Crary, M. I. Desai, A. De Los Santos, D. Demkee, J. Dickinson, D. Everett, T. Finley, A. Gribanova, R. Hill, J. Johnson, C. Kofoed, C. Loeffler, P. Louarn, M. Maple, W. Mills, C. Pollock, M. Reno, B. Rodriguez, J. Rouzaud, D. Santos-Costa, P. Valek, S. Weidner, P. Wilson, R. J. Wilson, and D. White. The Jovian Auroral Distributions Experiment (JADE) on the Juno Mission to Jupiter. *Space Science Reviews*, 213(1-4): 547–643, 2017. ISSN 15729672. . URL http://dx.doi.org/10.1007/s11214-013-9990-9.

Seán McEntee. SeanMcEntee/CXO_and_GOES_analyses: Release of alternative go_chandra and new PI filtering method for analysing Jupiter's X-rays using Chandra HRC-I, November 2021. URL https://doi.org/10.5281/zenodo.5657142.

Albert E. Metzger, David A. Gilman, Joe L. Luthey, Kevin C. Hurley, Herbert W. Schnopper, Frederick D. Seward, and James D. Sullivan. Detection of X Rays From Jupiter. *Journal of Geophysical Research*, 88(A10):7731–7741, 1983. ISSN 01480227. .

S. E. Milan. Modeling Birkeland currents in the expanding/contracting polar cap paradigm. *Journal of Geophysical Research: Space Physics*, 118(9):5532–5542, 2013. ISSN 21699402. .

Alessandro Moirano, Alessandro Mura, Alberto Adriani, Vincent Dols, Bertrand Bonfond, Jack H. Waite, Vincent Hue, Jamey R. Szalay, Ali H. Sulaiman, Bianca M. Dinelli, Federico Tosi, Francesca Altieri, Andrea Cicchetti, Gianrico Filacchione, Davide Grassi, Alessandra Migliorini, Maria L. Moriconi, Raffaella Noschese, Giuseppe Piccioni, Roberto Sordini, Diego Turrini, Christina Plainaki, Giuseppe

Sindoni, Stefano Massetti, Robert L. Lysak, Stavro L. Ivanovski, and Scott J. Bolton. Morphology of the Auroral Tail of Io, Europa, and Ganymede From JIRAM L-Band Imager. *Journal of Geophysical Research: Space Physics*, 126(9):e29450, September 2021. .

Kimberly M. Moore, Rakesh K. Yadav, Laura Kulowski, Hao Cao, Jeremy Bloxham, John E.P. Connerney, Stavros Kotsiaros, John L. Jørgensen, José M.G. Merayo, David J. Stevenson, Scott J. Bolton, and Steven M. Levin. A complex dynamo inferred from the hemispheric dichotomy of Jupiter's magnetic field. *Nature*, 561 (7721):76–78, 2018. ISSN 14764687. . URL http://dx.doi.org/10.1038/s41586-018-0468-5.

Kaya Mori, Charles Hailey, Gabriel Bridges, Shifra Mandel, Amani Garvin, Brian Grefenstette, William Dunn, Benjamin J Hord, Graziella Branduardi-Raymont, John Clarke, Caitriona Jackman, Melania Nynka, and Licia Ray. Observation and origin of non-thermal hard X-rays from Jupiter. *Nature Astronomy*, feb 2022. ISSN 2397-3366. . URL https://www.nature.com/articles/s41550-021-01594-8.

S. K. Morley, A. P. Rouillard, and M. P. Freeman. Recurrent substorm activity during the passage of a corotating interaction region. *Journal of Atmospheric and Solar-Terrestrial Physics*, 71(10-11):1073–1081, July 2009. .

J. U. Ness, J. H.M.M. Schmitt, and J. Robrade. Detection of Saturnian X-ray emission with XMM-Newton. *Astronomy and Astrophysics*, 414(3):49–52, 2004a. ISSN 00046361. .

J. U. Ness, J. H.M.M. Schmitt, S. J. Wolk, K. Dennerl, and V. Burwitz. X-ray emission from Saturn. *Astronomy and Astrophysics*, 418(1):337–345, 2004b. ISSN 00046361. .

Jan-Uwe Ness and Juergen H. M. M. Schmitt. A Search for X-ray emission from Saturn, Uranus and Neptune. *Astronomy and Astrophysics*, 355(1):394–397, jan 2000. ISSN 00046361. URL http://arxiv.org/abs/astro-ph/0001131.

J. D. Nichols, J. T. Clarke, J. C. Gérard, D. Grodent, and K. C. Hansen. Variation of different components of jupiter's auroral emission. *Journal of Geophysical Research: Space Physics*, 114(6):1–18, 2009. ISSN 21699402. .

J. D. Nichols, B. Cecconi, J. T. Clarke, S. W.H. Cowley, J. C. Grard, A. Grocott, D. Grodent, L. Lamy, and P. Zarka. Variation of Saturn's UV aurora with SKR phase. *Geophysical Research Letters*, 37(15):1–5, 2010. ISSN 00948276. .

J. D. Nichols, S. V. Badman, E. J. Bunce, J. T. Clarke, S. W.H. Cowley, G. J. Hunt, and G. Provan. Saturn's northern auroras as observed using the Hubble Space Telescope. *Icarus*, 263:17–31, 2016. ISSN 10902643. . URL http://dx.doi.org/10.1016/j.icarus.2015.09.008.

J. D. Nichols, S. V. Badman, F. Bagenal, S. J. Bolton, B. Bonfond, E. J. Bunce, J. T. Clarke, J. E. P. Connerney, S. W. H. Cowley, R. W. Ebert, M. Fujimoto, J.-C. Gérard, G. R. Gladstone, D. Grodent, T. Kimura, W. S. Kurth, B. H. Mauk, G. Murakami, D. J. McComas, G. S. Orton, A. Radioti, T. S. Stallard, C. Tao, P. W. Valek, R. J. Wilson, A. Yamazaki, and I. Yoshikawa. Response of Jupiter's auroras to conditions in the interplanetary medium as measured by the Hubble Space Telescope and Juno. *Geophysical Research Letters*, 44(15):7643–7652, aug 2017. ISSN 00948276. . URL http://doi.wiley.com/10.1002/2017GL073029.

J. D. Nichols, A. Kamran, and S. E. Milan. Machine Learning Analysis of Jupiter's Far-Ultraviolet Auroral Morphology. *Journal of Geophysical Research (Space Physics)*, 124(11):8884–8892, November 2019. .

K Nykyri and A Otto. Plasma transport at the magnetospheric boundary due to reconnection in Kelvin-Helmholtz vortices. *Geophysical Research Letters*, 28(18): 3565–3568, sep 2001. ISSN 00948276. . URL http://doi.wiley.com/10.1029/2001GL013239.

Albert G. Opp. Scientific results from the Pioneer Saturn encounter: Summary. *Science*, 207(4429):401–403, 1980. ISSN 00368075. .

Mathew J. Owens and Robert J. Forsyth. The Heliospheric Magnetic Field. *Living Reviews in Solar Physics*, 10(1):5, November 2013. .

N. Ozak, D. R. Schultz, T. E. Cravens, V. Kharchenko, and Y. W. Hui. Auroral X-ray emission at Jupiter: Depth effects. *Journal of Geophysical Research: Space Physics*, 115 (11):1–13, 2010. ISSN 21699402. .

Laurent Pallier and Renée Prangé. More about the structure of the high latitude Jovian aurorae. *Planetary and Space Science*, 49(10-11):1159–1173, August 2001. .

E. N. Parker. Dynamics of the Interplanetary Gas and Magnetic Fields. *Astrophysical Journal*, 128:664, November 1958. .

Paul P. Plucinsky, Akos Bogdan, Herman L. Marshall, and Neil W. Tice. The complicated evolution of the ACIS contamination layer over the mission life of the Chandra X-ray Observatory. In Jan-Willem A. den Herder, Shouleh Nikzad, and Kazuhiro Nakazawa, editors, *Space Telescopes and Instrumentation 2018: Ultraviolet to Gamma Ray*, volume 10699 of *Society of Photo-Optical Instrumentation Engineers (SPIE) Conference Series*, page 106996B, July 2018. .

E. R. Priest. The sun and its magnetohydrodynamics. In Kivelson, Margaret G. and Russell, Christopher T., editor, *Introduction to Space Physics*, chapter 3, pages 58–90. Cambridge University Press, 1995.

E. R. Priest and T. G. Forbes. The magnetic nature of solar flares. *Astronomy and Astrophysics Review*, 10(4):313–377, January 2002. .

M. H. Quenouille. Problems in Plane Sampling. *The Annals of Mathematical Statistics*, 20(3):355–375, 1949. ISSN 0003-4851. . URL http://projecteuclid.org/euclid.aoms/1177706647http://projecteuclid.org/euclid.aoms/1177729989.

M. H. Quenouille. Notes on Bias in Estimation. *Biometrika*, 43(3/4):353, 1956. ISSN 00063444. .

A. Radioti, J. C. GéRard, D. Grodent, B. Bonfond, N. Krupp, and J. Woch. Discontinuity in Jupiter's main auroral oval. *Journal of Geophysical Research (Space Physics)*, 113(A1):A01215, January 2008. .

I. J. Rae, E. F. Donovan, I. R. Mann, F. R. Fenrich, C. E.J. Watt, D. K. Milling, M. Lester, B. Lavraud, J. A. Wild, H. J. Singer, H. Rème, and A. Balogh. Evolution and characteristics of global Pc5 ULF waves during a high solar wind speed interval. *Journal of Geophysical Research: Space Physics*, 110(A12):1–16, 2005. ISSN 21699402. .

J. J. Reed, C. M. Jackman, L. Lamy, W. S. Kurth, and D. K. Whiter. Low-Frequency Extensions of the Saturn Kilometric Radiation as a Proxy for Magnetospheric Dynamics. *Journal of Geophysical Research: Space Physics*, 123(1):443–463, 2018. ISSN 21699402. .

Christopher T. Russell. A brief history of Solar-Terrestrial Physics. In Kivelson, Margaret G. and Russell, Christopher T., editor, *Introduction to Space Physics*, chapter 1, pages 1–26. Cambridge University Press, 1995.

George B. Rybicki and Alan P. Lightman. *BREMSSTRAHLUNG*. John Wiley & Sons, Ltd, 1986.

B. R. Sandel, D. E. SHEMANSKY, A. L. BROADFOOT, J. L. BERTAUX, J. E. BLAMONT, M. J. S. BELTON, J. M. AJELLO, J. B. HOLBERG, S. K. ATREYA, T. M. DONAHUE, H. W. Moos, D. F. STROBEL, J. C. MCCONNELL, A. DALGARNO, R. GOODY, M. B. McELROY, and P. Z. TAKACS. Extreme Ultraviolet Observations from Voyager 2 Encounter with Jupiter. *Science*, 206(4421):962–966, 1979. ISSN 0036-8075. . URL https://www.sciencemag.org/lookup/doi/10.1126/science.206.4421.962.

B. R. Sandel, D. E. SHEMANSKY, A. L. BROADFOOT, J. B. HOLBERG, G. R. SMITH, J. C. MCCONNELL, D. F. STROBEL, S. K. ATREYA, T. M. DONAHUE, H. W. MOOS, D. M. HUNTEN, R. B. POMPHREY, and S. LINICK. Extreme Ultraviolet Observations from the Voyager 2 Encounter with Saturn. *Science*, 215(4532):548–553, jan 1982. ISSN 0036-8075. . URL https://www.sciencemag.org/lookup/doi/10.1126/science.215.4532.548.

E. J. Smith, Jr. Davis, L., D. E. Jones, Jr. Coleman, P. J., D. S. Colburn, P. Dyal, C. P. Sonett, and A. M. A. Frandsen. The planetary magnetic field and magnetosphere of Jupiter: Pioneer 10. *Journal of Geophysical Research*, 79(25):3501, January 1974. .

D J Southwood and M G Kivelson. A new perspective concerning the influence of the solar wind on the Jovian magnetosphere. *Journal of Geophysical Research*, 106(1): 6123–6130, 2001. .

David J. Southwood and Margaret G. Kivelson. Magnetospheric interchange motions. *Journal of Geophysical Reserach*, 94:299–308, January 1989. .

T. S. Stallard, S. Miller, S. W. H. Cowley, and E. J. Bunce. Jupiter's polar ionospheric flows: Measured intensity and velocity variations poleward of the main auroral oval. *Geophysical Research Letter*, 30(5):1221, March 2003. .

Tom Stallard, Steve Miller, Makenzie Lystrup, Nicholas Achilleos, Emma J Bunce, Christopher S Arridge, Michele K Dougherty, Stan W H Cowley, Sarah V Badman, Dean L Talboys, Robert H Brown, Kevin H Baines, Bonnie J Buratti, Roger N Clark, Christophe Sotin, Phil D Nicholson, and Pierre Drossart. Complex structure within Saturn's infrared aurora. *Nature*, 456:214–217, 2008a. .

Tom Stallard, Steve Miller, Henrik Melin, Makenzie Lystrup, Stan W H Cowley, Emma J Bunce, Nicholas Achilleos, and Michele Dougherty. Jovian-like aurorae on Saturn. *Nature*, 453:1083–1085, 2008b. .

A. H. Sulaiman, G. B. Hospodarsky, S. S. Elliott, W. S. Kurth, D. A. Gurnett, M. Imai, F. Allegrini, B. Bonfond, G. Clark, J. E. P. Connerney, R. W. Ebert, D. J. Gershman, V. Hue, S. Janser, S. Kotsiaros, C. Paranicas, O. Santolík, J. Saur, J. R. Szalay, and S. J. Bolton. Wave-Particle Interactions Associated With Io's Auroral Footprint: Evidence of Alfvén, Ion Cyclotron, and Whistler Modes. *Geophysical Research Letters*, 47(22): e88432, November 2020. .

B. G. Swithenbank-Harris, J. D. Nichols, and E. J. Bunce. Jupiter's Dark Polar Region as Observed by the Hubble Space Telescope During the Juno Approach Phase. *Journal of Geophysical Research: Space Physics*, 124(11):9094–9105, 2019. ISSN 21699402. .

B. G. Swithenbank-Harris, J. D. Nichols, F. Allegrini, F. Bagenal, B. Bonfond, E. J. Bunce, G. Clark, W. S. Kurth, B. H. Mauk, and R. J. Wilson. Simultaneous Observation of an Auroral Dawn Storm With the Hubble Space Telescope and Juno. *Journal of Geophysical Research: Space Physics*, 126(4):1–15, 2021. ISSN 21699402. .

Chihiro Tao, Ryuho Kataoka, Hiroshi Fukunishi, Yukihiro Takahashi, and Takaaki Yokoyama. Magnetic field variations in the Jovian magnetotail induced by solar wind dynamic pressure enhancements. *Journal of Geophysical Research: Space Physics*, 110(A11):1–9, 2005. ISSN 21699402. .

N. Thomas, F. Bagenal, T. W. Hill, and J. K. Wilson. The Io neutral clouds and plasma torus. In Fran Bagenal, Timothy E. Dowling, and William B. McKinnon, editors, *Jupiter. The Planet, Satellites and Magnetosphere*, volume 1, pages 561–591. University Cambridge Press, 2004.

M. F. Thomsen, S. V. Badman, C. M. Jackman, X. Jia, M. G. Kivelson, and W. S. Kurth. Energy-banded ions in Saturn's magnetosphere. *Journal of Geophysical Research: Space Physics*, 122(5):5181–5202, 2017. ISSN 21699402. .

Rudolf A. Treumann. The electron-cyclotron maser for astrophysical application. *The Astronomy and Astrophysics Review*, 13(4):229–315, August 2006. .

Vytenis M. Vasyliūnas. Plasma distribution and flow. In A. J. Dessler, editor, *Physics of the Jovian Magnetosphere*, chapter 11, pages 395–453. Cambridge University Press, Cambridge, jan 1983. . URL https://www.cambridge.org/core/product/identifier/CBO9780511564574A082/type/book{_}part.

S. Vaughan. A simple test for periodic signals in red noise. *Astronomy and Astrophysics*, 431(1):391–403, 2005. ISSN 00046361. .

Marissa F. Vogt, Margaret G. Kivelson, Krishan K. Khurana, Raymond J. Walker, Bertrand Bonfond, Denis Grodent, and Aikaterini Radioti. Improved mapping of Jupiter's auroral features to magnetospheric sources. *Journal of Geophysical Research: Space Physics*, 116(3), 2011. ISSN 21699402. .

Marissa F. Vogt, Caitriona M. Jackman, James A. Slavin, Emma J. Bunce, Stanley W. H. Cowley, Margaret G. Kivelson, and Krishan K. Khurana. Structure and statistical properties of plasmoids in Jupiter's magnetotail. *Journal of Geophysical Research: Space Physics*, 119(2):821–843, 2014. ISSN 21699291. . URL http://adsabs.harvard.edu/cgi-bin/nph-data{_}query?bibcode=2014JGRA..119.5364B{&}link{_}type=EJOURNAL{%}5Cnpapers3://publication/doi/10.1002/2013JA019607.

Marissa F. Vogt, Emma J. Bunce, Margaret G. Kivelson, Krishan K. Khurana, Raymond J. Walker, Aikaterini Radioti, Bertrand Bonfond, and Denis Grodent. Magnetosphere-ionosphere mapping at Jupiter: Quantifying the effects of using different internal field models. *Journal of Geophysical Research: Space Physics*, 120(4): 2584–2599, 2015. ISSN 21699402. .

Marissa F. Vogt, Szilard Gyalay, Elena A. Kronberg, Emma J. Bunce, William S. Kurth, Bertalan Zieger, and Chihiro Tao. Solar Wind Interaction With Jupiter's Magnetosphere: A Statistical Study of Galileo In Situ Data and Modeled Upstream Solar Wind Conditions. *Journal of Geophysical Research: Space Physics*, pages 1–30, 2019. ISSN 21699402. .

Jr. Waite, J. H., J. T. Clarke, T. E. Cravens, and C. M. Hammond. The Jovian Aurora: Electron or ion precipitation? *Journal of Geophysical Research: Space Physics*, 93(A7): 7244–7250, July 1988. .

Jr. Waite, J. H., F. Bagenal, F. Seward, C. Na, G. R. Gladstone, T. E. Cravens, K. C. Hurley, J. T. Clarke, R. Elsner, and S. A. Stern. ROSAT observations of the jupiter aurora. *Journal of Geophysical Research: Space Physics*, 99(A8):14799–14810, August 1994. .

D. M. Weigt, C. M. Jackman, W. R. Dunn, G. R. Gladstone, M. F. Vogt, A. D. Wibisono, G. Branduardi-Raymont, D. Altamirano, F. Allegrini, R. W. Ebert, P. W. Valek, M. F. Thomsen, G. Clark, and R. P. Kraft. Chandra Observations of Jupiter's X-ray Auroral Emission During Juno Apojove 2017. *Journal of Geophysical Research: Planets*, 125(4):e2019JE006262, apr 2020. ISSN 2169-9097. . URL https://onlinelibrary.wiley.com/doi/abs/10.1029/2019JE006262.

D. M. Weigt, C. M. Jackman, M. F. Vogt, H. Manners, W. R. Dunn, G. R. Gladstone, R. Kraft, G. Branduardi-Raymont, C. K. Louis, and S. C. McEntee. Characteristics of Jupiter's X-Ray Auroral Hot Spot Emissions Using Chandra. *Journal of Geophysical Research: Space Physics*, 126(9), 2021a. ISSN 2169-9380. . URL https://onlinelibrary.wiley.com/doi/10.1029/2021JA029243.

D M Weigt, W R Dunn, C M Jackman, R Kraft, G Branduardi-Raymont, J D Nichols, A D Wibisono, M F Vogt, and G R Gladstone. Searching for Saturn's X-rays during a rare Jupiter Magnetotail crossing using Chandra. *Monthly Notices of the Royal Astronomical Society*, 506(1):298–305, jul 2021b. ISSN 0035-8711. . URL https://academic.oup.com/mnras/article/506/1/298/6298248.

Dale Weigt. waledeigt/zeno-py: Release of python sso_freeze and go_chandra for analysing jovian X-rays from Chandra, November 2021. URL https://doi.org/10.5281/zenodo.5654904.

Martin C. Weisskopf, Harvey D. Tananbaum, Leon P. Van Speybroeck, and Stephen L. O'Dell. Chandra X-ray Observatory (CXO): overview. *X-Ray Optics, Instruments, and Missions III*, 4012(July 2000):2–16, 2000. .

D. R. Went, M. G. Kivelson, N. Achilleos, C. S. Arridge, and M. K. Dougherty. Outer magnetospheric structure: Jupiter and Saturn compared. *Journal of Geophysical Research: Space Physics*, 116(4):1–14, 2011. ISSN 21699402. .

A. D. Wibisono, G. Branduardi-Raymont, W. R. Dunn, A. J. Coates, D. M. Weigt, C. M. Jackman, Z. H. Yao, C. Tao, F. Allegrini, D. Grodent, J. Chatterton, A. Gerasimova, L. Kloss, J. Milović, L. Orlandiayni, A. K. Preidl, C. Radler, L. Summhammer, and D. Fleming. Temporal and Spectral Studies by XMM-Newton of Jupiter's X-ray Auroras During a Compression Event. *Journal of Geophysical Research: Space Physics*,

125(5):e2019JA027676, 2020. ISSN 21699402. . URL http://doi.wiley.com/10.1029/2019JA027676.

A. D. Wibisono, G. Branduardi-Raymont, W. R. Dunn, T. Kimura, A. J. Coates, D. Grodent, Z. H. Yao, H. Kita, P. Rodriguez, G. R. Gladstone, B. Bonfond, and R. P. Haythornthwaite. Jupiter's X-ray aurora during UV dawn storms and injections as observed by XMM-Newton, Hubble, and Hisaki. *Monthly Notices of the Royal Astronomical Society*, 507(1):1216–1228, October 2021. .

Belinda J Wilkes, Raffaele D'Abrusco, and Rafael Martínez-Galarza. Chandra x-ray observatory overview. In *The Chandra X-ray Observatory*, 2514-3433, pages 2–1 to 2–30. IOP Publishing, 2019. ISBN 978-0-7503-2163-1. . URL http://dx.doi.org/10.1088/2514-3433/ab43dcch2.

R. J. Wilson and M. K. Dougherty. Evidence provided by galileo of ultra low frequency waves within Jupiter's middle magnetosphere. *Geophysical Research Letters*, 27(6):835–838, 2000a. ISSN 00948276. .

R. J. Wilson and M. K. Dougherty. Evidence provided by galileo of ultra low frequency waves within Jupiter's middle magnetosphere. *Geophysical Research Letters*, 27(6):835–838, 2000b. ISSN 00948276. .

R. J. Wilson, P. A. Delamere, F. Bagenal, and A. Masters. Kelvin-Helmholtz instability at Saturn's magnetopause: Cassini ion data analysis. *Journal of Geophysical Research: Space Physics*, 117(A3):n/a–n/a, 2012. ISSN 01480227. . URL http://doi.wiley.com/10.1029/2011JA016723.

Hans Wolter. Spiegelsysteme streifenden einfalls als abbildende optiken für röntgenstrahlen *("Glancing Incidence Mirror Systems as Imaging Optics for X-ray")*. *Annalen der Physik*, 445(1):94–114, January 1952. .

E. E. Woodfield, R. B. Horne, S. A. Glauert, J. D. Menietti, and Y. Y. Shprits. The origin of Jupiter's outer radiation belt. *Journal of Geophysical Research: Space Physics*, 119(5): 3490–3502, May 2014. .

G. Xystouris, E. Sigala, and H. Mavromichalaki. A Complete Catalogue of High-Speed Solar Wind Streams during Solar Cycle 23. *Solar Physics*, 289(3):995–1012, 2014. .

Z. H. Yao, B. Bonfond, G. Clark, D. Grodent, W. R. Dunn, M. F. Vogt, R. L. Guo, B. H. Mauk, J. E.P. Connerney, S. M. Levin, and S. J. Bolton. Reconnection- and Dipolarization-Driven Auroral Dawn Storms and Injections. *Journal of Geophysical Research: Space Physics*, 125(8), 2020. ISSN 21699402. .

Zhonghua Yao, William R Dunn, Emma E Woodfield, George Clark, Barry H Mauk, Robert W Ebert, Denis Grodent, Bertrand Bonfond, Dongxiao Pan, I Jonathan Rae, Binbin Ni, Ruilong Guo, Graziella Branduardi-Raymont, Affelia D Wibisono, Pedro

Rodriguez, Stavros Kotsiaros, Jan-uwe Ness, Frederic Allegrini, William S Kurth, G Randall Gladstone, Ralph Kraft, Ali H Sulaiman, Harry Manners, Ravindra T Desai, and Scott J Bolton. Revealing the source of Jupiter's x-ray auroral flares. *Science Advances*, 7(28):eabf0851, jul 2021. ISSN 2375-2548. . URL https://advances.sciencemag.org/lookup/doi/10.1126/sciadv.abf0851.

Philippe Zarka. Auroral radio emissions at the outer planets: Observations and theories. *Journal of Geophysical Research: Planets*, 103(E9):20159–20194, aug 1998. ISSN 01480227. . URL http://doi.wiley.com/10.1029/98JE01323.

B. Zhang, P. A. Delamere, X. Ma, B. Burkholder, M. Wiltberger, J. G. Lyon, V. G. Merkin, and K. A. Sorathia. Asymmetric Kelvin-Helmholtz Instability at Jupiter's Magnetopause Boundary: Implications for Corotation-Dominated Systems. *Geophysical Research Letters*, 45(1):56–63, 2018. ISSN 19448007. .

Binzheng Zhang, Peter A. Delamere, Zhonghua Yao, Bertrand Bonfond, D. Lin, Kareem A. Sorathia, Oliver J. Brambles, William Lotko, Jeff S. Garretson, Viacheslav G. Merkin, Denis Grodent, William R. Dunn, and John G. Lyon. How Jupiter's unusual magnetospheric topology structures its aurora. *Science Advances*, 7 (15):1–7, 2021. ISSN 23752548. .

Bertalan Zieger and Kenneth C. Hansen. Statistical validation of a solar wind propagation model from 1 to 10 AU. *Journal of Geophysical Research: Space Physics*, 113(A8):A08107, August 2008. .